University of Nevada, Reno

Computational, Synthetic, and Spectroscopic Investigations of PTA and Derivatives Towards Drug Development and Rare Earth Metal Extraction from Aqueous Media

A dissertation submitted in partial fulfillment of the requirements
for the degree of
Doctor of Philosophy in Chemistry

by

Travis Cournoyer

Dr. Brian J. Frost/Dissertation Advisor

August, 2017

UNIVERSITY OF NEVADA RENO **THE GRADUATE SCHOOL**

We recommend that the dissertation
prepared under our supervision by

TRAVIS COURNOYER

entitled

Computational, Synthetic, and Spectroscopic Investigations of PTA and Derivatives Towards Drug Development and Rare Earth Metal Extraction from Aqueous Media

be accepted in partial fulfillment of the
requirements for the degree of

DOCTOR OF PHILOSOPHY

Brian Frost, Ph.D., Advisor

Sean Casey, Ph.D., Committee Member

Andrew Geraci, Ph.D., Committee Member

Wesley Chalifoux, Ph.D., Committee Member

Sage Hiibel, Ph.D., Graduate School Representative

David W. Zeh, Ph.D., Dean, Graduate School

August, 2017

Abstract

The synthesis of novel upper-rim PTA-amides, where PTA is 1,3,5-triaza-7-phosphaadamantane, was attempted through several synthetic routes including those utilizing both amine and carboxylic acid-based PTA starting materials. Nitrogen-carbon amide bond formation was attempted between upper-rim PTA-enamines and nitrogen-protected amino acids with the coupling agent 3-[bis(dimethylamino)methyliumyl]-3H-benzotriazol-1-oxide (HBTU) and diisopropylethylamine (DIPEA). The upper-rim benzylamide of PTA was prepared by nucleophilic attack of methyl-1,3,5-triaza-7-phosphatricyclo[3.3.1.1]-decane-6-carboxylate (PTA-CO_2Me) by benzylamine, facilitated by sodium methoxide in THF. Hydrochloride salts of butylamine and benzylamine as well as methyl ester-protected amino acids histidine and glycine were coupled to lithium 1,3,5-triaza-7-phosphaadamantane-6-carboxylate (PTA-CO_2Li) with the assistance of HBTU and DIPEA in DMF. These upper-rim PTA amides were characterized with both NMR spectroscopy and Fourier-Transform Infrared Spectroscopy (FT-IR) and selectivity as high as 100% was observed when the reaction was conducted with alkyl and aryl substrates.

The oxidation of upper-rim PTA enamines was optimized and the isomerization kinetics of one derivative PTA=C[$C_5H_2(OMe)_3$]NH_2 were investigated with time-resolved $^{31}P\{^1H\}$ NMR at variable temperatures. Equilibrium constants of 0.871, 0.866, and 0.897 were determined for the isomerization at 25 ºC, 35 ºC, and 45 ºC, respectively. Rate constants for conversion of the E isomer to the Z isomer were found to be 1.42×10^{-2}, 2.52×10^{-2}, and 5.27×10^{-2} at the same temperatures as well, respectively.

The coordination modes of PTA were investigated with Density Functional Theory (DFT) to elucidate the location of electron density around the nucleophilic phosphorus and nitrogen atoms of the phosphine. It was found that most of the electron density of the Highest Occupied Molecular Orbital (HOMO) is centered around a nitrogen atom, which potentially explains the observed borane substitution behavior that has been referenced in previous publications, at least in part. The coordination modes of several metal-PTA and metal-O=PTA complexes were also investigated with nickel and Ln^{3+}, respectively, where Ln^{3+} is La, Ce, Eu, Sm, and Yb. Characterization with $^{31}P\{^{1}H\}$ NMR spectroscopy (solid state and solution state), single-crystal X-ray diffraction, and FT-IR suggests that the nickel-PTA complexes are phosphorus-bound, as opposed to nitrogen-bound as was previously eluded to in the literature. Characterization of lanthanide complexes with O=PTA reveal oxygen-coordination is the exclusive coordination mode between the phosphine oxide and the metals.

The pH-dependent precipitation of lanthanides from aqueous media with the use of lithium 1,3,5-triaza-7-phosphaadamantane-6-carboxylate (PTA-CO_2Li) was investigated and optimized. The pK_a of [PTA-CO_2^-][H^+] was experimentally determined to be 6.1 ± 0.2 through an NMR titration, and relative energy calculations comparing the different isomers of the ligand suggest that protonation of the 3-nitrogen yields the most stable structure and the carboxylic acid is the least stable. The pK_a of [PTA-$(CO_2)_2^-$][H^+] was experimentally determined to be 6.09 ± 0.52 through an NMR titration as well. Reaction conditions required to precipitate lanthanides (La^{3+}, Gd^{3+}, and Yb^{3+}) from aqueous media with [PTA-CO_2^-][H^+] *via* hydrothermal treatment were investigated and optimized. It was found that the precipitation of lanthanides form aqueous media is most efficient when the initial

reaction pH lies close to 4 and the phosphine to lanthanide ratio exceeds 3:1. Finally, dilution of these precipitates in acidic media with chloride salts followed by basification with sodium hydroxide to pH > 10 yields the lanthanide hydroxides, which can be calcined to yield lanthanide oxides in a more carbon-neutral manner than the lanthanide oxalates which are currently being utilized in the industry to precipitate lanthanides from aqueous media.

Dedicated to my family

Acknowledgements

I would like to thank Dr. Brian J. Frost for being a phenomenal advisor and human being. There will never be enough words to express my sincere gratitude to Dr. Frost for taking me into his research group and giving me the chance to continue my pursuit of knowledge throughout this graduate program. His outstanding mentorship crafted me into the chemist I am today, for which I am eternally grateful. Also, I would like to thank Dr. Frost for allowing me to abandon my studies for months at a time throughout my graduate school experience as I pursued a career in electric vehicle design and manufacturing through internships and an early career head-start.

I would also like to extend my sincere gratitude to all of the committee members Dr. Sean Casey, Dr. Wesley Chalifoux, and Dr. Andrew Geraci for their time, attention, and recommendations for both my Comprehensive Examination as well as the work herein. I would also like to extend my thanks to Dr. Hongfei Lin for his time, attention, and recommendations for my Comprehensive Examination whilst acting as a thesis committee member for a brief time. I would also like to acknowledge Dr. Sage Hiibel for agreeing to be a committee member on my thesis committee on such short notice for defending the work proposed herein. I would also like to thank the faculty and staff of the chemistry building who went above and beyond to make my stay in Reno and the Chemistry Department fun, memorable, exciting, and never boring.

I would like to thank Dr. Stephen Spain and Mike Zierten for maintaining the department-owned hardware and software, respectively, that was absolutely necessary for this dissertation to be completed. I would also like to send out a special thanks to the

graduate students throughout the department and throughout my years of study who helped me complete this work either through lending chemicals, a good suggestion, or an hour lesson to teach me how an instrument worked. A special thanks to Dr. Jason Weedon for maintaining a ridiculously organized research notebook, the structure of which I adopted for mine own. Also, an enormous thank you to Danil Kaliakin, PhD for all of his help with teaching me the basics of computational chemistry enough for me to get the work done you will find herein. I would also like to thank all of the group members of the Frost research lab, with an emphasis on Linglee Ounkham who was a wonderful mentor and was extremely patient with me as I learned to be efficient in the laboratory. Also, I would like to specially thank Jacob Holmstrom, who was greatly helpful in determining the pK_a of both $[PTA\text{-}CO_2^-][H^+]$ and $[PTA\text{-}(CO_2)_2^-][H^+]$.

I would like to thank the entire Cell Quality and Materials Analysis team at Tesla Motors for welcoming me to the team as an intern for 15 months and making every minute of it enjoyable. The skills and lessons I learned during that time were greatly valuable and mostly to thank for how quickly I was able to complete the work you will find in this dissertation. I would like to give a special thanks to Dr. Bill Stockton and Dr. Ken Zemach both for convincing me to stick with the PhD program and not drop down to a Masters at a time when I was very close to doing so because I erroneously thought it might be a better career move. However, a bigger thanks to the Battery Design team at Faraday Future for hiring me knowing that I still had a dissertation to write, believing I would do it, and giving me the breathing room necessary to get it done during such a trying time for the company. There aren't enough words for how much I appreciate the overwhelming support and kindness I have been shown by individuals on the team and throughout the company at

such a difficult point in my life. Special thanks to Phil Weicker for making work more enjoyable than I ever imagined it could be through hilarity and ingenious design concepts.

I would like to thank my parents DPC and DMC, brother and sister Jarod and Nicole, and the rest of my family for their unconditional love and support throughout my graduate studies. A special thank you and I love you to JoAnn Noble, the best second Mom I was ever lucky enough to have. Finally, and most importantly, I would like to thank my wife Emily for her continuous love and support as she has supported me throughout my graduate studies and all of the work you'll find herein.

Table of Contents

List of Tables

List of Figures

List of Schemes

Compound Numbers

1	2	3	4	5a
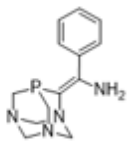	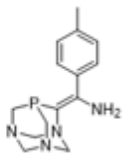	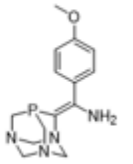	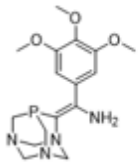	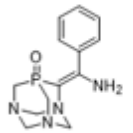

6a	7a	8a	9	10
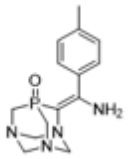	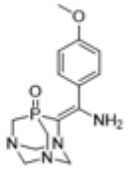	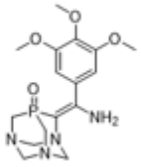	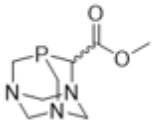	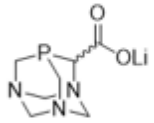

11	12	13	14	15
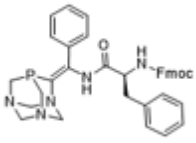	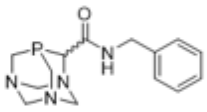	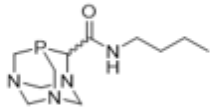	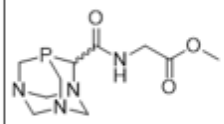	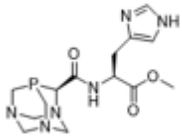

16	17	18	19	20
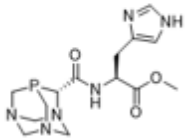	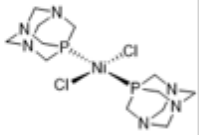	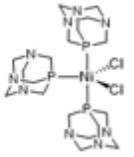	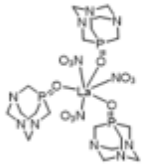	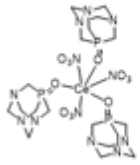

21	22	23	24	25
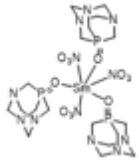	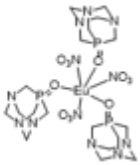	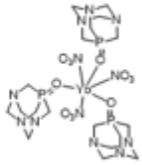	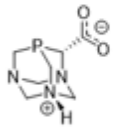	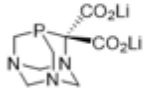

26	27	28	29	30
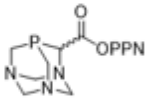	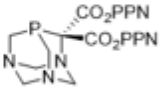	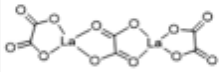	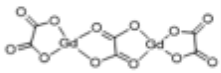	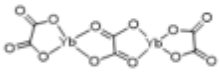

31	32	33	33
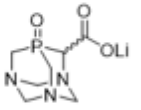	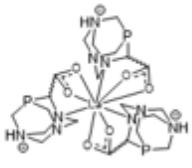	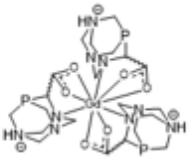	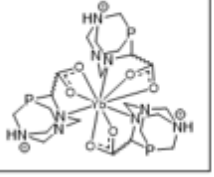

1 Chapter 1. Introduction

1.1 The Characteristics of 1,3,5-triaza-7-phosphaadamantane (PTA)

The phosphine 1,3,5-triaza-7-phosphaadamantane (PTA) was first reported in the literature by Daigle *et al.* in in 1974.[1] In the years since, PTA has maintained a steady presence throughout scientific literature in part because it is highly water soluble[2] (approx. 235 g/L) and has been derivatized into several useful compounds.[3–10] The water solubility of PTA is often assigned to the nucleophilic nitrogen atoms that can participate in hydrogen bonding with the hydrogen atoms of the solvent.[11] Until recently, most derivatized variations of PTA were found to be less soluble in water than the parent PTA itself.[12–14] PTA, rather than its derivatives, dominated much of the PTA coordination chemistry published in the first few decades after its first appearance in the literature.[15–27]

The synthesis of PTA can be completed in ambient conditions with readily available commercial reagents at the 100-gram scale. Combining a mixture of sodium hydroxide and *tetrakis*(hydroxymethyl)phosphonium chloride (THPC) with formaldehyde and hexamethylenetetramine (HMTA) in ice water following the literature method yields the phosphine between 60 – 80% yield.[13] PTA is soluble in dilute acids, methanol, hot ethanol, DMSO, acetone, chloroform, and dichloromethane, but not hydrocarbon solvents such as toluene, benzene, or hexane.[14] PTA has a measured cone angle of 103º similar to that of the alkyl phosphines, but its measured Tolman electronic parameter suggests that it is only about as electron donating as triphenyl phosphine.[23,28,29] Unlike the similarly sized alkyl phosphines, PTA is stable to air and water. Protonation of PTA with dilute acids regioselectively takes place at the nitrogen center to generate $[PTA\text{-}H]^+$ with a pK_a of 5.70, whereas respective protonation of the oxide generates $[O{=}PTA\text{-}H]^+$ with a pK_a of 2.52.[14]

1.2 Transition Metal Complexes of PTA

According to a review of PTA from 2004, "the coordination chemistry of PTA is significantly scarce when compared to other tertiary phosphines although its synthesis and characterization has been known for about thirty years."[14] Some coordination chemistry PTA compounds that have been investigated extensively in the literature include cytotoxic ruthenium drugs[30,31] and a wide variety of catalysts. The development and detailed discussion of ruthenium-PTA chemotherapeutic agents and their mechanisms will be discussed in detail in Chapter 3 of this dissertation. The transition metal complexes of PTA that have been developed and investigated as catalysts will be discussed here, however, as they have been a major driving force for much of the chemistry published by previous graduates from the Frost research group.[32–37]

Transition metal PTA complexes have been investigated as catalysts for several transformations including hydrogenation,[38] hydroformylation,[39] hydration,[37,40–43] and atom transfer radical addition.[44,45] A small sample of some PTA transition metal catalysts is shown in Figure 1.1 to give a general idea for what they often look like.[22,40,46,47]

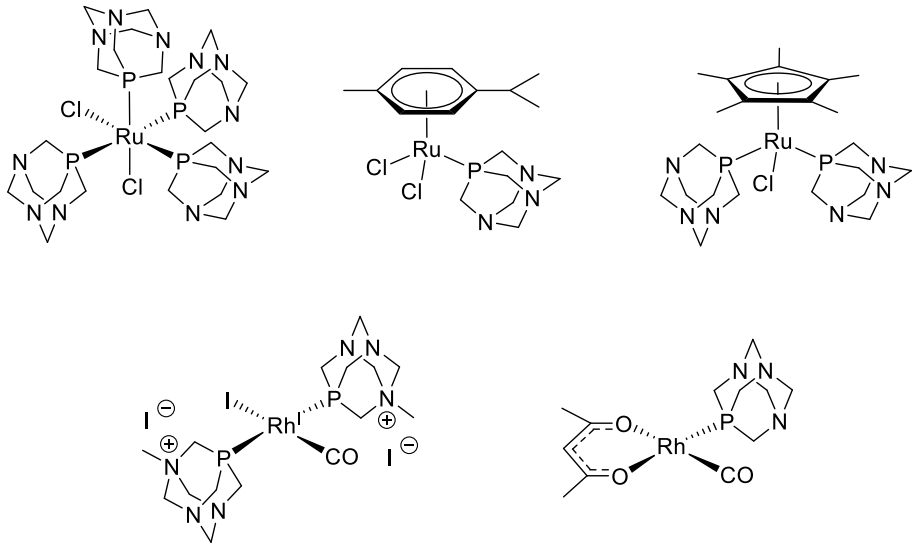

Figure 1.1: A selection of published ruthenium- and rhodium-based PTA catalysts.

$RuCl_2(PTA)_4$ has been found to be an effective aqueous-phase nitrile hydration catalyst for a wide range of substrates with as low as 0.001 mol % catalyst loading.[40] $RuCl_2(\eta^6$-cymene)PTA, commonly referred to as "RAPTA-C" was found to catalyze the hydrogenation of arenes in either water or tetrafluoroborate ionic liquids with turnover frequencies (TOF) as high as 206 per hour.[48] The complex $[Cp^*RuCl(PTA)_2]$ has been investigated as a hydrogenation catalyst for both benzylidene acetone[32,47] and carbonate.[38] Square planar [Rh(acac)(CO)(PTA)][22] and $[RhI(CO)(m\text{-}PTA^+\ I^-)_2]$[46] have both been investigated as hydroformylation catalysts with 1-hexene. Unfortunately, even though these transition metal complexes have demonstrated marked improvements in catalytic activity over traditional PPh_3-based catalysts,[40] some were found to underperform other water-soluble phosphine derivatives.[22,46] Of late, investigations are focusing on how these complexes can be made more active towards catalysis through derivation of PTA.[37,49–51]

1.3 **Upper-Rim Derivatives of PTA**

Up until the mid-2000's, all modifications of PTA took place on either the phosphorus atom, amine moieties, or carbon atoms along the triazacyclohexane ring.[52] The first modification of the upper-rim alkyl carbons was reported in 2006 when Frost *et al.* reported the synthesis of 1,3,5-triaza-7-phosphaadamantane-6-yllithium (PTA-Li).[49] Several more upper-rim PTA derivatives, the general structures for which can be seen in Figure 1.2, have been reported in the time since.[37,42,49,50,53,54]

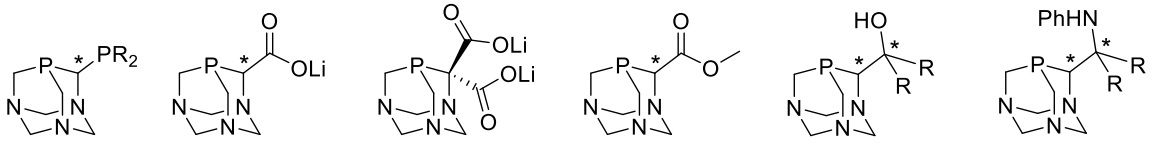

Figure 1.2: The general structure for some published upper-rim PTA derivatives.

These upper-rim derivatives are prepared by lithiation of the upper-rim alkyl carbon with *n*-BuLi followed by S_N2 addition to electrophiles such as aryl phosphine chlorides, carbon dioxide,

aldehydes, ketones, and imines. An exhaustive list of published upper-rim derivatives to date, minus the corresponding phosphine oxides, can be seen in Table 1.1.

Table 1.1
^{31}P-NMR chemical shifts and water solubility data for PTA and its upper-rim derivatives.

Ligand	^{31}P {^{1}H}[a]	*M*	S^{o}_{25} (*g / L*)	*Ref*
PTA	-102.3	1.5	235	[14]
PTA-PPh_2	-100.1, -19.8	--	--	[49]
PTA-P(*i*-Pr)$_2$	-98.3, -3.3	0.049	13.3	[42]
PTA-P(N*i*-Pr)$_2$(CH$_2$)$_2$	-100.4, -100.2	0.030	10	[42]
PTA-CPh_2OH	-95.5	0.017	5.9	[50]
PTA-C($C_6H_4OMe)_2OH$	-96.4	0.027	10.6	[50]
PTA-CH(C_6H_4OMe)OH	-102.6, -105.7	0.038	11.1	[50]
PTA-CH(ferrocenyl)OH	-100.6, -103.1	0.011	3.9	[50]
PTA-CH(MeIm)OH	-103.39	1.2	320	[54]
PTA-C(MeIm)$_2$OH	-97.55	0.22	78	[54]
PTA-CHPhNHPh	-102.4, -105.9	0.014	4.8	[37]
PTA-CPh_2NHPh	-97.7	0.0065	2.7	[37]
PTA-CH(*p*-C_6H_4OMe)NHPh	-102.1, -105.9	0.013	4.9	[37]
PTA-CO_2Li[b]	-88	3.8	800	[50]
PTA-($CO_2Li)_2$[b]	-88.4	[d]	[d]	--
PTA-CO_2Me[c]	-93.7	[d]	[d]	--

[a] In $CDCl_3$. [b] In D_2O. [c] In CD_3OD. [d] Not measured.

Most of the published upper-rim PTA derivatives have been coordinated to metals to elucidate their efficacy as catalysts. Krogstad *et al.* prepared K^2-*P,N*-[RuCl(η^6-cymene)(PTA-CH(1-MeIm)OH)]Cl and K^2-*P,N*-[RuCl(η^6-cymene)(PTA-C(1-MeIm)$_2$OH)]Cl complexes and investigated their potential for hydrogenation of acetophenone and the reduction of cyclohexanone.[54] Frost *et al.* synthesized [K^2-*P,N*-RuCl(η^6-toluene)(PTA-CPh_2NHPh)]PF_6 and measured a TOF of 285 per hour for the hydration of benzonitrile with a catalyst loading of 0.001 mol %.[37] Variable K^1 and K^2 coordination modes were observed in ruthenium complexes with upper-rim β-aminophosphines depending on solvent and counterion,[37] and even though their activity as nitrile hydration catalysts was impressive overall, it still did not exceed the performance

of $Ru(PTA)_4Cl_2$.[40] Meanwhile, the upper-rim carbonyl derivatives of PTA have been left relatively unexplored as ligands for catalysts since their first publication.[50]

1.4 Upper-Rim PTA Carbonyls

Lithium 1,3,5-triaza-7-phosphaadamantane-6-carboxylate (PTA-CO_2Li) can be prepared *via* one of the two synthetic routes outlined in Scheme 1.1. The racemate is easily prepared by bubbling gaseous carbon dioxide through a cold dispersion of lithiated PTA (PTA-Li) in THF. Conducting the reaction without solvent, however, yields a mixture of PTA-CO_2Li, PTA-$(CO_2Li)_2$, and PTA, where the latter two are produced in a 1:1 ratio.[50] This led to the assumption that generation of the bis-carboxylate followed a synthetic mechanism by which PTA-CO_2Li is generated, deprotonated at the alpha position by another PTA-Li molecule, and carboxylated again. Since both of these carbonyl derivatives of PTA are insoluble in organic solvents, washing with chloroform or dichloromethane easily removes any residual PTA from the product mixture.

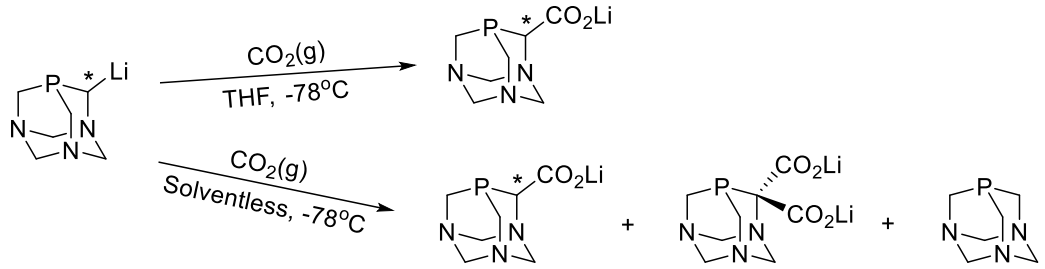

Scheme 1.1: Synthesis of PTA-CO_2Li via two synthetic routes.

Both PTA-CO_2li and PTA-$(CO_2Li)_2$ are highly soluble in water, methanol, DMSO, and DMF and insoluble in organic solvents such as chloroform, hexane, and ether. The two phosphines can easily be distinguished with $^{31}P\{^1H\}$ NMR in water, with chemical shifts of -88.4 ppm for PTA-CO_2Li and -87.4 ppm for PTA-$(CO_2Li)_2$. Addition of trimethylsilyl chloride to a methanolic solution of PTA-CO_2Li yields PTA-CO_2Me in an approximate 47% yield. This ligand was found to be stable to air in the solid state like most PTA derivatives, but in solution appeared to more air

sensitive, as crystal growth of the ligand also oxidized it to yield O=PTA-CO_2Me. Single crystal X-Ray Diffraction (XRD) of the resultant crystalline product revealed an elongated P1 – C1 bond length, where C1 is the substituted carbon, compared to P1 – C2 and P1 – C3 bond lengths.[49,50]

1.5 Organization and Scope

The two primary projects of this dissertation are the attempted syntheses of PTA amides for cancer drug development and the precipitation of REEs from aqueous media with PTA-CO_2Li. Also included are the results of computational and crystallographic experiments focused on improving our understanding behind the multimodal nature of PTA and its derivatives in general. This dissertation is divided into 6 chapters with a terminal appendix. Chapter 1 outlines the general background of PTA, its upper-rim derivatives, and the research trajectories for both. In chapter 2 I review my efforts to elucidate the kinetics and thermodynamics of *E* to *Z* isomerization for oxidized upper-rim PTA enamines. Chapter 3 discusses the several different chemical recipes utilized to prepare novel upper-rim PTA amides with subsequent characterization to support each. Chapter 4 focuses on computational, crystallographic, and spectroscopic investigations behind PTA and O=PTA with nickel and lanthanides, respectively. Chapter 5 is entirely devoted to my efforts utilizing PTA-CO_2Li to precipitate rare earth elements (REEs) from aqueous media. The main conclusions of these projects, future work left to be done for each, and eventual expected impact to respective fields are enumerated in chapter 6. The Appendix is included for referenced data that would likely overwhelm the reader if it was included within these chapters.

1.6 References

(1) Daigle, D. J.; Pepperman, A. B.; Vail, S. L. *J. Heterocycl. Chem.* **1974**, *11* (3), 407–408.

(2) Joó, F. *Aqueous Organometallic Catalysis*; Kluwer Academic Publishers: Dordrecht, 2001.

(3) Čaplar, V.; Šunjić, V.; Kafjež, F. *J. Heterocycl. Chem.* **1974**, *11* (6), 1055–1060.

(4) Daigle, D. J.; Pepperman, A. B. *J. Chem. Eng. Data* **1975**, *20* (4), 448–449.

(5) Navech, J.; Kraemer, R.; Majoral, J.-P. *Tetrahedron Lett.* **1980**, *21* (15), 1449–1452.

(6) Frank, A. W.; Daigle, D. J. *Phosphorus and Sulfur* **1981**, *10*, 255–260.

(7) Cowley, A. H.; Lattman, M.; Stricklen, P. M.; Verkade, J. G. *Inorg. Chem.* **1982**, *21* (3), 543–549.

(8) Forward, J. M.; Staples, R. J.; Liu, C. W.; Fackler, J. P. *Acta Crystallogr. Sect. C Cryst. Struct. Commun.* **1997**, *53* (2), 195–197.

(9) Blunden, B. M.; Lu, H.; Stenzel, M. H. *Biomacromolecules* **2013**, *14* (12), 4177–4188.

(10) Ferretti, V.; Fogagnolo, M.; Marchi, A.; Marvelli, L.; Sforza, F.; Bergamini, P.; Chimiche, S.; Fossato, V. *Inorg. Chem.* **2014**, *53*, 4881–4890.

(11) Lanorio, J. P. Synthesis, Characterization, and Reactivity of the Half-Sandwich Ruthenium (II) Hydride Complexes of 1,3,5-Triaza-7-Phosphaadamantane, University of Nevada, Reno, 2014.

(12) Darensbourg, D. J.; Yarbrough, J. C.; Lewis, S. J. *Organometallics* **2003**, *22* (10), 2050–2056.

(13) Daigle, D. J. *Inorg. Synth.* **1998**, *32*, 40–45.

(14) Phillips, A. D.; Gonsalvi, L.; Romerosa, A.; Vizza, F.; Peruzzini, M. *Coord. Chem. Rev.* **2004**, *248*, 955–993.

(15) Darensbourg, M. Y.; Daigle, D. *Inorg. Chem.* **1975**, *14* (5), 1217–1218.

(16) Darensbourg, D. J.; Kump, R. L. *Inorg. Chem.* **1978**, *17* (9), 2680–2682.

(17) Alyea, E. C.; Fisher, K. J.; Johnson, S. *Can. J. Chem.* **1989**, *67* (8), 1319–1323.

(18) Asali, K. J.; Awad, H. H.; Kimbrough, J. F.; Lang, B. C.; Watts, J. M.; Dobson, G. R. *Organometallics* **1991**, *10* (6), 1822–1826.

(19) Alyea, E. C.; Fisher, K. J.; Foo, S.; Philip, B. *Polyhedron* **1993**, *12* (5), 489–492.

(20) Forward, J.; Jr, J. F.; Staples, R. *Organometallics* **1995**, *14*, 4194–4198.

(21) Schibli, R.; Katti, K. V; Volkert, W. A.; Barnes, C. L. *Inorg. Chem.* **1998**, *37* (20), 5306–5312.

(22) Pruchnik, F. P.; Smoleński, P.; Wajda-Hermanowicz, K. *J. Organomet. Chem.* **1998**, *570* (1), 63–69.

(23) Alyea, E. C.; Ferguson, G.; Kannan, S. *Polyhedron* **1998**, *17* (16), 2727–2732.

(24) Krogstad, D. A.; Halfen, J. A.; Terry, T. J.; Young, V. G. *Inorg. Chem.* **2001**, *40* (3), 463–471.

(25) Assefa, Z.; Omary, M. A.; McBurnett, B. G.; Mohamed, A. A.; Patterson, H. H.; Staples, R. J.; Fackler, J. P. *Inorg. Chem.* **2002**, *41* (24), 6274–6280.

(26) Darensbourg, D. J.; Phelps, A. L.; Adams, M. J.; Yarbrough, J. C. *J. Organomet. Chem.* **2003**, *666* (1–2), 49–53.

(27) Dyson, P. J.; Ellis, D. J. *Adv. Synth. Catal.* **2003**, *345* (12), 211–215.

(28) Tolman, C. A. *Chem. Rev.* **1977**, *77* (3), 313–348.

(29) Britvin, S. N.; Lotnyk, A. *J. Am. Chem. Soc.* **2015**, *137* (16), 5526–5535.

(30) Wee, H. A.; Dyson, P. J. *Eur. J. Inorg. Chem.* **2006**, No. 20, 4003–4018.

(31) Hartinger, C. G.; Dyson, P. J. *Chem. Soc. Rev.* **2009**, *38* (2), 391–401.

(32) Frost, B. J.; Mebi, C. a. *Organometallics* **2004**, *23* (7), 5317–5323.

(33) Weeden, J. a.; Huang, R.; Galloway, K. D.; Gingrich, P. W.; Frost, B. J. *Molecules* **2011**, *16*, 6215–6231.

(34) Mebi, C. a.; Frost, B. J. *Zeitschrift für Anorg. und Allg. Chemie* **2007**, *633* (Ii), 368–371.

(35) Frost, B. J.; Miller, S. B.; Rove, K. O.; Pearson, D. M.; Korinek, J. D.; Harkreader, J. L.;

Mebi, C. a.; Shearer, J. *Inorganica Chim. Acta* **2006**, *359*, 283–288.

(36) Mebi, C. A.; Nair, R. P.; Frost, B. J. *Organometallics* **2007**, *26*, 429–438.

(37) Lee, W. C.; Sears, J. M.; Enow, R. A.; Eads, K.; Krogstad, D. A.; Frost, B. J. *Inorg. Chem.* **2013**, *52*, 1737–1746.

(38) Bosquain, S. S.; Dorcier, A.; Dyson, P. J.; Erlandsson, M.; Gonsalvi, L.; Laurenczy, G.; Peruzzini, M. *Appl. Organomet. Chem.* **2007**, *21* (11), 947–951.

(39) Legrand, F.-X.; Hapiot, F.; Tilloy, S.; Guerriero, A.; Peruzzini, M.; Gonsalvi, L.; Monflier, E. *Appl. Catal. A Gen.* **2009**, *362* (1–2), 62–66.

(40) Lee, W.-C.; Frost, B. J. *Green Chem.* **2012**, *14*, 62–66.

(41) Ahmed, T. J.; Knapp, S. M. M.; Tyler, D. R. *Coord. Chem. Rev.* **2011**, *255* (7), 949–974.

(42) Sears, J. M.; Lee, W. C.; Frost, B. J. *Inorganica Chim. Acta* **2015**, *431*, 248–257.

(43) Mager, N.; Robeyns, K.; Hermans, S. *J. Organomet. Chem.* **2015**, *794*, 48–58.

(44) Nair, R. P.; Kim, T. H.; Frost, B. J. *Organometallics* **2009**, *28* (25), 4681–4688.

(45) Nair, R. P.; Pineda-Lanorio, J. a.; Frost, B. J. *Inorganica Chim. Acta* **2012**, *380*, 96–103.

(46) Pruchnik, F. P.; Smoleñski, P.; Gałdecka, E.; Gałdecki, Z. *New J. Chem.* **1998**, *22* (12), 1395–1398.

(47) Akbayeva, D. N.; Gonsalvi, L.; Oberhauser, W.; Peruzzini, M.; Vizza, F.; Brüggeller, P.; Romerosa, A.; Sava, G.; Bergamo, A. *Chem. Commun. (Camb).* **2003**, No. 2, 264–265.

(48) Dyson, P. J.; Ellis, D. J.; Henderson, W.; Laurenczy, G. *Adv. Synth. Catal.* **2003**, *345* (1–2), 216–221.

(49) Wong, G. W.; Harkreader, J. L.; Mebi, C. A.; Frost, B. J. *Inorg. Chem.* **2006**, *45* (17), 6748–6755.

(50) Wong, G. W.; Lee, W. C.; Frost, B. J. *Inorg. Chem.* **2008**, *47*, 612–620.

(51) Huang, R.; Frost, B. J. *Inorg. Chem.* **2007**, *46* (26), 10962–10964.

(52) Bravo, J.; Bolaño, S.; Gonsalvi, L.; Peruzzini, M. *Coord. Chem. Rev.* **2010**, *254* (5–6), 555–

607.

(53) Gonsalvi, L.; Guerriero, A.; Hapiot, F.; Krogstad, D. A.; Monflier, E.; Reginato, G.; Peruzzini, M. *Pure Appl. Chem.* **2012**, *85* (2), 385–396.

(54) Krogstad, D. A.; Guerriero, A.; Ienco, A.; Manca, G.; Peruzzini, M.; Reginato, G.; Gonsalvi, L. *Organometallics* **2011**, *30* (22), 6292–6302.

2 The Kinetics and Thermodynamics of *E*- to *Z*- Isomerization in Upper-Rim PTA Enamines

2.1 Introduction

2.1.1 Aminophosphines

Aminophosphines have received considerable attention because of their unique characteristics that make them useful ligands in catalysts[1] and synthons for chemical synthesis.[2] These types of ligands have been reported to stabilize transition metal complexes for catalysis.[3] The sterics and electronics of PN ligands can easily be tuned.[1,4] PN transition metal complexes have been demonstrated as effective catalysts for asymmetric hydrogenation,[5,6] hydrosilylation,[7,8] hydroarylation,[9] hydroboration,[10–13] and hydroformylation.[14–16] Some examples of catalysts prepared with these ligands are shown in Figure 2.1. The iron complex shown in that figure was found to catalyze the enantioselective hydrosilylation of $MesPhSiH_2$ with *ee* as high as 98%.[7] A turnover frequency of 20900 mol amide / mol catalyst (hr) was determined for $Ru(acac)_2(PPh_2py)_2$ as a catalyst for the hydration of benzonitrile.[17] In both of these publications, the authors mention that coordination to the ancillary nitrogen atoms likely facilitate the catalyzed reaction. Recently, PN aminophosphines have also been reported as more economical precursors for the synthesis of indium phosphide nanocrystals for optical applications.[18] Our research group has reported the synthesis and characterization of upper-rim substituted diastereomers of PTA aminophosphines.[19] These ligands were investigated as hemilabile ligands installed on ruthenium catalysts for aqueous-phase nitrile hydration. One catalyst, $[(\eta^6\text{-toluene})RuCl(PTA\text{-}CPh_2NHPh)][Cl]$, showed excellent efficiency as a catalyst and has high tolerance to several functional groups and air, although the specifics behind why are unclear.[19]

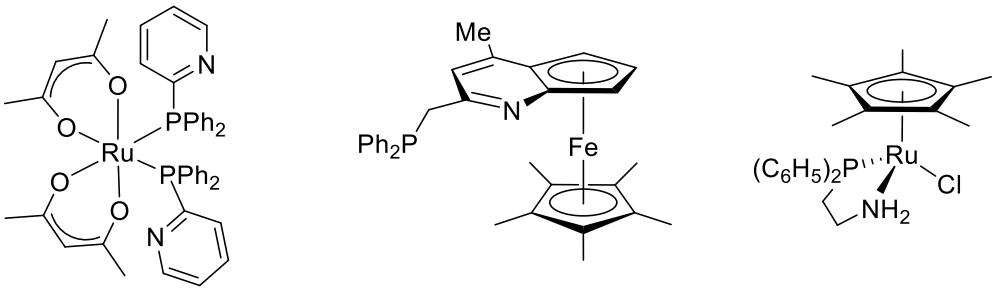

Figure 2.1: Some catalysts prepared with P,N aminophosphines.

More recently, our group reported the synthesis of upper-rim PTA enamines following the synthetic protocol in Scheme 2.1.[20] The synthesis was assumed to proceed *via* the imine tautomer, although the enamine products were all that were observed after the synthesis. The phenyl (**1**), tolyl (**2**), *p*-methoxy phenyl (**3**), and 3,4,5 tris-methoxy phenyl (**4**) enamines were prepared with 49 – 90% yield. These novel phosphines are the first PTA derivatives in which a carbon of the PTA cage is sp^2 hybridized. Coordination with tungsten carbonyl compounds was found to happen in a K^2-*P,N* chelate, where the ancillary enamine functional group has tautomerized to the imine as shown in Scheme 2.2. However, PPh_3 substitution at the tungsten metal center was found to displace the imine.

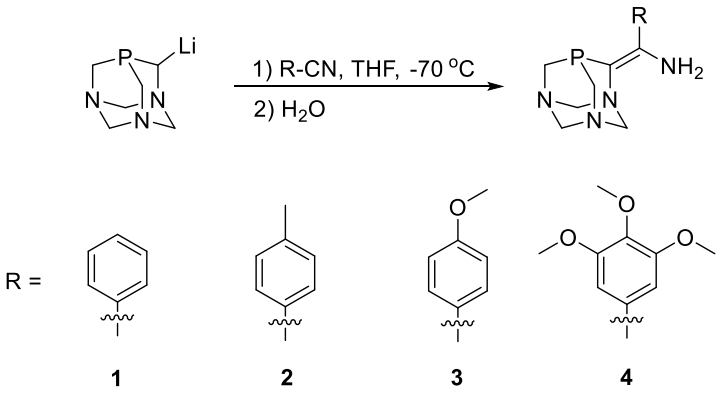

Scheme 2.1: Synthesis of upper-rim PTA enamines **1** - **4**.

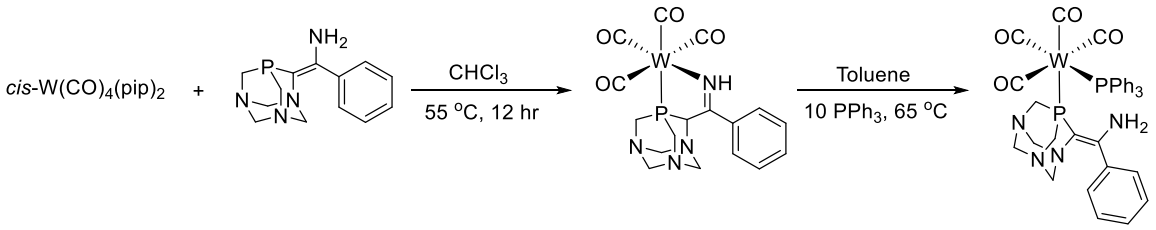

Scheme 2.2: Synthesis of tungsten compounds with upper-rim PTA enamines **1** - **4**.

Treatment of **1**- **4** with excess peroxide in THF yielded the *E* isomers of the respective oxides, **5a** – **8a** as shown in Figure 2.2 alongside the respective *Z* isomers **5b** – **8b**. These oxides were characterized with $^{31}P\{^{1}H\}$ NMR, $^{13}C\{^{1}H\}$ NMR, ^{1}H NMR, FT-IR, and single-crystal X-ray Crystallography. When dissolved in $CDCl_3$, each of these phosphine oxides were found to reach equilibrium with their respective *Z* isomers **5b** – **8b** in less than a few hours. The goal of this chapter will be to outline my efforts optimizing the synthesis for the oxidation of these compounds, investigating their recrystallization thermodynamics, and establishing constants for the kinetics and thermodynamics of *E* to *Z* isomerization between **8a** and **8b**.

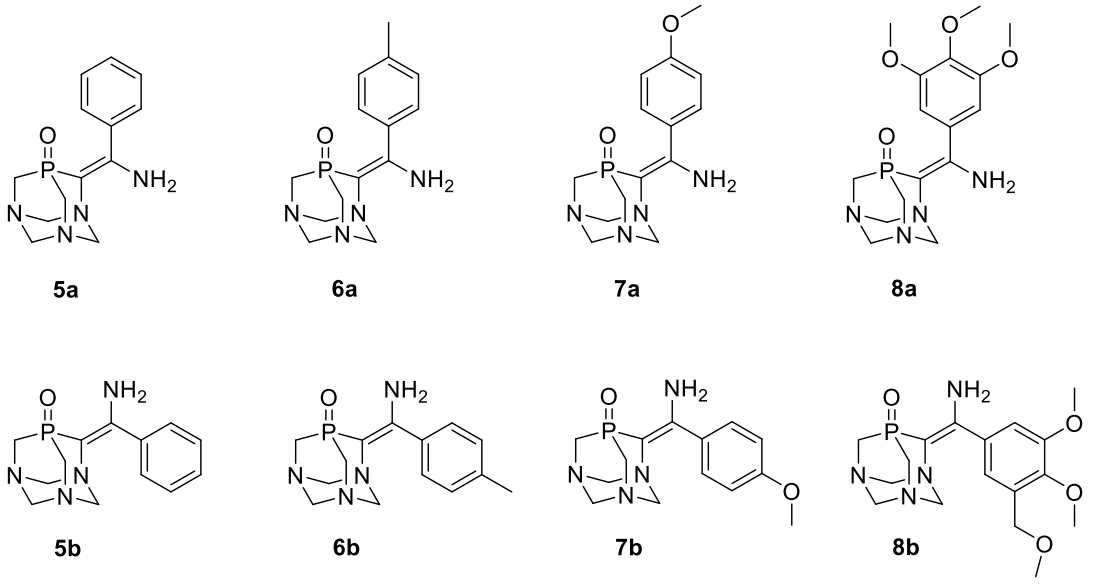

Figure 2.2: The *E* and *Z* isomers **5a**,**b** – **8**,**b**.

2.2 Results & Discussion

2.2.1 Synthesis and Purification of O=PTA=C[R]NH_2 Derivatives

Synthesis of O=PTA=C[R]NH_2 derviatives followed a slightly modified version of that previously reported by our group.[20] After synthesis of **1** – **4** according to the procedure previously reported by our research group, the oxides **5** – **8a** were prepared following the procedure outlined in Scheme 2.3. The products were dried over excess magnesium sulfate to remove excess water from the crude product. The product is extracted into DCM before recrystallization from a 1:1 mixture of Hexanes : DCM. The drying and with magnesium sulfate was not done for **8a** since it precipitates from the solution as a crystalline white powder that is easily separated from the reaction mixture *via* filtration.

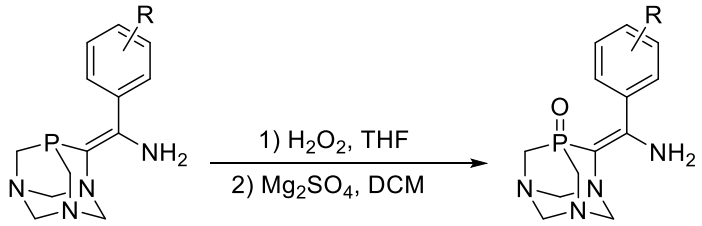

Scheme 2.3: Synthesis of **5a** – **7a**. Synthesis of **8a** only required Step 1 and filtration.

For **5a**, **6a**, and **7a**, $^{31}P\{^1H\}$ NMR of the crude products in THF before product isolation reveals a single peak corresponding to the *E*- isomer, as seen in the stacked spectra in Figure 2.3. This peak has previously been identified as the one corresponding to the *E* isomer by Dr. Enow, who determined this peak corresponds to that isomer by capturing single-crystal X-ray crystallography of the crystallized ligands prior to $^{31}P\{^1H\}$ NMR spectrum acquisition. This same $^{31}P\{^1H\}$ NMR spectrum was not included in this dissertation for **8a** because the ligand precipitates out of solution as it is formed, so the NMR spectrum does not reveal any peaks. Recrystallization of **5a** – **7a** from 1:1 mixtures of Hexanes : DCM yielded crystalline mixtures of *E* and *Z* isomers for each of these compounds. Attempts were made several times to crystallize pure crystals of the

E isomer for each of these compounds, but were unsuccessful except for a small sample of **6a** that was isolated for the work found in section 2.2.2 of this chapter. The $^{31}P\{^{1}H\}$ NMR spectrum for each of these compounds reveals that the peak for the *E* isomer is shifted upfield from that of the *Z* isomer by about 8 ppm each.

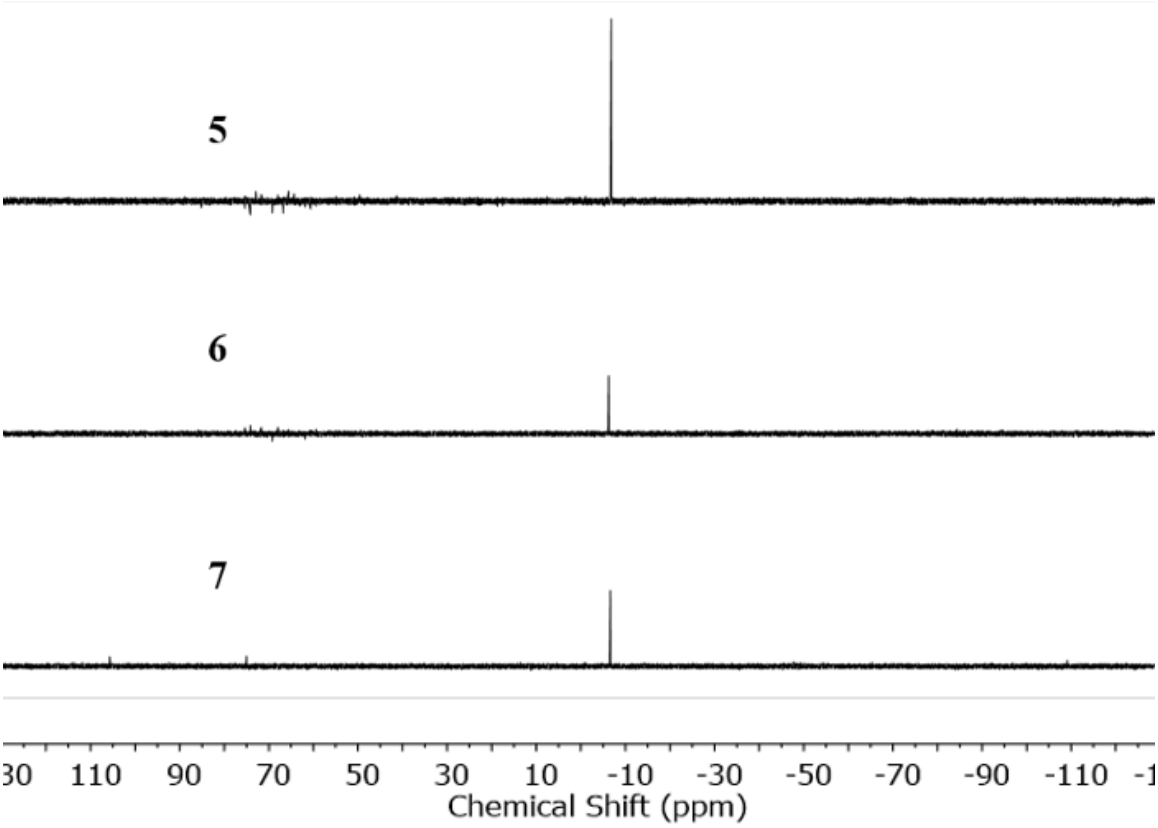

Figure 2.3: Stacked $^{31}P\{^{1}H\}$ NMR of crude **5a** – **7a** in THF after synthesis from **1** – **3**, respectively.

2.2.2 Selective Recrystallization of O=PTA=C[*p*-Tol]NH_2

The recrystallization method for **6** was investigated by $^{31}P\{^{1}H\}$ NMR spectroscopy in $CDCl_3$. A 16.8 mg sample of **6** was weighed carefully, diluted in a mixture of 1:1 Hexanes:DCM, and left in the freezer to recrystallize. The 9.6 mg of crystallized product was filtered and dried in vacuo, and the $^{31}P\{^{1}H\}$ NMR spectrum in $CDCl_3$ was collected revealing a single peak

corresponding to the E isomer for the compound. The filtrate from the recrystallization was concentrated under reduced pressure *via* rotary evaporation and the remaining product was weighed carefully, 7.2 mg. This product was then also then dissolved in $CDCl_3$ for ^{31}P $\{^1H\}$ NMR spectroscopy. These two NMR spectra are stacked with the ^{31}P $\{^1H\}$ NMR spectrum for **6** in $CDCl_3$ before recrystallization in Figure 2.4. The respective masses of starting sample, crystallized **6a**, and **6a** from recrystallization filtrate can be found compared against the E/Z ratio from the integrated peaks for each in Table 2.1.

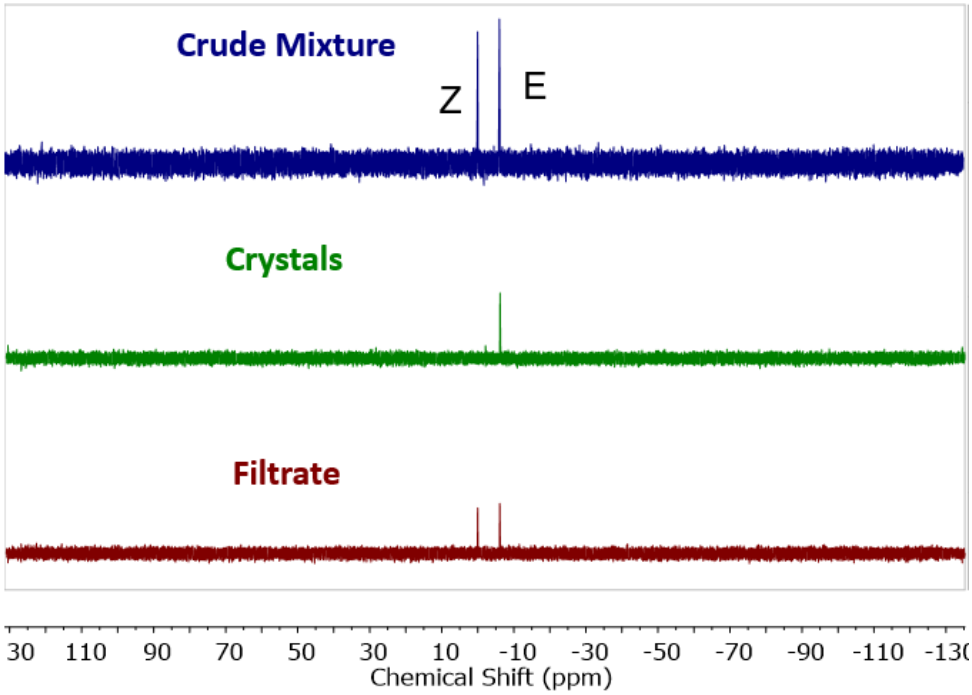

Figure 2.4: Stacked ^{31}P $\{^1H\}$ NMR of a crude mixture of **6a** and **6b**, crystals after recrystallization, and filtrate after recrystallization, all in $CDCl_3$.

Table 2.1: Mass and E/Z mole ratios of crude **6**, the isolated compound from the filtrate after recrystallization, and crystals of the **6a**.

	Mass [mg]	Mass %	**6a** / **6b** Ratio[a]
Crude mixture	16.8	100	1.17
Crystals	9.6	57	5.25
Filtrate	7.2	43	1.17

[a] From integrated areas under peaks from ^{31}P $\{^1H\}$ NMR in $CDCl_3$

As can be seen by the results in Table 2.1, the ratio of **6a** to **6b** is identical in both the crude mixture and the filtrate from the recrystallization. Further, while the mass of **6a** is only 9.1 mg in the crude mixture of the two isomers at equilibrium, there is 12.2 mg of **6a** combined between the crystals from recrystallization and in the remaining filtrate after recrystallization. Both of these results suggest that the mixture of **6a** and **6b** reach equilibrium in solution as the E isomer crystallizes out of solution as opposed to merely selectively recrystallizing **6a** rather than **6b**.

2.2.3 Kinetics and Thermodynamics of E to Z Isomerization of O=PTA=C[3,4,5-$C_5H_2(OMe)_3$]NH_2

The isomerization kinetics of **8a** to **8b** as shown in Scheme 2.4 were investigated with variable-temperature $^{31}P\{^1H\}$ NMR. The crystals of **8a** which had precipitated out of the reaction mixture during synthesis were dissolved in deuterated chloroform in an NMR tube and NMR spectra were recorded every 2 minutes for 4 hours. The experiment was run for 4 hours to allow plenty of time for **8a** to **8b** to reach equilibrium in solution. The ratio of **8a** to **8b** over time for each experiment was determined through peak height of the corresponding peaks (-2 ppm for **8b**, -8 ppm for **8a**) in each spectrum over the course of the experiment. The results from conducting this experiment at 25 ºC, 35 ºC, and 45 ºC can be seen in Figure 2.5. The raw spectra for each experiment at the three temperatures, as well as the tabulated peak heights utilized to generate the graph from the data can be found in the appendix (Figures A.1 – A.6).

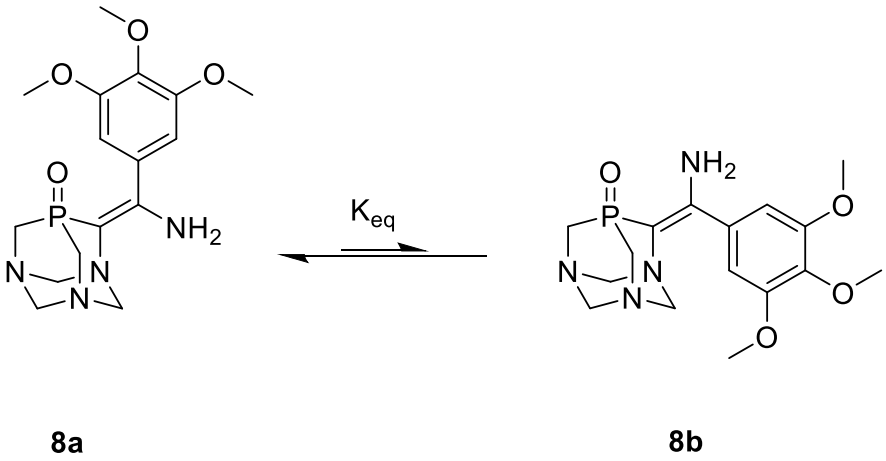

8a **8b**

Scheme 2.4: Isomerization of **8a** to **8b**.

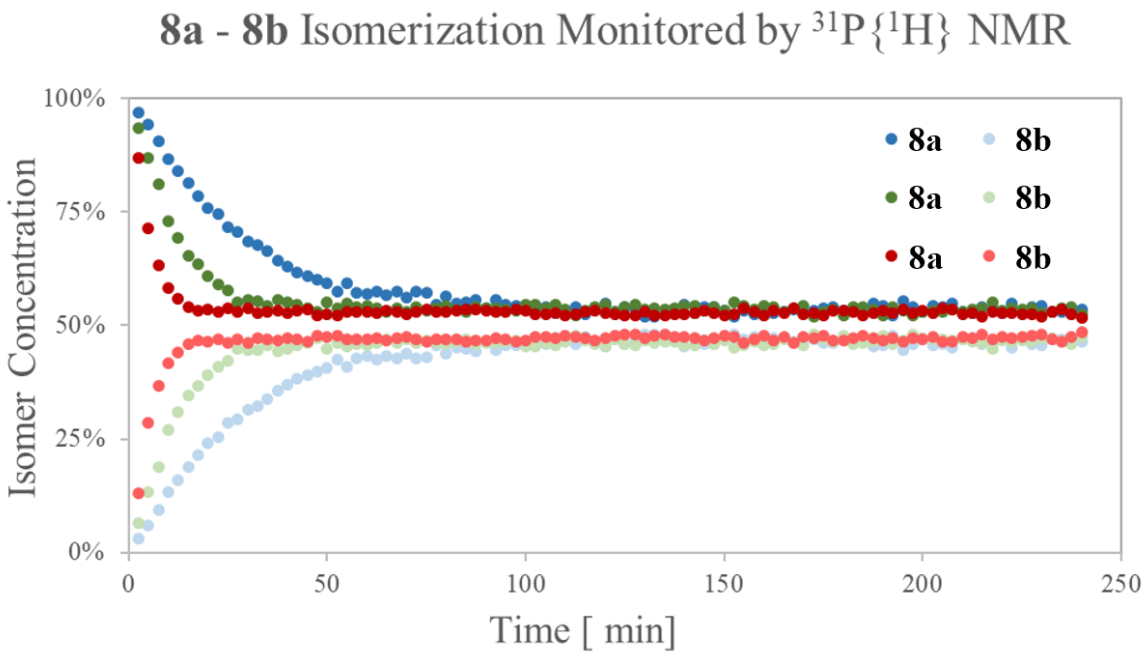

Figure 2.5: Isomerization kinetics of **8a** to **8b** in $CDCl_3$ at 25 ºC (*blue*), 35 ºC (*green*), and 45 ºC (*red*). For each temperature investigated, the darker color spectrum represents mole fraction of **8a** and the lighter color represents the mole fraction of **8b**, both as determined by peak heights from ^{31}P {^{1}H} NMR.

The data for all three experiments were utilized to elucidate both the equilibrium constant and rate constant for the isomerization of **8a** to **8b**. The equilibrium mole fractions of **8a** and **8b**

were calculated as the average ratio of peak heights for all samples after 100 minutes for each trial and applied to Equation 2.1 to yield the determined equilibrium constants at each temperature as seen in Table 2.2. The resulting K_{eq} values at each temperature for the isomerization are all within 4% of each other with no clear trend, indicative of a temperature-independent equilibrium between the isomers.

$$K_{eq} = \frac{Z\ Isomer}{E\ Isomer} \qquad \textbf{(2.1)}$$

Table 2.2: Averaged mole fractions[a] of both **8a** and **8b** at equilibrium at 25 ºC, 35 ºC, and 45 ºC, as well as the determined K_{eq} for the isomerization between the two at each temperature.

	Mole fraction of **8a**	Mole fraction of **8b**	K_{eq}
25 ºC	53.4	46.6	0.871
35 ºC	53.6	46.4	0.866
45 ºC	52.7	47.2	0.897

[a] Determined from peak height of each corresponding peak from $^{31}P\ \{^{1}H\}$ NMR in $CDCl_3$

First order reaction kinetics were assumed to calculate the rate constant for the isomerization of **8a** to **8b**. The initial reaction data from each variable temperature $^{31}P\ \{^{1}H\}$ NMR spectrum were substituted into the integrated rate law for first order kinetics, Equation 2.2, and plotted against time as seen in Figure 2.6. The rate constants in min^{-1} determined at 25 ºC, 35 ºC, and 45 ºC were $1.42 \times 10^{-2} \pm 2.42 \times 10^{-4}$, $2.52 \times 10^{-2} \pm 1.7 \times 10^{-3}$, and $5.27 \times 10^{-2} \pm 2.8 \times 10^{-3}$, respectively. The determined rate constants roughly double with each 10 ºC rise in temperature. The linear shape of the data in Figure 2.5 indicates first order reaction kinetics as would be expected for the isomerization. The data for this isomerization at 25 ºC, 35 ºC, and 45 ºC is included in the appendix of this dissertation in tabulated form in Figures A.2, A.4, and A.6, respectively.

$$\ln[\mathbf{8a}]_t = kt + \ln[\mathbf{8a}]_0 \qquad \textbf{(2.2)}$$

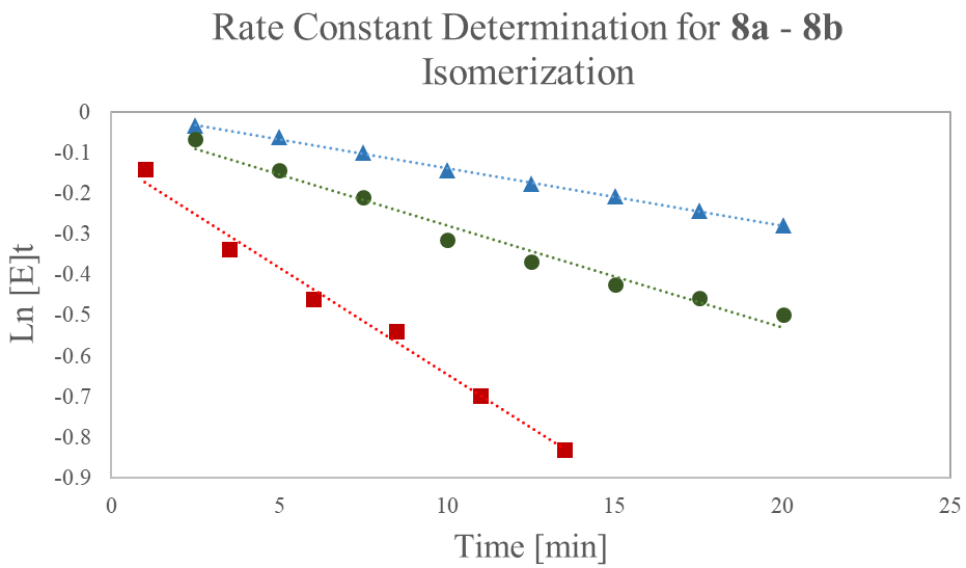

Figure 2.6: Initial reaction rate data for the isomerization of **8a** to **8b** at 25 ºC (*blue triangles*), 35 ºC (*green circles*), and 45 ºC (*red squares*).

2.2.4 Concluding Remarks

The phosphines **1** – **4** and the phosphine oxides **5a** – **8a** were prepared following previously reported procedures, although synthesis of the phosphine oxides was slightly improved upon. The recrystallization of **6a** was closely monitored so that the crystallization process could be better understood. It was found that the recrystallization of the compound takes place in parallel to the establishment of equilibrium between **6a** and **6b** as opposed to merely selectively crystallizing **6a** and leaving **6b** dissolved in solution. Time-resolved $^{31}P\{^{1}H\}$ NMR of **8a** in $CDCl_3$ was obtained at three different temperatures. From these data, equilibrium constants and rate constants were determined for each temperature. The equilibrium constants and rate constants determined at 25 ºC, 35 ºC, and 45 ºC were 0.871, 0.866, and 0.897 and rate constants were $1.42 \times 10^{-2} \pm 2.42 \times 10^{-4}$, $2.52 \times 10^{-2} \pm 1.7 \times 10^{-3}$, and $5.27 \times 10^{-2} \pm 2.8 \times 10^{-3}$, respectively. For future work on this project, the starting enamines **5a**, **6a**, and **7a** should be purified by chromatography prior to crystal growth to ensure good enough purity to fully characterize their thermodynamics and kinetics of *E* to *Z*

isomerization. Conducting time-resolved $^{31}P\{^{1}H\}$ NMR on the purified *E* isomers should further elucidate the behavior of these types of PTA derivatives.

2.3 Experimental

2.3.1 Methods & Materials

Unless otherwise noted, all manipulations were performed on a double-manifold Schlenk vacuum line under nitrogen or in a nitrogen-filled glovebox. Benzonitrile, *p*-tolunitrile, 4-methoxybenzonitrile, 3,4,5-trimethoxybenzonitrile, 30% hydrogen peroxide, and 2,5 *M* *n*-BuLi were all purchased from commercial sources and used as provided. Tetrakis(hydroxymethyl)phosphonium chloride was obtained from Cytec and used without further purification. Tetrahydrofuran (THF) was freshly distilled from sodium/benzophenone. Dichloromethane and chloroform were degassed with nitrogen gas and dried over molecular sieves. 1,3,5-triaza-7-phosphaadamantane (PTA),[21] PTA-Li,[22] and **1** – **4**[20] were prepared following a previously reported method. All NMR spectra were recorded with a Varian NMR System 400 spectrometer. Phosphorus NMR signals were referenced to an external standard of 85% phosphoric acid in D_2O, where all chemical shifts downfield the reference were assigned as positive.

2.3.2 Synthesis

Synthesis of O=PTA=C[R]NH_2

For the synthesis of **5a** – **7a**, 0.77 mmol of **1** – **3**, respectively, were dissolved in 20 mL THF. With stirring, 86.9 μL of 30% H_2O_2 (0.84 μmol, 1.1 equiv.) was added dropwise to the reaction mixture over the course of 5 minutes. After stirring for 4 hours under positive pressure of N_2 (g), the reaction mixture was dried over magnesium sulfate, concentrated under reduced pressure *via* rotary evaporation, and left to dry in vacuo overnight. 100% conversion to the oxidized *E* isomers confirmed with $^{31}P\{^1H\}$ NMR of the crude reaction mixture in THF for **5a**, **6a**, and **7a**. Detailed characterization for each of these phosphines has been previously reported.[20]

For the synthesis of **8a**, 0.77 mmol of **4** was dissolved in 20 mL THF. 86.9 μL of 30% H_2O_2 (0.84 μmol, 1.1 equiv.) was added dropwise to the reaction mixture over the course of 5 minutes. After stirring for 1 hour, the product **8a** had precipitated out of the reaction mixture as a crystalline product. The crude reaction mixture was left in the freezer overnight to crystallize more of the product. 100% conversion of **4** to **8a** determined by $^{31}P\{^1H\}$ NMR in $CDCl_3$. (Note: The *E* isomer starts isomerizing to the *Z* isomer very quickly after dissolving **8a** in chloroform, so this $^{31}P\{^1H\}$ NMR spectrum must be obtained immediately after dissolving the product in chloroform for accurate conversion.)

Time-resolved $^{31}P\{^1H\}$ NMR of 8a – 8b Isomerization

A small sample (~15 mg) of **8a** was loaded into an NMR tube under N_2 (g). This NMR tube was then placed in an oil bath set to the experiment temperature for 2 hours to equilibrate to temperature before the time-resolved experiment. The NMR was set to the experiment temperature and allowed to equilibrate for 1 hour. Immediately preceding the NMR experiment, 600 μL of $CDCl_3$ was added to the NMR tube, the sample was agitated, and the NMR tube was loaded into the spectrometer. The 'pad' parameter was set to record a $^{31}P\{^1H\}$ NMR spectrum every 32

seconds, each spectrum was collected with 50 scans, and a total of 96 spectra were collected at each temperature. The mole fraction of each isomer in solution was determined by peak height for each of the respective isomers **8a** (-8 ppm) and **8b** (-2 ppm). These peaks were assigned from previous experiments reported by our group. The crystals from recrystallization were characterized with X-ray crystallography before $^{31}P\{^{1}H\}$ NMR spectroscopy, which revealed a peak at -5.4 ppm and the slow growth of a peak at 0.2 ppm until equilibrium was established.

2.4 References

(1) Magee, M. P.; Luo, W.; Hersh, W. H. *Organometallics* **2002**, *21* (2), 362–372.

(2) Gopalakrishnan, J. *Appl. Organomet. Chem.* **2009**, *23* (8), 291–318.

(3) Grotjahn, D. B.; Incarvito, C. D.; Rheingold, A. L. *Angew. Chemie - Int. Ed.* **2001**, *40* (20), 3884–3887.

(4) Lindner, R.; Van Den Bosch, B.; Lutz, M.; Reek, J. N. H.; Van Der Vlugt, J. I. *Organometallics* **2011**, *30* (3), 499–510.

(5) Ito, M.; Koo, L. W.; Himizu, A.; Kobayashi, C.; Sakaguchi, A.; Ikariya, T. *Angew. Chemie - Int. Ed.* **2009**, *48* (7), 1324–1327.

(6) Chan, A.; Chen, C. C.; Cao, R.; Lee, M. R.; Peng, S. M.; Lee, G. H. *Organometallics* **1997**, *16* (10), 3469–3473.

(7) Tao, B.; Fu, G. C. *Angew. Chemie - Int. Ed.* **2002**, *41* (20), 3892–3894.

(8) Nishibayashi, Y.; Segawa, K.; Ohe, K.; Uemura, S. *Organometallics* **1995**, *14* (8), 5486–5487.

(9) Brunel, J. M.; Heumann, A.; Buono, G. *Angew. Chemie - Int. Ed.* **2000**, *39* (11), 1946–1949.

(10) Son, S. U.; Jang, H.-Y.; Han, J. W.; Lee, I. S.; Chung, Y. K. *Tetrahedron: Asymmetry* **1999**, *10*, 347–354.

(11) Doucet, H.; Fernandez, E.; Layzell, T. P.; Brown, J. M. *Chem. - A Eur. J.* **1999**, *5* (4), 1320–1330.

(12) McCarthy, M.; Guiry, P. J. *Polyhedron* **2000**, *19* (5), 541–543.

(13) McCarthy, M.; Hooper, M. W.; Guiry, P. J. *Chem. Commun.* **2000**, No. 14, 1333–1334.

(14) Arena, C. G.; Nicolo, F.; Drommi, D.; Bruno, G.; Faraone, F. *J. Chem. Soc. Chem. Commun.* **1994**, *30* (5), 2251–2252.

(15) Basoli, C.; Botteghi, C.; Cabras, M. A.; Chelucci, G.; Marchetti, M. *J. Organomet. Chem.* **1995**, *488* (1–2), C20–C22.

(16) Chelucci, G.; Cabras, M. A.; Botteghi, C.; Basoli, C.; Marchetti, M. *Tetrahedron Asymmetry* **1996**, *7* (3), 885–895.

(17) Oshiki, T.; Yamashita, H.; Sawada, K. *Organometallics* **2005**, *24* (26).

(18) Tessier, M. D.; De Nolf, K.; Dupont, D.; Sinnaeve, D.; De Roo, J.; Hens, Z. *J. Am. Chem. Soc.* **2016**, *138* (18), 5923–5929.

(19) Lee, W. C.; Sears, J. M.; Enow, R. A.; Eads, K.; Krogstad, D. A.; Frost, B. J. *Inorg. Chem.* **2013**, *52*, 1737–1746.

(20) Enow, R. A. E. Hemilabile [beta]-aminophosphine ligands derived from 1,3,5-Triaza-7-phosphaadamantane: Application in aqueous ruthenium catalyzed nitrile hydration, University of Nevada, Reno, 2014.

(21) Daigle, D. J. *Inorg. Synth.* **1998**, *32*, 40–45.

(22) Wong, G. W.; Lee, W. C.; Frost, B. J. *Inorg. Chem.* **2008**, *47*, 612–620.

3 Synthesis of Novel Upper-Rim PTA Amides

3.1 Introduction

3.1.1 Metal-Based Chemotherapy

The anti-cancer properties of diamminedichloro(II)platinum ("cisplatin") were first published the same year as the discovery of PTA.[1] Since then, the drug has led to remission of testicular cancer in 90% of patients, leading to widespread use of the drug to treat several types of cancer over the past few decades.[2] However, the low degree of specificity for cisplatin along with increased prevalence of cisplatin-resistant strains of cancer has left researchers investigating alternate metal-based anti-cancer drugs. These investigations have so far yielded several drug candidates, including the two ruthenium drugs KP1019 and NAMI-A shown in Figure 3.1, that have been investigated for their anti-cancer fighting capabilities.[3,4]

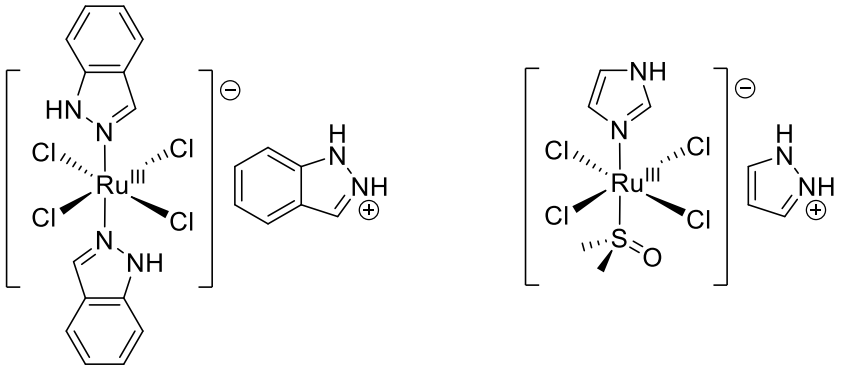

Figure 3.1: Two ruthenium-based drugs, KP1019 (*left*) and NAMI-A (*right*) were investigated in Phase 1 Human Trials for their efficacy as chemotherapeutic agents.

NAMI-A was found to stop the growth of metastatic tumors while inducing severe side-effects in patients, leading the researchers to recommend phase 2 trials not be pursued with the drug.[3] The Phase 1 trial investigating KP1019, however, yielded much more promising results. The drug caused no serious side-effects and led to complete remission of approximately 1/3 of all tumors for the six patients studied.[4] This, combined with the complete stabilization of 5 out of 6

patients studied for as long as ten weeks, led the researchers to recommend phase II trials. Alongside investigations of these drug candidates, several other metal-based compounds have been studied for antiproliferative and cytotoxic capabilities in recent times.[5] Of these, the compounds that have shown the most promise are "RAPTA" compounds, named such because of their general structure which includes ruthenium metal center, arene, and a PTA ligand.[6]

3.1.2 RAPTA Drugs for Cancer Treatment

The first RAPTA drug investigated for cytotoxicity was $RuCl_2(\eta^6$-cymene)(PTA) "RAPTA-C," seen with some other similar RAPTA drugs in Figure 3.2, which was found by Allardyce et al. in 2001 to unravel DNA in aqueous solutions with pH below 7.5.[6] Since cancerous cells tend to be more acidic through a phenomenon known as the Warburg effect,[7] this unraveling of DNA at lower pH sparked much more interest in these compounds for chemotherapy.

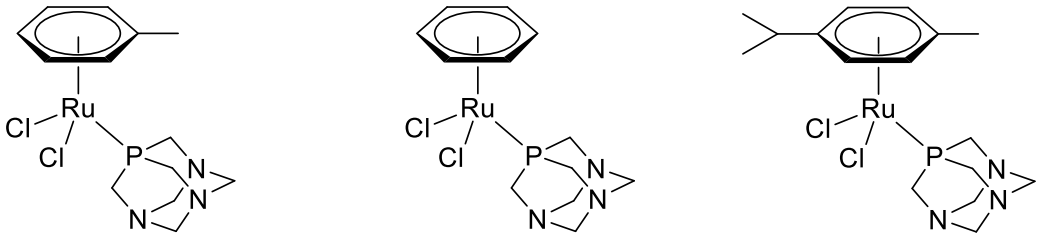

Figure 3.2: Some $RuCl_2(\eta^6$-arene)(PTA) complexes that have been investigated for their anti-cancer activity.

In 2005, the three RAPTA drugs investigated were only found to be active towards cancer treatment at markedly higher concentrations than for cisplatin, as seen in Table 3.1.[8] The RAPTA compounds tested exhibited no toxicity towards healthy cells at concentrations greater than the test's upper limit but toxicity for cancerous cells at concentrations as low as 74 μM, suggesting a selectivity for cancer that far outweighs that witnessed with cisplatin. In cancer treatment in living

beings, this would translate to a chemotherapeutic method with significantly less toxic side-effects typically seen with cisplatin today, as the pK_a-based cytotoxic mechanism would grant remarkable selectivity for cancerous masses over healthy tissues.

Table 3.1: In vitro IC_{50} concentrations for different RAPTA compounds with healthy human embryonic kidney (HEK293) and cancerous adenocarcinoma (TS/A) cells.[8]

	HEK293	TS/A
Cisplatin	7.3	0.53
RAPTA-B	> 300	231
RAPTA-C	> 300	> 300
RAPTA-T	> 300	74

The drawbacks to using RAPTA-C for chemotherapy include its low solubility, low toxicity, and the side-reactions that it undergoes with healthy tissue as it travels throughout the body on its way to cancerous masses.[5] As such, most of the published research surrounding the topic in recent years has focused on ways to increase the solubility,[9] cytotoxicity,[10–12] and rate of delivery[13] for these drugs. A computational DFT investigation from 2007 suggested that the cytotoxic mechanism for these RAPTA drugs is derived from the pK_a of labile water ligands after chloride displacement from the drug's original form.[14] It was found in other investigations that covalently attaching biologically active compounds to RAPTA drugs directly on the metal center,[11] on the arene,[10,15] or on the PTA ligand[9] such as with those compounds in Figure 3.3,[9,10,12,16] toxicity tends to increase but selectivity tends to go down. Also, the introduction of chirality to RAPTA drugs like those shown in Figure 3.4 revealed that chirality changes between RAPTA drugs have drastic effects on both cytotoxicity and selectivity for cancerous cells, as demonstrated by a difference in roughly 400 μM IC_{50} values for HEK293 cells for the two enantiomers of the compound on the left and a difference in roughly 26 μM IC_{50} values for A2780 cancerous cells for the two enantiomers of the compound on the right.[16] Further, a ruthenium PTA compound Ru(PTA)(curcumin)(η^6-cymene) was found to have greater selectivity for and activity against cancerous cell lines, demonstrated by IC_{50} values of 30 ± 1.0 μM for healthy HEK293 cells and

1.18 ± 0.02 μ*M* for cisplatin-resistant A2780cisR cells while the respective IC_{50} values for cisplatin are 7.3 ± 0.6 μ*M* and 25 ± 3.0 μ*M*.[11]

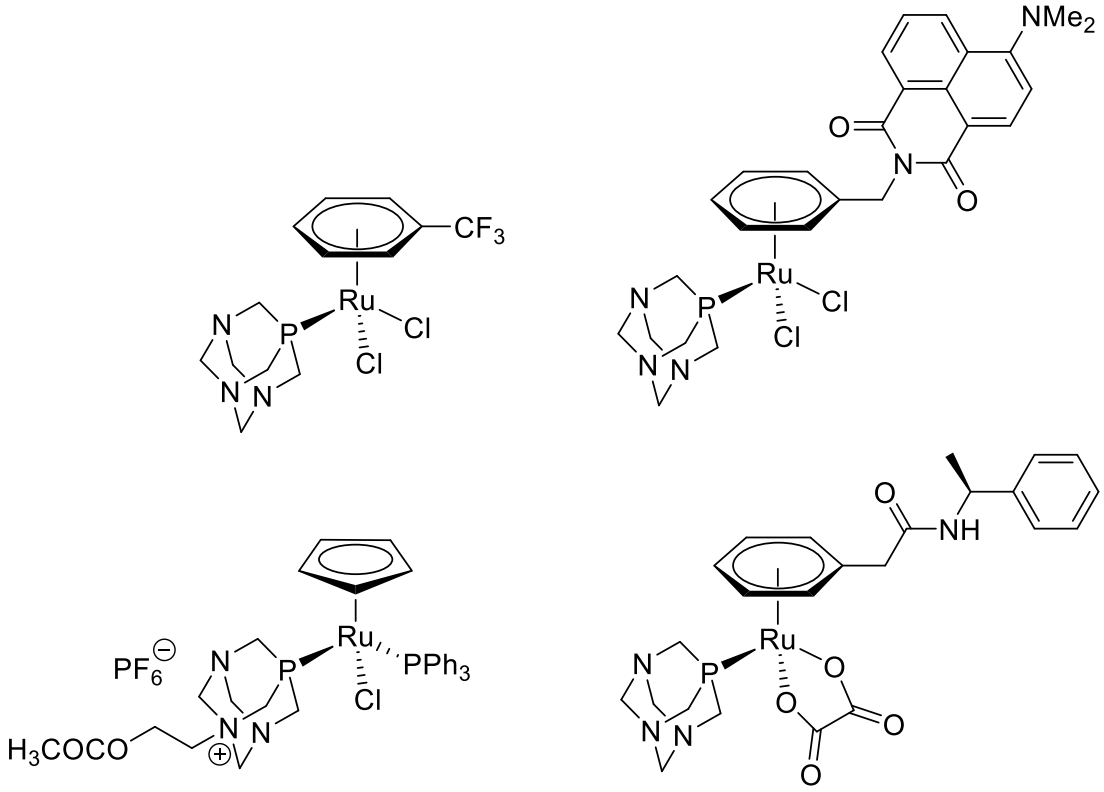

Figure 3.3: RAPTA derivatives that have been prepared and investigated for their cytotoxicity against cancerous cell lines.

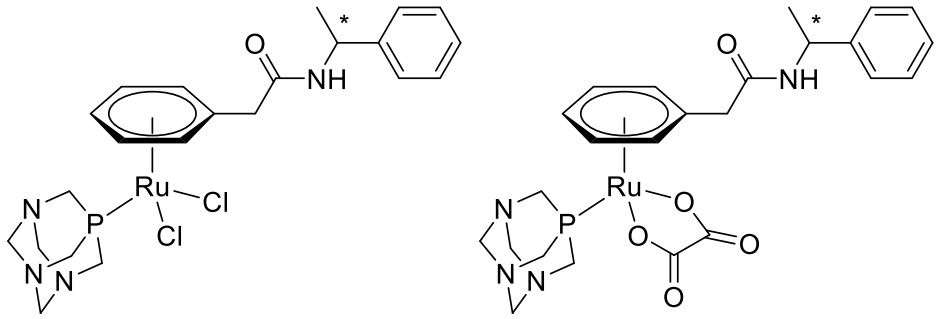

Figure 3.4: Two RAPTA drugs that have shown orders of magnitude variable anti-cancer potency between their constituent enantiomers.

Several studies have further shown that the cytotoxicity of RAPTA drugs can be greatly increased through pK_a modulation *via* arene fluorination,[12] embedding the complexes in arene

ruthenium metalla-cages,[17] and more recently through attachment to micelles[18] or self-assembling nanotubes.[19] Unfortunately, the interesting approach of combination treatment with RAPTA drugs and peptides has remained unexplored even though this approach with cisplatin was found through an *in vivo* study to achieve similar anti-tumor efficacy as typical chemotherapy but with lower dosages, improving quality of life for the tumor-bearing hosts.[20] If this approach is followed with RAPTA compounds, one of the likely concerns will be where and how the peptides are covalently linked for this type of treatment.

3.1.3 Peptide Synthesis

Peptide synthesis through amide bond formation is one of the most well-developed fields in synthetic chemistry, with several reviews published covering the subject extensively.[21–24] Typically, peptides are prepared via solid-phase peptide synthesis (SPPS), where an amino acid is anchored to a solid-state support, the peptide is grown through a series of subsequent deprotection & amino acid coupling steps, and the product is cleaved from the support once peptide growth is complete. This process, shown in Scheme 3.1, follows what is commonly referred to as linear N → C growth, where the unprotected amine terminus of one amino acid is reacted with the unprotected carboxyl group of another.

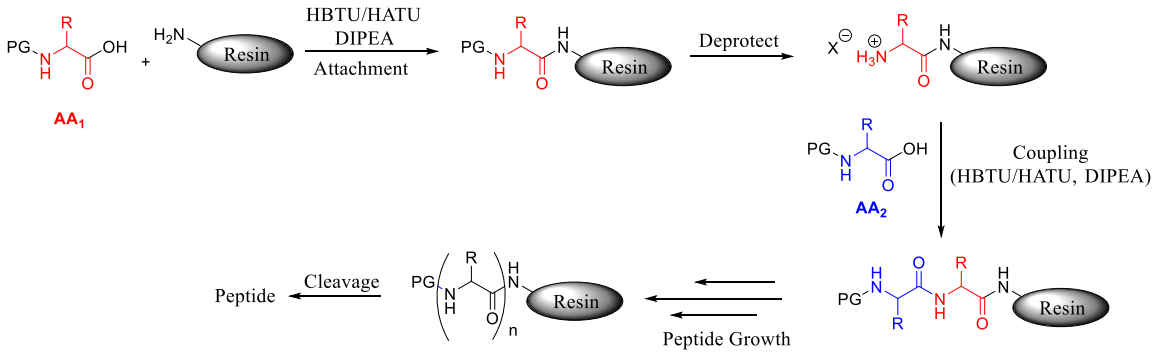

Scheme 3.1: Linear SPPS, where PG is a protecting group and the reagents required for each step depend on whether PG is Boc or Fmoc.

Linear growth of peptides through SPPS, while well-developed and understood, tends to result in poor yields because of the repeated deprotection and reaction steps which can result in undesired reactions with reactive side-chains. Convergent synthesis of peptides, where blocks of the peptide are synthesized in solution with N → C or C → N growth and purified separately before they are reacted together to yield the desired product, is the approach industry experts follow to generate kilogram quantities of peptides to date since it generally produces greater yields.[24] Thus, in order to more fully develop PTA-peptide chemistry, a method for N → C growth as well as C → N growth should be developed. Herein we report the detailed synthesis and characterization of upper-rim PTA amides generated from PTA=C[Ph]NH_2, PTA-CO_2Me, and PTA-CO_2Li along with a discussion of the relevance of each towards linear or convergent peptide synthesis for eventual use in peptide-based RAPTA anti-cancer drug candidates.

3.2 Results & Discussion

3.2.1 Synthesis of PTA=C[Ph]NH(AA)Fmoc from PTA=C[Ph]NH_2

This chapter covers the attempted synthesis and characterization of upper-rim modified PTA-amides from PTA starting materials PTA=C[Ph]NH_2 **(1)**, PTA-CO_2Me **(9)** and PTA-CO_2Li

(10). In the first part of this project, the coupling of **1** to an Fmoc-protected amino acid following a traditional peptide coupling protocol was attempted.[25] This synthesis, shown in Scheme 3.2, would be ideal for peptides that are prepared *via* convergent synthesis in solution as it leaves a protected amine functionality that can be deprotected and reacted further after purification of the product. Specifically, **1** was combined with Fmoc-protected *L*-phenylalanine (HO-Phe-Fmoc) in DMF with amide coupling reagents 3-[bis(dimethylamino)methyliumyl]-3H-benzotriazol-1-oxide hexafluorophosphate (HBTU) and N,N-diisopropylethylamine (DIPEA). The goal was to activate the carboxylic acid of Fmoc-*L*-phenylalanine by stirring in DMF with HBTU for one hour, after which followed the addition of **1** and DIPEA and stirring for another hour.

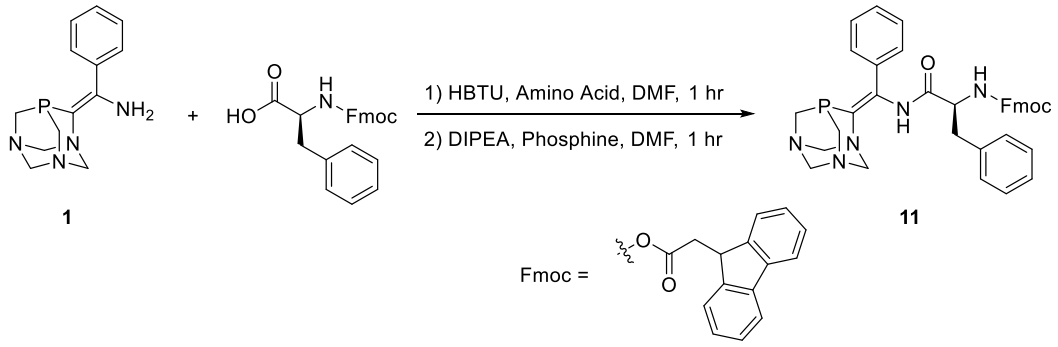

Scheme 3.2: Synthetic method followed for the attempted synthesis of **11**.

Solution-state ^{31}P {^{1}H} NMR of the crude product from this reaction revealed a single peak with a chemical shift of -85.50 ppm which compares with that of the starting material at -86.74, as shown in Figure 3.5. Crude ^{13}C {^{1}H} NMR and ^{1}H NMR of the product in $CDCl_3$, Figures 3.6 and 3.7, respectively, were also obtained for the crude product. The peaks in the $^{13}C\{^{1}H\}$ NMR were tentatively assigned using chemical intuition, but the resulting P-C coupling constants are all greater than 10 Hz higher than expected compared with those for **1**.[26] A broad peak is observed in the ^{1}H NMR with a chemical shift of 10.5 ppm, likely a carboxylic acid peak, suggestive of deprotection of the Fmoc protecting group. The product was subsequently purified with column

chromatography after these spectra. NMR spectroscopy of the purified product after separation by column chromatography will likely elucidate the efficacy of the reaction in much greater detail.

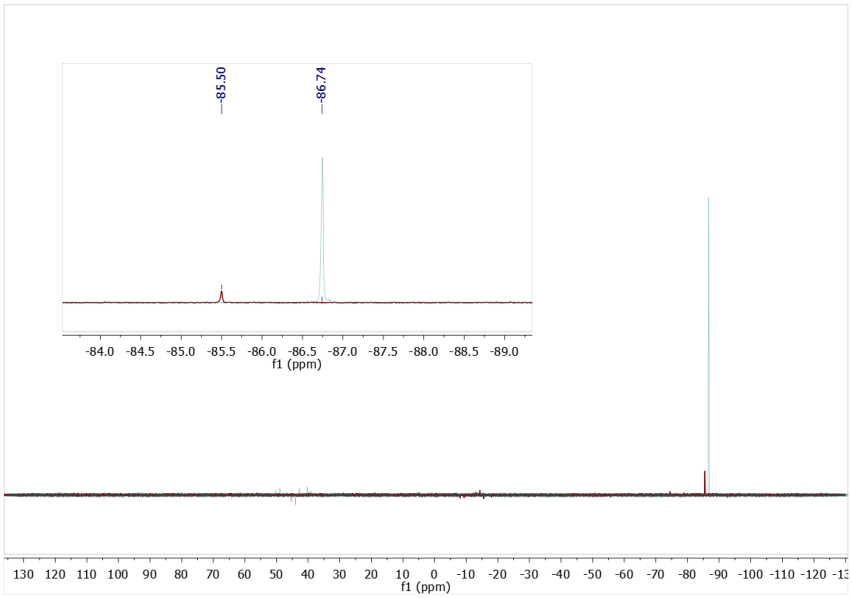

Figure 3.5: Crude solution-state $^{31}P\{^{1}H\}$ NMR of **11** (*maroon*) and **10** (*blue*) in DMF.

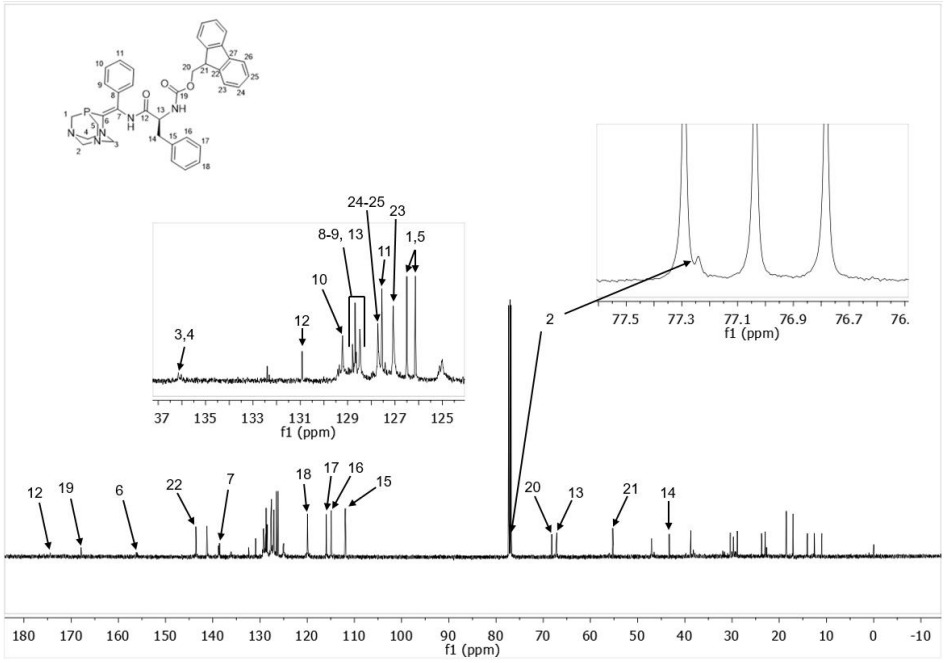

Figure 3.6: Solution-state $^{13}C\{^{1}H\}$ NMR of crude **11** in $CDCl_3$ with tentative peak assignments based on spectra for the starting materials.

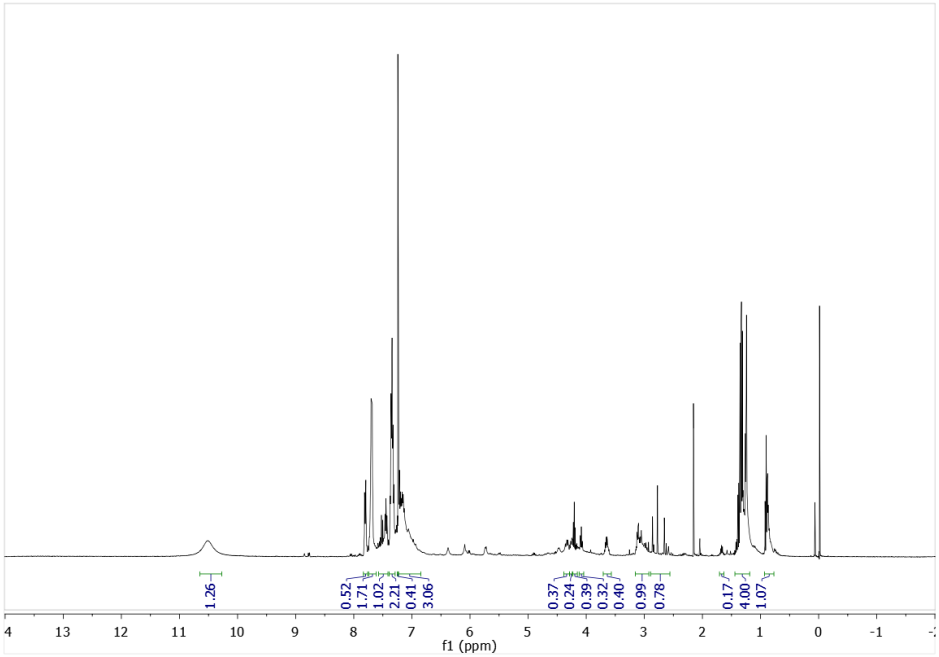

Figure 3.7: Solution-state ^{1}H NMR of crude **11** in $CDCl_3$ with tentative peak assignments loosely based on similar compounds.

Solid-state Fourier Transform Infrared spectroscopy (ssFTIR) of **11** after isolation with chromatography, Figure 3.9, reveals fingerprint PTA C-N absorptions in the 2,800 – 3,000 cm^{-1} range, a sharp amide C=O absorption at 1,675 cm^{-1}, the phenylalanine-characteristic $\upsilon_{C\text{-}C[ring]}$ absorption at 1,496 cm^{-1},[27] and a prominent amide N-H out-of-plane (oop) absorption at 835 cm^{-1}. This synthesis was repeated with **1** and Fmoc-*L*-glycine, and crude $^{31}P\{^{1}H\}$ NMR spectroscopy of the crude reaction mixture upon reaction completion, Figure 3.8, reveals several peaks from -90 ppm to 130 ppm with a major peak at -84.66 ppm which is shifted downfield from that of **1**, located at -86.75 ppm, by 2.04 ppm. Future work regarding synthesis of amides from this route should focus on developing robust purification methods for the resulting products with reverse-phase chromatography, as the highly polar nature of PTA combined with that of many amino acids is expected to yield products that will be difficult to isolate from the similarly polar reaction byproducts.

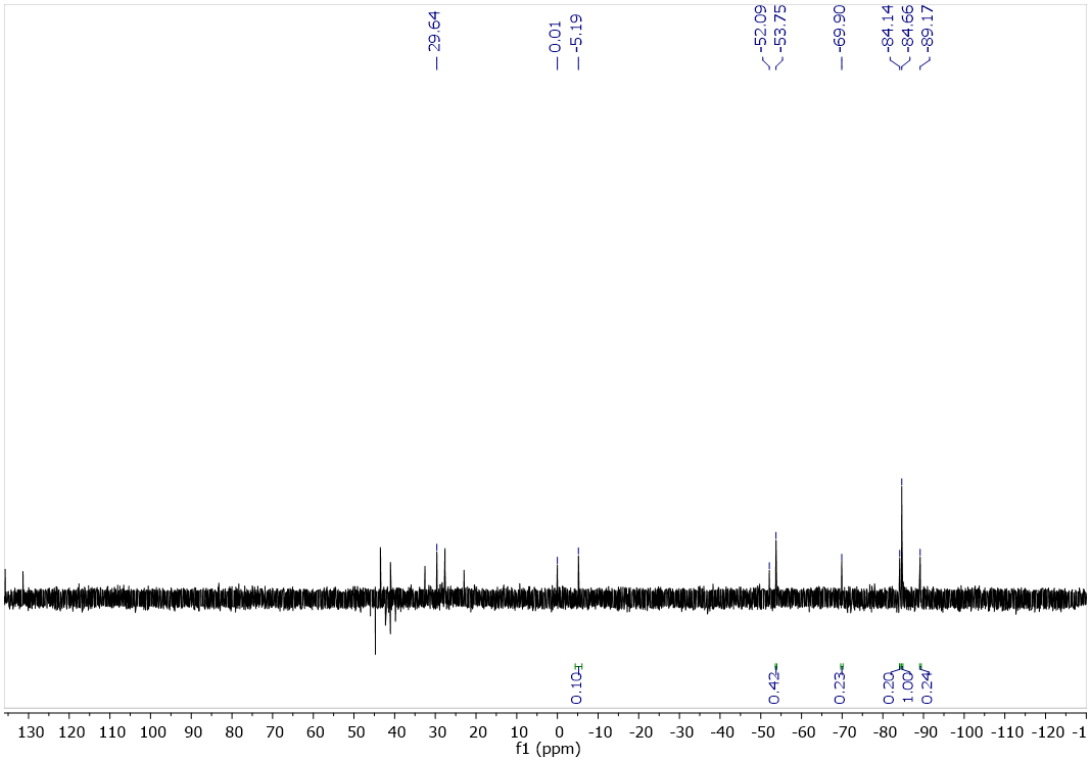

Figure 3.8: Crude solution-state $^{31}P\{^{1}H\}$ NMR spectrum obtained in DMF of the attempted synthesis of PTA=C[Ph]NH[Glycine]NHFmoc.

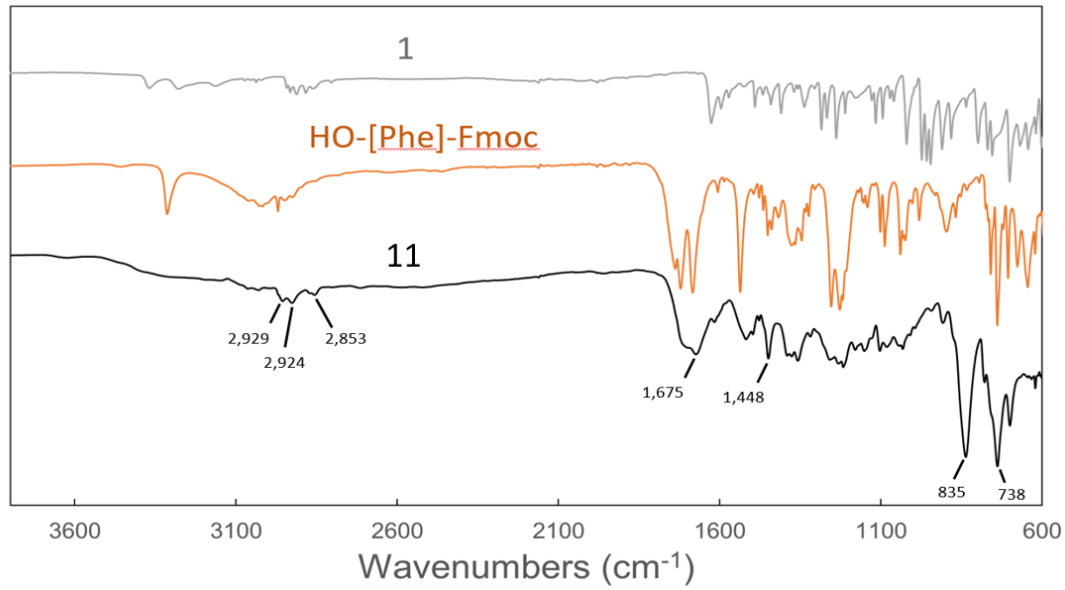

Figure 3.9: ssFTIR spectra of **1** (*gray*), Fmoc-protected phenylalanine (*orange*), and **11** (*black*) after purification by TLC.

3.2.2 Synthesis of PTA-CONHBn from PTA-CO_2Me

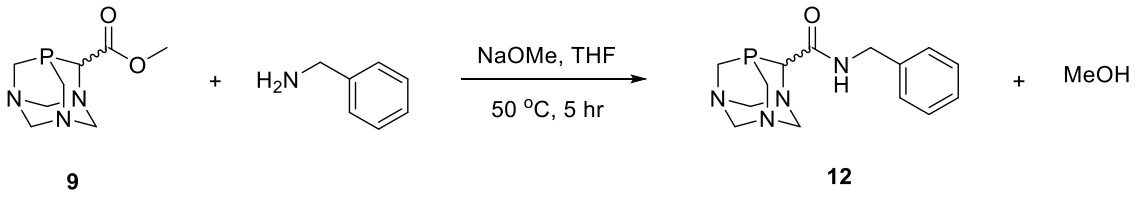

9 **12**

Scheme 3.3: Synthesis of **12** from **9** and benzylamine.

An upper-rim PTA amide PTA-CONHBn **(12)** was prepared with **9** and benzylamine following Scheme 3.3 following a modified literature procedure.[28] The $^{31}P\{^1H\}$ NMR spectrum of the crude product in CD_3OD, shown in Figure 3.10, reveals three peaks at -97.85 ppm, -90.26 ppm, and -3.61 ppm in a 0.06 : 1 : 0.17 ratio, respectively. The major peak observed in this spectrum is shifted downfield from that of the starting material by 7.59 ppm. Since the methoxide base used to deprotonate the amine for nucleophilic attack is the same as the leaving group for the methyl ester of **9**, the reaction should not generate any byproducts other than methanol. This is evidenced by the relatively clean ^1H NMR of the crude product in deuterated methanol, Figure 3.11, after concentration and without any further purification steps. The assigned PTA peaks in this NMR spectrum, specifically those in the range between 3.5 and 5.0 ppm, are found in similar integrated ratios and have been assigned to this region of ^1H NMR spectroscopy in previous reports for both **9** and PTA-CO_2Li (**10**).[29] The combined implications from both of these spectra results from this reaction are promising, and this approach for amide synthesis should be pursued. The product from this reaction was never fully isolated because the reaction was done with dririte in the flask as per the literature procedure that the synthetic method was adapted from, and attempts to separate out the residual dririte after the reaction led to loss of product. However, repeating this reaction with dry solvent instead of dririte should mitigate these issues of separation on future attempts to prepare amides from this direction.

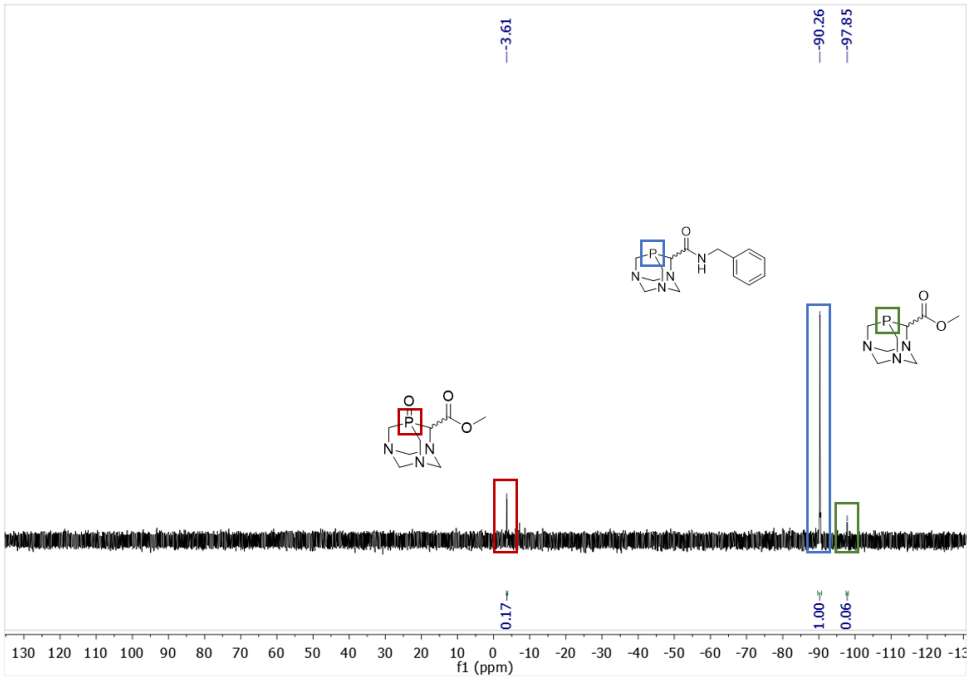

Figure 3.10: $^{31}P\{^{1}H\}$ NMR spectrum of crude **12** in CD_3OD after synthesis from **9** and benzylamine.

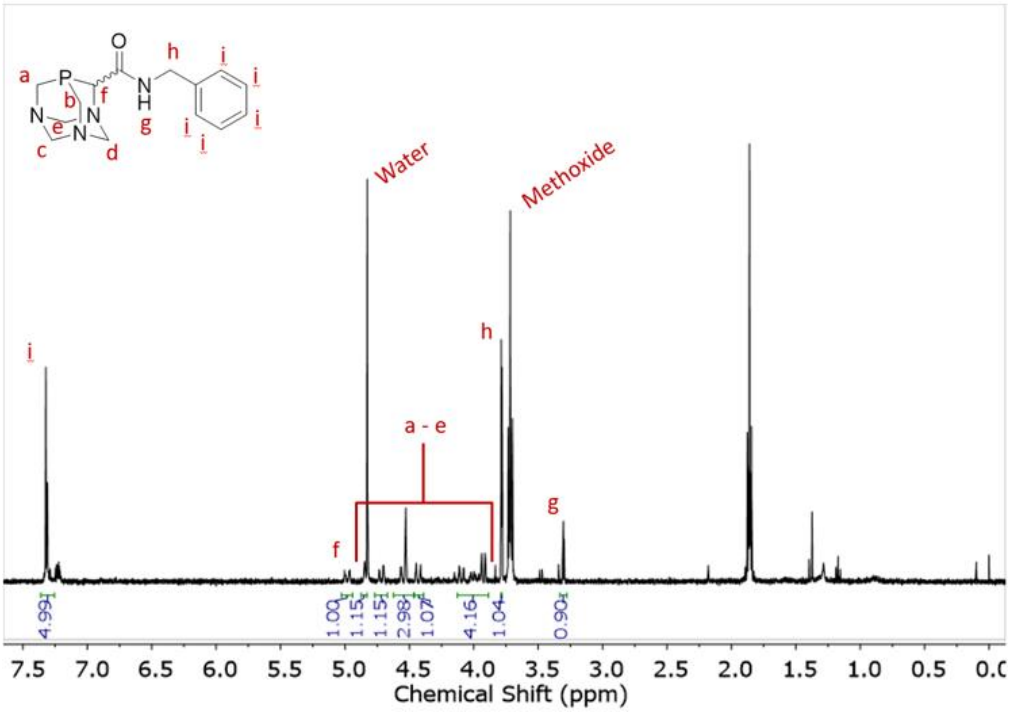

Figure 3.11: ^{1}H NMR spectrum of crude **12** in CD_3OD after synthesis from **9** and benzylamine.

While this method of preparing upper-rim PTA amides from the methyl ester of PTA would be ideal for linear SPPS, **9** has only been prepared from PTA-CO_2Li **(10)** following a literature procedure that yields approximately 31% of the methyl ester.[29] Combined with the fact that SPPS already typically has low yields due to side-chain reactions, a more robust approach to insertion of PTA into peptides *via* linear SPPS would be necessary. Optimization of the synthesis for **9** was attempted but unsuccessful, resulting in another investigation focused on upper-rim PTA amide synthesis with a more easily prepared PTA substrate.

3.2.3 Synthesis of PTA-CONHR from PTA-CO_2Li: Ammonium Salts

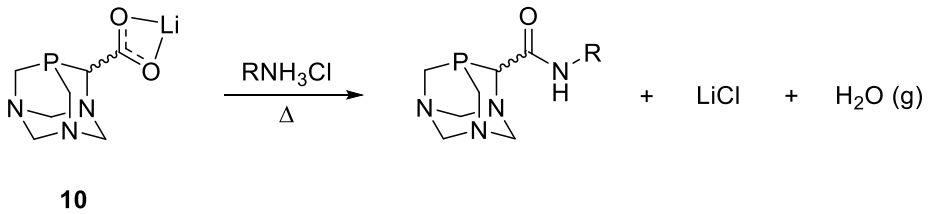

10

Scheme 3.4: Attempted synthesis of upper-rim PTA amides from **10**.

Synthesis of upper-rim derivatized PTA amides was first attempted following a modified approach for traditional amide bond synthesis, outlined in Scheme 3.4, where a carboxylate and ammonium salt are heated in air.[30,31] Amide bond synthesis was attempted with both ammonium chloride and benzylammonium chloride, and the reactions were left stirring at 180 ºC overnight in efforts to push the reaction to completion. The product of the reaction was orange and crystalline for both reactions. Upon reaction completion, droplets of water were observed on the top portions of the flask, indicative of water generation. The ssFTIR of the product from the reaction between **10** and ammonium chloride can be seen in Figure 3.12, where it is stacked atop the ssFTIR spectrum for **10**. Other than an additional broad absorption located at 3,200 – 3,450 cm^{-1} and an increase in intensity for the shoulder located at ~1,650cm^{-1}, the two spectra appear to be almost identical in

their peak patterns. Solution-state $^{31}P\{^{1}H\}$ NMR in methanol of the orange crystalline product resulting from this reaction revealed a single peak located at -90.17 ppm, shifted downfield 0.38 ppm from that of **10**, found at -90.55 (appendix Figure A.7). However, dissolving this orange crystalline product in water for $^{31}P\{^{1}H\}$ NMR spectroscopy revealed a peak with the exact same chemical shift as **10** in water.

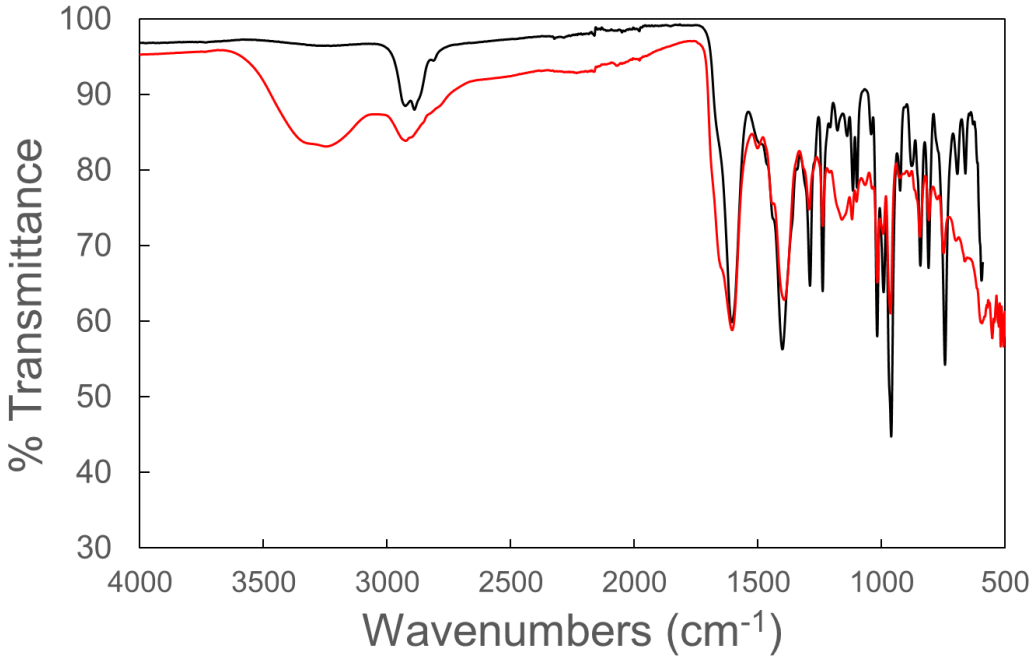

Figure 3.12: Solid state FTIR of **10** (*black*) and the phosphine after it was heated at 180 ºC in the presence of ammonium chloride overnight (*red*).

It is likely that this reaction was not successful, evidenced in part because of the similarity between ssFTIR spectra between the product and **10**, as the product should have yielded a single sharp $\nu_{C=O}$ stretching frequency for the ketone red-shifted from that of the symmetric and assymetric stretching frequencies of **10**. Further, the oop ν_{N-H} absorption in the range of 800 cm^{-1} should be seen in the ssFTIR for the product. Neither of these absorptions were witnessed in the final product. It was hypothesized that the product resulting from this reaction was just a protonated form of **10**. If this were correct, the broad absorption centered at 3,300 cm^{-1} would likely indicate

N-H stretching, albeit at one of the nitrogen atoms of the PTA ligand rather than on an amide nitrogen. The protonated form of **10** has not currently been isolated as a solid, but capturing ssFTIR of this ligand after isolation would be ideal as it would further elucidate whether the red spectrum seen in Figure 3.12 is in fact a protonated form of **10** or not.

This reaction was repeated between **10** and benzylammonium chloride following the same reaction protocol shown in Scheme 3.4. Multiple overlapping peaks, broadening of the $\nu_{C=O}$ absorption at 1,642 cm^{-1}, and the presence of ring breathing modes for the aryl ring at 804, 747, and 698 cm^{-1} are all observed in the ssFTIR spectrum for the product, Figure 3.13. Low-resolution mass spectrometry of the product in methanol reveals a small peak at 291.6 m/z where the product peak is expected, as seen in Figure 3.14, with a much larger parent ion at 248.0 m/z which could possibly be the fragmented PTA-CONHKLi$^+$ (expected mass = 245.21). $^{31}P\{^1H\}$ NMR spectroscopy of the crude product in CD_3OD (appendix Figure A.8) reveals several peaks including a two broad peaks at both -85 ppm and 50 ppm.

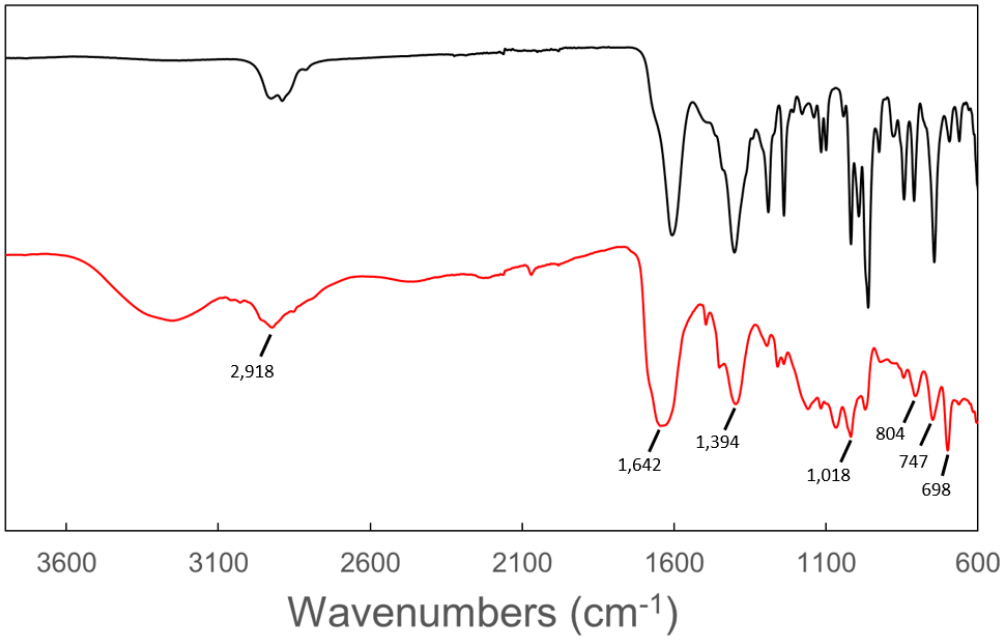

Figure 3.13: Solid state FTIR of **10** (*black*) and the phosphine after it was heated at 180 ºC in the presence of benzylammonium chloride overnight (*red*).

It is possible that this reaction was successful since a mass/charge ratio of 291 m/z was observed where it is expected for the product. Also, the aforementioned observed peaks in the ssFTIR spectrum fall where they are expected. The highly polar nature of the reaction starting materials, byproducts, and product were similar enough to make separation too difficult to accomplish. Separation with reverse-phase chromatography would likely assist in the separation of the product from the reactants due to the expected highly polar nature of the product.

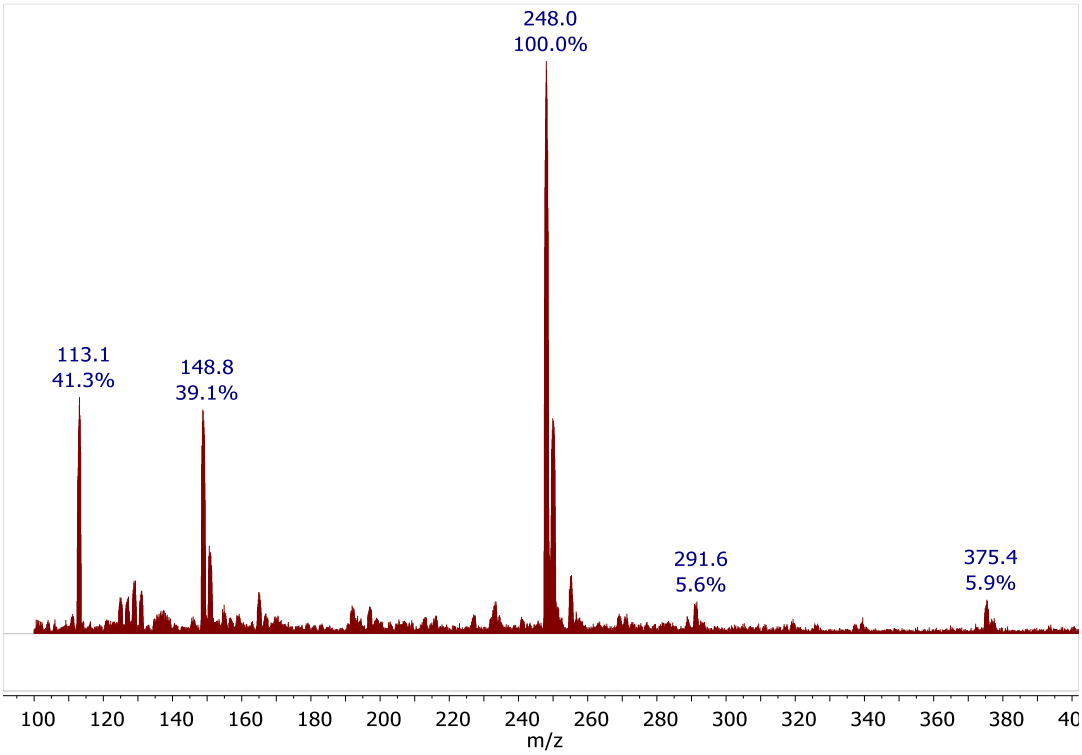

Figure 3.14: Mass spectrum of the crude reaction mixture in methanol of the product from heating **10** with benzylammonium chloride at 180 ºC overnight.

3.2.4 Synthesis of PTA-CONHR from PTA-CO_2Li: DCC and DIC

Amide bond synthesis was attempted with **10** and benzylamine following a traditional protocol for amide bond synthesis from peptide synthesis, following the reaction outlined in Scheme 3.5. This approach included the use of common coupling reagents dicarbohexylcarbodiimide (DCC) and diisopropylcarbodiimide (DIC) coupling carboxylate and

amine functional groups.[22] In a solution of THF, **3** was dissolved with 12-crown-4 and stirred for an hour to facilitate dissociation of the Li^+ ion from the phosphine. The coupling agent DCC and benzyamine was then added and the reaction mixture left to stir overnight under ambient conditions. Afterwards, $^{31}P\{^1H\}$ NMR spectroscopy of the crude reaction mixture revealed peak with a chemical shift identical to that for **10**. Further, GCMS of the product reaction mixture revealed the presence of the starting materials **10**, 12-crown-4, and DCC, indicating a 0% conversion of starting materials. The reaction was repeated again with DIC in the hopes that its increased solubility would assist in pushing the reaction to completion, but the same result was observed.

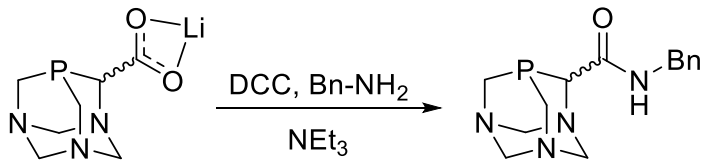

10 **12**

Scheme 3.5: Synthesis of **12** from **10** utilizing the coupling agent DCC.

3.2.5 Synthesis of PTA-CONHR from PTA-CO_2Li: HBTU and DIPEA

Upper-rim PTA amides were prepared utilizing **10** and HCl salts of several amines following a procedure, Scheme 3.6, outlined specifically for lithiated carboxylates and HCl salts of amines.[32]. This method was approached since it was the only literature approach that could be found that specifically outlined the synthesis of amides with lithiated carboxylate and hydrochloride ammonium salts as the starting materials and because quantitative yield was reported with the given reaction conditions. The reaction was screened with **10** and the hydrochloride salts of benzylamine, butylamine, methyl ester-protected Glycine (HCl · H_2N-Gly-OMe), and methyl ester-protected *L*-Histidine (HCl · H_2N-His-OMe) to yield **12**, **13**, **14**, and the diastereomers **15** and **16**, respectively. This amide bond synthesis was attempted in DMF, which appeared for the first time to quickly and

fully dissolve all starting materials for this reaction. $^{31}P\{^{1}H\}$ NMR of the resulting crude products, indicates an approximate 3 ppm upfield shift from that of **10**, as can be seen in Table 3.2.

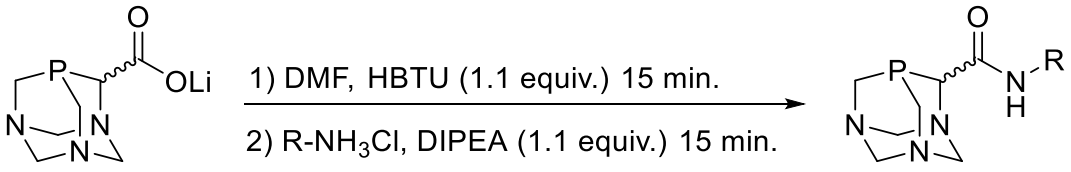

Scheme 3.6: Synthesis of upper-rim PTA amides from **10**.

Table 3.2

^{31}P-NMR chemical shifts of amides prepared from **10**.

Ligand	$^{31}P\ \{^{1}H\}^{a}$	Δ [ppm]^{b}
PTA-CO_2Li (**10**)	-97.46	--
PTA-CONHBn (**12**)	-100.77	3.31
PTA-CONHBu (**13**)	-100.62	3.16
PTA-CONH[Gly]OMe (**14**)	-101.09	3.63
PTA-CONH[His]OMe (**15 & 166**)	-100.27, -100.45	2.81, 2.99

[a] In DMF. [b] Upfield $^{31}P\ \{^{1}H\}$ NMR shift from that of **3**.

Crude $^{31}P\{^{1}H\}$ NMR were captured for the reaction products (Figure A.9) revealed singlets for each substrate except that generated with the chiral *L*-Histidine (HCl · H_2N-His-OMe), which exhibits two peaks of equal intensity shifted upfield 2.81 and 2.99 ppm, respectively, from the chemical shift of **10**. This is understandable since protected *L*-Histidine (HCl · H_2N-His-OMe) is the only chirally resolved amine coupled to **10** that would yield two diastereomers. Isolation of **13** and **14** has been unsuccessful, but **12** and the 50 / 50 mixture of **15** and **16** were obtained as they each precipitate out of solution throughout the course of the reaction. Both ^{1}H NMR and ssFTIR (Figure A.10 and A.11, respectively) of **12** reveal peak patterns as would be expected for the product; a broad peak in the NMR spectrum at -9.30 ppm integrates to 1 against the peaks in the range 3.5 to 5.0 where protons of the PTA-CO_2Li cage have been assigned previously,[29] while a $\nu_{N\text{-}H}$ is seen at 3,342 and 2,941 cm^{-1}, $\nu_{C=O}$ is seen at 1,649cm^{-1}, and ring breathing modes can be identified at 840, 745, and 699 cm^{-1} in the FTIR spectrum. While **13** could not be successfully isolated, ^{1}H NMR of the crude product in d^6-DMSO reveals a spectrum with peaks where one would

expect for the product (Figure A.12). As can be seen in the ^{1}H NMR for both of these products, drying each reaction mixture under a stream of air does not entirely remove all DMF from the reaction mixture. While removing the solvent on the rotary evaporator may have mitigated this issue, the elevated temperature required to evaporate the solvent was thought to possibly hydrolyze the product in the presence of any ambient humidity. However, enough DMF is removed under a stream of air that the remaining product peaks are not drowned into the baseline in the crude ^{1}H NMR. Crude ssFTIR of **15** and **16**, superimposed with that of **10** in Figure 3.15, reveals an absorption at 1,650 cm^{-1} where one would expect to see amide $\upsilon_{C=O}$ stretch.[27]

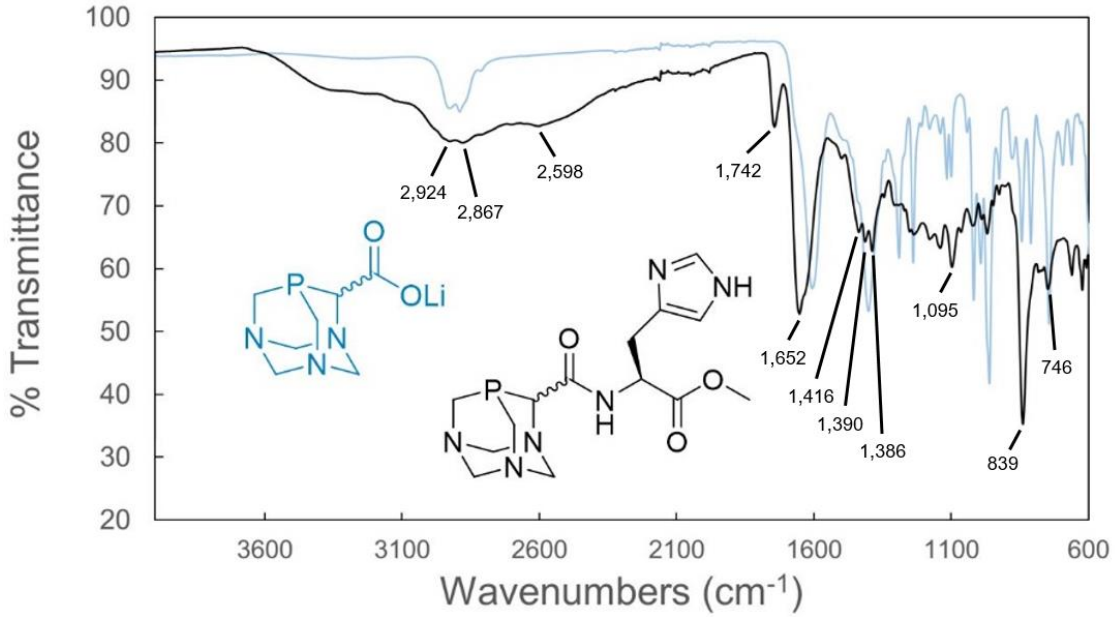

Figure 3.15: *ss*FT-IR of the diastereomeric mixture of **15** and **16** superimposed with that of **10** for comparison.

Other relevant absorptions in these spectra include out-of-plane (oop) N-H bending[33] of the imidazole amine at 833 cm^{-1}, and several absorptions in the 1,390 – 1,430 cm^{-1} range tentatively assigned as $\upsilon_{C=N}$ as expected for the amino acid side-chain. ssFTIR of **12** reveals a sharp absorption at 1,649 cm^{-1} where again one would expect to see amide $\upsilon_{C=O}$ stretching, but also the ring breathing modes one would expect to see for the phenyl ring of the Bn functional group (Figure A.13)

between 650 and 850 cm^{-1}. There are several aspects to this reaction that make it the best viable candidate for insertion of PTA into peptides for RAPTA compounds *via* SPPS. The published procedure indicates 60 minutes are required for insertion of the deprotonated amine into the activated carboxylate,[32] but kinetic data generated for the reaction from time-resolved solution-state $^{31}P\{^{1}H\}$ NMR, shown in Figure 3.16, suggests that the product is prepared within 10 to 15 minutes of amino acid addition.

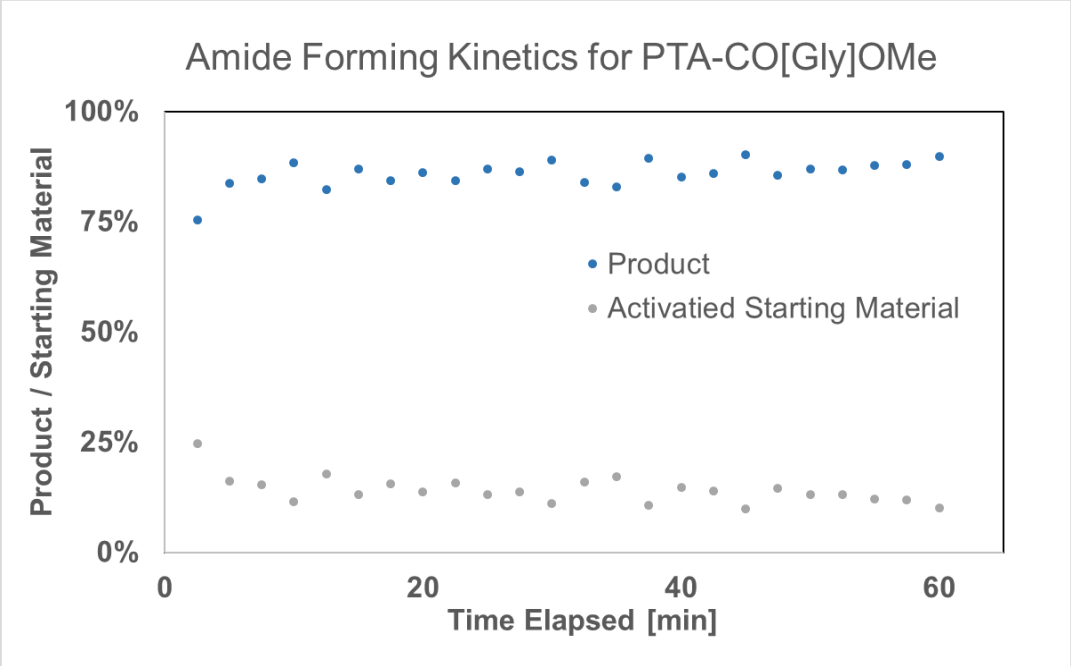

Figure 3.16: Kinetics for the formation of **14** after the addition of HCl · H_2N-Gly-OMe. Ratio of species was measured by peak height of time-delayed $^{31}P\{^{1}H\}$ NMR in DMF (Figure A.13).

This reaction was conducted in glassware that wasn't dried and under ambient air. The speed of this reaction coupled with this ease and supposed high yield are promising for generating several more upper-rim modified derivatives of PTA. These initial results, while promising, require expansion and much more investigation to prove out this synthetic method as successful in preparing upper rim PTA-CONHR amides. The required remaining activities include obtaining $^{13}C\{^{1}H\}$ NMR and ^{1}H NMR spectroscopy of all products, high-resolution mass spectrometry after

isolation, deuterium-exchange experiments to check against predicted N-D shifts in FTIR spectra, and in-situ ReactIR so that the steady growth of the amide N-H stretching frequency can be observed over the course of the reaction.

3.2.6 Concluding Remarks

Finding a synthetic method to couple PTA into a peptide with an amide bond is highly important as it could lead to better, more effective anti-cancer RAPTA drugs through the use of targeting peptides covalently attached to the cancer drugs through the phosphine. In this chapter, I have outlined three efforts to prepare this type of bond, with data that suggests product formation is possible from each approach. Of the synthetic approaches outlined in this chapter, that which utilizes the phosphine enamine **1** would be most relevant for solution-phase convergent synthesis of peptides, as the PTA derivative is the nitrogen donor, and the resulting product contains an Fmoc-protected amine that can be deprotected for further peptide growth. Amide formation from **10** is a highly desirable approach to cap peptides with linear SPPS, as deprotection of the terminal peptide amine would generate the nitrogen donor on the peptide's end required for coupling with **10**.

This chapter outlined my attempts to prepare upper-rim amides of PTA. None of the methods described herein resulted in proof of amide bond formation for any derivatives, but there are several spectra that directionally suggest the reaction may possibly have been successful. Future work should include optimizing the synthesis and purification of amides from all three of these approaches. Synthesis from **10** and hydrochloride salts of amines should be repeated for a full substrate scope with amino acids to elucidate necessary isolation conditions. Further, it would be useful to utilize ^{1}H-NMR and ^{13}C{^{1}H} NMR for full product characterization and as a better indicator of reaction completion. Finally, attempts should be pursued to grow single crystals of reaction products for single-crystal X-ray Diffraction. Amide coupling from **9**, while ideal from a product isolation viewpoint, will require optimization of the synthesis for **9**.

3.3 Experimental

3.3.1 Methods & Materials

Unless otherwise noted, all manipulations were performed on a double-manifold Schlenk vacuum line under nitrogen or in a nitrogen-filled glovebox. Anhydrous *N*,*N*-dimethylformamide (DMF), 3-[bis(dimethylamino)methyliumyl]-3H-benzotriazol-1-oxide hexafluorophosphate (HBTU), *N*,*N*-diisopropylethylamine (DIPEA), butylamine hydrochloride, benzylamine hydrochloride, glycine methyl ester hydrochloride, histidine methyl ester dihydrochloride, sodium methoxide, Fmoc-*L*-phenylalanine, and Fmoc-*L*-glycine were all purchased from commercial sources and used as provided. Tetrahydrofuran (THF) was freshly distilled from sodium/benzophenone. 1,3,5-triaza-7-phosphaadamantane (PTA),[34] lithium 1,3,5-triaza-7-phosphaadamantane-6-carboxylate (PTA-CO_2Li),[29] methyl-1,3,5-triaza-7-phosphatricyclo[3.3.1.1]-decane-6-carboxylate (PTA-CO_2Me),[29] and phenyl 1,3,5-triaza-7-phosphatricyclo[3.3.1.1]-decane-6-enamine (PTA=C[Ph]NH_2)[26] were published according to the literature methods. Solid state infrared spectra were obtained with a Nicolet 6700 FT-IR spectrophotometer. All NMR spectra were recorded with a Varian Unity Plus 500 FT-NMR and Varian NMR System 400 spectrometer. ^{1}H NMR and ^{13}C {^{1}H} NMR were referenced to solvent residual and tetramethylsilane (TMS). Phosphorus NMR signals were referenced to an external standard of 85% phosphoric acid in D_2O, where all chemical shifts downfield the reference were assigned as positive.

3.3.2 Synthesis

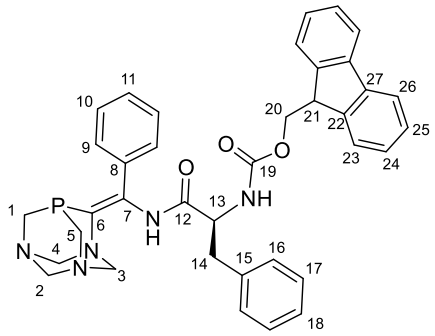

Synthesis of PTA=C[Ph]NH(Phe)Fmoc, 11 followed typical amide coupling conditions. Fmoc-*L*-phenylalanine (58.0 mg, 150 μmol) and HBTU (62.6 mg, 170 μmol, 1.1 equiv.) were loaded into a 20 mL scintillation vial with a stirbar and dissolved in 2 mL DMF. The solution was stirred for 1 hour at room temperature, yielding a uniformly yellow solution. Separately, **1** (39.0 mg, 150 μmol, 1 equiv.) and DIPEA (28.7 μL, 170 μmol, 1.1 equiv.) were dissolved in 2 mL DMF in a scintillation vial. The phosphine mixture was transferred to the activated amino acid mixture under nitrogen *via* syringe and the resulting bright yellow mixture was stirred for another hour. The reaction mixture was concentrated with a steady stream of air for 24 hours before dissolution in chloroform. The product was isolated by column chromatography (stationary phase: silica gel, mobile phase: acetone, product R_f = 0.8) and extracted into chloroform. The precipitate from this dissolution was removed by gravity filtration, and concentration of the filtrate under reduced pressure yielded the product as a light orange solid. (27.2 mg, 43.2 μmol, 29%) ^{31}P $\{^1H\}$ NMR (162 MHz, DMF): -85.5 (s). ^{13}C $\{^1H\}$ NMR (126 MHz, $CDCl_3$) δ 156.1 (d, $^1J_{PC}$ = 31.36 Hz, C6), 138.7 (d, $^2J_{PC}$ = 25.29, C7), 77.2 (s, C2), 126.3 (d, $^1J_{PC}$ = 44.40 Hz, C1,5), 136.1 (d, $^3J_{PC}$ = 15.55 Hz, C3,4), 128.7 (d, $^3J_{PC}$ = 19.13 Hz, C8), 128.7 (s, C9,13), 129.5 (s, C10), 130.92 (s, C12), 127.6 (s, C11), 174.44 (s, C12), 67.14 (s, C13), 47.03 (s, C14), 111.9 (s,C15), 114.9 (s, C16), 115.93 (s, C17), 119.94 (s, C18), 167.9 (s, C19), 55.28 (s, 21), 143.58 (s, 22), 127.1 (s, C23), 127.0 (s, C24),

127.7 (s, C25), 127.68 (shoulder, C27). Solid state IR [cm^{-1}]: 2954, 2924, 2854 (C-N_{PTA}), 1670 (C=O_{Amide}), 1496 ($CC_{Phe\ Ring}$), 835 (N-H_{oop}).

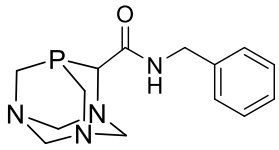

Synthesis of PTA-CONHBn, 12 followed one of two new synthetic methods:

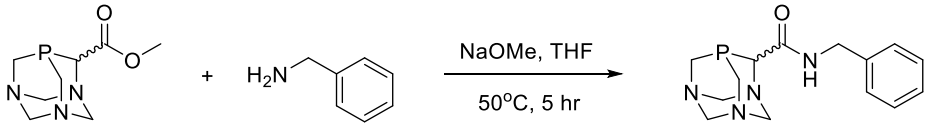

The first synthesis followed a slightly modified literature approach.[28] Drierite (2g) was placed in a flame-dried 50 mL round-bottom flask with a stirbar. **9** (43.5 mg, 0.20 mmol) was combined with sodium methoxide (8.0 mg, 0.15 mmol) and the mixture was diluted with 30 mL THF. Benzylamine (30 μL, 0.27 mmol) was added and the reaction mixture was brought to reflux in an oil bath and left that way for 24 hours. The heat source was then removed and the reaction mixture was allowed to cool to room temperature naturally. The crude mixture was concentrated under reduced pressure to yield the crude product as a yellow oil. (Vide infra for spectroscopic data)

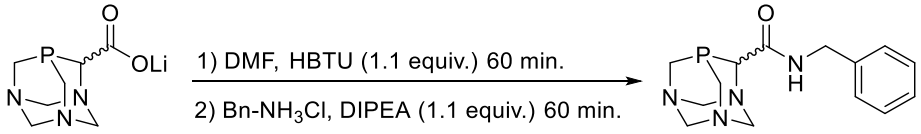

A 20 mL scintillation vial was loaded with **10** (15.5 mg, 75 μmol), HBTU (31.7 mg, 84 μmol, 1.1 equiv.) and 1 mL anhydrous DMF. The mixture was sonicated for 5 minutes before it was left to stir for one hour under ambient conditions. Meanwhile, a separate vial was loaded with benzylamine hydrochloride (10.8 mg, 75 μmol, 1 equiv.), DIPEA (15.0 μL, 86 μmol, 1.1 equiv.)

and 1 mL anhydrous DMF. This second solution was added to the former *via* syringe and the resulting mixture was stirred at room temperature for another hour. The mixture was then left evaporating under a stream of air for 24 hours, resulting in a yellow oil. Addition of acetone to this oil resulted in the precipitation of the product as a pale beige solid. Quantitative conversion determined by $^{31}P\{^{1}H\}$ NMR. $^{31}P\{^{1}H\}$ NMR (162 MHz, DMF): -101.35 (s). ^{1}H NMR (400 MHz, CD_3OD) δ 7.27 – 7.35 (m, 5H, Ph), 4.56 – 5.05, 4.42 (m, 6H, NCH_2N), 4.53 (s, 2H, NHCH_2Ph), 3.92 (d, 1H, PC*H*N, $^{2}J_{HAHB}$ = 10.62), 3.78 – 3.79 (m, 4H, PCH_2N). Solid state IR [cm^{-1}]: 3344, 3230 (N-$H_{stretch}$), 2937, 2800, 2794 (C-N_{PTA}), 1651 (C=O_{Amide}), 1450 (C$C_{Aryl\ Ring}$), 840 (N-H_{oop}).

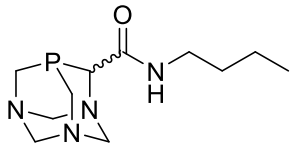

Synthesis of PTA-CONHBu, 13 followed a literature method for amide coupling between lithium carboxylate salts and the hydrochloride salts of amines.[32] A 20 mL scintillation vial was loaded with **10** (31.9 mg, 0.15 mmol), HBTU (62.6 mg, 0.172 mmol, 1.1 equiv.) and 2 mL anhydrous DMF. The mixture was sonicated for 5 minutes before it was left to stir for one hour under ambient conditions. Meanwhile, a separate vial was loaded with butylamine hydrochloride (16.7 mg, 0.15 mmol, 1 equiv.), DIPEA (287 μL, 0.172 mmol, 1.1 equiv.) and 2 mL anhydrous DMF. This second solution was added to the former *via* syringe and the resulting mixture was stirred at room temperature for another hour. The mixture was then left evaporating under a stream of air for 24 hours, resulting in a yellow oil. Quantitative conversion determined by $^{31}P\{^{1}H\}$ NMR. $^{31}P\{^{1}H\}$ NMR (162 MHz, DMF): -100.58 (s). ^{1}H NMR (400 MHz, CD_3OD) δ 9.39 (broad singlet, 1H, CON*H*), 3.2 – 5.3 (m, 10H, PCH_2N, NCH_2N), 3.07 (m, 1H, PC*H*N), 1.49 (AB quintet, 2H, $CH_2CH_2CH_2$, $^{3}J_{HAHB}$ = 7.8 Hz), 1.26 (AB septet, 2H, $CH_2CH_2CH_3$, $^{3}J_{HAHB}$ = 7.8 Hz), 1.23 (t, 2H, CONHCH_2CH_2, $^{3}J_{HAHB}$ = 7.4 Hz), 0.82 (t, 3H, CH_3, $^{3}J_{HAHB}$ = 7.5 Hz).

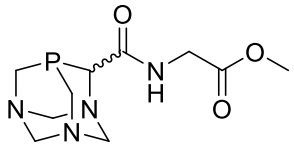

Synthesis of PTA-CO[Gly]OMe, 14 followed the slightly modified version of a literature method for amide coupling between lithium carboxylate salts and the hydrochloride salts of amines.[32] A 100 mL round-bottom flask was loaded with **10** (155.3 mg, 0.75 mmol), HBTU (310 mg, 0.817 mmol, 1.1 equiv.) and 10 mL anhydrous DMF in air. The mixture was sonicated for 5 minutes before it was left to stir for fifteen minutes at room temperature. Meanwhile, a separate 100 mL round-bottom flask was loaded with glycine methyl ester hydrochloride (94.6 mg, 0.75 mmol, 1 equiv.), DIPEA (144 μL, 0.817 mmol, 1.1 equiv.) and 10 mL anhydrous DMF in air. This second solution was added to the former *via* syringe and the resulting mixture was stirred at room temperature for another fifteen minutes. The mixture was then left evaporating under a stream of air for 24 hours, resulting in a yellow oil. 58% conversion determined by ^{31}P {^{1}H} NMR. ^{31}P {^{1}H} NMR (162 MHz, DMF): -101.09 (s).

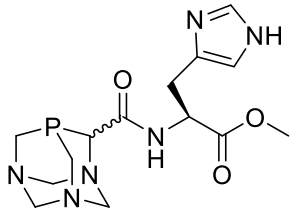

Synthesis of *S,R*- (15) and *R,R*- (16) PTA-CO[His]OMe followed the slightly modified version of a literature method for amide coupling between lithium carboxylate salts and the hydrochloride salts of amines.[32] A 100 mL round-bottom flask was loaded with **10** (155.4 mg, 0.75 mmol), HBTU (310 mg, 0.817 mmol, 1.1 equiv.) and 10 mL anhydrous DMF in air. The mixture was sonicated for 5 minutes before it was left to stir for fifteen minutes at room temperature. Meanwhile, a separate 100 mL round-bottom flask was loaded with histidine methyl ester dihydrochloride (181.8

mg, 0.75 mmol, 1 equiv.), DIPEA (288 μL, 1.65 mmol, 2.2 equiv.) and 10 mL anhydrous DMF in air. This second solution was added to the former *via* syringe and the resulting mixture was stirred at room temperature for another fifteen minutes. The mixture was left evaporating under a stream of air for 24 hours, and the diastereomeric products **15** and **16** were precipitated from the resulting yellow oil as a light yellow solid by washing with several aliquots of cold ethanol. (57% conversion determined by ^{31}P $\{^{1}H\}$ NMR. 93.4 mg, 0.265 mmol, 35% isolated yield) ^{31}P $\{^{1}H\}$ NMR (162 MHz, DMF): -100.30 (s), -100.50 (s).

3.4 References

(1) Higby, D. J.; Wallace, H. J.; Albert, D. J.; Holland, J. F. *Cancer* **1974**, *33* (5), 1219–1215.

(2) Milito, A. De; Luciani, F.; Fais, S. *Platinum and Other Heavy Metal Compounds in Cancer Chemotherapy*; 2009.

(3) Leijen, S.; Burgers, S. A.; Baas, P.; Pluim, D.; Tibben, M.; Van Werkhoven, E.; Alessio, E.; Sava, G.; Beijnen, J. H.; Schellens, J. H. M. *Invest. New Drugs* **2015**, *33* (1), 201–214.

(4) Hartinger, C. G.; Jakupec, M. a; Zorbas-Seifried, S.; Groessl, M.; Egger, A.; Berger, W.; Zorbas, H.; Dyson, P. J.; Keppler, B. K. *Chem. Biodivers.* **2008**, *5* (10), 2140–2155.

(5) Callari, M.; Aldrich-Wright, J. R.; De Souza, P. L.; Stenzel, M. H. *Prog. Polym. Sci.* **2014**, *39* (9), 1614–1643.

(6) Allardyce, C. S.; Dyson, P. J.; Ellis, D. J.; Heath, S. L. *Chem. Commun.* **2001**, No. 15, 1396–1397.

(7) Kato, Y.; Ozawa, S.; Miyamoto, C.; Maehata, Y.; Suzuki, A.; Maeda, T.; Baba, Y. *Cancer Cell Int.* **2013**, *13* (1), 89–97.

(8) Scolaro, C.; Bergamo, A.; Brescacin, L.; Delfino, R.; Cocchietto, M.; Laurenczy, G.; Geldbach, T. J.; Sava, G.; Dyson, P. J. *J. Med. Chem.* **2005**, *48* (12), 4161–4171.

(9) Ferretti, V.; Fogagnolo, M.; Marchi, A.; Marvelli, L.; Sforza, F.; Bergamini, P.; Chimiche, S.; Fossato, V. *Inorg. Chem.* **2014**, *53*, 4881–4890.

(10) Kilpin, K. J.; Clavel, C. M.; Edafe, F.; Dyson, P. J. *Organometallics* **2012**, *31* (20), 7031–7039.

(11) Pettinari, R.; Marchetti, F.; Condello, F.; Pettinari, C.; Lupidi, G.; Scopelliti, R.; Mukhopadhyay, S.; Riedel, T.; Dyson, P. J. *Organometallics* **2014**, *33* (14), 3709–3715.

(12) Renfrew, A. K.; Phillips, A. D.; Tapavicza, E.; Scopelliti, R.; Rothlisberger, U.; Dyson, P. J. *Organometallics* **2009**, *28* (17), 5061–5071.

(13) Sersen, S.; Kljun, J.; Kryeziu, K.; Panchuk, R.; Alte, B.; Körner, W.; Heffeter, P.; Berger,

W.; Turel, I. *J. Med. Chem.* **2015**, *58*, 3984–3996.

(14) Gossens, C.; Dorcier, A.; Dyson, P. J.; Rothlisberger, U. *Organometallics* **2007**, *26* (16), 3969–3975.

(15) Ang, W. H.; Daldini, E.; Scolaro, C.; Scopelliti, R.; Juillerat-Jeannerat, L.; Dyson, P. J. *Inorg. Chem.* **2006**, *45* (22), 9006–9013.

(16) Kilpin, K. J.; Cammack, S. M.; Clavel, C. M.; Dyson, P. J. *Dalton Trans.* **2013**, *42* (6), 2008–2014.

(17) Furrer, M. A.; Schmitt, F.; Wiederkehr, M.; Juillerat-Jeanneret, L.; Therrien, B. *Dalt. Trans.* **2012**, *41* (24), 7201–7211.

(18) Blunden, B. M.; Lu, H.; Stenzel, M. H. *Biomacromolecules* **2013**, *14* (12), 4177–4188.

(19) Blunden, B. M.; Chapman, R.; Danial, M.; Lu, H.; Jolliffe, K. A.; Perrier, S.; Stenzel, M. H. *Chemistry* **2014**, *20* (40), 12745–12749.

(20) Su, X.; Dong, C.; Zhang, J.; Su, L.; Wang, X.; Cui, H.; Chen, Z. *Cell Biosci.* **2014**, *4* (1), 7–19.

(21) Isidro-Llobet, A.; Alvarez, M.; Albericio, F. *Chem Rev* **2009**, *109* (6), 2455–2504.

(22) Montalbetti, C. A. G. N.; Falque, V. *Tetrahedron*. 2005, pp 10827–10852.

(23) Valeur, E.; Bradley, M. *Chem. Soc. Rev.* **2009**, *38* (2), 606–631.

(24) Lloyd-Williams, P.; Albericio, F.; Giralt, E. *Chemical approaches to the synthesis of peptides and proteins*; CRC Press: Boca Raton, 1997.

(25) Chandrudu, S.; Simerska, P.; Toth, I. *Molecules* **2013**, *18* (4), 4373–4388.

(26) Enow, R. A. E. PhD Dissertation. University of Nevada, Reno, 2014.

(27) Barth, a. *Prog. Biophys. Mol. Biol.* **2000**, *74* (3–5), 141–173.

(28) Ohshima, T.; Hayashi, Y.; Agura, K.; Fujii, Y.; Yoshiyama, A.; Mashima, K. *Chem. Commun.* **2012**, *48* (44), 5434–5436.

(29) Wong, G. W.; Lee, W. C.; Frost, B. J. *Inorg. Chem.* **2008**, *47*, 612–620.

(30) Starkey, L. S. *Introduction to Strategies for Organic Synthesis*; John Wiley & Sons, Inc.: Hoboken, NJ, USA, 2012.

(31) Cossy, J.; Pale-Grosdemange, C. *Tetrahedron Lett.* **1989**, *30* (21), 2771–2774.

(32) Goodreid, J. D.; Duspara, P. a.; Bosch, C.; Batey, R. a. *J. Org. Chem.* **2014**, *79* (3), 943–954.

(33) Ramasamy, R. *Armen. J. Phys.* **2015**, *8* (1), 51–55.

(34) Daigle, D. J. *Inorg. Synth.* **1998**, *32*, 40–45.

4 Synthesis & Characterization of Multimodal M-PTA Complexes

4.1 Introduction

4.1.1 Nitrogen coordination of PTA

As with RAPTA compounds and all PTA-containing ruthenium catalysts, most PTA research focuses on metal complexes where the phosphine is bound to the metal center *via* the phosphorus atom. However, based on the Pearson's hard-soft acid-base concept, the phosphorus and nitrogen atoms of PTA should also be able to coordinate to soft and hard atoms, respectively. Thus, when one considers the relatively hard nature of nickel, it is unsurprising that the first mention of a potentially nitrogen-bound PTA metal complex was made by Darensbourg *et al.* when they tentatively described a blue, nickelous transient species as $Ni(PTA)_{6-n}(H_2O)_n]^{2+}$, where the PTA ligands were possibly coordinated to the metal center *via* the nitrogen atom.[1]

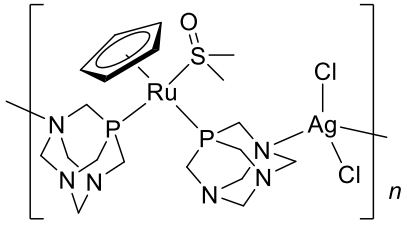

Figure 4.1: The first published nitrogen-bound 1D coordination polymer of PTA.

The first definitively nitrogen-bound PTA coordination complex was published by Peruzzini *et al.* in 2005 when they demonstrated κ^1-N coordination between silver and the PTA ligand of a ruthenium complex *via* a crystal structure.[2] The structure of this 1D coordination polymer, seen in Figure 4.1, was the first proof that nitrogen coordination can take place with PTA, albeit with assistance from phosphorus coordination or oxidation.[2,3] In 2006, our group published the synthesis and crystal structure of $Mn(PTA)_2(H_2O)_2X_2$, where X is Cl^- and Br^-, as the first reported κ^1-N transition metal complex with PTA that left the phosphorus atom uncoordinated.[4]

That same year, our group and another[5] also published the synthesis and characterization of κ^1-N PTA-BH_3,[6] where several forms of spectroscopic and computational analyses suggested the κ^1-P PTA-BH_3 analogue is not preferred. Interestingly though, when the ratio of borane to PTA was increased as in Scheme 4.1, successive substitution of the borane onto the PTA ligand had no preference between phosphorus or nitrogen substitution.

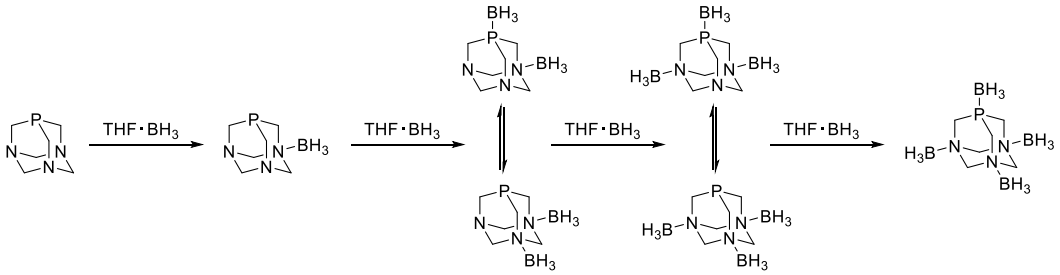

Scheme 4.1: Stepwise addition of borane to PTA.

The first mention in the literature of that potentially nitrogen-bound PTA metal complex, however, was not really investigated past its brief mention in the publication.[1] The complex was not characterized with XRD support, but rather observed as a transient intermediate during the synthesis of $Ni(PTA)_4$, according to Scheme 3.2 adapted from the publication. It was reasoned that the blue species was likely a nitrogen-bound PTA complex because octahedral nickel amines tend to be characteristically blue in color. In attempts to support this hypothesis, the authors explained, "…the measured pK_a of 5.70 ± 0.01 of a nitrogen-bound proton in $PTAH^+$ would suggest it to be a suitable ligand towards Ni(II)."[7] However, the authors mentioned that no color change was observed when they repeated this reaction with the nitrogenous analogue of PTA, hexamethylenetetraamine. In the first part of this chapter, I will explain my attempts to elucidate the structure of this blue transient nickel species of PTA utilizing solution-state and solid-state $^{31}P\{^1H\}$ NMR spectroscopy and single-crystal X-Ray crystallography.

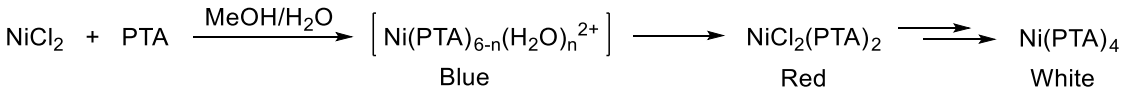

Scheme 4.2: Suggested scheme for synthesis of $Ni(PTA)_4$. (Adapted from ref)[1]

4.1.2 O=PTA Coordination to Metals

Also of interest to our group is the interaction between the oxide of PTA, 1,3,5-triaza-7,7'-phosphaadamantane oxide (O=PTA) and metals. The addition of borane to O=PTA was found to yield nitrogen-only coordination by X-ray spectroscopy.[6] In 2008, our group published the first example of oxygen bound O=PTA in the form of two different cobalt species.[8] The first was prepared by reflux of cobalt chloride with PTA in acetone and x-ray spectroscopy revealed O=PTA bound to cobalt *via* the nitrogen atom. However, when heat was removed from the reaction scheme, the resulting cobalt species exhibited oxygen coordination as well as nitrogen coordination. Although these two cobalt-bound O=PTA species, seen in Figure 3.2, suggest oxygen bound O=PTA is possible, they both fail to exhibit that exclusive oxygen coordination of O=PTA can take place without activation of a nitrogen atom. This same trend was seen with two more investigations focused on coordination between group 12 metals and the ligand.[3] In the second part of this chapter, I will expand on both my attempt to coordinate PTA directly to lanthanum and to coordinate O=PTA to the lanthanides lanthanum, cerium, samarium, europium, and ytterbium. All of the resulting complexes were characterized with solid-state FT-IR spectroscopy, the lanthanum and cerium complexes were characterized with solid-state ^{31}P $\{^{1}H\}$ NMR, and the cerium complex was also characterized with single-crystal X-ray crystallography.

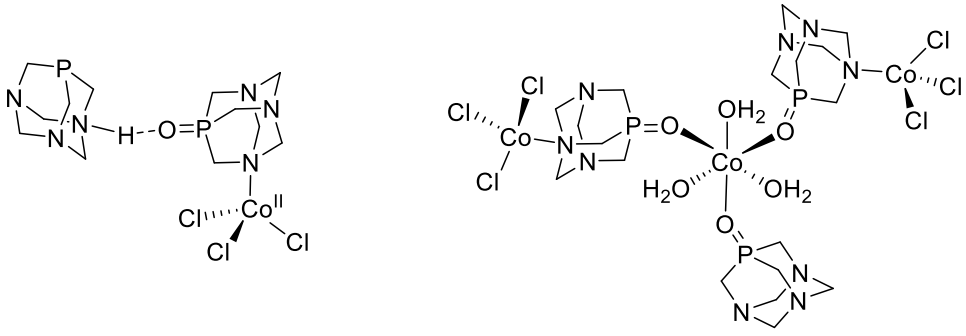

Figure 4.2: Two cobalt-bound O=PTA complexes our group reported previously.

4.2 Results and Discussion

4.2.1 Synthesis of $Ni(PTA)_2(X)_2$ Compounds *(X = Cl, Br)*

The blue transient species observed during the synthesis of $NiCl_2(PTA)_2$, as shown in Scheme 3.3, was characterized *via* three methods to elucidate its chemical structure. First, the reaction was monitored with solution state $^{31}P\ \{^1H\}$ NMR in the methanol-based reaction medium, with results shown in Figure 4.3 below and another stacked profile shows just the first and last spectra in Figure 4.4 for clarity.

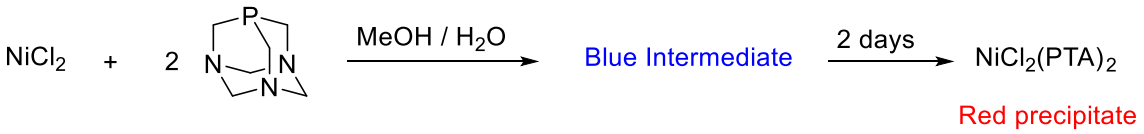

Scheme 4.3: Synthesis of $NiCl_2(PTA)_2$ and the unknown blue, intermediate species.

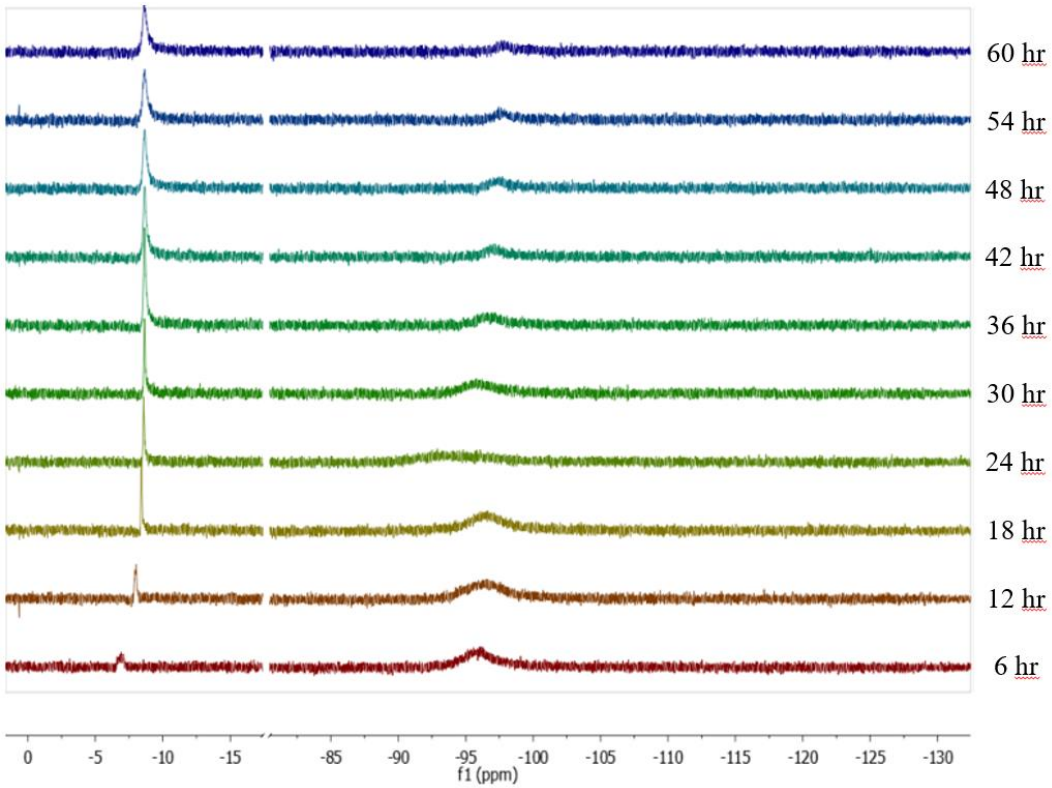

Figure 4.3: Time-resolved $^{31}P\ \{^1H\}$ NMR of the synthesis of $NiCl_2(PTA)_2$ in methanol.

A peak centered at -4 ppm is observed to grow in intensity as the reaction proceeds. Further, this peak appears to shift upfield 5 ppm in the first 18 hours of the experiment, followed by broadening throughout the course of the rest of the experiment. Also, a broad peak centered between -95 and -97 ppm decreases in intensity as the reaction goes to completion. By the end of the 60-hour experiment, the peak with a chemical shift of -95ppm had shifted upfield 2 ppm. Outside of the zoomed in areas shown in Figure 3.4, no peaks were observed whatsoever. The broadening of the peak between -95 and -97 ppm is possibly due to PTA exchange on the nickel metal center. However, the steady decrease in intensity for the peak indicates that the species the peak indicates is depleting from the reaction mixture over the course of the reaction. Broadening in the peak closer to 0 ppm could indicate either coordination of the phosphorus species to the now-reduced nickel metal center or exchange of the supposed oxidized PTA at the nickel metal center in solution. This peak is not the peak corresponding to the red species $NiCl_2(PTA)_2$, because it precipitates out of solution just like the reference suggests it does over the course of the reaction.

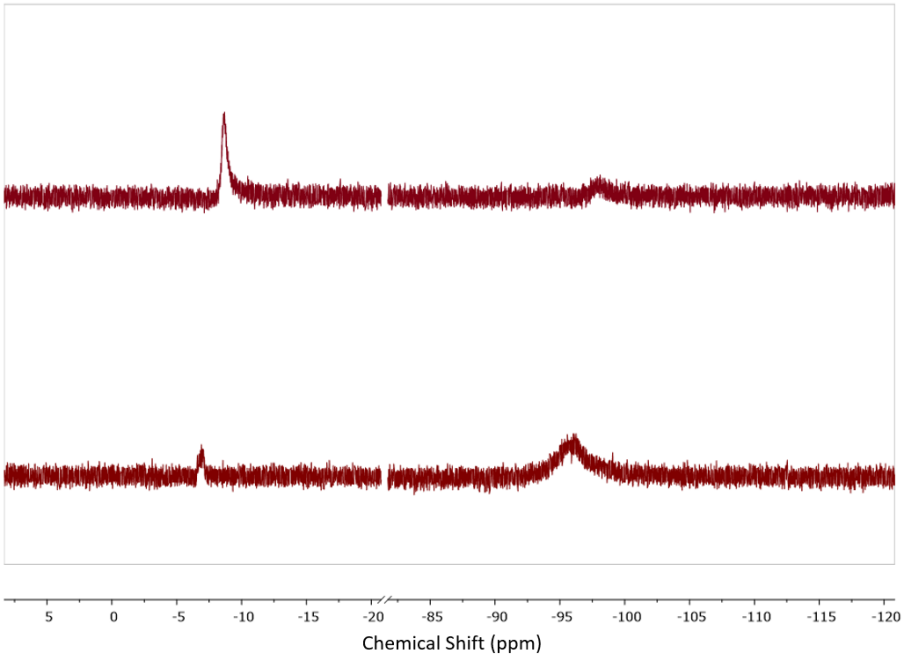

Figure 4.4: First (*bottom*) and last (*top*) $^{31}P\{^{1}H\}$ NMR from the time-resolved synthesis of $NiCl_2(PTA)_2$ in methanol, shown for clarity.

As was eluded to in the literature, the solution turned a dark, navy blue as soon as the starting materials were combined in the solvent. However, by the end of this time-resolved $^{31}P\{^{1}H\}$ NMR experiment, the solution was more of a faded blue color and there was a noticeable collection of red precipitate at the bottom of the NMR tube, as shown in Figure 4.5. It was assumed that the peak centered at -6 ppm does not correspond to the red product $NiCl_2(PTA)_2$ because it precipitates out of solution as the reaction is completed, which is likely why the $^{31}P\{^{1}H\}$ NMR chemical shift for the compound was never included in the original publication documenting its synthesis.[1]

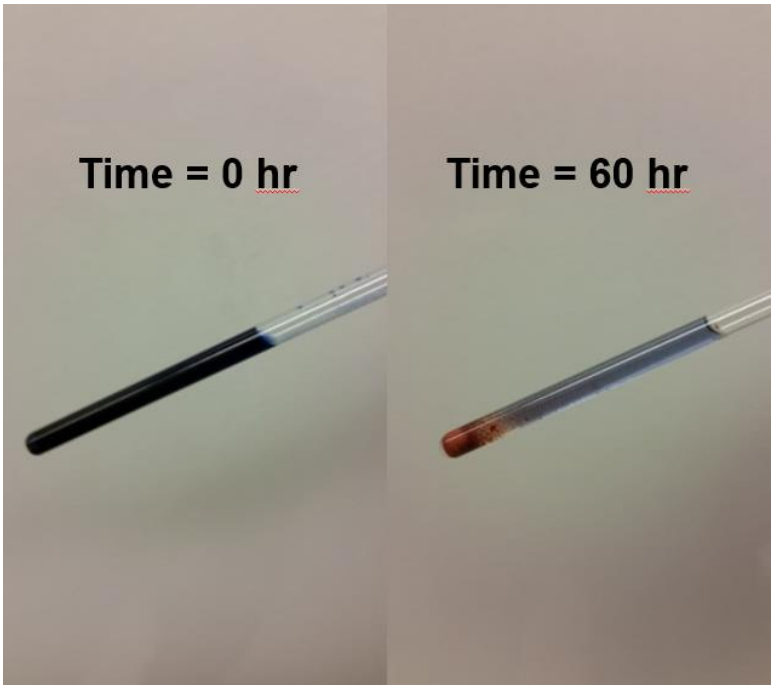

Figure 4.5: Before and after pictures of time-resolved $^{31}P\{^{1}H\}$ NMR for the synthesis of $NiCl_2(PTA)_2$.

In hopes to gain better insight into the differences between $NiCl_2(PTA)_2$ (**17**) and the blue intermediate during its synthesis (**18**), each were isolated as solids and characterized with solid-state $^{31}P\{^{1}H\}$ NMR, where all samples were referenced to an external standard of potassium phosphate. The chemical shifts for both **17** and **18** as well as some reference compounds that were also measured can be seen in Table 4.1. The structure of $ZnCl_2(PTA)_2$ has previously been reported

as determined with X-ray crystallography, which reveals that both PTA ligands coordinate to the zinc metal center *via* the nitrogen atoms.[9] Since several phosphorus-bound metal PTA complexes have a $^{31}P\{^{1}H\}$ NMR shift in the range of -50 to -70 ppm, it was assumed that the chemical shift of **17**, with a chemical shift of -65.0 ppm in the solid state, likely indicates that it is a phosphorus-coordinated metal-PTA complex. However, the determined solid-state $^{31}P\{^{1}H\}$ NMR spectrum of $ZnCl_2(PTA)_2$, reveals a sharp absorption at -99.0 ppm, roughly 9 ppm downfield that of PTA. The chemical shift of **18**, at -108.3 ppm, is only shifted 0.2 ppm upfield that of the chemical shift for PTA alone, seen at -108.1 ppm. Although these results seem to indicate that the structure of **17** is likely a phosphorus-bound complex, these data are not conclusive enough to assume the structure of **18**. The solid-state $^{31}P\{^{1}H\}$ NMR for PTA, **17**, and **18** is shown in Figure 4.6.

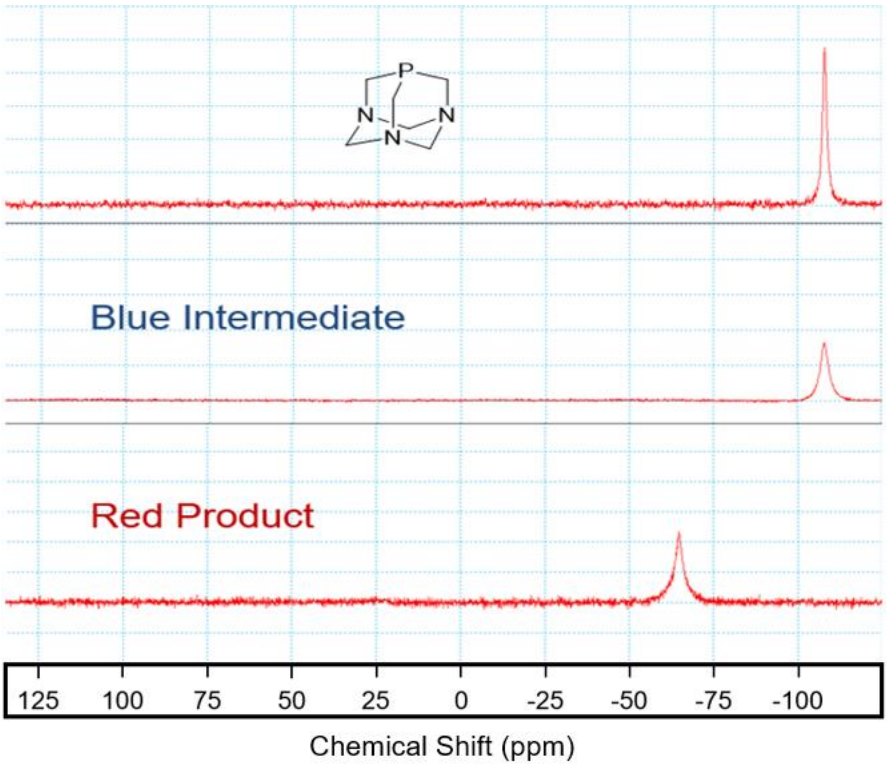

Figure 4.6: Solid-state $^{31}P\{^{1}H\}$ NMR of reagents and products in the synthesis of $NiCl_2(PTA)_2$. Spectra were obtained with samples spinning at 16,000 Hz.

Table 4.1: Solid-state $^{31}P\{^{1}H\}$ NMR chemical shifts for PTA, some derivatives, and metal complexes. The final column indicates the difference in chemical shift between the given compound and that of PTA.

	Chemical Shift [ppm]	Δ [ppm]
PTA	-108.1	--
O=PTA	-14.1	94.0
$ZnCl_2(PTA)_2$	-99.0	9.1
17	-65.0	43.1
18	-108.3	-0.2

Finally, X-ray quality crystals were grown of both the red and blue nickelous-PTA species. The solid-state structure of each compound was determined by X-ray crystallography. The resulting thermal ellipsoid representation for both the red species and blue species, seen in Figures 4.7 and 4.8, reveals their structures as *trans*-$NiCl_2(PTA)_2$ (**17**) and trigonal bipyramidal $NiCl_2(PTA)_3$ (**18**), respectively. The structure of **17** agrees with what is expected from its solid-state $^{31}P\{^{1}H\}$ NMR chemical shift observed while the broadening of the upfield peak in solution-state NMR could possibly be the result of PTA ligands exchanging at the metal center of **18**. However, the structure of blue **18** conflicts with its observed solid-state NMR spectrum, as the symmetry of the molecule should yield two separate, individual peaks in a 2:1 ratio corresponding to the two axial and single equatorial PTA ligands, respectively. However, it should be noted that the isolation technique for the solid state blue nickel species was different than that for the crystals of the blue species, so it is possible that the solid-state NMR sample was mostly unreacted PTA with a small amount of **18**. Especially when one considers that it only takes minor impurities to drastically vary the visual color of most transition metal species, it is possible that the solid-state sample for NMR was mostly unreacted PTA with a small amount of **18**.

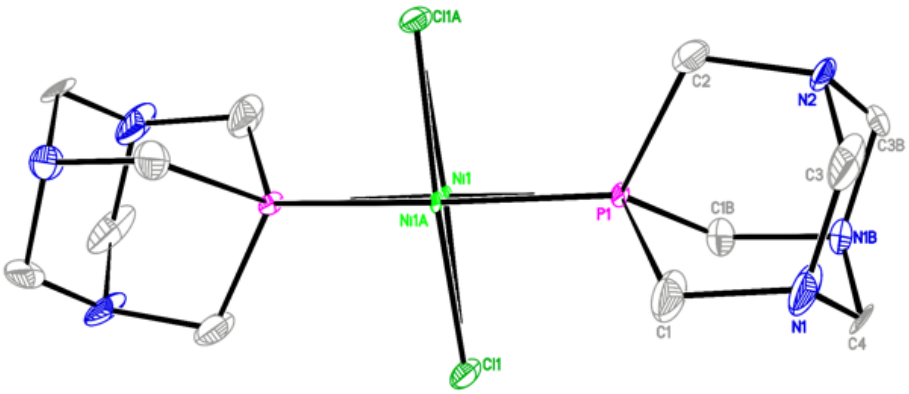

Figure 4.7: Thermal ellipsoid representation (50% probability) of $NiCl_2(PTA)_2$ **17** with the atomic numbering scheme. Hydrogen atoms have been omitted for clarity. Selected bond lengths (Å) and angles (deg): Ni1-P1 = 2.173(3); Ni1-Cl = 2.135(3); P1-C1 = 1.804(11); P1-C2 = 1.818(13); P1-Ni1-Cl1 = 92.34(13).

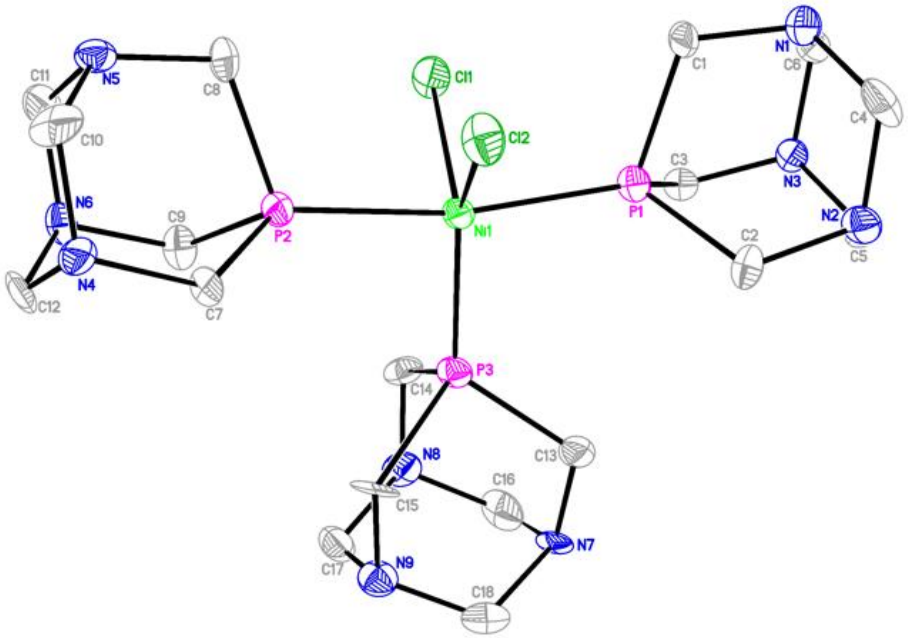

Figure 4.8: Thermal ellipsoid representation (50% probability) of $NiCl_2(PTA)_3$ **18** with the atomic numbering scheme. Hydrogen atoms have been omitted for clarity. Selected bond lengths (Å) and angles (deg): Ni1-P1 = 2.174(3); Ni1-P3 = 2.140(3); Ni1-Cl1 = 2.370(3); P1-Ni1-P2 = 168.76(11); P1-Ni1-P3 = 96.79(10); Cl1-Ni1-Cl2 = 113.05(11).

The crystal structure of **17** was solved with two nickel metal centers in 0.88 Å proximity to one another. While it is most likely that this is an error in the final crystal structure due to poor quality of the crystal utilized to determine this structure, the square-planar structure is what one would expect to see considering that most 4-coordinate first-row transition metal complexes are square planar. The observed P-Ni-Cl bond angle of 92.34(13) suggests that the structure is slightly twisted square planar, although again this could be due to the poor quality of the crystal. The steric bulk of the PTA ligands in **18** slightly distorts the trigonal bipyramidal geometry of the structure, evidenced by a P1-Ni1-P2 bond angle of 168.76(11). In both **17** and **18**, the nickel-phosphorus bond lengths fall between 2.140(3) and 2.174(3) Å, which compares with 2.167(3) for a previously published Ni-PTA metal complex.[10] The average (N)C-N bond lengths for **17** and **18**, 1.455(56) and 1.439(78), respectively, are not elongated from that of PTA. When compared with the data in Table 4.2, this appears to suggest that the PTA ligands are neither coordinated to a metal nor protonated. Future work should include attempting to grow crystals of the red nickel-PTA species **17** again so that higher quality crystal data might be obtained.

4.2.2 Synthesis of $Ln(O{=}PTA)_3(NO_3)_3$ Compounds (Ln = La^{3+}, Ce^{3+}, Sm^{3+}, Eu^{3+}, Gd^{3+}, Yb^{3+})

The novel interactions between both PTA and O=PTA with lanthanides were investigated, and the resulting complexes where characterized with crystallography, solid-state $^{31}P\{^{1}H\}$ NMR, and solid-state FT-IR. First, the addition of PTA to a solution of $La(NO_3)_3$ in acetonitrile yielded large, block crystals. Single-crystal XRD revealed protonated PTA in the second coordination sphere of nitrate-saturated lanthanum metal center, as seen in Figure 4.9. It is likely that trace water in the solvent coordinated to the metal center, in turn lowering its pK_a enough so that a proton could protonate the PTA molecule, and this mixture of PTA-H^+ and lanthanum with coordinated water molecules crystallized out of solution. Elongation of the N-C bonds at the proposed protonated nitrogen atom is observed in much the same way as literature examples of protonated PTA nitrogen

atoms, as can be seen in Table 4.2 where the bond lengths are compared. Further, crystallization of PTA in the second coordination sphere of lanthanides is expected because it mirrors the effect seen with PTA's nitrogenous analogue hexamethylenetetraamine (HMTA) and lanthanides in the literature.[11,12]

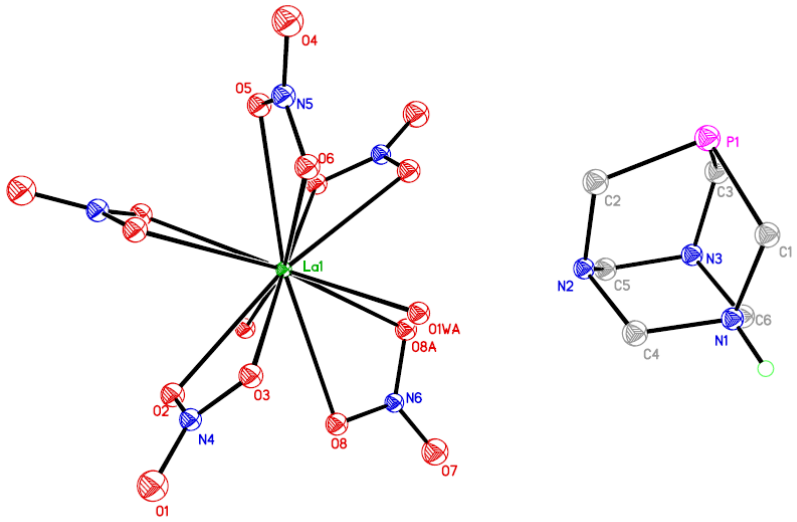

Figure 4.9: Thermal ellipsoid representation (50% probability) of the prepared complex $[La(NO_3)_5(OH_2)_2][PTA\text{-}H]$. Hydrogen atoms were omitted for clarity with the exception of the supposed hydrogen atom coordinated to a nitrogen atom of the PTA ligand.

Table 4.2: Typical (R)N – C bond lengths for PTA substituted at the nitrogen atom.

	$[La(NO_3)_5(OH_2)_2][PTA\text{-}H]^-$	$PTA\text{-}BH_3$	$Zn(PTA)_2Cl_2$	PTA
(R)N - C_{avg} [Å]	1.516	1.503[6]	1.504[9]	1.464[3]

When the oxide O=PTA is reacted with lanthanides though, the results differ in a generally expected fashion. Addition of O=PTA to the nitrates of lanthanum, cerium, samarium, europium, gadolinium, and ytterbium in methanol yielded uniform white powders which precipitated out of solution. From previous literature examples, when the oxide of PTA is coordinated to a metal center *via* the oxygen atom, the $\upsilon_{P=O}$ stretching frequency should red-shift approximately 20 cm^{-1} in the solid-state FT-IR (ssFTIR) spectrum.[13] As can be seen below in Figure 4.10 and with the detailed

analysis in Table 4.3, this shift is observed in the ssFTIR spectrum for each of the lanthanide O=PTA species prepared, suggesting that the oxygen atom of O=PTA is likely how each molecule coordinates to lanthanides.

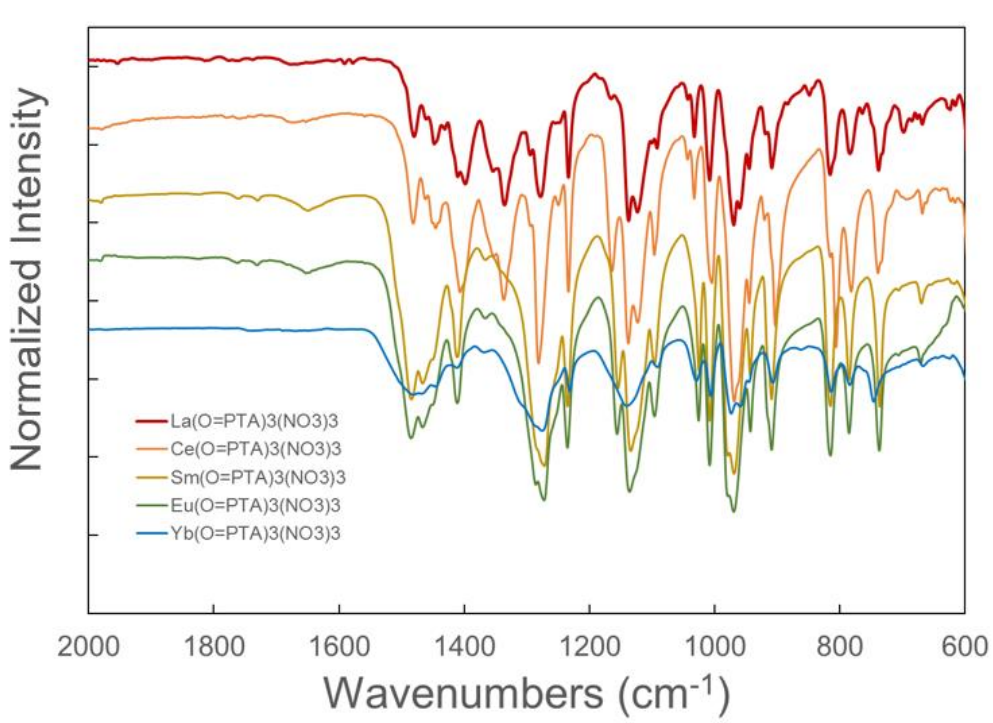

Figure 4.10: Stacked solid-state FT-IR spectra for $Ln(O{=}PTA)_3(NO_3)_3$ (Ln = La, Ce, Sm, Eu, Yb).

Table 4.3: P=O stretching frequency & red-shifts for Ln-bound O=PTA metal complexes.

	O=PTA	La^{3+}	Ce^{3+}	Sm^{3+}	Eu^{3+}	Yb^{3+}	Zn^{2+}	Cd^{2+}
$\nu_{P=O}$ [cm^{-1}]	1162	1138	1137	1133	1135	1139	1139[a]	1156[a]
Δ [cm^{-1}]	--	24	25	29	27	23	23	6

[a] = Values obtained from the literature[3]

The decrease in red-shift from lanthanum to ytterbium is likely artificial since the resolution of the instrument used is 4 cm^{-1}. Solid-state $^{31}P\{^1H\}$ NMR of O=PTA, $La(O{=}PTA)_3(NO_3)_3$ and $Ce(O{=}PTA)_3(NO_3)_3$, shown in Figure 4.11, reveal downfield shifts of 11.3 ppm and 34.6 ppm for the La^{3+} and Ce^{3+} complexes, respectively.

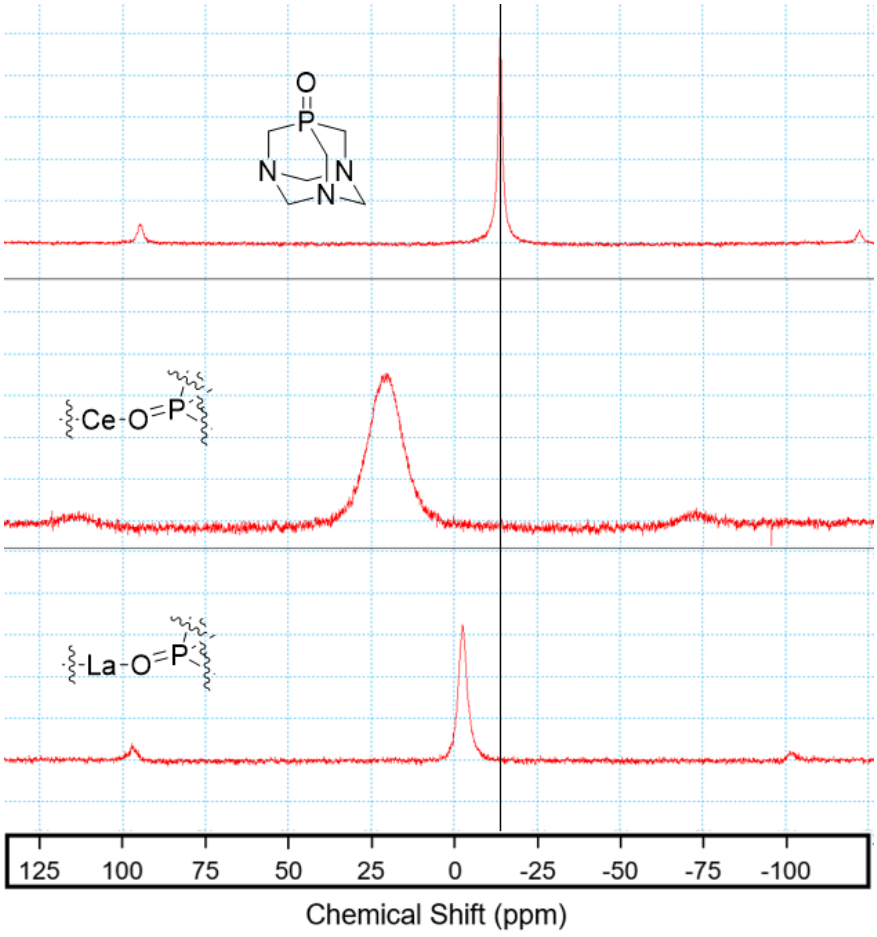

Figure 4.11: Stacked solid-state $^{31}P\{^{1}H\}$ NMR spectra for O=PTA and $Ln(O=PTA)_3(NO_3)_3$ (Ln = La, Ce). The black line is added as a visual aide for the downfield shifts for the metal complexes from O=PTA. Spectra were obtained from samples spinning at 16,000 Hz.

Finally, an X-ray quality crystal of $Ce(O=PTA)_3(NO_3)_3$, was grown from the slow evaporation of a solution of the compound in methanol over the course of 2 days. The solid-state structure of the compound was determined by X-ray crystallography and its thermal ellipsoid representation can be seen in Figure 4.12. The most interesting bond lengths have been outlined and compared with some other O=PTA metal complexes in Table 4.4 below.

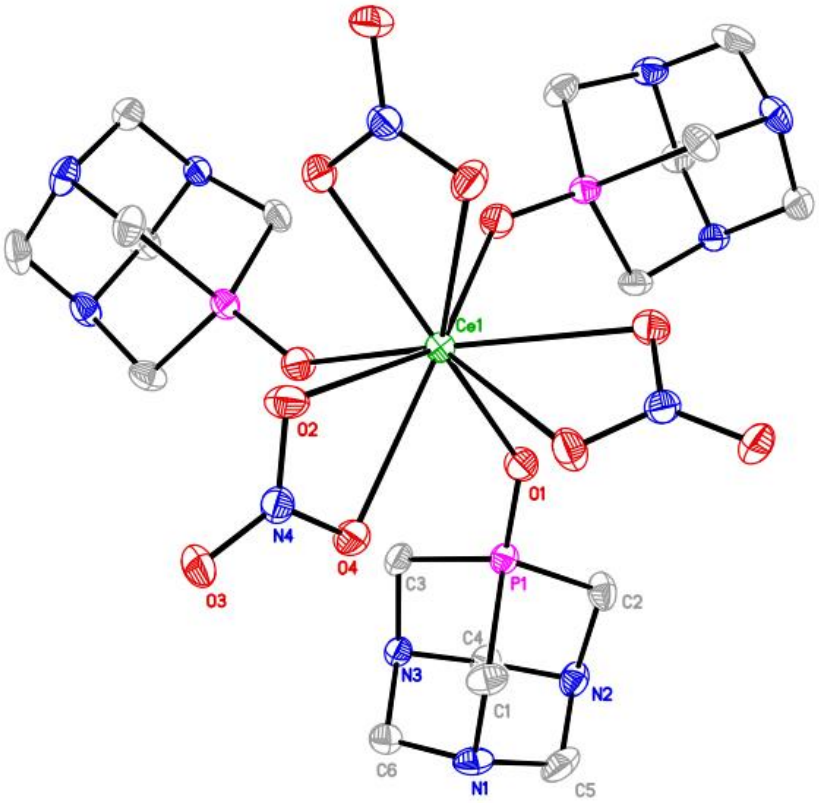

Figure 4.12: Thermal ellipspoid representation (50% probability) of $Ce(O{=}PTA)_3(NO_3)_3$, **20** with atomic numbering scheme. Hydrogen atoms have been omitted for clarity. Selected bond lengths (Å) and angles (deg): Ce1-O1 = 2.399(3); Ce1-O2 = 2566(4); Ce1-O4 = 2.611(4); O1-P1 = 1.500(4); N1-C6 = 1.469(7); N3-C6 = 1.460(7); N2-C4 = 1.473(7); O1-Ce1-O1 = 82.31(13); O1-Ce1-O2 = 125.30(12); O1-Ce1-O4 = 150.75(12).

Table 4.4: Bond distances for some O=PTA metal complexes.

	M - O(P)	P=O	(N)C – N_{avg}	Ref
O=PTA	--	1.476	1.465	[14,15]
$Ce(O{=}PTA)_3(NO_3)_3$	2.399	1.500	1.468	--
$[Co((O{=}PTA)CoCl_3)_2(OH_2)_3(O{=}PTA)]$*	2.059	1.491	1.472	[8]
$ZnCl_2(O{=}PTA)_2$	2.01	1.508	1.507	[3]

* Data for the O=PTA ligand that has all nitrogen atoms uncoordinated.

The extended metal – oxygen bond distance for the lanthanide compound compared with the others can be attributed to the ionic nature of lanthanide binding that is generally observed due

to spatial sequestration of the valence 4f orbitals by the 5s and 6p orbitals and agrees with what has previously been seen for P=O coordination to lanthanides with other phosphine oxides.[16] The highly electrophilic nature of the cerium metal center is likely the cause for significant lengthening of the P=O bond, as depletion of the electron density around the oxygen atom decreases the strength of the bond. Finally, the lack of significant elongation for the lower-rim nitrogen-carbon bonds indicates that the O=PTA ligands of the cerium complex are not likely protonated or otherwise substituted, suggesting these lanthanide O=PTA species are indeed the first prepared solely oxygen-bound O=PTA metal complexes to date.

4.2.3 Concluding Remarks

This chapter outlined some early efforts to understand how PTA and O=PTA interact with nickel and lanthanides. The structure of a blue intermediate species observed during the synthesis of $Ni(PTA)_4$ was found *via* single-crystal X-ray crystallography to be $Ni(PTA)_3Cl_2$ (**10**) rather than nitrogen-bound $[Ni(PTA)_{6-n}(H_2O)_n^{2+}]$, as had been eluded to in the literature.[1] The structure of the red precipitate formed as another intermediate in this reaction was also elucidated *via* single-crystal X-ray crystallography and found to confirm the original authors' assumption of $Ni(PTA)_2Cl_2$, however with the added geometrical identification of the *trans*- isomer (**18**). Solid-state ^{31}P $\{^1H\}$ NMR and solution state ^{31}P $\{^1H\}$ NMR were not enough to fully characterize both of these metal compounds due to difficulty in dispersion of **18** in solvent without reduction of the nickel metal center and the difficulty in isolating analytically pure solid-state samples of **17**.

Attempts to coordinate PTA directly to lanthanum were unsuccessful, as elucidated with single-crystal X-ray crystallography of large, block crystals resulting from the attempted synthesis. The crystal data revealed PTA in the second coordination sphere of a $La(NO_3)_5$ derivative, but through bond-lengthening of the (N)C-N bond lengths of the PTA molecule it was determined that the ligand had been protonated with trace amounts of water during the reaction.

Finally, in this chapter I have outlined the synthesis and characterization of the first lanthanide-bound O=PTA complexes that leave all nitrogen atoms available for binding. The x-ray data for the crystallized cerium O=PTA compound reveals bond length data that could possibly be helpful for elucidating nitrogen vs. oxygen coordination in future O=PTA coordinated complexes, and the ssFTIR data reveals $\nu_{P=O}$ red-shifts similar to what has been observed with other oxygen-bound O=PTA metal complexes.[3,8] Future work should include investigating nickel-bound PTA with other halide salts of nickel and crystallizing lanthanides in the middle of the series as well as at the end of the series so that the different crystallization patterns can be investigated as a function of lanthanide size. Crystallizing the remaining lanthanide salts with O=PTA will be useful as the different crystal patterns should reveal differences, if any, in crystal packing and stacking.

4.3 Experimental

4.3.1 Methods & Materials

Unless otherwise noted, all manipulations were performed on a double-manifold Schlenk vacuum line under nitrogen or in a nitrogen-filled glovebox. Reagent-grade acetonitrile (MeCN), methanol (MeOH), hexaaqua lanthanide nitrate salts, and nickel(II)chloride were all purchased from commercial sources and used as provided. Tetrakis(hydroxymethyl)phosphonium chloride was provided by Cytec and used as received without purification. 1,3,5-triaza-7-phosphaadamantane (PTA) and 1,3,5-triaza-7-phosphaadamantane-7-oxide (O=PTA) and were prepared according to the literature methods.[17] Solid-state FT infrared spectra were obtained with a Nicolet 6700 FT-IR spectrophotometer. All solution-state NMR spectra were recorded with a Varian NMR System 400 spectrometer with phosphorus NMR signals referenced to an external standard of 85% phosphoric acid in D_2O. All solid-state NMR spectra were recorded with a 2-channel 400 MHz Tecmag Discovery with an NMR Service GmbH MAS H-X broadband probe with phosphorus NMR signals referenced to an external standard of potassium phosphate. Crystallographic X-ray data were collected at low temperature (100 ±1 K) on a Bruker APEX CCD diffractometer with Mo Kα radiation (λ = 0.71073 Å) and a detector-to-crystal distance of 4.94 cm. Data collection was optimized with APEX2 software using a 0.5^o rotation about ω between frames and an exposure time of 10 s per frame. Integration of data, correction for Lorentz and polarization effects, and final cell refinement were performed with SAINTPLUS, and corrected for absorption using SADABS. The crystal structures were solved following direct methods with successive least squares refinement on F^2 using the SHELXTL 5.12 software package. Theoretical calculations using GAMESS were carried out at the B3LYP level of density functional theory (DFT) adopting Dunning's correlation consistent (cc)-pVTZ basis set.[18]

4.3.2 Synthesis

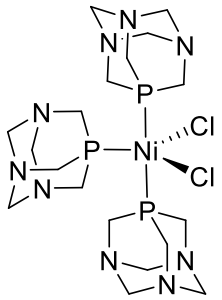

Synthesis of *cis*-tris(1,3,5-triaza-7-phosphaadamantane) nickel(II)chloride, 18 followed a modification of the literature method.[1] A mixture of $NiCl_2$ (51.3 mg, 0.38 mmol) and PTA (124.0 mg, 0.77 mmol) was diluted with 10 mL of methanol. The mixture was stirred for five minutes, filtered to remove **11**, and concentration of the filtrate yielded the product as a uniformly blue powder. (105.7 mg, 0.176 mmol, 44.4%) ^{31}P $\{^1H\}$ NMR (162 MHz, MeOH): -96.5 (s). Solid-State (ss)^{31}P $\{^1H\}$ NMR (162 MHz): -108.3 (s). Solid state IR [cm^{-1}]: 2938, 2898, 2806 (C-N_{PTA}). Blue crystals suitable for X-ray diffraction were obtained as plates by slow evaporation of a MeOH solution of the complex over the course of a few days.

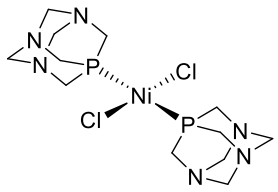

Synthesis of *trans*-bis(1,3,5-triaza-7-phosphaadamantane) nickel(II)chloride, 17 followed the literature procedure. A mixture of $NiCl_2$ (212.5 mg, 1.64 mmol) and PTA (491.3 mg, 3.13 mmol) was diluted with 10 mL of methanol. The solution was left to stir for 2 days, after which the product was collected by filtration. Washing with ether yielded the product as a red powder. (528.0 mg, 1.19 mmol, 73%) Solid state IR [cm^{-1}]: 2953, 2912, 2864 (C-N_{PTA}), 651.8 (Ni-P_{PTA}). Solid state ^{31}P $\{^1H\}$ NMR (162 MHz): -65.0 (s). Red crystals suitable for X-ray diffraction were obtained as plates by slow evaporation of a MeOH solution of the complex over the course of a few days.

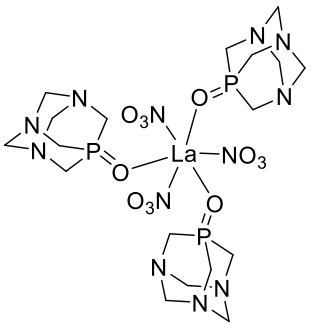

Synthesis of tris(1,3,5-triaza-7-phosphaadamantane) lanthanum(III)nitrate, 19 began with dissolving O=PTA (119.4 mg, 0.69 mmol) in 10 mL of dried acetonitrile. This solution was then transferred *via* cannula into a flask containing lanthanum nitrate hexahydrate (103.3 mg, 0.23 mmol). The reaction mixture was stirred for 15 hours and the solvent was removed under reduced pressure. The crude white product was washed with several generous portions of chloroform to remove unreacted O=PTA, yielding the product as a white solid. (70.6 mg, 83.6 μmol, 35.0%) Solid State ^{31}P {^{1}H} NMR (162 MHz): -2.8 (s). Solid state IR (Figure A.14) [cm^{-1}]: 1138 (P=O), 1335 ($O\text{-}N\text{-}O_{sym}$), 1131 ($O\text{-}N\text{-}O_{asym}$).

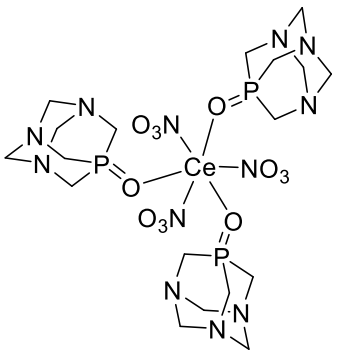

Synthesis of tris(1,3,5-triaza-7-phosphaadamantane) cerium(III)nitrate, 20 began with dissolving O=PTA (176.8 mg, 1.0 mmol) in 10 mL of dried acetonitrile. This solution was then transferred *via* cannula into a flask containing cerium nitrate hexahydrate (97.4 mg, 0.15 mmol). The reaction mixture was stirred for 15 hours and the solvent was removed under reduced pressure to yield a white solid (268 mg crude). Solid State ^{31}P {^{1}H} NMR (162 MHz): 20.5 (broad singlet).

Solid state IR (Figure A.15) [cm^{-1}]: 1137 (P=O), 1336 (O-N-O_{sym}), 1123 (O-N-O_{asym}). Colorless crystals suitable for X-ray diffraction were obtained as blocks by slow evaporation of a MeOH solution of the complex over the course of a few weeks.

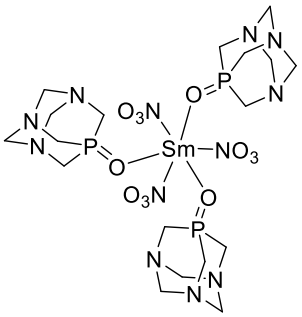

Synthesis of tris(1,3,5-triaza-7-phosphaadamantane) samarium (III)nitrate, 21 began with dissolving O=PTA (23.3 mg, 0.14 mmol) in 10 mL of dried acetonitrile. This solution was then transferred *via* cannula into a flask containing cerium nitrate hexahydrate (20.2 mg, 45.0 μmol). The reaction mixture was stirred for 15 hours and the solvent was removed under reduced pressure. yielding the product as a white solid. (38.3 mg crude) Solid state IR (Figure A.16) [cm^{-1}]: 1133 (P=O), 1465 (O-N-O_{sym}), 1153 (O-N-O_{asym}).

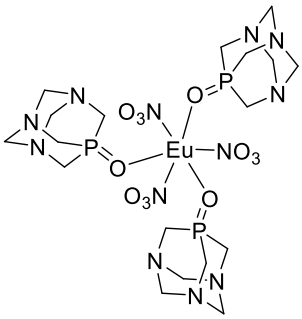

Synthesis of tris(1,3,5-triaza-7-phosphaadamantane) europium(III)nitrate, 22 began with dissolving O=PTA (50.1 mg, 0.11 mmol) in 10 mL of dried acetonitrile. This solution was then transferred *via* cannula into a flask containing lanthanum nitrate hexahydrate (58.1 mg, 0.34 mmol). The reaction mixture was stirred for 15 hours and the solvent was removed under reduced pressure.

The crude white product was washed with several generous portions of chloroform to remove unreacted O=PTA, yielding the product as a white solid. (59.4 mg, 69.3 μmol, 61.6%) Solid state IR (Figure A.17) [cm^{-1}]: 1135 (P=O), 1271 (O-N-O_{sym}), 1156 (O-N-O_{asym}).

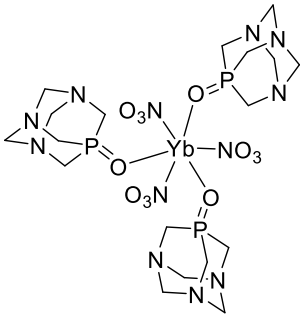

Synthesis of tris(1,3,5-triaza-7-phosphaadamantane) ytterbium(III)nitrate, 23 began with dissolving O=PTA (101.8 mg, 0.60 mmol) in 10 mL of dried acetonitrile. This solution was then transferred *via* cannula into a flask containing lanthanum nitrate hexahydrate (94.1 mg, 0.20 mmol). The reaction mixture was stirred for 15 hours and the solvent was removed under reduced pressure. The crude white product was washed with several generous portions of chloroform to remove unreacted O=PTA, yielding the product as a white solid. (80.2 mg, 91.3 μmol, 43.6%) Solid state IR (Figure A.18) [cm^{-1}]: 1139 (P=O), 1307 (O-N-O_{sym}), 1156 (O-N-O_{asym}).

4.4 References

(1) Darensbourg, D. J.; Robertson, J. B.; Larkins, D. L.; Reibenspies, J. H. *Inorg. Chem.* **1999**, *38* (10), 2473–2481.

(2) Lidrissi, C.; Romerosa, A.; Saoud, M.; Serrano-Ruiz, M.; Gonsalvi, L.; Peruzzini, M. *Angew. Chemie* **2005**, *117* (17), 2624–2628.

(3) Frost, B. J.; Lee, W.-C.; Pal, K.; Kim, T. H.; VanDerveer, D.; Rabinovich, D. *Polyhedron* **2010**, *29* (11), 2373–2380.

(4) Frost, B. J.; Bautista, C. M.; Huang, R.; Shearer, J. *Inorg. Chem.* **2006**, *45* (9), 3481–3483.

(5) Bolan, S.; Albinati, A.; Bravo, J.; Gonsalvi, L.; Peruzzini, M. *Inorg. Chem. Commun.* **2006**, *9*, 360–363.

(6) Frost, B. J.; Mebi, C. A.; Gingrich, P. W. *Eur. J. Inorg. Chem.* **2006**, *2006* (6), 1182–1189.

(7) Phillips, A. D.; Gonsalvi, L.; Romerosa, A.; Vizza, F.; Peruzzini, M. *Coord. Chem. Rev.* **2004**, *248*, 955–993.

(8) Frost, B. J.; Harkreader, J. L.; Bautista, C. M. *Inorganic Chemistry Communications*. 2008, pp 580–583.

(9) Smoleński, P.; Benisvy, L.; Da Silva, M. F. C. G.; Pombeiro, A. J. L. *Eur. J. Inorg. Chem.* **2009**, *2* (9), 1181–1186.

(10) Mebi, C. a.; Frost, B. J. *Zeitschrift für Anorg. und Allg. Chemie* **2007**, *633* (Ii), 368–371.

(11) Trzesowska-Kruszynska, A.; Kruszynski, R.; Zalewicz, M.; Bartczak, T. J. *J. Coord. Chem.* **2010**, *63* (6), 1013–1028.

(12) Zalewicz, M. *Thermochim. Acta* **1990**, *171*, 131–146.

(13) Frost, B. J.; Lee, W.-C.; Pal, K.; Kim, T. H.; VanDerveer, D.; Rabinovich, D. *Polyhedron* **2010**, *29*, 2373–2380.

(14) Daigle, D. J.; Pepperman, A. B.; Vail, S. L. *J. Heterocycl. Chem.* **1974**, *11* (3), 407–408.

(15) Daigle, D. J.; Pepperman, A. B. *J. Chem. Eng. Data* **1975**, *20* (4), 448–449.

(16) Ayi, A. A.; Kinnibrugh, T. L.; Clearfield, A. *Front. Chem.* **2014**, *2* (94), 1.

(17) Daigle, D. J. *Inorg. Synth.* **1998**, *32*, 40–45.

(18) Dunning Jr, T. H. *J. Chem. Phys.* **1989**, *90* (1989), 1007–1023.

5 Precipitation of Rare Earth Elements (REEs) from Aqueous Media with PTA-CO_2Li

5.1 Introduction

5.1.1 Rare Earth Elements

Rare earth elements (REEs) comprising yttrium, scandium, and the 14 lanthanides are required for many commercial applications utilized across the globe. These applications, listed in Table 5.2, span several industries including aerospace, cancer treatment, energy storage, transportation, displays, and petroleum refining, to name a few.[1]

Table 5.1: Uses of Rare Earth Elements across various industries spanning the globe.

Rare Earth Element	Uses in Industry
Scandium	Alloys with aluminum for aerospace framework, high-intensity discharge light
Yttrium	Televisions, chemotherapeutics, alloy strength enhancement
Lanthanum	Camera lenses, studio lighting, battery electrodes, lighter flints, biological tracer for calcium
Cerium	Catalytic converters, steel production, glass polishing, hydrogen storage
Praseodymium	Super-strong magnets, welding goggles, lasers
Neodymium	Ludicrously strong permanent magnets, electric motors for automobiles, lasers
Promethium	Nuclear batteries
Samarium	Cancer treatment, nuclear reactor control rods, x-ray lasers
Europium	TV screens, fluorescent glass, biological imaging, genetic screening tests
Gadolinium	Nuclear reactor shielding, nuclear marine propulsion, durability alloying, MRI contrast
Terbium	TV screens, fuel cells, sonar systems
Dysprosium	Commercial lighting, hard disk drives, transducers
Holmium	Lasers, glassing coloring, high-strength magnets
Erbium	Glass colorants, signal amplification for fiber optic cables, metallurgy
Thulium	High efficiency lasers, portable x-ray instruments, high temperature superconductors
Ytterbium	Stainless steel alloying, lasers, ground monitoring devices, ceramics
Lutetium	Petroleum refining, LED light bulbs, integrated circuit manufacturing

REEs have unique mechanical,[2] magnetic,[3] electrical,[4,5] catalytic,[6,7] and optical[8,9] properties that make them uniquely suited for these applications. Yttrium is most commonly utilized for alloying with magnesium to develop stronger metals because the atomic radii differences between the two elements combined with the wide range of solubility which greatly aids in manufacturing.[10] Gadolinium is often used as an MRI contrast agent because it is the most paramagnetic element which greatly affects the relaxation rate of inner-sphere exchanging water molecules.[5,11] Cerium has been used in and reviewed extensively for its use in automotive three-way catalytic converters (TWC) because of its uniquely high oxygen storage capacity (OSC).[7] Terbium[12,13] and europium[14] have been investigated extensively in bioimaging because of their abnormally long triplet state emission lifetimes (10^{-6} seconds) and their "fingerprint" emission profiles, which together allow one to view the high-purity lanthanide emission long after short-lived fluorescence *in vivo*.[9]

All of these properties are intrinsic to REEs for a few main reasons. First, the trivalent lanthanides are atypically small in ionic radii because of a phenomenon known as the lanthanide contraction.[1] This term describes the tendency for these elements to decrease in ionic radii faster than would typically be expected with increasing atomic number because of poor shielding of the fully populated 5s and 5p electrons by the 4f orbitals as shown in Figure 5.1. Further, the 4f orbitals containing valence electrons are spatially sequestered by the 5s and 5p orbitals,[15] so bonds between these elements and ligands tends to be relatively weak and ionic as ligands.[16] This sequestration is also in part why lanthanide emission is so pure; it is centered around f* → f transitions which do not participate in binding with ligands.[17] These main properties are inherent to REEs specifically and thus not easily replicated with any other metals or compounds, so it is hard to argue against the importance of REEs to the applications mentioned in Table 5.1.

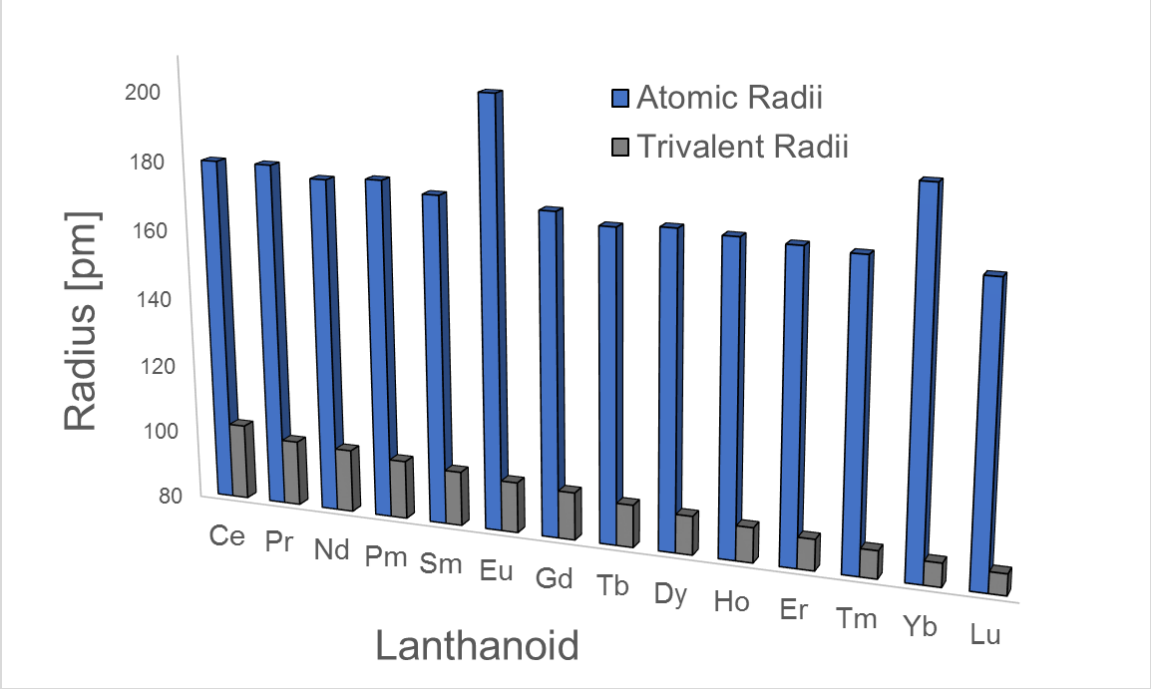

Figure 5.1: Variation of atomic and 3+ radius for the lanthanoid elements.

5.1.2 REE Supply Risk

Fortunately, the term 'rare' in Rare Earth Elements is a bit of a misnomer, as REEs are actually quite abundant in the Earth's crust.[18] However, they are typically only found in 10-300 ppm concentrations throughout minerals as mixtures of silicates, carbonates, phosphates, and halides,[19] making their commercialization difficult. As such, the extraction protocol to retrieve the REEs from these minerals as high-purity rare earth oxides (REOs) is typically energy-intensive and involves several complex steps. While more than 250 REE-containing minerals have been discovered to date, the only ones extracted until recently on a commercial scale were Bastnäsite, Monazite, and Xenotime.[20]

Normalizing the mineral extraction protocol for REEs from these three minerals helped to generate a stable supply of these elements to keep up with the demand as the aforementioned applicable areas in industry steadily grew over the past few decades. More recently, industry experts and academics alike have been raising concern about the economic and environmental

impacts regarding an upcoming global shortage of REEs. Regarding the economic impacts of the upcoming shortage, the United States Department of Defense has quoted an annual loss of up to $3.2 billion in critical materials if no action is taken to increase U.S. production of REEs.[21] Concerning the environment, the United States Department of Energy produced the chart seen in Figure 5.2 to accurately reflect the upcoming supply risk for materials that are critical to a global transition to clean energy between 2015 and 2025.[22]

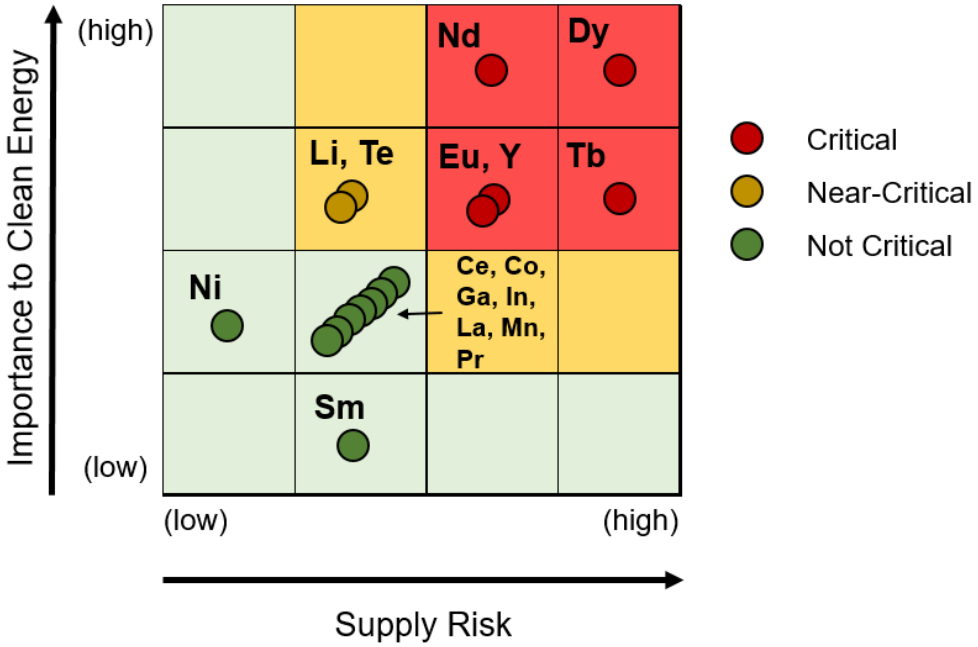

Figure 5.2: Metals important to clean energy vs. their predicted supply risk up to 2025 (Redrawn from literature).[22]

This upcoming shortage is being predicted mostly because of regulatory control in China, which currently dominates REE supply as can be seen in Figure 5.3. More specifically, the Chinese government is both shrinking allowable export quotas and shutting down more illegal mines.[23] The illegal mining operations are particularly troubling because they are unregulated and thus do not operate within the country's environmental guidelines, yet they produce greater than 30% of the country's entire REE export by some estimates. Therefore, interestingly, attempting to shut down

the illegal mines will help China's environment while simultaneously putting numerous other countries' at risk by limiting their REE supply required for green technologies.

In response to these upcoming shortages, REE mines are opening up for business across the planet. Several of these new mines are planning to commence production with REE minerals and ore compositions that have never been successfully processed before, which is pushing academics and industry professionals alike to innovate quickly enough with new materials and methods to keep up with expansion plans.[20]

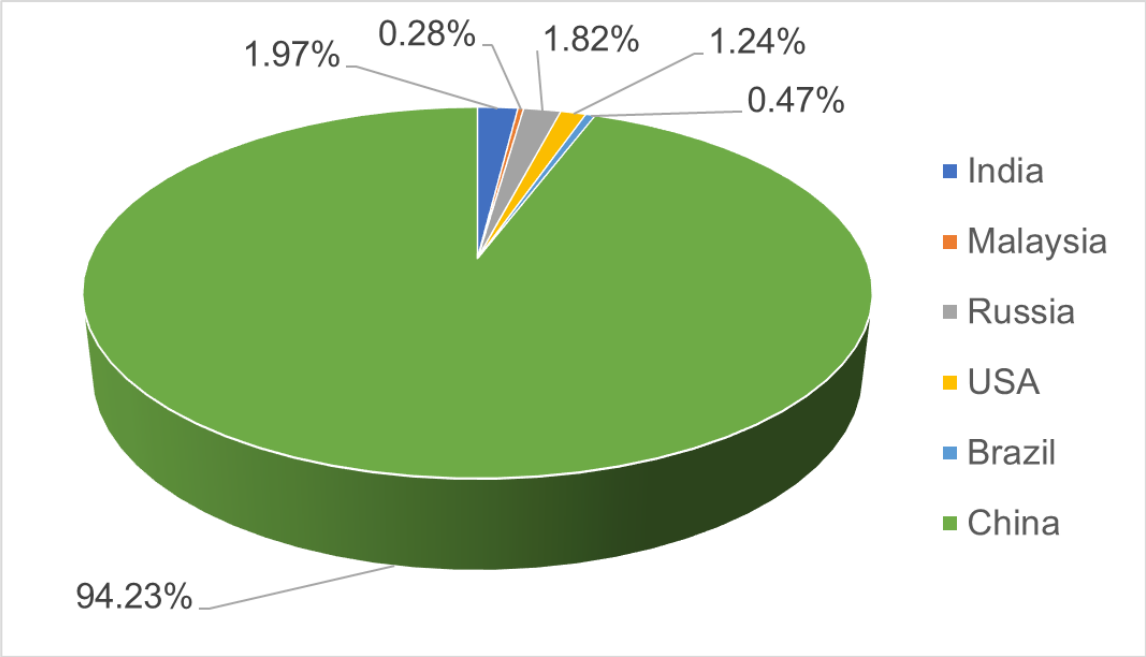

Figure 5.3: The world REE supply as of 2009. (Redrawn from literature)[18]

5.1.3 Extraction of REEs from Minerals

The first step of extracting REEs from minerals is referred to as beneficiation, and for REE minerals this process is most often froth flotation.[24,25] The REEs are first liberated from the ore through 'comminution,' crushing and grinding the ore down to particles between 0.7 – 100 μm in diameter. This fine ore powder is then 'conditioned' by dissolving in a fluid known as a lixiviant, which is either a strong acid, base, or oxidant that separates the REE ions from the rest of the mineral, a process commonly referred to as 'digestion.' The product of this step is then mixed with

surfactants then placed into a reactor for foam generation and separation. The foam is generated with a combination of forced air and an agitation, and the REE minerals adhere to the surface of the resulting bubbles which float to the top of the mixture. The foam is referred to as either 'REE concentrate' or 'leachate,' while the remaining pulp at the bottom of the reactor is referred to as the 'tailings.' The concentrate is collected while the tailings are placed into another reactor to repeat the process and increase yield of REEs in the leachate. A diagram visually representing this process can be seen in Figure 5.4.

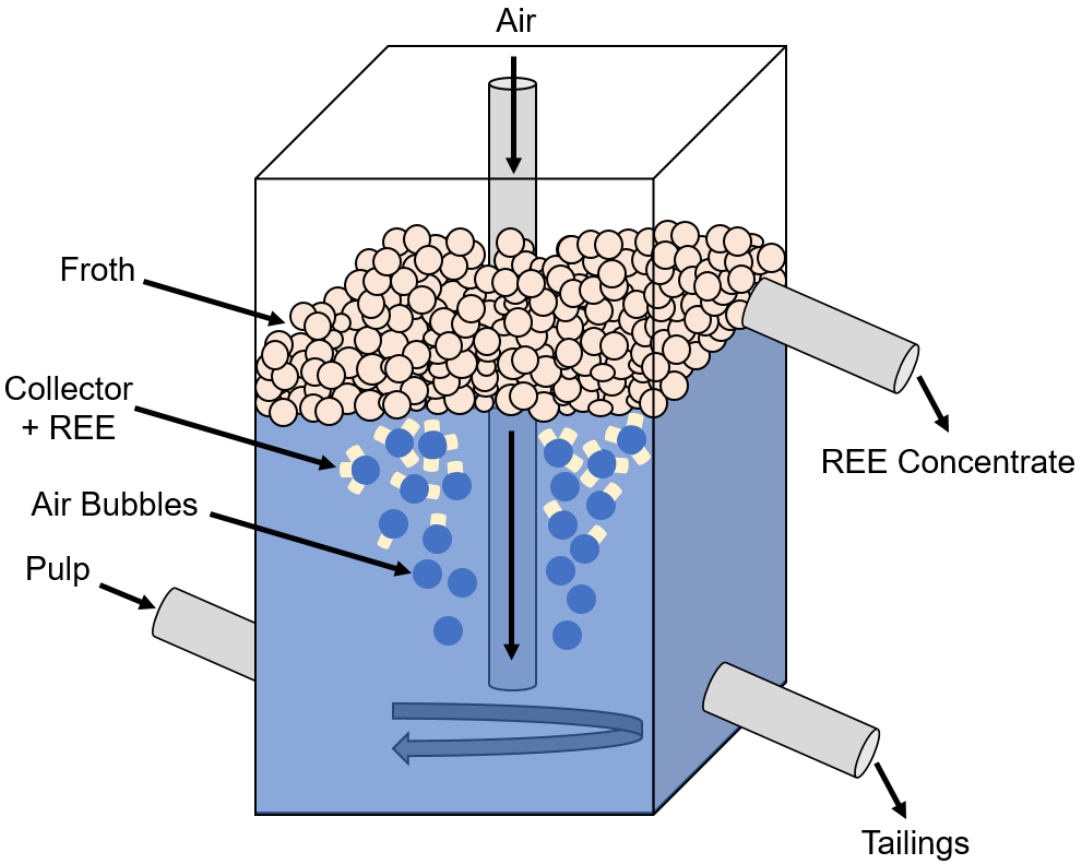

Figure 5.4: The typical froth flotation leaching process.

Several chemical reagents are required throughout the froth flotation process, but they are all broadly classified into three categories: Collectors, modifiers, and frothers.[26] Collectors are the surfactants that adsorb to the surface of minerals in the pulp, decreasing their hydrophilicity and

facilitating their flotation in the organic leachate. Modifiers are added to the mixture to enhance this process through any of several means including pH modulation to enhance adsorption of collectors, removal of unwanted minerals from the concentrate through adsorption and precipitation, or even by changing the viscosity of the pulp so that bubbles rise faster through the mixture.[27] Finally, frothing agents, commonly referred to as 'frothers,' are added to ensure the air bubbles are able to rise through the mixture in a controllable manner.

5.1.4 The Chemistry of REE Beneficiation

The general structure of collectors is that of a polar headgroup which adsorbs to the mineral surface and a nonpolar backbone for emulsification and adsorption of the mineral to the froth.[26] Some of the most widely used collectors to date are shown in Figure 5.5. For the most common sulfide-based minerals, the polar headgroup of collectors is one or several sulfur functional groups. Non-sulfur minerals, meanwhile, generally interact with the harder nitrogen and oxygen atoms of carboxylate- or amine-terminated collectors. The organic side-chains of these collectors are often long-chain hydrocarbons from petroleum.

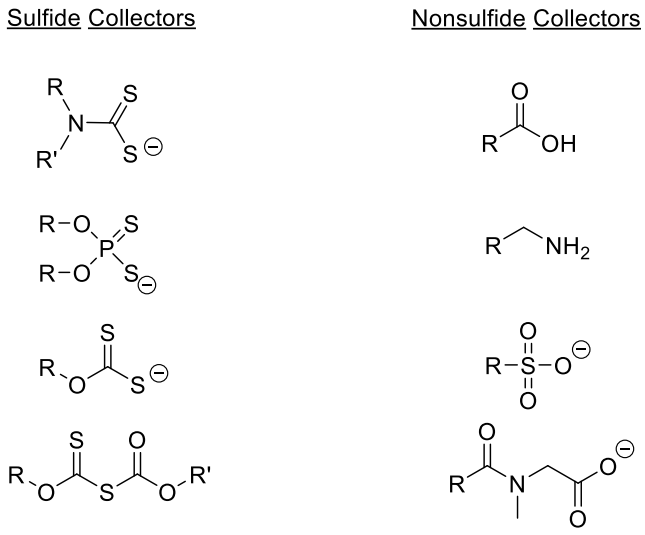

Figure 5.5: The general structure of collectors used in froth flotation for both sulfide and non-sulfide minerals. (Figure redrawn from reference)[26]

Modifiers include polysaccharides, carboxymethyl-cellulose, guar, zinc and sodium cyanide, sulfate salts, lignin, and sodium sulfide to name a few. Each of these reagents affects collector adsorption to the surface of value minerals by modifying the collector pK_a, hydrophobicity, selectivity, or froth stability. For non-sulfide flotation, modifiers are important because they are required for better selectivity than with sulfide flotation. The most common frothing agents are polypropylene glycols and ethers.

Since the highest REE-containing minerals bastnäsite, monazite, and xenotime are all non-sulfide minerals, their respective collectors usually adsorb to the mineral surface with oxygen- or nitrogen-containing functional groups. The general structure for bastnäsite is (REE)CO_3F, where the dominant REE is cerium, lanthanum, or yttrium, while monazite and xenotime are both phosphate minerals with a higher content of the heavy REEs. To-date, the most commonly used collectors for flotation of REE-bearing minerals are hydroxamic acids, fatty acids, dicarboxylic acids, and organic phosphoric acids.[28] The structures of two collectors that have been patented as collectors for flotation of REE-bearing minerals is shown in Figure 5.6.[29] These compounds are often used in conjuction with oils which, since they are not water soluble and don't readily dissolve in the pulp, are used in excess and generate high volumes of waste.

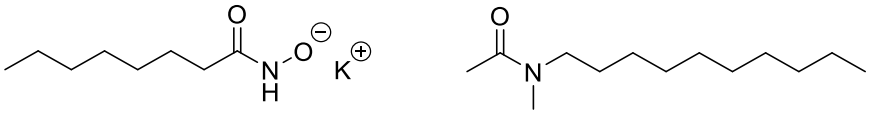

Figure 5.6: Two collectors that have been investigated for and patented as collectors for REE-bearing minerals.

5.1.5 The Chemistry of REE Isolation

After separation from the gangue through beneficiation, the REE ions are extracted from the concentrate into an organic solution, typically kerosene, with an extractant. These extractants

are referred to as either acidic, cationic, or neutral, as demonstrated with a few of the commercialized examples in Figure 5.7.[30]

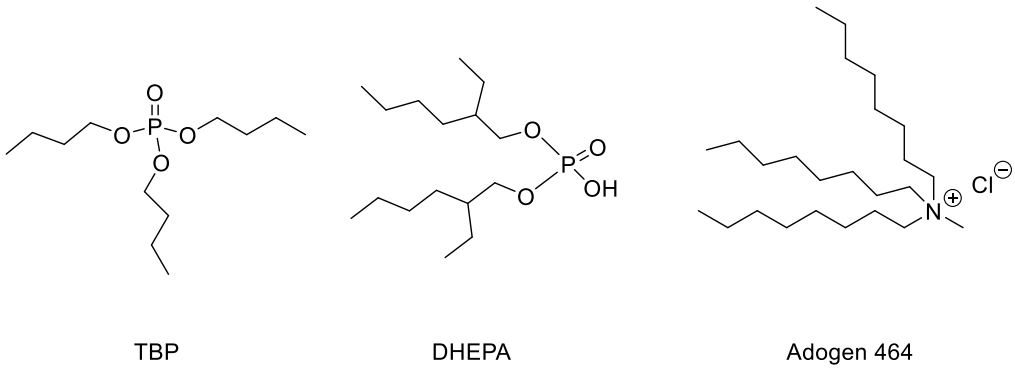

Figure 5.7: A neutral, acidic, and cationic extractant for REE extraction.

The efficacy of these extractants is typically measured by two factors, the distribution coefficient D_M and the separation factor $\beta_{M1/M2}$. The equation for determining the distribution coefficient can be seen in equation 5.1 as:

$$D_M = \frac{[\overline{M}]}{[M]} \quad \textbf{(5.1)}$$

where $[\overline{M}]$ is the concentration of the metal ion in the organic phase and [M] is the concentration of the corresponding ion in the aqueous phase.[30] Correspondingly, the separation factor is defined with equation 5.2 as:

$$\beta_{M1/M2} = \frac{D_{M1}}{D_{M2}} \quad \textbf{(5.2)}$$

and compares the distribution coefficient for one metal ion vs. another. By slightly adjusting the concentration of extractant, $\beta_{M1/M2}$ can be drastically varied to favor and disfavor particular REEs for selective extraction into the organic phase. As an example, Figure 5.8 demonstrates the separation factors for recycled REEs from neodymium magnet leachate with a 0.3 *M* solution of DHEPA in several different organic solvents.[31] This figure reveals the most ideal solvent for this

extraction is hexane because the separation factor for all REEs involved is higher than in any other solvent.

After extraction, which separates the individual REE ions, REEs are 'stripped' from the extractants to yield free REE ions. The REEs are stripped out of the organic phase and back into an aqueous phase with solutions of dilute acids. From the aforementioned study involving extracting REEs from Nd-magnet recycling, it was found that 100% of the REEs could be stripped from the 0.3 *M* DHEPA / hexane solution into an aqueous solution of 2 *M* HCl by agitating a mixture of the two solutions for 20 minutes.[31] In industry, this stripping typically takes several steps and requires as much as 1,000 Liters of dilute acid per 100 grams of REE recovered.[1]

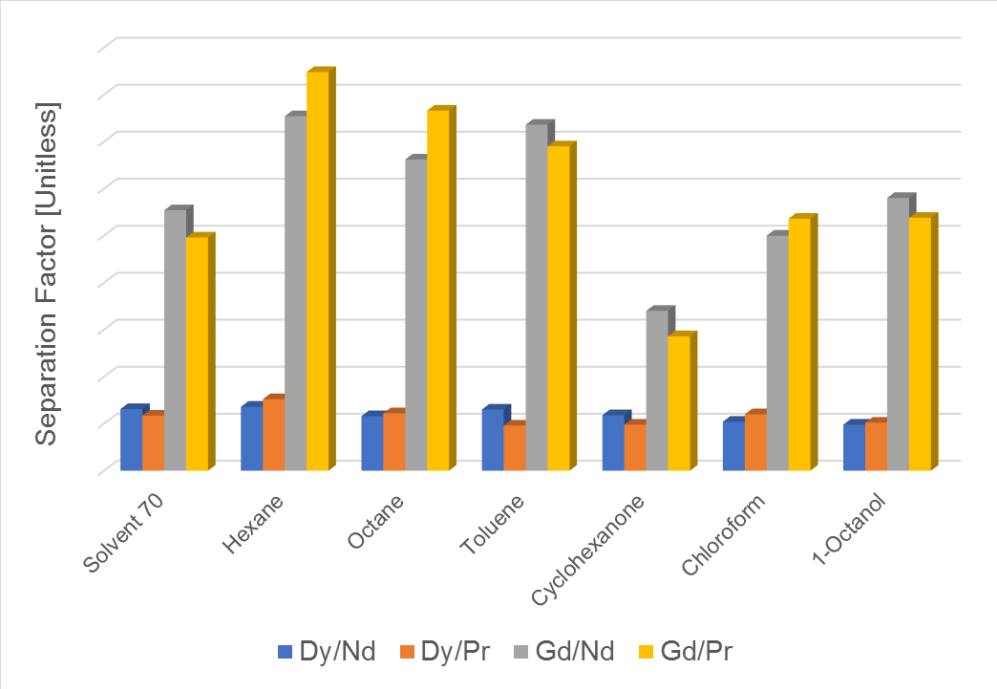

Figure 5.8: Separation factors for Nd-magnet leachate extraction in several organic solvents.

The final step in isolating high-purity REEs is typically to precipitate them out of solution with subsequent calcination to yield rare earth oxides (REOs). The REOs are the most ideal composition of REEs to provide in industry because they are the most stable oxides of almost all other elements on the periodic table,[1] one of the few REE lattices that is not hygroscopic, and they

are easily derivatized, making them suitable starting materials. These REOs are typically obtained through precipitation with either sodium hydroxide or sodium oxalate in leaching processes referred to as the 'alkali' or 'acidic' treatments, respectively. The alkali treatment refers to a leaching protocol called "decomposition," where the collector is a solution of 60-70% sodium hydroxide and the solution is heated to 140-150ºC to dissolve REEs into the REE concentrate while precipitating out early alkali phosphates for easy removal.[32] The acidic treatment, meanwhile, utilizes a strongly acidic collector such as sulfuric[33] or phosphoric[34] acids, and REE-oxalate precipitation takes place when the pH is lowered below 4 after extraction and stripping.[30]

5.1.6 PTA-CO_2Li for REE Precipitation

According to a review investigating the sustainability and environmental impacts of REE mining, it was advised that the best way to reduce the total greenhouse gas impact associated with the process is to reduce the acid and energy consumption during processing (extraction and stripping).[35] Thus, the goal of this investigation was to focus on replacement of the reagents used in extraction and stripping that require a high degree of acidification, waste water generation, and energy consumption.

As a highly water-soluble amphoteric molecule with both oxygen- and nitrogen-containing functional groups, PTA-CO_2Li could potentially serve as a new viable collector for the flotation of REE-bearing minerals. Since it is so water soluble, it is possible that PTA-CO_2Li would not need to be used in excess for efficient flotation to take place. However, in order to understand how this phosphine would work as a collector, its interaction with REEs in aqueous media has to be better understood. Furthermore, PTA-CO_2Li could potentially serve as a precipitation agent for separation of the REEs from strip solutions. Current precipitation agents after isolation currently include peroxicarbonate,[36] sulfate,[37] phosphate,[38] and most often, sodium oxalate.[1,3,34,39,40] The use of peroxicarbonates requires the use of excess hydrogen peroxide, which can be difficult to scale

because of the reagent's sensitivity to explosion.[41] Sulfate and phosphate precipitation of the REEs, meanwhile, utilizes concentrations of sulfuric[42] and phosphoric[38] acids high enough to yield a solution pH less than 0.5, requiring a large volume of NaOH to neutralize solutions before disposal. Finally, the low solubility of sodium oxalate requires using a large volume of acid to generate the more soluble oxalic acid for precipitation to take place.[40]

The use of **10** for REE precipitation from strip liquor would be preferable to these precipitating agents for two main reasons. From a structural standpoint **10** has the potential to coordinate to REEs *via* its carboxylate functionality as well as one of its basic amine-type nitrogen atoms, which should enhance the propensity for REE chelation over the other chelates currently utilized. Next, the water solubility of **10** (ca. 3.8 *M*)[43] is 13 times greater than for sodium oxalate (ca. 0.276 *M*) at room temperature. This suggests that, assuming that complexes with **10** precipitate out of solution upon coordination, precipitation of REEs with **10** could possibly take place with a lower molar loading than compared with oxalate. Thus, the goals of this investigation were to identify the propensity for **10** to precipitate REEs out of aqueous solution, elucidate and optimize the reaction conditions for the precipitation, and to demonstrate that REEs were successfully removed from solution *via* spectroscopic and gravimetric methods.

5.2 Results & Discussion

5.2.1 Acidification of PTA-CO_2Li

Since one of the key factors in REE precipitation from the strip liquors is reaction pH (as described at the end of section 5.1.5 of this chapter), a $^{31}P\{^1H\}$ NMR titration of **10** was conducted (raw spectra in Figure A.19) to determine if the ligand can be protonated. A solution of **10** and PTA-$(CO_2Li)_2$ **(25)** in water was prepared and the pH was increased to 10 with the addition of sodium hydroxide. The solution was then incrementally acidified with the addition of dilute hydrochloric acid, and the chemical shift of the $^{31}P\{^1H\}$ NMR after each increment was measured to generate the curve seen in Figure 5.9 for **10**. Since the smooth curve that can be drawn between the data points from pH 3 to 10 appears very similar to that of the titration of a weak base, protonation at a single site on the ligand was assumed to have taken place. However, below pH 3, the deviation from the smooth curve is suggestive of a second protonation below that pH.

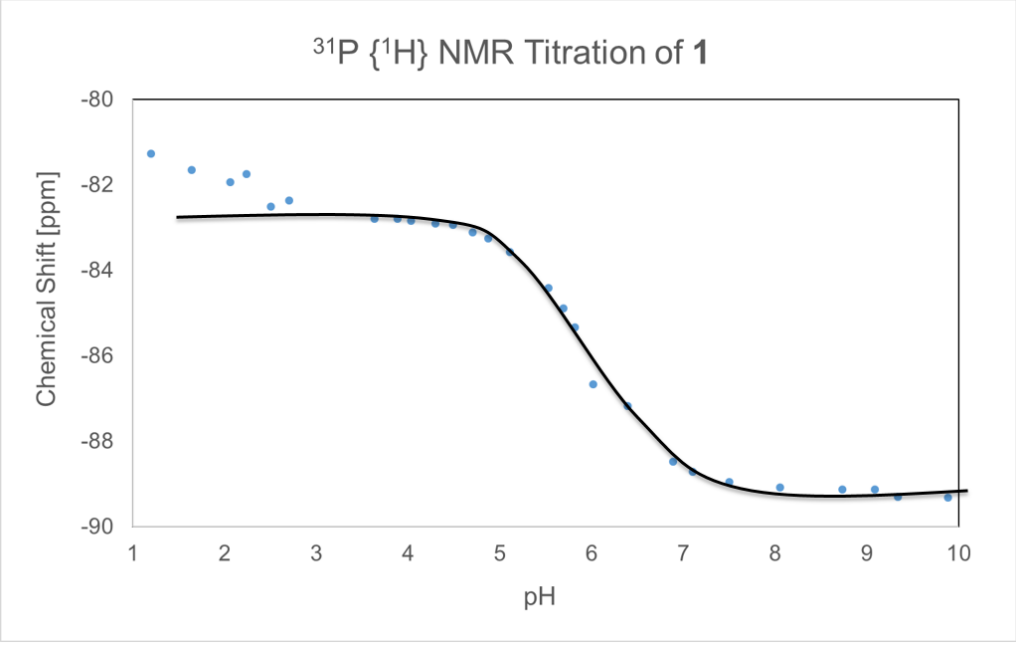

Figure 5.9: Solution state $^{31}P\{^1H\}$ NMR titration curve for **10** in water. The black line is included to guide the eye; a pK_a of 6.1 ± 0.2 for the protonated form of **10** was calculated from the data.

These data were utilized to calculate a pK_a of 6.1 ± 0.2 following a literature approach,[44] which is very similar to the reported pK_a of 5.70 for PTA-H$^+$.[45] The analysis of these data utilizes the assumption that the chemical shift observed at each pH is the sum of contributions from the protonated and unprotonated forms of the ligand times their respective mole ratios. Using equation 5.3, where the chemical shift for the protonated and unprotonated forms are ν_{BH+} and ν_B, respectively and x_{BH+} and x_B are the respective mole ratios, the mole ratio of acid and base were calculated for each spectrum at each pH.

$$\nu = (\nu_{BH+})\,(x_{BH+}) + (\nu_B)\,(x_B) \qquad \textbf{[5.3]}$$

With these data, the mole ratio and pH for each mass spectrum were used in equation 5.4 to calculate the pKa for each spectrum.

$$pK_a = pH + \log \frac{x_{BH+}}{x_B} \qquad \textbf{[5.4]}$$

The data points below pH 3 appear to deviate from the expected titration curve of a monoprotic acid, likely suggestive of protonation at another site on the ligand. Ring-opening is not expected since ring-opened PTA derivatives have typically have $^{31}P\{^1H\}$ NMR chemical shifts between -20 to -30 ppm and those seen throughout the titration never exit the range of -80 to -90 ppm.[46]

Density Functional Theory (DFT) calculations were carried out with Dunning's correlation consistent triple-zeta (cc-pVTZ) basis set and a B3LYP functional to determine the most stable isomer of protonated **10**. Structures resulting from protonation of the carboxylate, phosphorus atom, and the three nitrogen atoms were each subject to geometry optimization, and the resulting relative energies of the isomers are displayed in Figure 5.10. According to these results, the least stable structure is the carboxylic acid, while the most stable structure is that in which nitrogen 3 is protonated, the zwitterionic species 1,3,5-triaza-7-phosphaadamantane-6-carboxylate-3-ammonium *N*-[PTA-CO_2^-][H^+] (**24**). These results are interesting because of the implication that

the most stable isomers of this protonation are those where the proton is not located on the carboxylate or the nitrogen atom directly adjacent to it. This is interesting because, when this zwitterion is generated in solution, the carboxylate functional group and adjacent nitrogen atom will likely remain unbound and available for Ln^{3+} coordination, making metal coordination at either or both sites sterically possible.

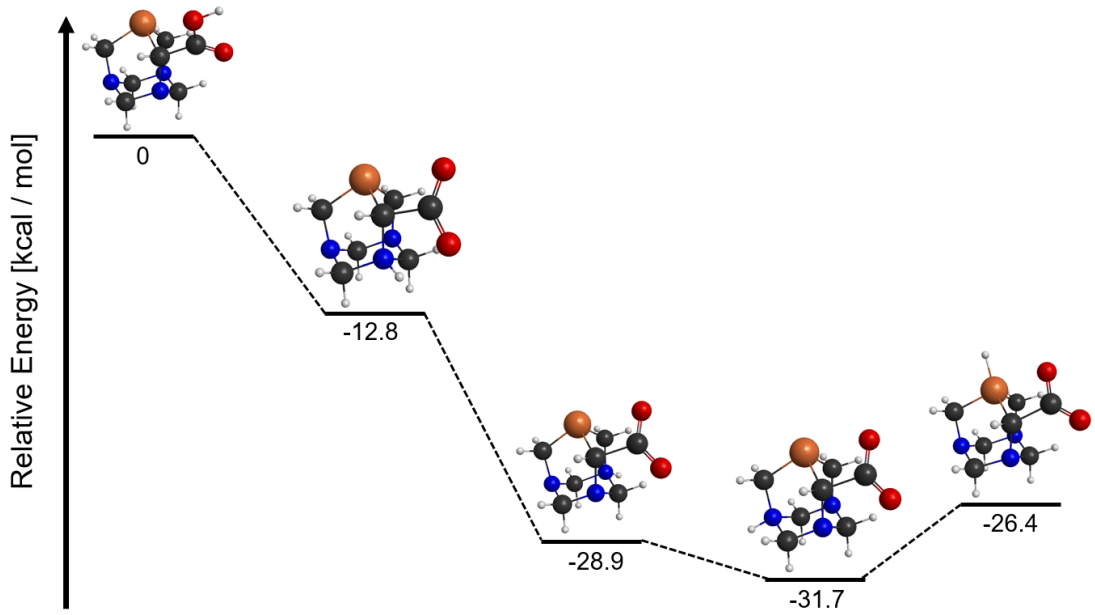

Figure 5.10: Relative energies for [PTA-CO_2^-][H^+]as calculated with DFT. The most stable isomer of the ligand according to the calculations is the zwitterionic species *N*-[PTA-CO_2^-][H^+] (**24**).

Since **10** has both carboxylate and amine functional groups, it is reasonable to assume that the pK_a of **24** might be similar to that of amino acids which have the same. It is long been understood that amino acids exhibit two pK_as at low and high pH corresponding to the carboxylic acid and the ammonium, respectively.[47] The isoelectronic point, where the ammonium / carboxylate zwitterion is the dominant species in solution, is characterized by the p*I*, or the pH that lies halfway between pK_a 1 and pK_a 2. As can be seen in Table 5.2 below where the pK_a 1, pK_a 2, and p*I* for most of the amino acids are identified, pK_a 1 is generally between 1 and 2, pK_a 2 is generally between 9 and 10, and the p*I* typically falls between 5 and 6. Between the experimentally determined pK_a, its

similarity to the p*I* of most amino acids, and the calculated relative energies which all agree, it is reasonable to assume that protonation of **10** yields **24**.

Table 5.2: The pK_a and pI values for amino acids most similar in structure to **10**.[47]

	pK_a 1	pK_a 2	pI
Alanine	2.34	9.49	6.00
Asparagine	2.02	8.8	5.41
Cysteine	1.96	10.28	5.07
Glutamine	2.17	9.13	5.65
Glycine	2.34	9.6	5.97
Histidine	1.82	9.17	7.59
Isoleucine	2.36	9.6	6.02
Leucine	2.36	9.6	5.98
Methionine	2.28	9.21	5.74
Phenylalanine	1.83	9.13	5.48
Proline	1.99	10.6	6.3
Serine	2.21	9.15	5.68
Threonine	2.09	9.1	5.6
Tryptophan	2.83	9.39	5.89
Tyrosine	2.2	9.11	5.66
Valine	2.32	9.62	5.96

5.2.2 Attempted Isolation of PTA-$(CO_2Li)_2$

When the synthesis and characterization of **10** was first published, the authors also indicated that repeating the reaction without solvent yields a mixture of **10**, PTA, and the dicarboxylate product PTA-$(CO_2Li)_2$ (**25**) as shown below in Scheme 5.1.[43] However, the purification of **25** was not elucidated. To the best of my knowledge, there exist no published reports for how to separate **25** from **10** after this synthesis, nor how to just prepare **25** alone. Thus, the goal of these investigations was to explore different ways to either convert **10** into **25** or separate **25** from **10**.

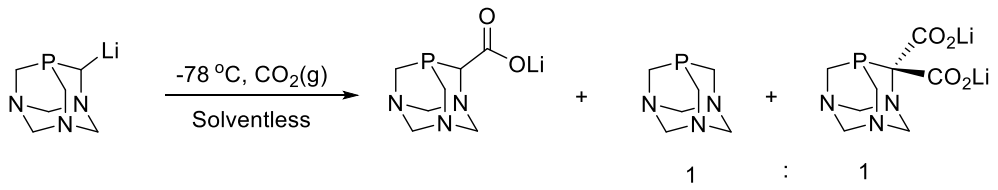

Scheme 5.1: Synthesis of **25**.

First, attempts were made to synthesize **25** from **10**. The lithiation of **10** was attempted in THF with *n*-BuLi. The procedure for this lithiation mirrored that of the lithiation of PTA, however the ^{31}P $\{^{1}H\}$ NMR of the resulting D_2O-quenched product, shown in Figure 5.11, revealed only a 61% conversion to product. Furthermore, a peak was observed with a chemical shift of -2.09, assumed to indicate that a portion of the product was oxidized in the synthesis. It was hypothesized that this transformation did not proceed in higher yield due to the low solubility of **10** in THF.

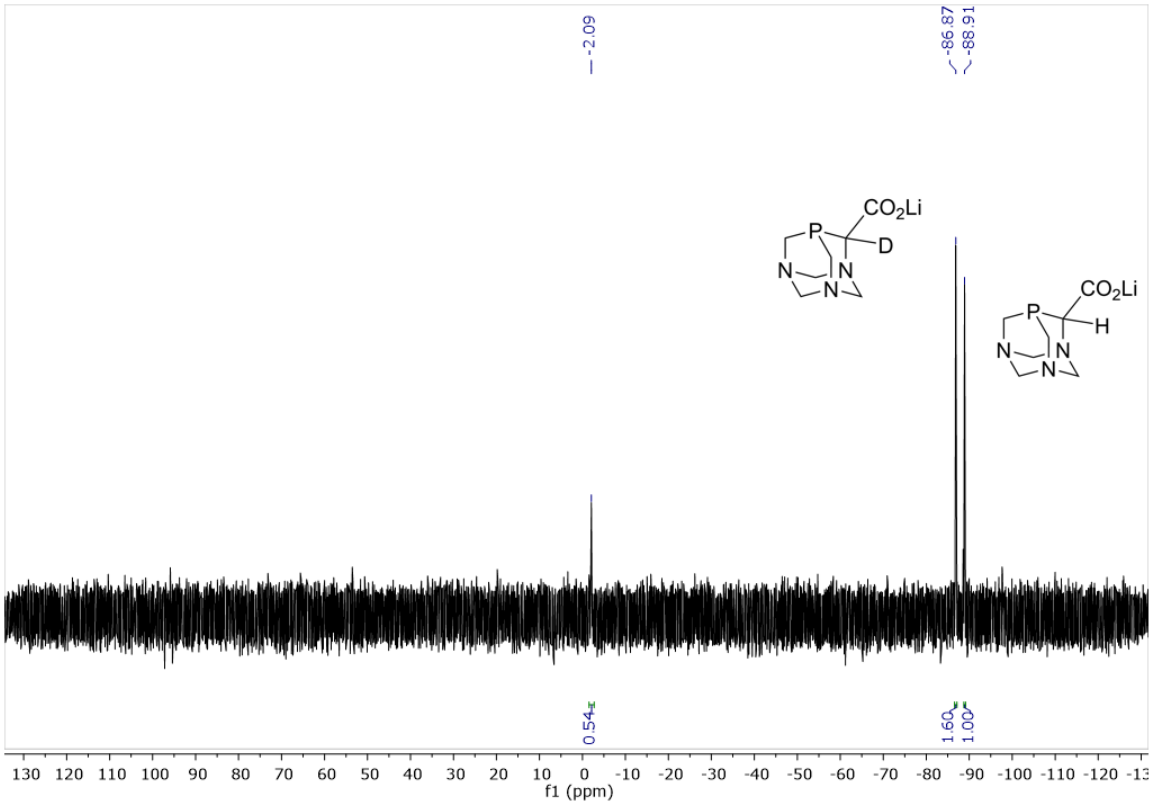

Figure 5.11: Solution state ^{31}P $\{^{1}H\}$ NMR of the D_2O-quenched product from the attempted lithiation of **10**.

The remaining efforts focusing on the isolation of **25** were directed towards synthesis following the published procedure and different methods to subsequently separate **25** from **10**. First, a cation-exchange experiment was conducted between **10** and bis(triphenylphosphine)iminium chloride (PPN-Cl). The hope was that, after cation exchange with the lithium atoms, the [PTA-CO_2][PPN] (**26**) and [PTA-$(CO_2)_2$][PPN]$_2$ (**27**) salts might exhibit different enough polarity for separation with column chromatography. The product **26** was prepared by mixing a THF solution of **10** with PPN-Cl in a 1:1 mole ratio, and $^{31}P\{^1H\}$ NMR of the resulting product, Figure 5.12, reveals two main peaks at -87.0 and 21.3 for the two phosphorus resonances expected in **26**. This reaction was repeated with a 3:1 mixture of **10** : **25** yielded both **26** and **27**, and $^{31}P\{^1H\}$ NMR of both the filtrate (Figure A.20 and precipitate (Figure A.21) from the reaction suggest that **27** stayed dissolved in solution while **26** precipitated out of solution. Further work will be required to refine this approach, but it appears from these initial results that this method might indeed separate the two molecules effectively.

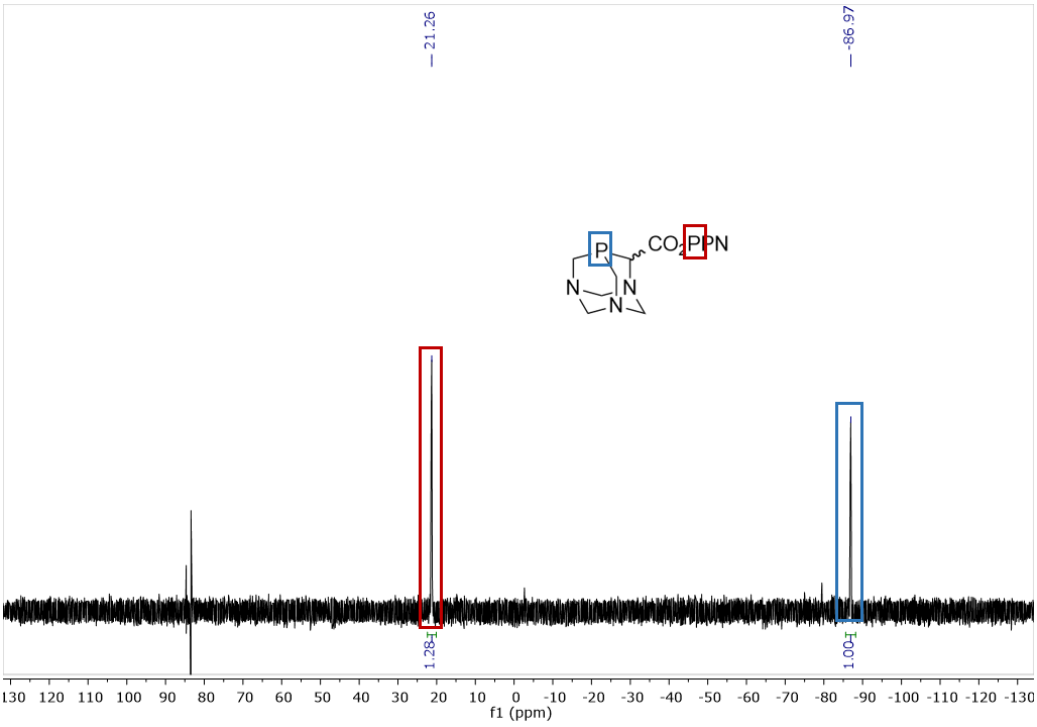

Figure 5.12: Solution state $^{31}P\{^1H\}$ NMR of **26** in water.

Another approach attempted to separate **10** from **25** was to coordinate the phosphines to a metal complex in hope that the resulting metal complexes could be more easily separated. A mixture of **10** and **25** was combined with the $RuCl_2(\eta^6\text{-toluene})]_2$ dimer in a solvent mixture of DCM and MeOH and refluxed overnight yielding a bright orange solution. Mass spectrometry of the resulting product revealed a parent ion at 480 $^m/_z$, but the isotopic distribution pattern differed slightly from what was expected for $RuCl(\eta^6\text{-toluene})(PTA\text{-}(CO_2Li)(CO_2))$ as can be seen in Figure 5.13 where the two are both displayed together. Solution state $^{31}P\{^1H\}$ NMR spectroscopy of the product in water revealed two peaks with chemical shifts of -2.2 and 2.3 ppm, respectively as would be expected for the diastereomeric products. (Figure A.22). This reaction was repeated with the $[RuCl_2(\eta^6\text{-cymene})]_2$ dimer but the mass spectrum (Figure A.23) of the crude product matched even less with the predicted isotopic distribution, suggesting this reaction requires further work.

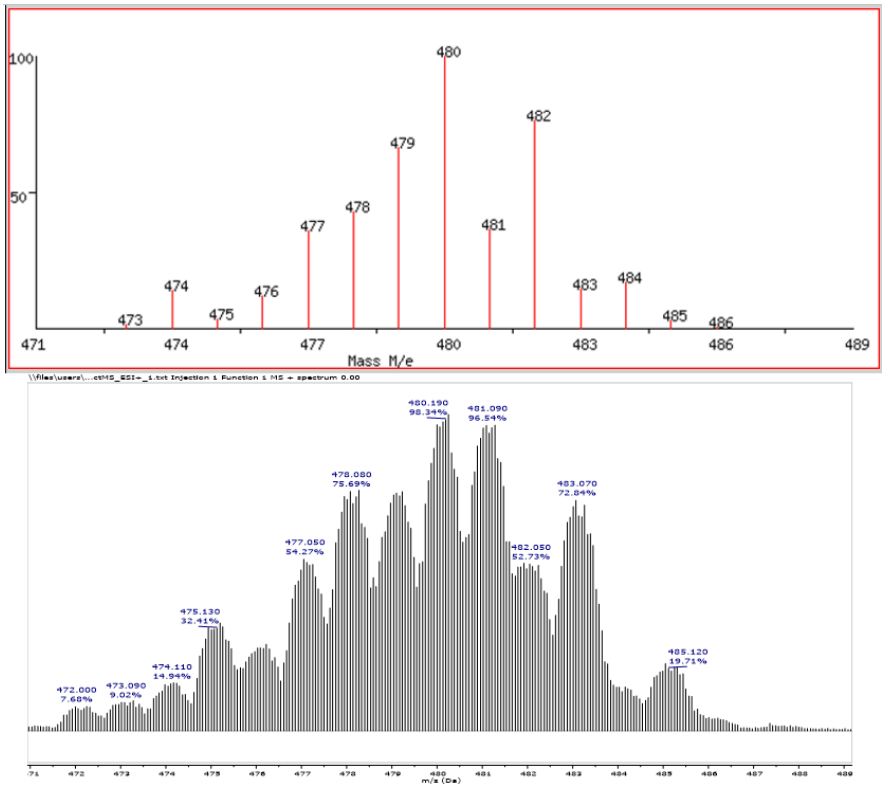

Figure 5.13: Predicted (*top*) isotopic distribution pattern for $RuCl(\eta^6\text{-toluene})(PTA\text{-}(CO_2Li)(CO_2))$ and experimental (*bottom*) mass spectrum for the crude product from its attempted synthesis.

Finally, the pK_a of the protonated **25** was investigated to see if it might differ enough from **10** to allow for a method to isolate the phosphines through acidification. From the same ^{31}P {^1H} NMR titration for **10** (see previous section), the pKa for **25** was determined. The resulting titration curve, shown in Figure 5.14, reveals a trend very similar to that of the curve for **10**. From the data, a pK_a of 6.1 ± 0.5 was calculated.

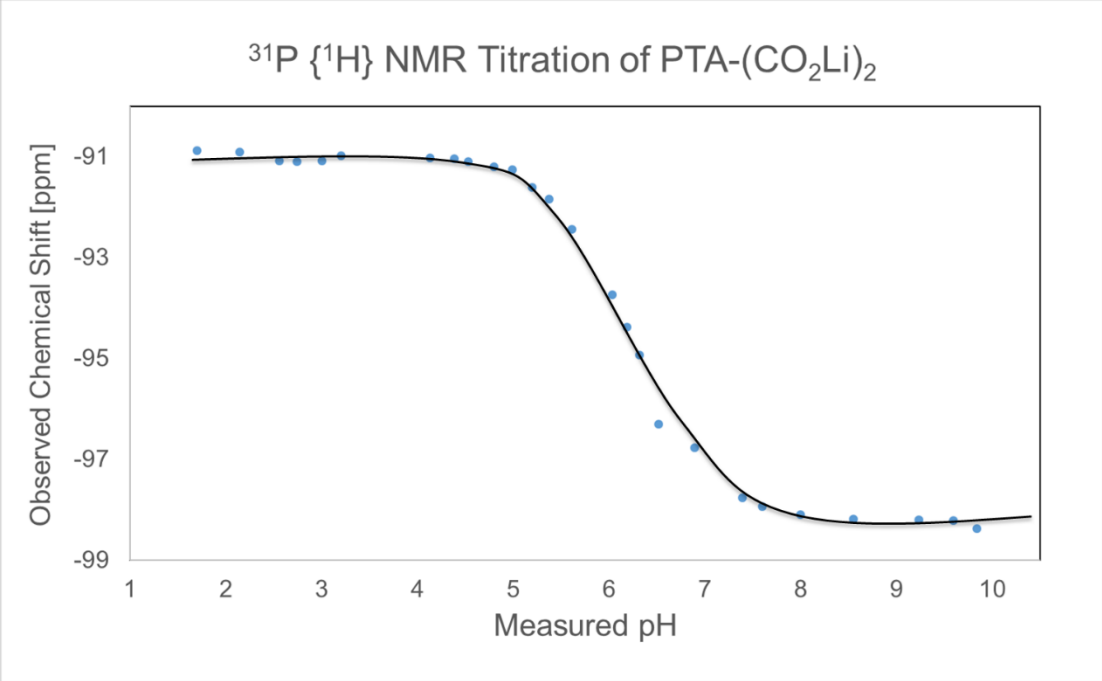

Figure 5.14: Solution state Phosphorus NMR titration curve for **25** in water. The black line is included to guide the eye; a pK_a of 6.1 ± 0.5 for protonated **25** was calculated from the data.

These protonation data do not suggest that pK_a differences between **26** and **27** are not likely sufficient enough to facilitate straight-forward separation of the two. However, **24** should have both a carboxylate and amine functional group available for coordination with metals in aqueous media. One could infer that **24** would potentially serve as a viable collector or depressant for rare earth elements from these data since, as mentioned earlier, non-sulfide REE minerals preferentially

coordinate with collectors containing hard donors like oxygen- and nitrogen-based functional groups.

5.2.3 Precipitation of REEs from Aqueous Media with *N*-[PTA-CO_2^-][H^+]

As a reference, the lanthanides La^{3+}, Gd^{3+}, and Yb^{3+} were hydrothermally precipitated from water with sodium oxalate to generate the $Ln_2(C_2O_4)_3$ complexes $La_2(C_2O_4)_3$ (**28**), $Gd_2(C_2O_4)_3$ (**29**), and $Yb_2(C_2O_4)_3$ (**30**) . A 1:6 mixture of $LaCl_3$: **10** was then diluted in 10 mL of water, the pH as adjusted to 3 with hydrochloric acid to convert **10** to **24** and the mixture was heated at 100ºC for 24 hours in an oil bath. This same process was repeated both without **10** and without $LaCl_3$ as control experiments, and the resulting solutions can be seen in Figure 5.15 below. The precipitate formed from the reaction is insoluble in organic solvents or water, easily separated from the aqueous reaction solution by filtration, and slightly cream-colored.

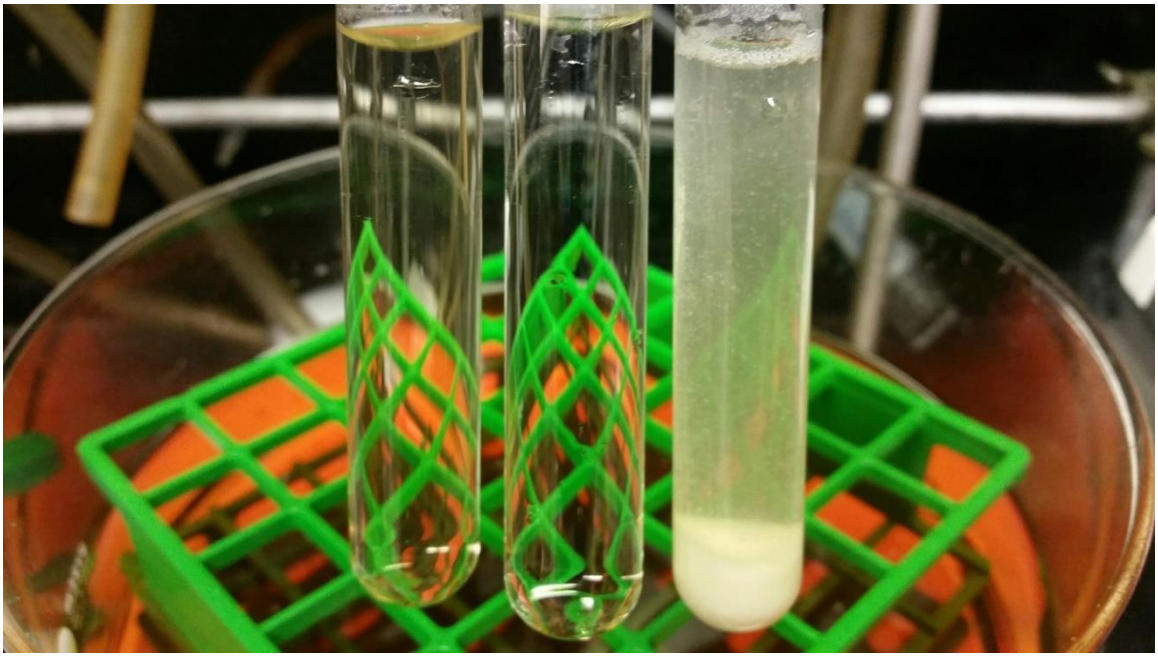

Figure 5.15: Results of thermally treating aqueous mixtures of HCl with *N*-[PTA-CO_2^-][H^+] (*left*), $LaCl_3$ (*middle*), and both the phosphine and the lanthanide (*right*) after heating in an oil bath at 100ºC for 24 hours.

The precipitation reaction was repeated with the hydrated nitrate salt of lanthanum and HNO_3 in place of HCl and found to produce a similar precipitate in similar quantities by weight.

This investigation was conducted to elucidate the efficacy of precipitating REEs from solutions regardless the anion content or concentration. Solid-state FT-IR spectroscopy of the resulting precipitates, see in Figure 5.16, reveals peak patterns that would be expected from carboxylate-coordinated Ln-(PTA-CO_2)$(H^+)_X$. Broad absorption around approximately 3,200 cm^{-1} likely indicates a mixture of protonated nitrogen atoms on the PTA cages and water molecules coordinated to the lanthanum metal center. The sharp absorptions at 1,600 and 1,050 cm^{-1}, red-shifted likely indicate the symmetric and asymmetric $\upsilon_{O\text{-}C\text{-}O}$ stretching frequencies, respectively. Finally, the overlap of the spectra suggest that the anions present in solution have little to no bearing over the precipitation of the lanthanide.

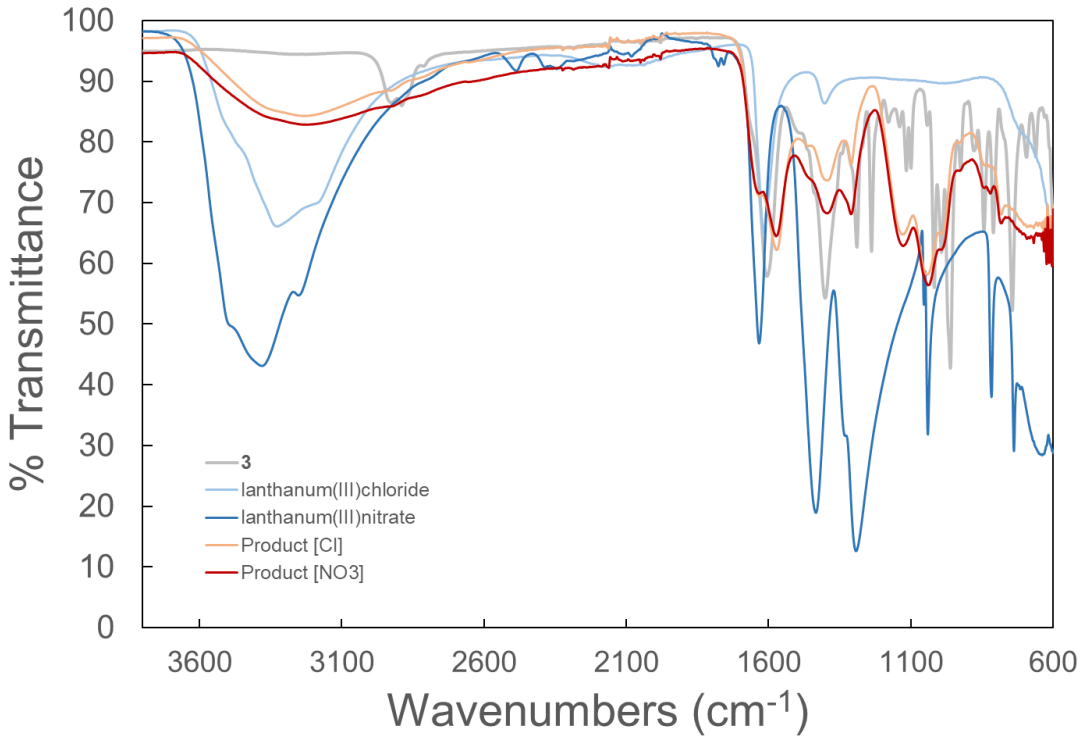

Figure 5.16: Solid-state FT-IR of the products precipitated out of aqueous media with $LaCl_3$ acidified with HCl (*light red*) and $La(NO_3)_3$ acidified with HNO_3 (*dark red*). The FT-IR spectra for starting materials are overlaid for reference.

These FT-IR spectra in the figure above have a distinct absorption located at 1,126 cm^{-1}, in the same region where P=O stretching was previously seen for O-bound Ln(O=PTA)-type complexes (see Chapter 4). Since this absorption possibly indicated that the precipitation of the La^{3+} oxidized the phosphine, the reaction was run again with O=PTA-CO_2Li (**31**) to see if a precipitate would be formed again. DFT calculations were also conducted again, but with **31** to identify if the zwitterionic *N*-[O=PTA-CO_2^-][H^+] would still be the most stable isomer formed upon protonation for the phosphine oxide. The relative energies of the various possible isomers as a result of these calculations, seen in Figure 5.17, indeed suggest again that the nitrogen-protonated zwitterionic form of the ligand is the most stable. However, when the reaction was run again with the same conditions, no precipitate was observed. This likely indicates that the product being formed does not oxidize the phosphorus, and likely contains phosphorus atoms that are either unbound or protonated. It is not expected that the phosphorus is coordinated to the lanthanum metal center because of the relatively soft nature of the phosphorus atom, an idea reinforced by the lack of directly coordinated lanthanide-phosphorus molecules under ambient conditions in the literature.

5.2.4 Optimization of REE Precipitation with 17

Several aspects of REE precipitation with **24** were investigated and optimized to increase the efficiency of REE removal from solution. First, the reaction was run with a chemical microwave instead of an oil bath. It was found that the precipitation of REEs from solution takes place in one hour at 160 ºC when conducted in the chemical microwave. The rest of the optimization studies took place with the chemical microwave to expedite their completion. Extraction of lanthanum from solution was then repeated several times after incrementally adjusting the pH with dilute HCl. Buffers were not used to modify the pH of these reactions because most buffers contain reactive carboxylate groups that could compete for coordination with the lanthanide and skew results. For these reactions, a the 1:6 ratio of La^{3+} : **10** was used and held constant. The mass of precipitate isolated as a function of initial reaction pH is outlined in Figure 5.18 while the numerical data is

presented in Table 5.3, and both appear to suggest that the most optimal pH for precipitation lies close to 4.

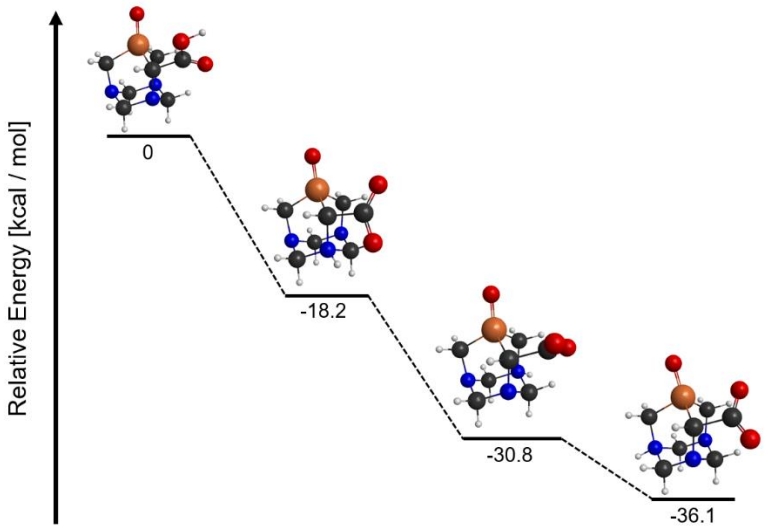

Figure 5.17: Relative energies for [O=PTA-CO_2^-][H^+] as calculated with DFT. The most stable isomer of the ligand according to the calculations is the zwitterionic species *N*-[O=PTA-CO_2^-][H^+].

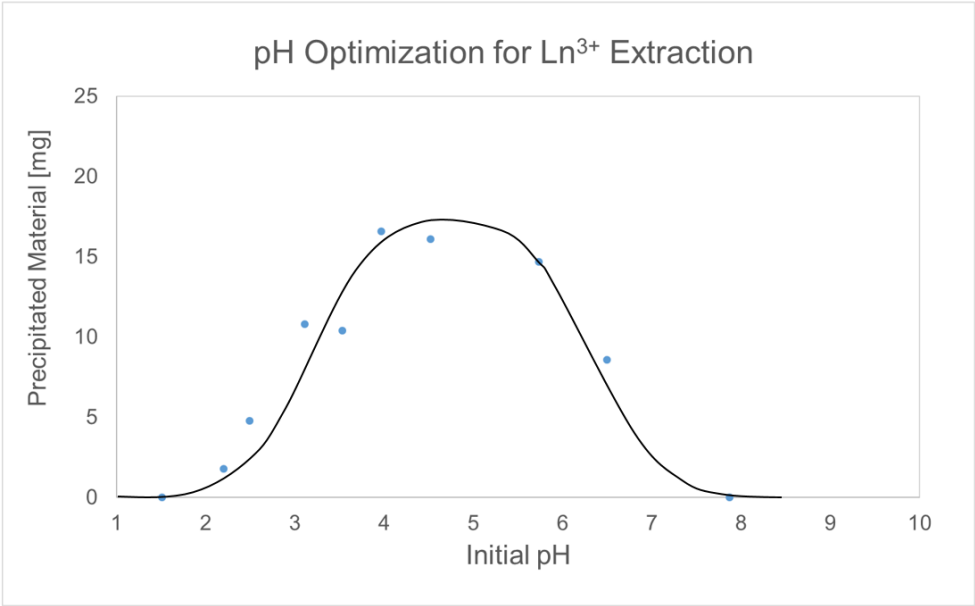

Figure 5.18: Lanthanum precipitate formed with **24** as a function of initial reaction pH. The black line is included to guide the eye.

Table 5.3: Effect of initial solution pH on the precipitation of lanthanum from solution.

Initial pH	Precipitate Formed [mg]
1.01	0.00
1.70	1.80
1.99	4.80
2.61	10.80
3.03	10.40
3.47	16.60
4.02	16.10
5.23	14.70
6.00	8.60
7.37	0.00

It is likely that precipitate is not formed at pH 1 or lower because the carboxylate of **24** is likely protonated, deactivating the carboxylate towards coordination. When the pH is greater than 7, no product is observed likely because the solution was not acidic enough generate the zwitterionic **24**necessary for coordination. Finally, the ratio of phosphine to lanthanum was varied to provide insight into the general structure of the precipitate formed from solution. The mass of precipitate isolated as a function of **10** to $LaCl_3$ ratio can be seen in Figure 5.19, and seems to level off at a ratio of 3 : 1, respectively.

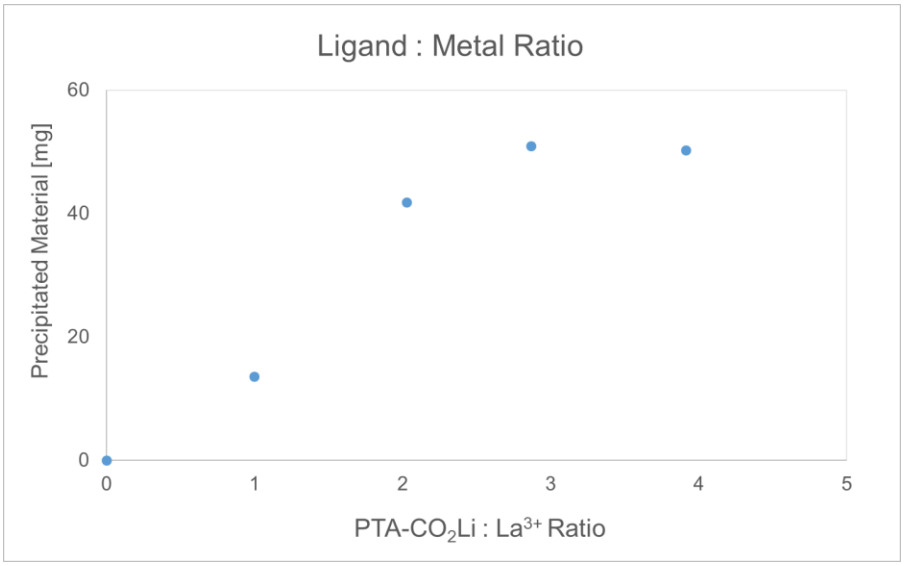

Figure 5.19: Lanthanum precipitate formed with **24** as a function of the ligand to metal ratio.

The data for this experiment is outlined below in Table 5.4. This ligand to metal ratio suggests a potential structure of $La(PTA\text{-}CO_2)_3$ (**32**) , which is reasonable if both the carboxylate functional group and the adjacent nitrogen coordinate to the metal center, which would saturate the lanthanide's coordination sphere of 9 assuming tridentate chelation. However, for the purposes of using **10** as a collector, the important takeaway from this study suggests that a minimum 3-fold excess of **10** to REE would be recommended if this ligand were utilized as a collector for froth flotation or precipitation agent from strip liquors for REEs.

Table 5.4: Effect of ligand-to-metal ratio on the precipitation of lanthanum from solution.

Trial #	Mass of **3** [mg]	Mass of $LaCl_3$ [mg]	**3** : La^{3+} Ratio	Precipitate [mg]
1	0	59.4	0	0
2	34.8	59.6	1.00	13.6
3	71.1	59.9	2.02	41.8
4	100.4	59.8	2.86	50.9
5	140.3	61.2	3.91	50.3

5.2.5 Catch and Release Lanthanide Precipitation

A small mass [30 mg] of **32** was dispersed in an aqueous solution acidified to pH 1 to see if the complex dissolves. After a slight excess [1.8 mmol] of sodium chloride was also added to the solution for cation exchange on the phosphine, all precipitates immediately dissolved into the reaction mixture. The reaction pH was then adjusted to 10 and the characteristically gel-like $La(OH)_3$ precipitated out of the solution. The $La(OH)_3$ gel was isolated by filtration and dried in vacuo to yield an off-white powder. This process, generalized in Figure 5.20, indicates that **10** can effectively remove lanthanum from aqueous media in a recyclable manner, allowing for **10** to be recovered after the reaction.

This same process was attempted with **28**, but the chelate did not dissolve at any pH so generation of the hydroxide from **28** is not readily accessible. The typical industry protocol involves

direct calcination of the lanthanide oxalates to Ln_2O_3, but this requires heating **28** to 800ºC for full decomposition to the product,[48] while calcination of $Ln(OH)_3$ to Ln_2O_3 only requires heating to 650ºC.[49] Further, the decomposition of **28** to Ln_2O_3 releases 6 moles of carbon dioxide into the air per complex, whereas the thermal decomposition of $Ln(OH)_3$ merely reduces water vapor into the air. Thus, exchanging sodium oxalate for **10** in mineral extraction protocols and adjusting treatment to that indicated in this chapter could potentially reduce carbon emissions from lanthanide extraction and isolation.

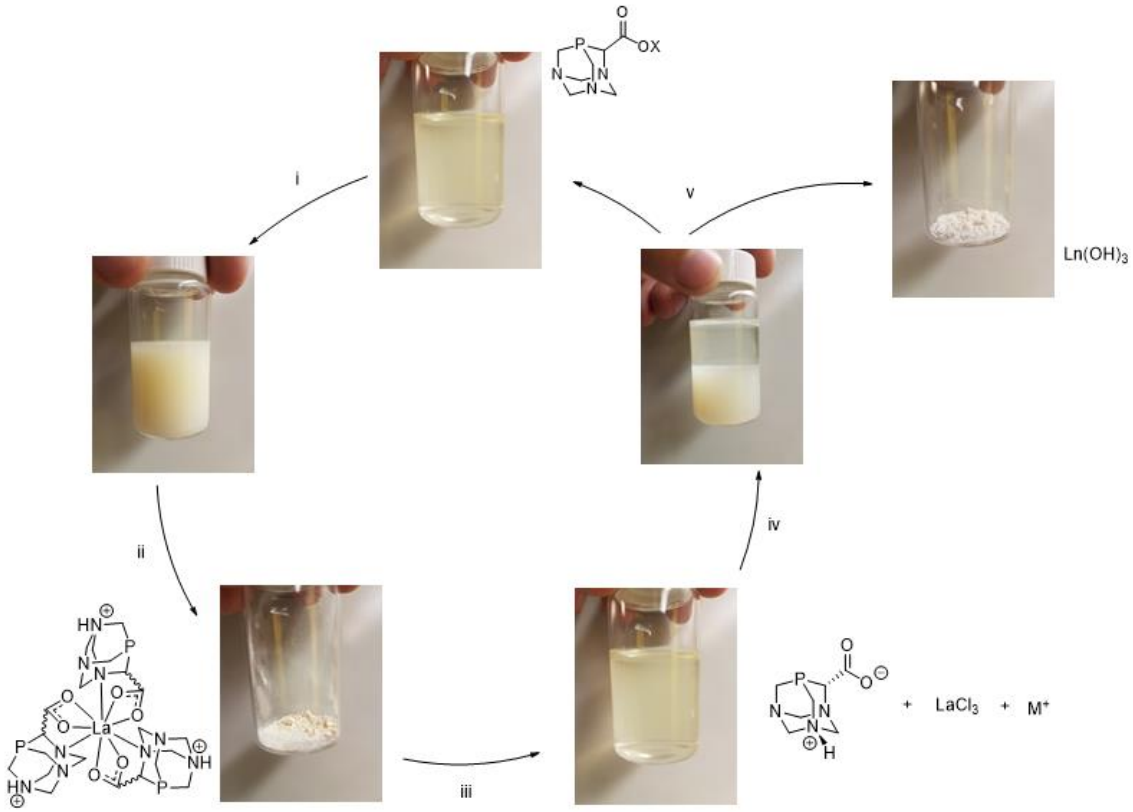

Figure 5.20: Proposed cycle for recyclable extraction of lanthanum from aqueous media with PTA-CO_2Li. **i)** pH = 3 – 6, LnX_3 (X = Cl^-, NO_3^-), 160ºC, 1 hr; **ii)** Filter; **iii)** Excess MCl (M = Na^+, Li^+), pH < 2; **iv)** pH = 10; **v)** Filter, dry precipitate in vacuo.

5.2.6 Concluding Remarks

The pK_a of **17** was determined experimentally through a $^{31}P\{^1H\}$ NMR titration and found to be 6.1 ± 0.2. The most stable isomer of [PTA-CO_2^-][H^+] was determined computationally with DFT and found to be the 3-N protonated form of the ligand. Interestingly, the 5-N product was not one of the most stable isomers of the ligand, even though one might assume it would be due to hydrogen-bonding stabilization with the carboxylate functional group. Several methods were investigated to potentially synthesize pure **25** or separate it from the synthesized mixture of **25** and **10**. Lithiation of **10** was found to proceed at about 60% yield, so subsequent carboxylation would still yield a mixture of the two phosphines. Separation of the two was investigated with cation exchange with PPN-Cl, reaction with ruthenium arenes, and with pK_a differences with varying success. The $^{31}P\{^1H\}$ NMR of **26** and **27** is suggestive of successful separation of the two phosphines, but the reaction conditions were not optimized and much more characterization will have to be conducted to elucidate the efficacy of separation. The pK_a of the dicarboxylate phosphine [PTA-(CO_2Li)(CO_2)$^-$][H^+] was also determined through $^{31}P\{^1H\}$ NMR and found to be 6.1 ± 0.5.

A novel method for hydrothermal precipitation of lanthanides from aqueous mixtures at low pH was then demonstrated with the lithium carboxylate salt of PTA and the chloride and nitrate salts of La^{3+}, Gd^{3+}, and Yb^{3+}. The sensitivity of the precipitation to reaction pH was investigated experimentally, and it was found that the precipitation takes place most efficiently when the initial reaction pH is adjusted so that it is close to 4. No precipitate is generated if the initial reaction pH is less than 1.5 or greater than 6.5, and it was hypothesized that this is likely due to protonation of the carboxylate and deprotonation of **24**, respectively. Further, the phosphine : lanthanide ratio was increased to lend insight into the structure of the precipitate, and it was revealed that more product is not formed if the ratio exceeds 3:1. Finally, **32** that was removed from aqueous media was then converted to its hydroxide salt through dilution into aqueous solutions of pH < 2, addition of a slight excess of NaCl or LiCl, and adjustment of the pH to greater than 10. Filtering the product

and drying in vacuo yielded $La(OH)_3$. This same approach was attempted with **28**, but it would not dissolve in solution for conversion to the hydroxide.

5.3 Experimental

5.3.1 Methods & Materials

Reagent-grade solvents, hexaaqua lanthanide nitrate salts, and hexaaqua lanthanide(III)chloride salts were all purchased from commercial sources. Tetrakis(hydroxymethyl)phosphonium chloride was provided by Cytec and used as received without purification. Tetrahydrofuran (THF) was freshly distilled from sodium/benzophenone. 1,3,5-triaza-7-phosphaadamantane (PTA), lithium 1,3,5-triaza-7-phosphaadamantane-6 carboxylate (PTA-CO_2Li), and dilithium 1,3,5-triaza-7-phosphaadamantane-6,6' bis-carboxylate (PTA-$(CO_2Li)_2$) and were prepared according to literature methods.[50] Microwave-scale reactions were conducted with a CEM Discover chemical microwave. Measurements of pH were conducted with Metler Toledo SevenEasy pH meter standardized to pH 4 red, pH 7 yellow, and pH 10 blue. Solid-state FT infrared spectra were obtained with a Nicolet 6700 FT-IR spectrophotometer. Thermogravimetric analysis was carried out with a TA TGA Q50 using a platinum pan. Mass spectrometry was carried out with a Water Micromass 20 ESI mass spectrometer (positive ion mode). Theoretical calculations using GAMESS were carried out at the B3LYP level of density functional theory (DFT) adopting Dunning's correlation consistent triple zeta (cc)-pVTZ basis set.[51]

Blank Study – Precipitation of $LaCl_3 \cdot 6H_2O$ with [PTA-CO_2^-][H^+] in the Oil Bath: $LaCl_3 \cdot 6H_2O$ (55.9 mg, 0.16 mmol) and PTA-CO_2Li (197.0 mg, 0.950 mmol, 6 equiv.) were combined in a 20 mL screw-cap test tube. The mixture was diluted with 10 mL distilled water, acidified with 3 drops of concentrated hydrochloric acid, and left in a 100ºC oil bath for 24 hours without stirring. A voluminous precipitate was observed within an hour of the onset of heating, but settled to the bottom of the test tube after the full test duration.

[La^{3+} Control]: $LaCl_3 \cdot 6H_2O$ (57.9 mg, 0.16 mmol) was loaded into a 20 mL screw-cap test tube, diluted with 10 mL distilled water, and acidified with 3 drops of concentrated hydrochloric acid. The resulting solution was left heating in a 100ºC oil bath for 24 hours. No precipitate was observed from this reaction by the end of the test period.

[PTA-CO_2Li Control]: PTA-CO_2Li (203.7 mg, 0.98 mmol) was loaded into a 20 mL screw-cap test tube, diluted with 10 mL distilled water, and acidified with 3 drops of concentrated hydrochloric acid. The resulting solution was left heating in a 100ºC oil bath for 24 hours. No precipitate was observed from this reaction by the end of the test period.

Attempted synthesis of (Li)PTA-(CO_2Li): 10 (25.7 mg, 0.121 mmol) was thoroughly dried in vacuo for a few hours and transferred to a 2-necked 50 mL round-bottom flask under positive pressure nitrogen. Following dilution with 25 mL THF, 1 mL of a 2.5 *M* *n*-BuLi solution was slowly added to the mixture dropwise over the course of ten minutes. The reaction mixture was allowed to stir under nitrogen for 2.5 hours, filtered under nitrogen, washed 3x with hexanes, and transferred to a drybox. A small portion of the product was dissolved in D_2O for ^{31}P {^1H} NMR to determine purity of the product. 61% conversion. ^{31}P {^1H} NMR (162 MHz, D_2O): -86.9 (s) [PTA-CO_2Li(D)]; -88.9 (s) [PTA-CO_2Li(H)].

Synthesis of PTA-CO_2PPN (26): 3 (51.8 mg, 0.242 mmol) and PPN-Cl (138.4 mg, 0.242 mmol) were combined in a flask under ambient conditions and diluted with 20 mL THF. The reaction mixture was stirred for 5 hours, during which time a white precipitate formed at the bottom of the flask. The precipitate was isolated by filtration. White solid (111 mg, 12% yield). ^{31}P {^{1}H} NMR (162 MHz, H_2O): -87.0 (s) [PTA-CO_2^-]; 21.3 (s) [PPN].

Synthesis of PTA-$(CO_2PPN)_2$ (27): A 30:70 mixture of **18**:**3** (101.3 mg) and PPN-Cl (327.3 mg, 0.570 mmol) were combined in a flask under ambient conditions and diluted with 35 mL THF. The reaction mixture was stirred for 8 hours in air, during which time a white precipitate formed at the bottom of the flask. The precipitate **19** was isolated by filtration while **20** was obtained from the filtrate *via* rotary evaporation of the solvent. 100% conversion of the starting materials determined by ^{31}P {^{1}H} NMR spectroscopy. ^{31}P {^{1}H} NMR (162 MHz, MeOH): [**19**] -82.8 (s) [PTA-CO_2^-]; 21.3 (s) [PPN]; [**20**] -81.0 (s) [PTA-$(CO_2^-)_2$]; 21.8 (s) [PPN].

Synthesis of O=PTA-CO_2Li (31): PTA-CO_2Li (500.8 mg, 2.4 mmol) was loaded into a 250 mL round-bottom flask and diluted with methanol. A solution of 30% hydrogen peroxide (0.3 mL, excess) was diluted with 5 mL methanol. This hydrogen peroxide – methanol solution was added dropwise to the reaction mixture over the course of 10 minutes in ambient conditions. The resulting reaction mixture was left to stir in air for 1 hour. The solvent was removed under reduced pressure *via* rotary evaporation to yield a yellow oil. Dilution with cold ethanol yielded a white precipitate, which was isolated by filtration. The oil was then washed with ample amounts of ethyl ether, precipitating out the remainder of the product as a white powder. (411.3 mg, 1.8 mmol, 76%). ^{31}P {^{1}H} NMR (162 MHz, DMF): -2.35 (s). Solid state IR [cm^{-1}]: 1169 (P=O); 1619 (O-C-$O_{asym.}$); 1389 (O-C-$O_{sym.}$).

Attempted synthesis of RuCl(η^6-toluene)(PTA-(CO_2Li)(CO_2)): A 30:70 mixture of **25**:**10** (51.3 mg) and [$RuCl_2$(η^6-toluene)]$_2$ (52.3 mg, 96.9 μmol) were combined in a 50 mL round-bottom flask under positive pressure of nitrogen. The mixture was diluted with a 25 mL of a 1:1 solvent mixture of DCM/MeOH. The reaction mixture was refluxed for two days. The reaction mixture was then allowed to cool to room temperature naturally. Removal of the solvent *via* rotary evaporation followed by drying in vacuo yielded the product as an orange solid (114.7 mg) ^{31}P {^{1}H} NMR (162 MHz, H_2O): -2.2 (s); -2.3 (s). LCMS (ESI, MeOH) m/z: [M + H] 480.

Attempted synthesis of RuCl(η^6-cymene)(PTA-(CO_2Li)(CO_2)): A 30:70 mixture of **25**:**10** (17.5 mg) and [$RuCl_2$(η^6-cymene)]$_2$ (20.8 mg, 32.6 μmol) were combined in a 50 mL round-bottom flask under positive pressure of nitrogen. The mixture was diluted with a 20 mL of a 1:1 solvent mixture of DCM/MeOH. The reaction mixture was overnight. The reaction mixture was then allowed to cool to room temperature naturally. Removal of the solvent *via* rotary evaporation followed by drying in vacuo yielded the product as a bright orange solid. LCMS (ESI, MeOH) m/z: [M + H] 564.42.

pK_a determination of [PTA-CO_2^-][H^+] (24): 203.7 mg (0.98 mmol) PTA-CO_2Li were diluted in 15 mL water. 3 mL concentrated hydrochloric acid were added and a ^{31}P {^{1}H} NMR spectrum was recorded. The pH of the mixture was then increased in intervals of approximately 0.5 with a dilute solution of sodium hydroxide, recording a ^{31}P {^{1}H} NMR spectrum after each interval. The resulting graph seen in Figure 4.7 was generated by reporting the chemical shift corresponding to the max peak height in each spectrum recorded at each determined pH.

pK_a determination of $[PTA\text{-}(CO_2)_2^-][H^+]$: 202.0mg of a 1:3 mixture of PTA-CO_2Li : PTA-$(CO_2Li)_2$ were diluted in 15 mL water. 1 mL concentrated hydrochloric acid was added and a ^{31}P $\{^1H\}$ NMR spectrum was recorded. The pH of the mixture was then increased in intervals of approximately 0.5 with a dilute solution of sodium hydroxide, recording a ^{31}P $\{^1H\}$ NMR spectrum after each interval. The resulting graph seen in Figure 4.10 was generated by reporting the chemical shift corresponding to the max peak height in each spectrum corresponding to the dicarboxylate phosphine recorded at each determined pH.

Attempted Precipitation of La^{3+} from Aqueous Media with O=PTA-CO_2Li: $LaCl_3 \cdot 6H_2O$ (100.1 mg, 0.28 mmol) and O=PTA-CO_2Li (95.9 mg, 0.43 mmol) were combined in a 20 mL screw-cap test tube and diluted with 10 mL distilled water. 2 mL of this reaction mixture were then loaded into a microwave vial and a pH of 5.30 was measured. The reaction mixture was subjected to microwave heating at 160ºC for one hour, yielding a uniformly dark yellow / brown solution. ^{31}P $\{^1H\}$ NMR of the product revealed three peaks shifted about 15 – 30 ppm downfield of the O=PTA-CO_2Li starting material, likely indicating ring-opening of the O=PTA cage.

Determination of pH Effect on Ln^{3+} precipitation: 28.7 mg (0.081 mmol) of $LaCl_3 \cdot 6H_2O$ and 100 mg (0.48 mmol, 6 equivalents) of PTA-CO_2Li were loaded into a microwave vial and diluted with 2 mL distilled water. The reaction mixture was acidified or basified with dilute solutions of HCl and NaOH, respectively, until the desired pH was obtained. Reaction vials were then capped and placed into the chemical microwave and subjected to 160ºC for 1 hour.* The resulting precipitates were then filtered, washed with acetone, dried under a stream of air, and weighed on the microbalance. The ss FT-IR spectrum for each precipitate generated was recorded and compared to ensure the same species was being precipitated of solution.

** = For solutions with pH ≤ 4, precipitates were generated through heating in an oil bath at 100 ºC for 24 hours instead of in the chemical microwave.*

General Procedure for Precipitation of Ln^{3+} (Ln^{3+} = La^{3+}, Gd^{3+}, Yb^{3+}) in the Chemical Microwave: $LnX_3 \cdot 6H_2O$ (0.3 mmol) and PTA-CO_2Li (0.9 mmol, 3 equiv.) were combined in a microwave vial with a stir bar and diluted with 2 mL distilled water. The mixture was acidified with HX acid (X = Ln anion) to pH ~ 3 and the vial was placed in the chemical microwave. The sample was heated to 160ºC over the course of 15 minutes and the temperature held for 60 minutes thereafter. The resulting precipitate was separated *via* filtration, washed with acetone, and dried under a steady stream of air for 15 minutes. *La_2(PTA-CO_2)$_3$ from $LaCl_3$* (**32a**): White solid (27.9 mg) Solid state IR (Figure A.24) [cm^{-1}]: 1616, 1570 (O-C-$O_{asym.}$); 1455, 1390 (O-C-$O_{sym.}$); 3225 (O-H); 782 (La-O).

La_2(PTA-CO_2)$_3$ from La(NO_3)$_3$ (**32b**): White solid (36.6 mg) Solid state IR (Figure A.25) [cm^{-1}]: 1609, 1573 (O-C-$O_{asym.}$); 1445, 1391 (O-C-$O_{sym.}$); 3220 (O-H); 780 (La-O).

Gd_2(PTA-CO_2)$_3$ from $GdCl_3$ (**33a**): White solid (101.7 mg) Solid state IR (Figure A.26) [cm^{-1}]: 1640, 1586 (O-C-$O_{asym.}$); 1315, 1392 (O-C-$O_{sym.}$); 3304 (O-H); 790 (Gd-O).

Gd_2(PTA-CO_2)$_3$ from Gd(NO_3)$_3$ (**33b**): White solid (37.4 mg) Solid state IR (Figure A.27) [cm^{-1}]: 1614, 1579 (O-C-$O_{asym.}$); 1313, 1388 (O-C-$O_{sym.}$); 3199 (O-H); 792 (Gd-O).

Yb_2(PTA-CO_2)$_3$ from $YbCl_3$ (**34a**): White solid (47.1 mg) Solid state IR (Figure A.28) [cm^{-1}]: 1583 (O-C-$O_{asym.}$); 1317, 1389 (O-C-$O_{sym.}$); 3225 (O-H); 796 (Yb-O).

Yb_2(PTA-CO_2)$_3$ from Yb(NO_3)$_3$ (**34b**): White solid (94.1 mg) Solid state IR (Figure A.29) [cm^{-1}]: 1587 (O-C-$O_{asym.}$); 1316, 1360 (O-C-$O_{sym.}$); 3346, 3182, 3052 (O-H); 796, 805 (Yb-O).

PTA-CO_2Li : La^{3+} Stoichiometry Investigation: Four samples of about 60 mg (0.17 mmol) $LaCl_3 \cdot 6\ H_2O$ were combined with PTA-CO_2Li [**n=1**: 34.8 mg, 0.17 mmol; **n=2**: 71.1 mg, 0.34 mmol; **n=3**: 100.4 mg, 0.48 mmol; **n=4**: 140.3 mg, 0.68 mmol] and loaded into a chemical microwave reaction vials. The mixtures were each diluted with 2 mL water. The pH of each reaction mixture was adjusted to 5.67 with dilute hydrochloric acid, and the vials were each subjected to microwave heating at 160ºC for 1 hour. The resulting precipitates were isolated by filtration, washed with ample amounts of acetone, and weighed on the microbalance to determine the resulting mass of precipitate formed.

5.4 References

(1) Krishnamurthy, N.; Gupta, C. *Extractive Metallurgy of Rare Earths, Second Edition*; CRC Press: Boca Raton, FL, 2015.

(2) Tekumalla, S.; Seetharaman, S.; Almajid, A.; Gupta, M. *Metals (Basel).* **2014**, *5* (1), 1–39.

(3) Yang, Y.; Walton, A.; Sheridan, R.; Güth, K.; Gauß, R.; Gutfleisch, O.; Buchert, M.; Steenari, B.-M.; Van Gerven, T.; Jones, P. T.; Binnemans, K. *J. Sustain. Metall.* **2017**, *3*, 122–149.

(4) Chen, K. F.; Xue, D. F. *Sci. China Technol. Sci.* **2015**, *58* (11), 1768–1778.

(5) Caravan, P.; Ellison, J. J.; McMurry, T. J.; Lauffer, R. B. *Chem. Rev.* **1999**, *99* (9), 2293–2352.

(6) Sousa-Aguiar, E. F.; Trigueiro, F. E.; Zotin, F. M. Z. *Catal. Today* **2013**, *218–219*, 115–122.

(7) Montini, T.; Melchionna, M.; Monai, M.; Fornasiero, P. *Chem. Rev.* **2016**, *116* (10), 5987–6041.

(8) Binnemans, K. *Chem. Rev.* **2009**, *109* (9), 4283–4374.

(9) Dong, H.; Du, S.-R.; Zheng, X.-Y.; Lyu, G.-M.; Sun, L.-D.; Li, L.-D.; Zhang, P.-Z.; Zhang, C.; Yan, C.-H. *Chem. Rev.* **2015**, *115* (19), 10725–10815.

(10) Gao, L.; Chen, R. S.; Han, E. H. *J. Alloys Compd.* **2009**, *472* (1–2), 234–240.

(11) Lauffer, R. B. *Chem. Rev.* **1987**, *87* (5), 901–927.

(12) Zairov, R.; Mustafina, A.; Shamsutdinova, N.; Nizameev, I.; Moreira, B.; Sudakova, S.; Podyachev, S.; Fattakhova, A.; Safina, G.; Lundstrom, I.; Gubaidullin, A.; Vomiero, A. *Sci. Rep.* **2017**, *7* (January), 1–10.

(13) Chan, J.; Dodani, S. C.; Chang, C. J. *Nat. Chem.* **2012**, *4* (12), 973–984.

(14) Bünzli, J.-C. *Nat. Chem.* **2010**, *2* (8), 696.

(15) Freeman, A. J.; Watson, R. E. *Phys. Rev.* **1962**, *127* (6), 2058–2075.

(16) Dehnicke, K.; Greiner, A. *Angew. Chemie - Int. Ed.* **2003**, *42* (12), 1340–1354.

(17) Werts, M. *Sci. Prog.* **2005**, *88* (2), 101–131.

(18) Chen, Z. *J. Rare Earths* **2011**, *29* (1), 1–6.

(19) Ley, S. I. *The Rare Earths*, second ed.; Edward Arnold & Co.: London, 1924.

(20) Jordens, A.; Cheng, Y. P.; Waters, K. E. *Miner. Eng.* **2013**, *41*, 97–114.

(21) Defense, S. of. *Strategic and Critical Materials 2015 Report on Stockpile Requirements*; 2015.

(22) Chu, S., E. A. *Critical Materials Strategy*; 2011.

(23) Packey, D. J.; Kingsnorth, D. *Resour. Policy* **2016**, *48*, 112–116.

(24) McKee, D. *Miner. Eng.* **1991**, *4*, 653–666.

(25) Shean, B. J.; Cilliers, J. J. *Int. J. Miner. Process.* **2011**, *100* (3–4), 57–71.

(26) Fuerstenau, M. C.; Jameson, G. J.; Yoon, R. H. *Froth flotation: a century of innovation*; Society for Mining, Metallurgy, and Exploration: Littleton, Colorado, 2007.

(27) Muzenda, E.; Afolabi, A. S.; Abdulkareem, A. S.; Ntuli, F. *Proc. World Congr. Eng. Comput. Sci. 2011 Vol II* **2011**, *II*, 19–22.

(28) Sarvaramini, A.; Azizi, D.; Larachi, F. *Appl. Surf. Sci.* **2016**, *387*, 986–995.

(29) Huddinge, P. S.; Nacka, T. W. Flotation collector composition and its use. US 4514290 A, 1985.

(30) Xie, F.; Zhang, T. A.; Dreisinger, D.; Doyle, F. *Miner. Eng.* **2014**, *56*, 10–28.

(31) Gergoric, M.; Ekberg, C.; Steenari, B.-M.; Retegan, T. *J. Sustain. Metall.* **2017**, 1–10.

(32) De Rohden, C.; Peltier, M. Treatment of Monazite. US Patent 2783125 A, 1957.

(33) Gaudernack, B. Process for separating yttrium values from the lanthanides. US Patent 3751553, 1973.

(34) Preston, J. S. *Hydrometallurgy* **1996**, *42* (2), 151–167.

(35) Haque, N.; Hughes, A.; Lim, S.; Vernon, C. *Resources* **2014**, *3* (4), 614–635.

(36) de Vasconcellos, M. E.; da Rocha, S. M. R.; Pedreira, W. R.; Queiroz, C. A. d S.; Abrão, A. *J. Alloys Compd.* **2008**, *451* (1–2), 426–428.

(37) Abreu, R. D.; Morais, C. A. *Miner. Eng.* **2010**, *23* (6), 536–540.

(38) El-Hefny, N. E.; El-Nadi, Y. A.; Aly, H. F. *Sep. Purif. Technol.* **2011**, *78* (3), 330–335.

(39) Jorjani, E.; Shahbazi, M. *Arab. J. Chem.* **2012**.

(40) Lee, C. H.; Chen, Y. J.; Liao, C. H.; Popuri, S. R.; Tsai, S. L.; Hung, C. E. *Metall. Mater. Trans. A Phys. Metall. Mater. Sci.* **2013**, *44* (13), 5825–5833.

(41) Satterfield, C. N.; Kavanagh, G. M.; Resnick, H. *Ind. Eng. Chem.* **1951**, *43* (11), 2507–2514.

(42) Bandara, H. M. D.; Field, K. D.; Emmert, M. H. *Green Chem.* **2015**, No. August 2016, 753–759.

(43) Wong, G. W.; Lee, W. C.; Frost, B. J. *Inorg. Chem.* **2008**, *47*, 612–620.

(44) Gift, A. D.; Stewart, S. M.; Bokashanga, P. K. *J. Chem. Educ.* **2012**, *89* (2), 1458–1460.

(45) Phillips, A. D.; Gonsalvi, L.; Romerosa, A.; Vizza, F.; Peruzzini, M. *Coord. Chem. Rev.* **2004**, *248*, 955–993.

(46) Huang, R.; Frost, B. J. *Inorg. Chem.* **2007**, *46* (26), 10962–10964.

(47) Lide, D. R. *Handbook of Chemistry and Physics*, 72nd ed.; CRC Press: Boca Raton, FL, 1991.

(48) Almeida, L. De; Grandjean, S.; Vigier, N.; Patisson, F. *Eur. J. Inorg. Chem.* **2012**, *31*, 4986–4999.

(49) Kim, S. J.; Han, W. K.; Kang, S. G.; Han, M. S.; Cheong, Y. H. *Solid State Phenom.* **2008**, *135* (3), 23–26.

(50) Daigle, D. J. *Inorg. Synth.* **1998**, *32*, 40–45.

(51) Dunning Jr, T. H. *J. Chem. Phys.* **1989**, *90* (1989), 1007–1023.

6 Conclusions

Upper rim PTA enamines PTA=C[Ph]NH_2 (**1**), PTA=[*p*-tol]NH_2 (**2**), PTA=[*p*-C_5H_4OMe]NH_2 (**3**) and PTA=C[1,3,5-$C_5H_2(OMe)_3$]NH_2 (**4**) were prepared and oxidized to E isomer of their respective oxides **5a** – **8a** following a slightly modified approach of what had been previously reported. Recrystallization of **6a** from Hexanes:DCM resulted in crystals of the E isomer, and $^{31}P\{^1H\}$ NMR of the crystals and filtrate was utilized to determine that the crystals are crystalized out of the solution after isomerization from Z to E isomer, instead of selectively just crystallizing the E isomer. Time-resolved $^{31}P\{^1H\}$ NMR of **8a** in $CDCl_3$ at 25 ºC, 35 ºC, and 45 ºC were recorded to elucidate the kinetics and thermodynamics of **8a** to **8b** isomerization. Equilibrium constants of 0.871, 0.866, and 0.8978 and rate constants of 1.42 x 10^{-2}, 2.52 x 10^{-2}, and 5.27 x 10^{-2} were recorded for the isomerization at these respective temperatures. Future work for this project should include preparing more pure crystals of **5a** and **7a** for the same detailed isomerization studies.

Attempts were made to synthesize and characterize novel upper-rim PTA amides from several synthetic routes. Attempts to prepare the first amide followed a method of coupling **1** with Fmoc-protected phenylalanine under typical amide-coupling conditions with HBTU and DIPEA. The resulting product was highly polar and thus difficult to separate from the similarly polar reaction byproducts. The synthesis was also attempted by coupling **9** with benzylamine in THF with sodium methoxide at high temperature for 5 hours. A 90% conversion of starting material was observed through $^{31}P\{^1H\}$ NMR spectroscopy, and ^1H NMR spectroscopy of the crude product suggests product formation possibly took place. However, synthesis of the required starting material **9** is difficult, timely, and not well-understood, making this overall approach to amide synthesis less desirable. A robust, easily repeatable synthesis of upper-rim amides was then conducted between **10** and butylamine, benzylamine, methyl-ester protected glycine, and methyl-ester protected histidine. Addition of the lithiated carboxylate **10** to the hydrochloride salts of amines with the

coupling agent HBTU and the base DIPEA seem to have afforded the desired amides. These amides were prepared at room temperature in air with solvent that had not been dried, and reaction kinetics probed with $^{31}P\{^{1}H\}$ NMR suggest reaction completion within 15 minutes of reagent combination. Future work for these projects preparing upper rim PTA amides should focus on increasing the substrate scope of prepared amides, monitoring the reaction progress with solution-state ReactIR to monitor the growth of the amide peak in solution, and conducting deuterium exchange experiments with the resulting products with subsequent FTIR to compare against expected absorptions predicted from calculations.

Crystal structures were grown of two colored nickel-PTA species, blue and red, and single-crystal X-Ray Diffraction (XRD) was utilized to determine the structure of each complex. Although it had been suggested in the literature previously that the blue complex was likely a nitrogen-coordinated nickel-PTA complex, the resulting crystal structure indicates that the complex is phosphorus coordinated $NiCl_2(PTA)_3$. The red $NiCl_2(PTA)_2$ species was confirmed as square planar *cis*-$NiCl_2(PTA)_2$ *via* the same method. Attempts were made to coordinate PTA to a lanthanide, but found to be unsuccessful. However, efforts did yield a crystal suitable for single-crystal XRD. The resulting structure revealed that PTA had crystallized in the second coordination sphere of the lanthanide, and bond lengthening of C-N bonds around a particular nitrogen atom of the phosphine suggested protonation of the atom. The first O=PTA lanthanide complexes were prepared by stirring O=PTA and lanthanide nitrates in acetonitrile under inert atmosphere. A crystal structure from single-crystal XRD of the complex formed between cerium nitrate and O=PTA reveals a structure of $Ce(O{=}PTA)_3(NO_3)_3$, the first O=PTA metal complex that leaves all nitrogen atoms unbound and available for coordination or protonation. The FT-IR spectra of complexes with La^{3+}, Ce^{3+}, Sm^{3+}, Eu^{3+}, and Yb^{3+} reveal red-shifts of the 1162 cm^{-1} absorption of the phosphine oxide bond by about 26 cm^{-1} on average, a diagnostic tool that could potentially be useful for synthesis between O=PTA derivatives and lanthanides in future studies. Future work for these investigations

include crystallizing the remaining lanthanide O=PTA complexes with detailed analysis of the resulting crystal patterns across the lanthanide series.

The pK_a for both [PTA-CO_2^-][H^+] and [PTA-$(CO_2)_2^-$][H^+] were experimentally determined through $^{31}P\{^1H\}$ NMR titrations to be 6.1 ± 0.2 and 6.09 ± 0.52, respectively. The most stable isomer of [PTA-CO_2^-][H^+] was computationally elucidated with DFT and found to be the 3-N protonated form of the ligand. The carboxylic acid was determined to be the least stable isomer of [PTA-CO_2^-][H^+]. A novel method for hydrothermal precipitation of lanthanides from aqueous mixtures was demonstrated with the lithium carboxylate salt of PTA and the chloride and nitrate salts of La^{3+}, Gd^{3+}, and Yb^{3+}. The sensitivity of the precipitation to reaction pH was determined experimentally by repeating the precipitation at variable pH, and it was found that the precipitation takes place most efficiently when the initial reaction pH is adjusted so that it is close to 4. No precipitate is generated if the initial reaction pH is less than 1.5 or greater than 6.5, and it was hypothesized that this is likely due to protonation of the carboxylate and deprotonation of [PTA-CO_2^-][H^+], respectively. Further, the precipitation reaction was repeated with incrementally increasing phosphine : lanthanide ratio to elucidate the structure of the precipitate, and it was revealed that precipitation increases until a ratio of 3:1 is possiblyreached. Lanthanide precipitates that were removed from aqueous media with [PTA-CO_2^-][H^+] were converted to hydroxide salts through dilution into aqueous solutions of pH < 2, addition of a slight excess of lithium or sodium salts, and adjustment of the pH to greater than 10. Filtering the product and drying in vacuo yielded $La(OH)_3$. This same approach was attempted with $La_2(C_2O_4)_3$, but the lanthanum oxalate product would not dissolve in solution for conversion to the hydroxide. Future work for this project should focus on expanding the ligand:metal ratio for precipitation reactions to solidify the proposal of a 3:1 structure. Also, attempts should be made to investigate whether the cycle of REE precipitation with [PTA-CO_2^-][H^+] is indeed recyclable *via* precipitation of more REE salts from the aqueous solution leftover from lanthanide hydroxide.

7 Appendix

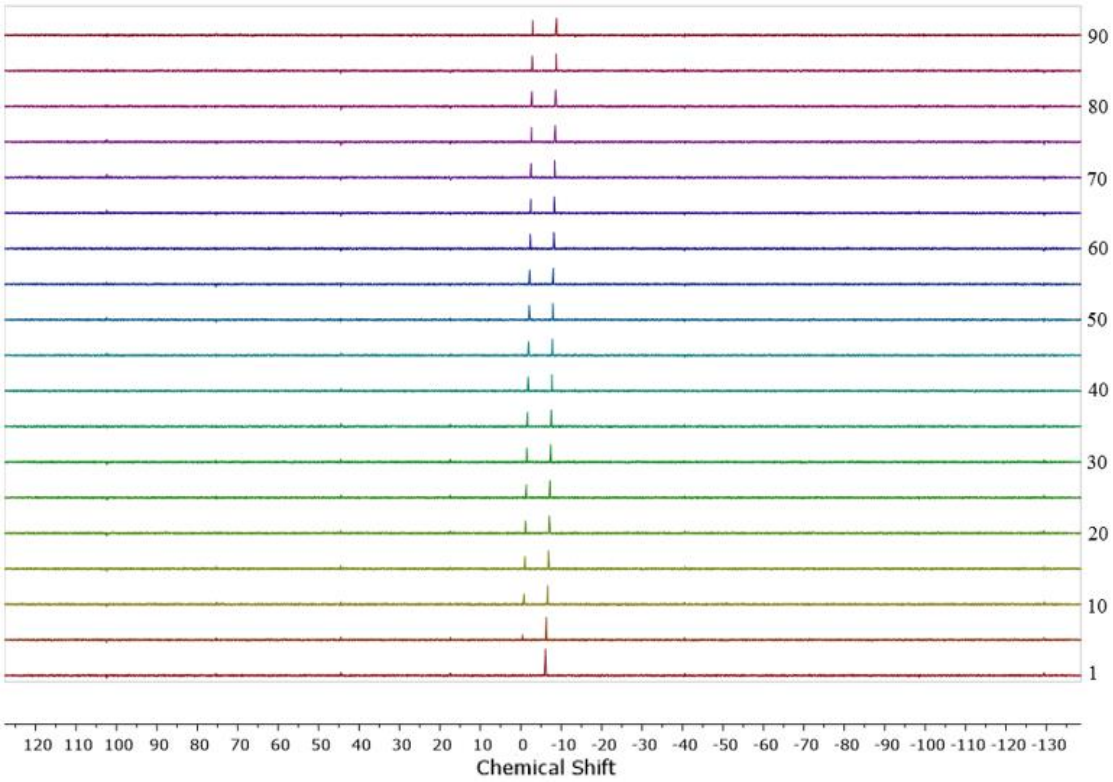

Figure A.1: Time-resolved $^{31}P\{^{1}H\}$ NMR of **8a** to **8b** isomerization in $CDCl_3$ at 25 °C. Every fifth spectrum of the full 96 collected is shown for clarity, as indicated by the spectrum numbers indicated to the side of the figure.

Time (min)	*8a*	*8b*
2.5	*0.62*	*18.78*
5	*1.08*	*17.25*
7.5	*1.74*	*16.76*
10	*2.6*	*16.84*
12.5	*3.11*	*16.29*
15	*3.69*	*16.02*
17.5	*4.28*	*15.61*
20	*4.92*	*15.4*
22.5	*5.25*	*15.36*
25	*5.75*	*14.45*
27.5	*6.25*	*14.98*
30	*6.73*	*14.62*
32.5	*6.39*	*13.42*
35	*6.97*	*13.7*
37.5	*7.27*	*13.09*
40	*7.95*	*13.53*
42.5	*8.02*	*12.9*
45	*8.22*	*12.85*
47.5	*8.56*	*12.86*
50	*8.86*	*12.92*
52.5	*8.89*	*12.02*
55	*8.61*	*12.5*
57.5	*9.09*	*12.16*
60	*9.29*	*12.24*
62.5	*8.98*	*12.1*
65	*9.13*	*11.96*
67.5	*9.23*	*12.4*
70	*9.31*	*11.97*
72.5	*8.95*	*12.03*
75	*9.09*	*12.11*
77.5	*9.95*	*11.9*
80	*9.3*	*11.99*
82.5	*9.75*	*11.83*
85	*9.87*	*12.1*
87.5	*9.92*	*12.45*
90	*10.09*	*11.68*
92.5	*9.5*	*11.86*
95	*9.92*	*11.85*
97.5	*9.9*	*11.82*
100	*10.14*	*11.81*
102.5	*9.97*	*11.42*
105	*10.03*	*11.77*
107.5	*10.23*	*11.43*
110	*10.08*	*11.31*
112.5	*9.79*	*11.52*
115	*10.26*	*11.34*
117.5	*10.15*	*11.83*
120	*9.73*	*11.77*
122.5	*10.12*	*11.46*
125	*9.83*	*11.59*
127.5	*10.35*	*11.87*
130	*10.21*	*11.08*
132.5	*10.46*	*11.35*
135	*10.28*	*11.35*
137.5	*10.23*	*11.56*
140	*9.73*	*11.73*
142.5	*10.4*	*11.62*
145	*10.02*	*11.77*
147.5	*9.73*	*11.49*
150	*10.05*	*11.4*
152.5	*10.4*	*11.23*
155	*9.81*	*11.14*
157.5	*10.32*	*11.44*
160	*10.38*	*11.62*
162.5	*10.24*	*11.45*
165	*9.95*	*11.16*
167.5	*9.84*	*11.37*
170	*10.32*	*11.57*
172.5	*9.93*	*11.26*
175	*9.9*	*11.49*
177.5	*9.96*	*11.68*
180	*9.99*	*11.36*
182.5	*10.16*	*11.55*
185	*10.12*	*11.45*
187.5	*9.98*	*12.05*
190	*9.82*	*11.71*
192.5	*10.53*	*11.49*
195	*9.99*	*12.4*
197.5	*9.88*	*11.64*
200	*10.37*	*11.68*
202.5	*10.15*	*12.04*
205	*10.03*	*11.81*
207.5	*10.08*	*12.23*
210	*10.24*	*11.53*
212.5	*10.51*	*11.76*
215	*10.24*	*12.04*
217.5	*10.41*	*12.15*
220	*10.74*	*11.97*
222.5	*9.98*	*12.17*
225	*10.57*	*11.97*
227.5	*10.3*	*12.13*
230	*9.97*	*11.84*
232.5	*10.32*	*11.65*
235	*10.49*	*11.85*
237.5	*10.49*	*12.11*
240	*10.32*	*11.86*

Figure A.2: Tabulated peak heights corresponding to **8a** and **8b** for each $^{31}P\{^{1}H\}$ NMR spectrum recorded at 25 ºC as a function of time since the beginning of the experiment.

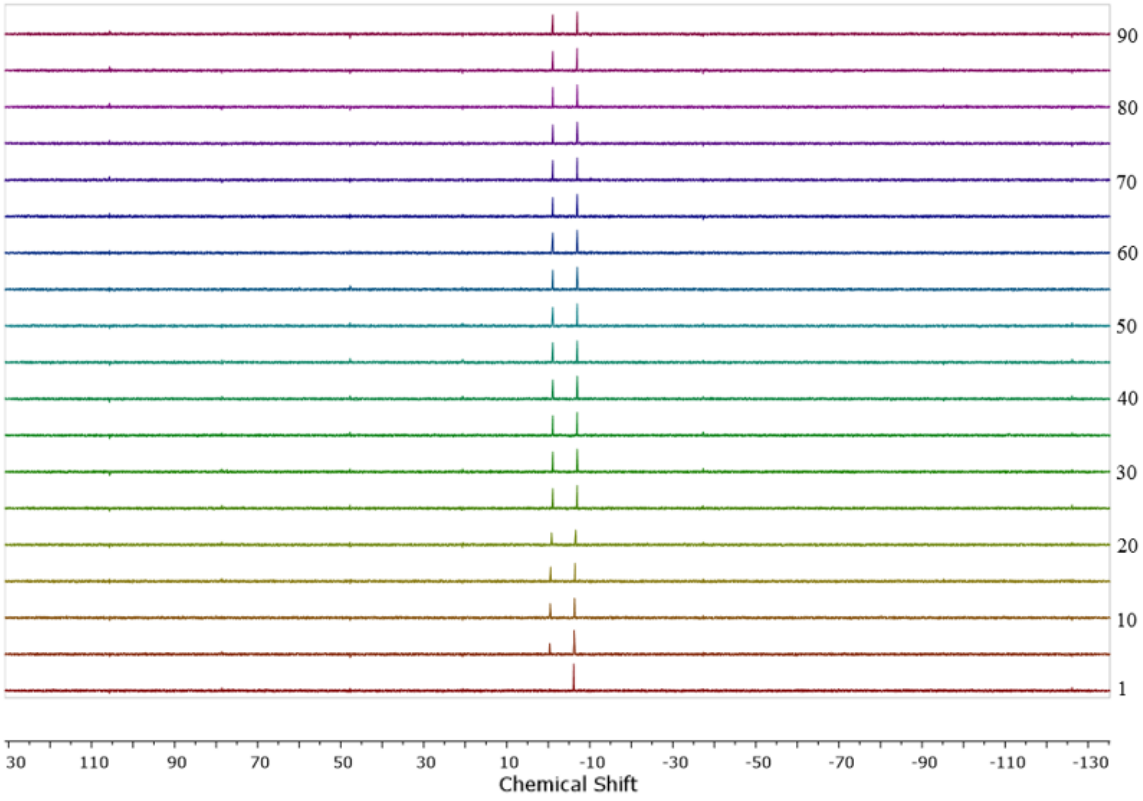

Figure A.3: Time-resolved $^{31}P\{^{1}H\}$ NMR of **8a** to **8b** isomerization in $CDCl_3$ at 35 ºC. Every fifth spectrum of the full 96 collected is shown for clarity, as indicated by the spectrum numbers indicated to the side of the figure.

Time (min)	*8a*	*8b*
2.5	*1.06*	*15.3*
5	*2.65*	*17.41*
7.5	*3.75*	*16.19*
10	*5.53*	*14.92*
12.5	*6.1*	*13.68*
15	*7.17*	*13.53*
17.5	*7.14*	*12.36*
20	*7.63*	*11.85*
22.5	*8.15*	*11.76*
25	*8.16*	*11.14*
27.5	*8.9*	*10.92*
30	*8.7*	*10.86*
32.5	*8.29*	*10.29*
35	*8.91*	*10.57*
37.5	*8.15*	*10.23*
40	*7.99*	*9.79*
42.5	*7.91*	*9.45*
45	*7.84*	*9.13*
47.5	*7.69*	*8.63*
50	*6.85*	*8.42*
52.5	*6.87*	*7.99*
55	*4.15*	*5.01*
57.5	*11.08*	*13.03*
60	*10.96*	*13.08*
62.5	*11.13*	*13*
65	*11.15*	*12.63*
67.5	*10.94*	*12.72*
70	*11.26*	*12.68*
72.5	*11.03*	*12.93*
75	*11.36*	*12.93*
77.5	*11.12*	*12.97*
80	*10.77*	*12.74*
82.5	*10.93*	*12.55*
85	*11.4*	*12.86*
87.5	*11.21*	*13.16*
90	*10.9*	*12.72*
92.5	*11.05*	*12.84*
95	*11.03*	*12.71*
97.5	*11.06*	*12.64*
100	*10.84*	*12.99*
102.5	*11.03*	*13.31*
105	*11.06*	*12.93*
107.5	*10.58*	*12.64*
110	*10.9*	*12.56*
112.5	*11.3*	*12.33*
115	*10.95*	*12.5*
117.5	*11.01*	*12.99*
120	*10.75*	*12.88*
122.5	*11.28*	*12.75*
125	*10.68*	*12.62*
127.5	*10.96*	*13.1*
130	*10.84*	*12.43*
132.5	*10.84*	*12.63*
135	*10.91*	*12.58*
137.5	*10.99*	*12.75*
140	*10.88*	*12.92*
142.5	*10.66*	*12.69*
145	*11.03*	*12.57*
147.5	*10.79*	*12.67*
150	*11.4*	*13*
152.5	*11.03*	*13.48*
155	*10.83*	*12.93*
157.5	*11.01*	*12.65*
160	*10.91*	*12.97*
162.5	*10.76*	*12.64*
165	*11.16*	*12.57*
167.5	*10.71*	*12.5*
170	*10.66*	*12.68*
172.5	*11.47*	*12.44*
175	*11.12*	*12.57*
177.5	*10.84*	*12.5*
180	*11.12*	*12.17*
182.5	*10.82*	*12.71*
185	*10.86*	*12.7*
187.5	*10.57*	*12.17*
190	*11.6*	*12.71*
192.5	*10.93*	*12.83*
195	*11.29*	*12.85*
197.5	*11.46*	*12.45*
200	*11.28*	*12.66*
202.5	*11.34*	*12.85*
205	*11.3*	*12.74*
207.5	*11.11*	*12.73*
210	*11.16*	*12.6*
212.5	*10.98*	*12.65*
215	*11.19*	*13.03*
217.5	*10.85*	*13.35*
220	*11.11*	*12.63*
222.5	*10.98*	*12.73*
225	*11.03*	*12.64*
227.5	*10.91*	*12.63*
230	*11.17*	*12.51*
232.5	*11.26*	*12.64*
235	*11.11*	*12.88*
237.5	*10.71*	*12.61*
240	*11.17*	*12.3*

Figure A.4: Tabulated peak heights corresponding to **8a** and **8b** for each $^{31}P\{^{1}H\}$ NMR spectrum recorded at 35 ºC as a function of time since the beginning of the experiment.

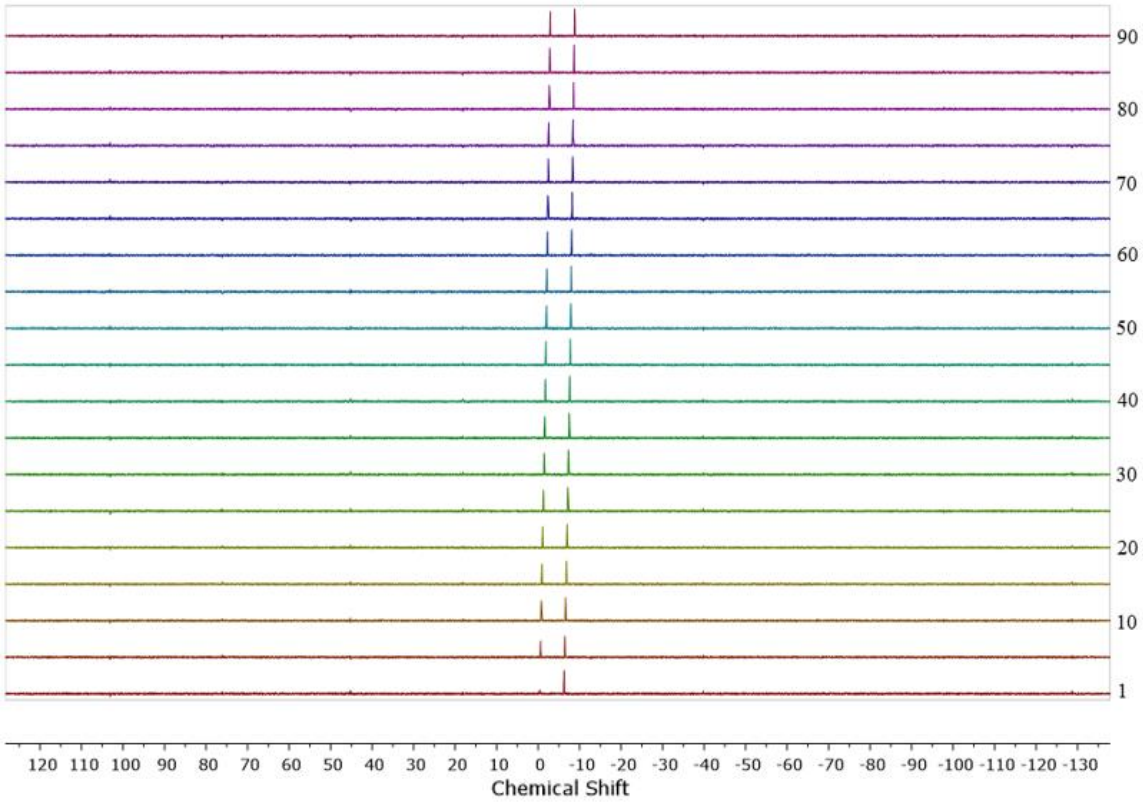

Figure A.5: Time-resolved $^{31}P\{^{1}H\}$ NMR of **8a** to **8b** isomerization in $CDCl_3$ at 45 ºC. Every fifth spectrum of the full 96 collected is shown for clarity, as indicated by the spectrum numbers indicated to the side

Time (min)	*8a*	*8b*
1	*2.52*	*16.59*
3.5	*7.42*	*18.54*
6	*9.59*	*16.46*
8.5	*11.87*	*16.59*
11	*11.64*	*14.79*
13.5	*12.96*	*15.28*
16	*13.35*	*15.28*
18.5	*12.9*	*14.92*
21	*13.84*	*15.66*
23.5	*14.13*	*16.41*
26	*13.69*	*15.46*
28.5	*13.81*	*16.07*
31	*13.59*	*15.23*
33.5	*13.82*	*15.64*
36	*14.31*	*16.32*
38.5	*14.42*	*16.09*
41	*14.29*	*16.19*
43.5	*14.64*	*16.83*
46	*14.5*	*15.81*
48.5	*15.09*	*16.67*
51	*14.74*	*16.17*
53.5	*14.55*	*16.43*
56	*15.25*	*17.2*
58.5	*14.65*	*16.55*
61	*14.95*	*16.73*
63.5	*14.8*	*16.9*
66	*15.04*	*16.89*
68.5	*15.98*	*17.69*
71	*14.71*	*16.64*
73.5	*15.29*	*17.57*
76	*15.11*	*17.06*
78.5	*15.3*	*17.32*
81	*15.69*	*17.8*
83.5	*15.21*	*17.48*
86	*15.31*	*17.54*
88.5	*15.18*	*17.26*
91	*15.17*	*17.03*
93.5	*16.44*	*18.6*
96	*15.51*	*17.84*
98.5	*15.78*	*18.03*
101	*16.23*	*17.92*
103.5	*15.94*	*17.6*
106	*16.37*	*18.22*
108.5	*16.94*	*18.48*
111	*16.76*	*18.53*
113.5	*16.87*	*18.95*
116	*15.79*	*18.07*
118.5	*16.46*	*18.4*
121	*16.67*	*18.31*
123.5	*16.14*	*17.54*
126	*16.41*	*17.85*
128.5	*16.54*	*18.55*
131	*17.48*	*19.06*
133.5	*17.41*	*18.92*
136	*16.41*	*18.2*
138.5	*17.13*	*18.96*
141	*16.47*	*18.39*
143.5	*16.75*	*19.07*
146	*16.94*	*18.95*
148.5	*16.77*	*18.28*
151	*16.9*	*18.61*
153.5	*16.46*	*19.14*
156	*17.46*	*19.66*
158.5	*17.34*	*18.93*
161	*16.37*	*18.65*
163.5	*17.01*	*18.88*
166	*16.83*	*19.6*
168.5	*16.81*	*18.53*
171	*17.09*	*19.03*
173.5	*16.77*	*18.34*
176	*16.5*	*18.81*
178.5	*16.85*	*19.15*
181	*16.85*	*18.91*
183.5	*17.28*	*18.91*
186	*16.53*	*18.48*
188.5	*16.66*	*19.03*
191	*16.9*	*18.83*
193.5	*17.01*	*19.55*
196	*17.83*	*19.84*
198.5	*16.87*	*19.14*
201	*16.72*	*18.57*
203.5	*16.36*	*18.97*
206	*16.67*	*19.28*
208.5	*16.66*	*18.45*
211	*17.52*	*19.64*
213.5	*17.22*	*18.58*
216	*16.96*	*19.09*
218.5	*17.04*	*18.93*
221	*16.93*	*18.94*
223.5	*17.43*	*19.25*
226	*16.32*	*17.95*
228.5	*17.38*	*18.8*
231	*16.04*	*18.08*
233.5	*16.01*	*18.41*
236	*16.13*	*17.85*
238.5	*16.38*	*17.46*

Figure A.6: Tabulated peak heights corresponding to **8a** and **8b** for each $^{31}P\{^{1}H\}$ NMR spectrum recorded at 45 ºC as a function of time since the beginning of the experiment.

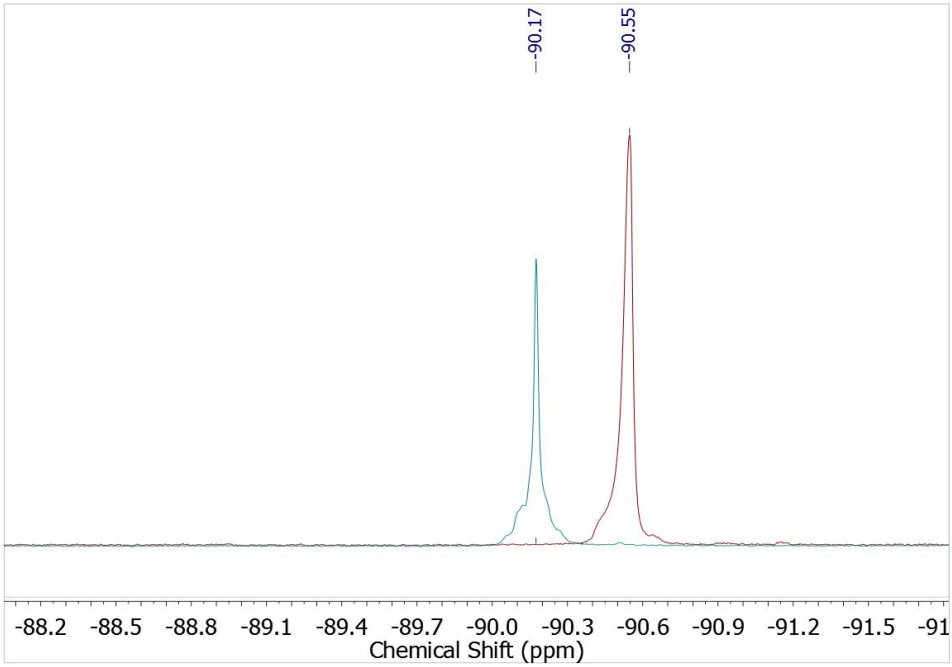

Figure A.7: Crude ^{31}P {^{1}H} NMR spectrum in methanol of **10** (*maroon*) and the phosphine after it was heated to 180 ºC in the presence of ammonium chloride overnight (*blue*).

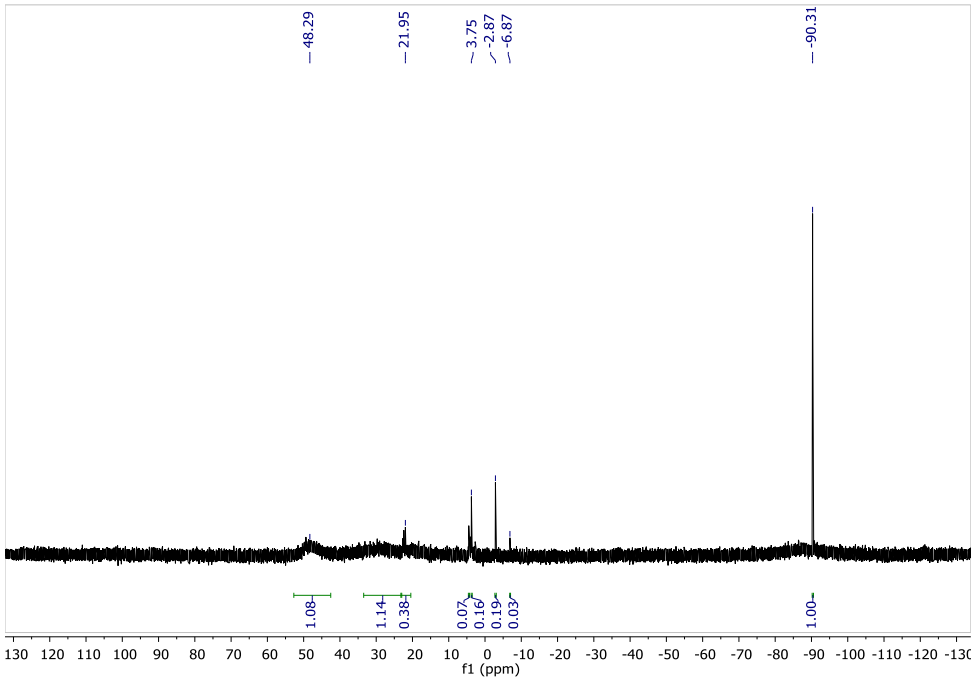

Figure A.8: Solution-state ^{31}P {^{1}H} NMR in CD_3OD of **10** after it was heated at 180 ºC in the presence of benzylammonium chloride overnight.

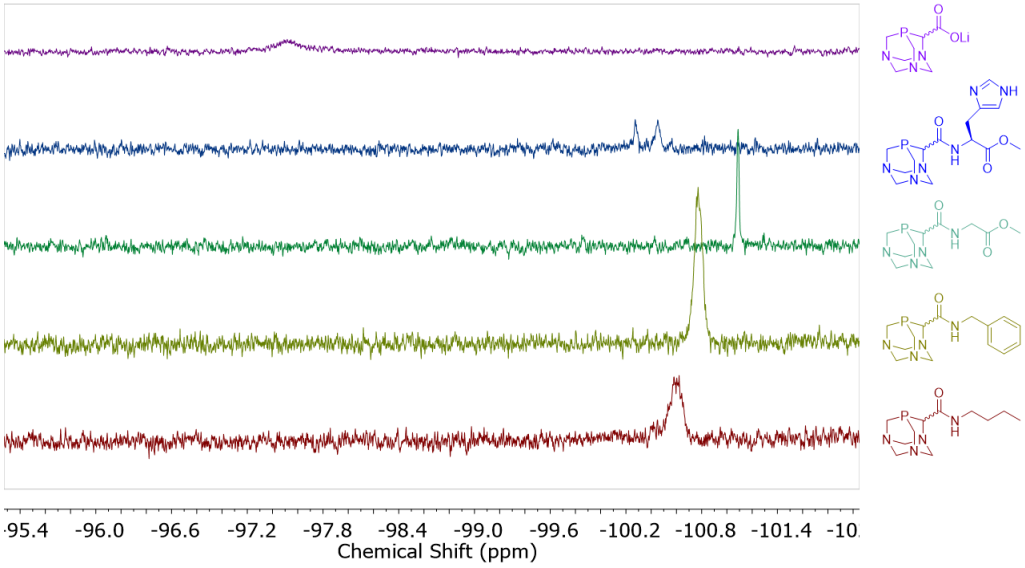

Figure A.9: Crude ^{31}P {^{1}H} NMR of **10**, **12**, **13**, **14**, **15**, and **16** in DMF.

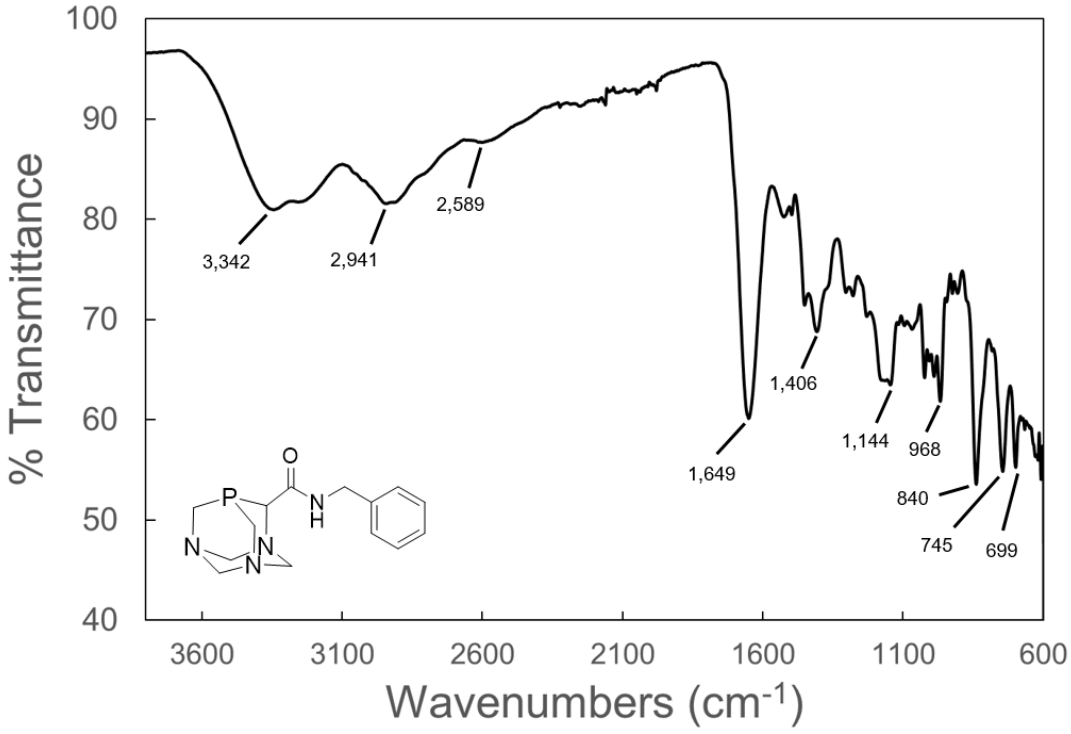

Figure A.10: Crude ssFTIR of **12** after synthesis from **10**.

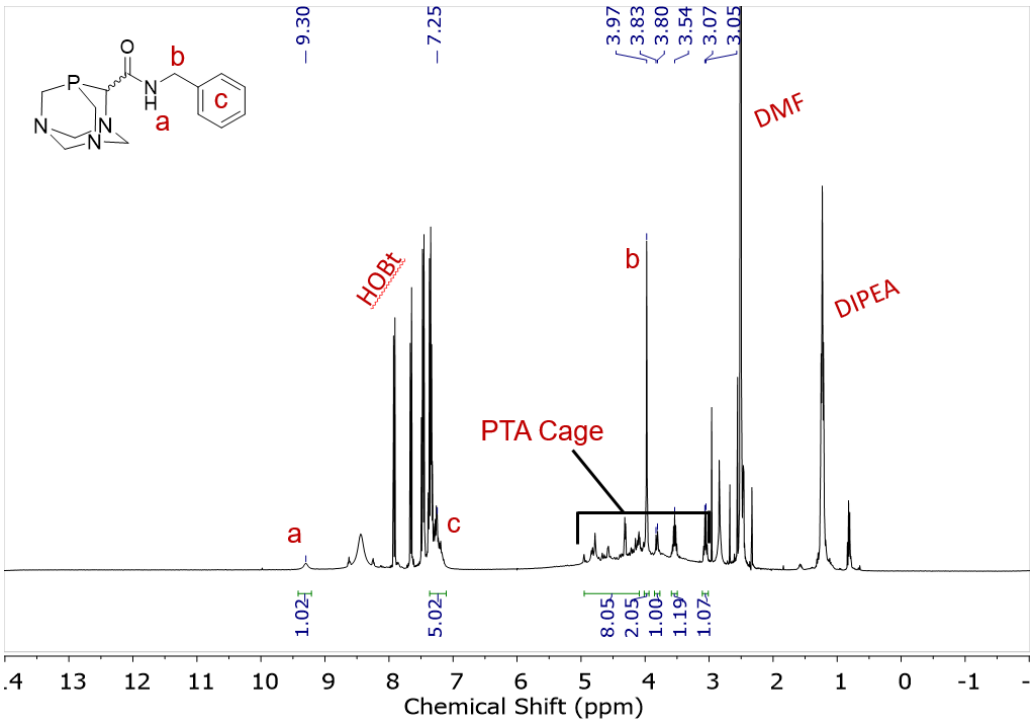

Figure A.11: Crude ^{1}H NMR spectrum of **5** in d^{6}-DMSO after synthesis from **10**.

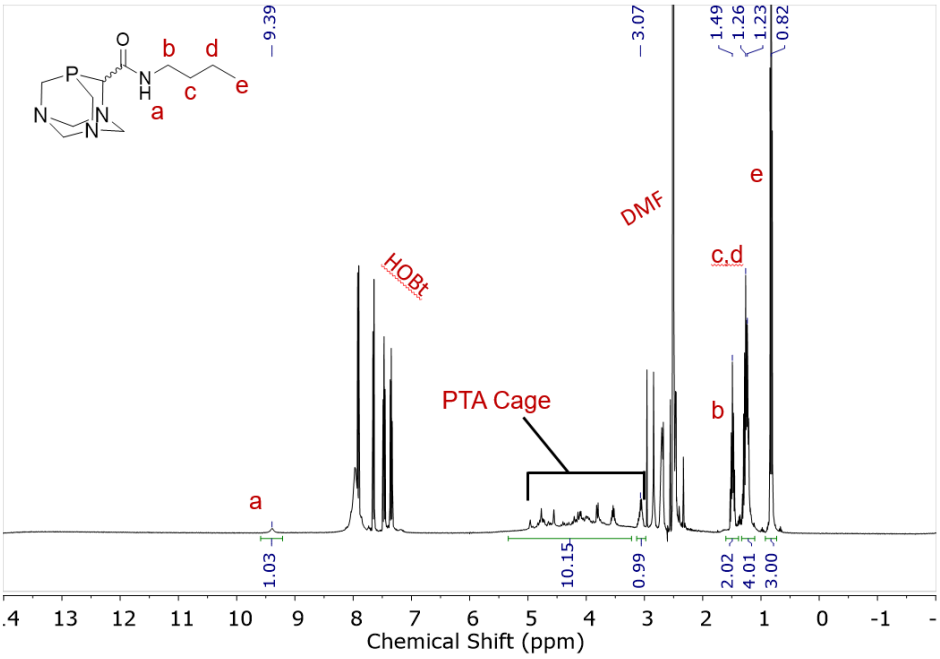

Figure A.12: Crude ^{1}H NMR spectrum of **13** in d^{6}-DMSO after synthesis from **10.**

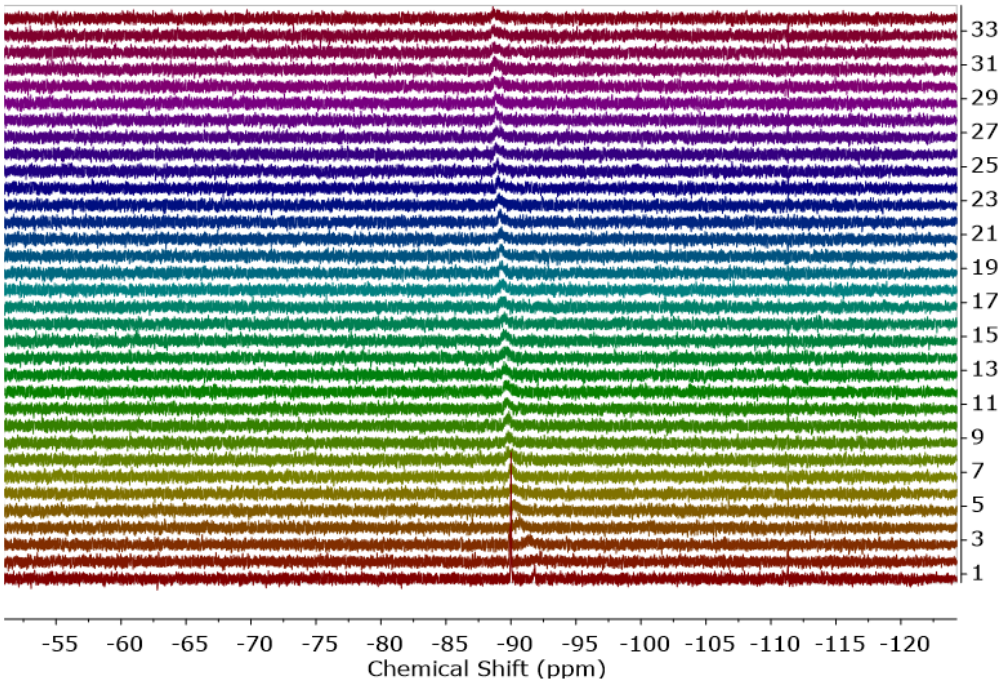

Figure A.13: ^{31}P {^{1}H} NMR spectra investigating the reaction kinetics of amide formation with **10** and HBTU. Spectra increase as you move up through the figure with T_0 being the bottom spectrum, and each subsequent spectrum was acquired after a 2 minute delay.

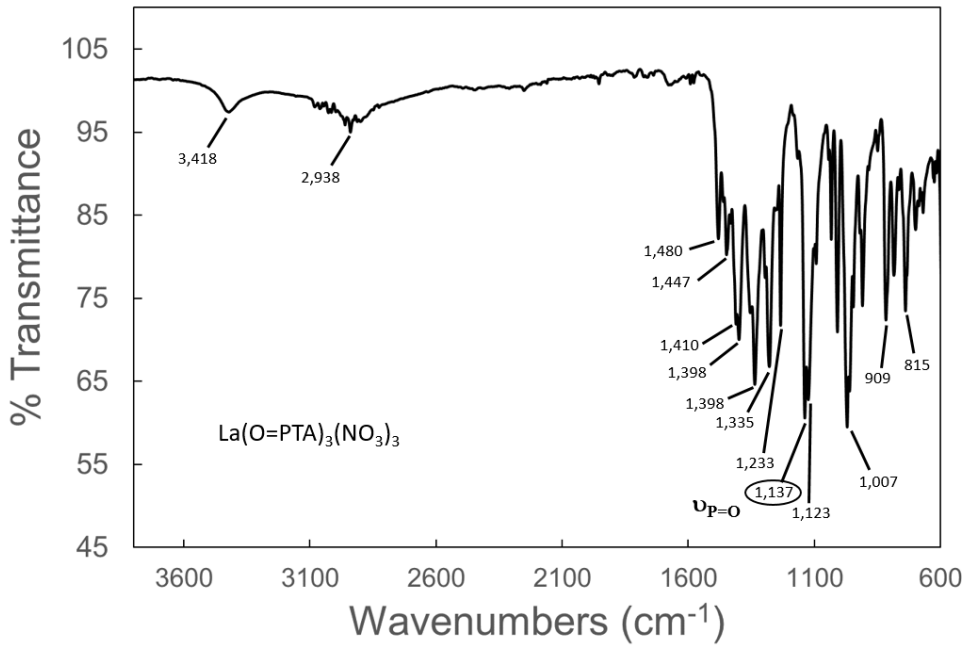

Figure A.14: ss FT-IR spectrum of **19**.

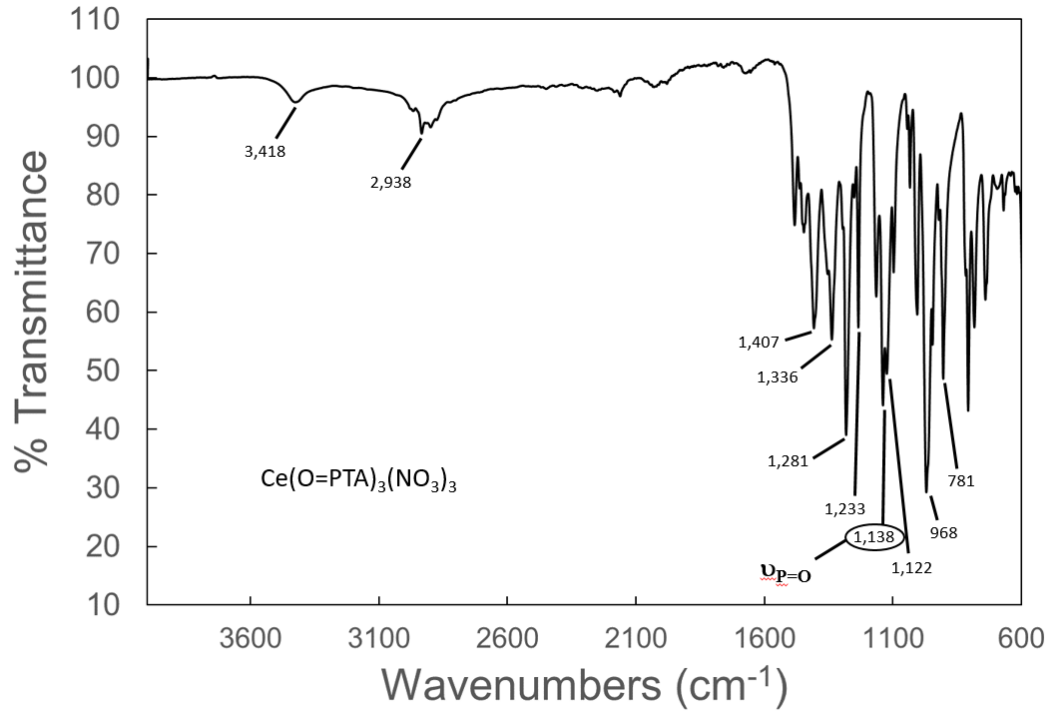

Figure A.15: ss FT-IR spectrum of **20.**

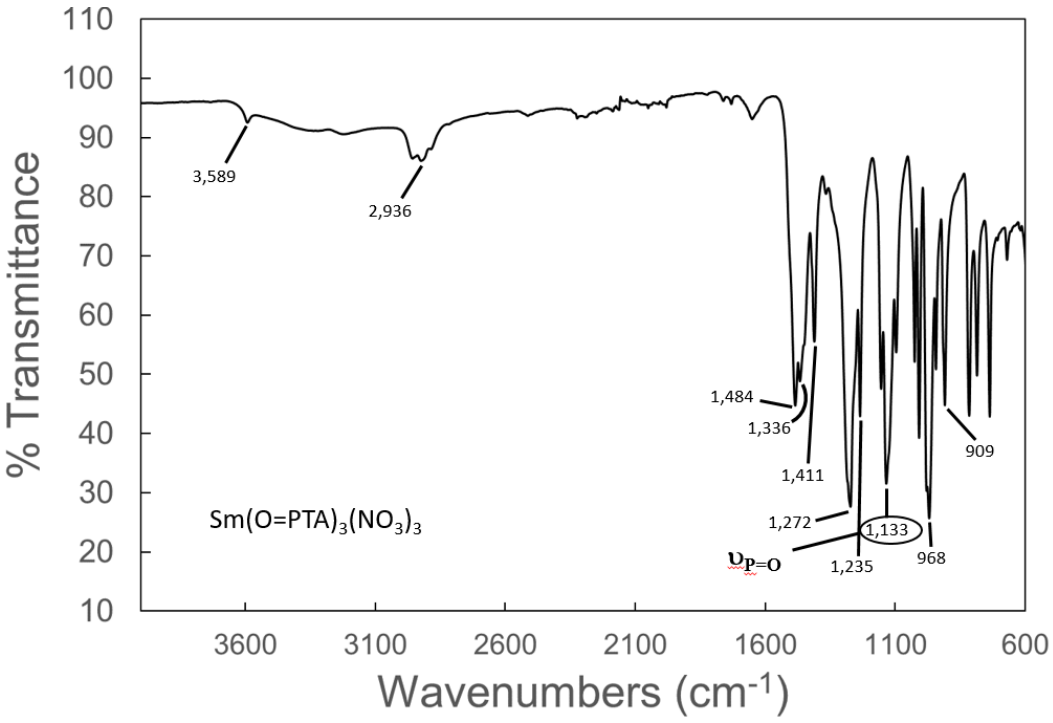

Figure A.16: ss FT-IR spectrum of **21.**

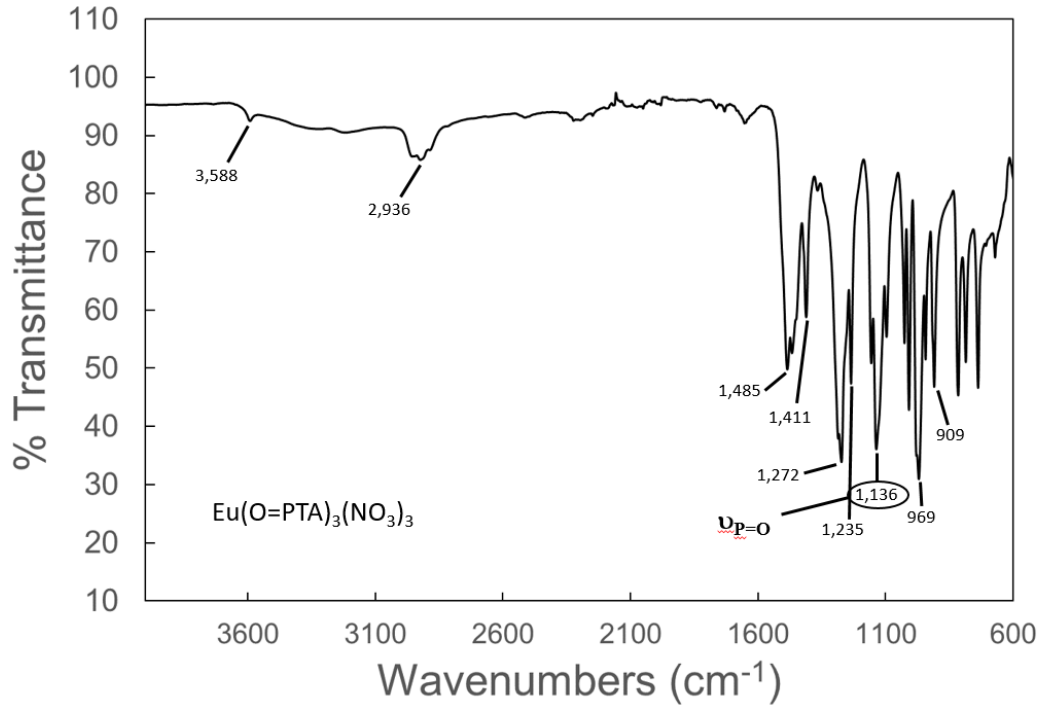

Figure A.17: ss FT-IR spectrum of **22.**

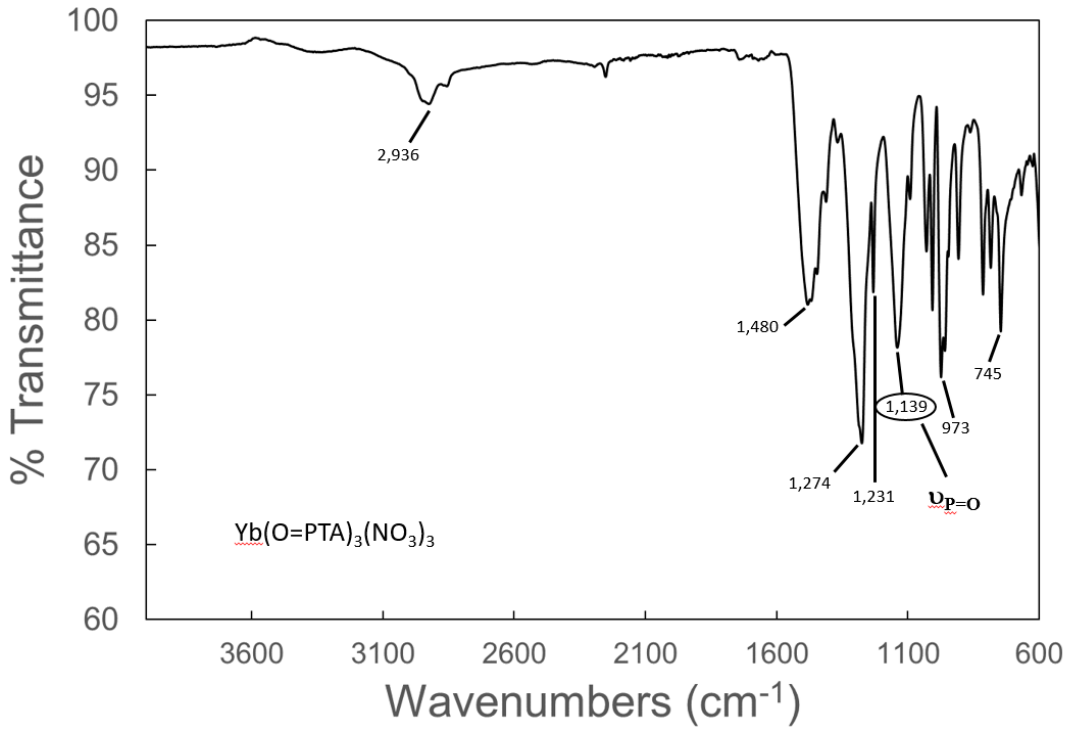

Figure A.18: ss FT-IR spectrum of **23**.

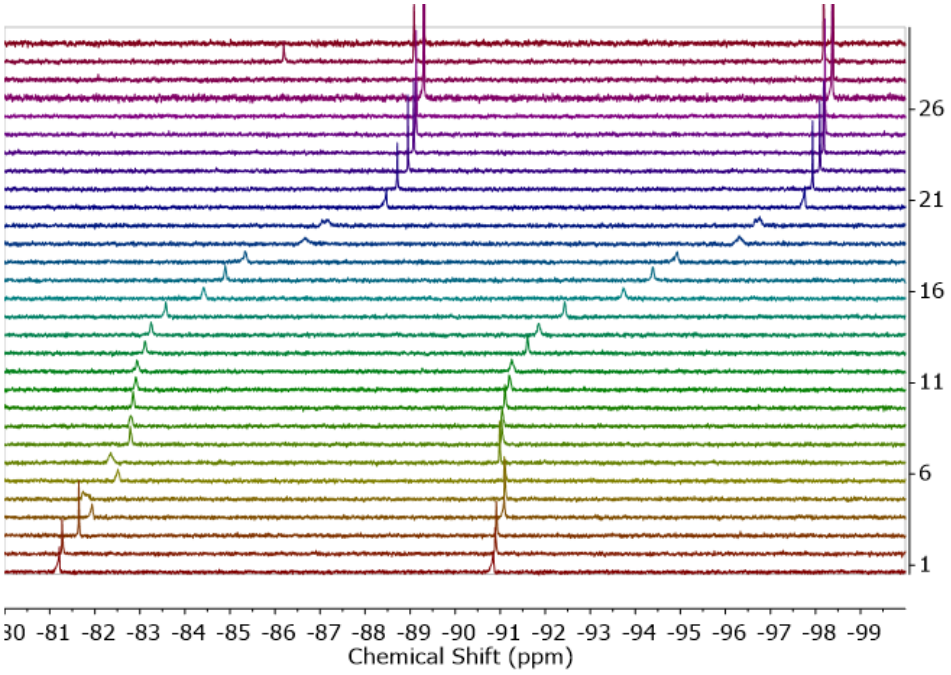

Figure A.19: ^{31}P {^{1}H} NMR titration of **10** and **25**. A 3:1 mixture of the two phosphines was first acidified to pH < 1, and then incrementally basified with dilute sodium hydroxide to yield the spectra above.

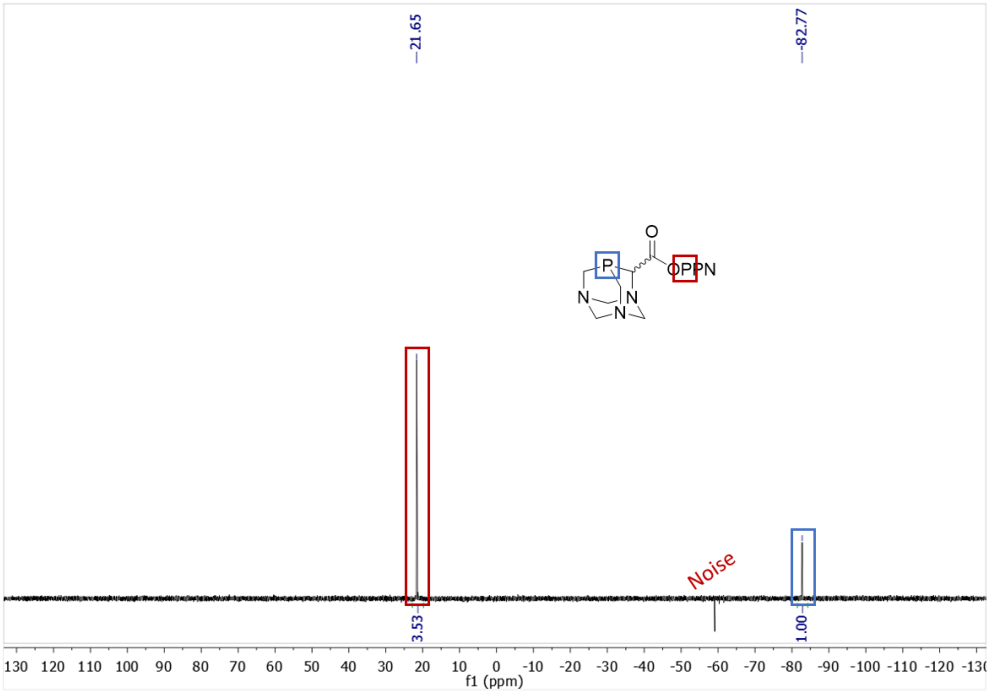

Figure A.20: Crude ^{31}P {^{1}H} NMR of the precipitate after attempted separation of **10** from **25** through cation exchange with PPN.

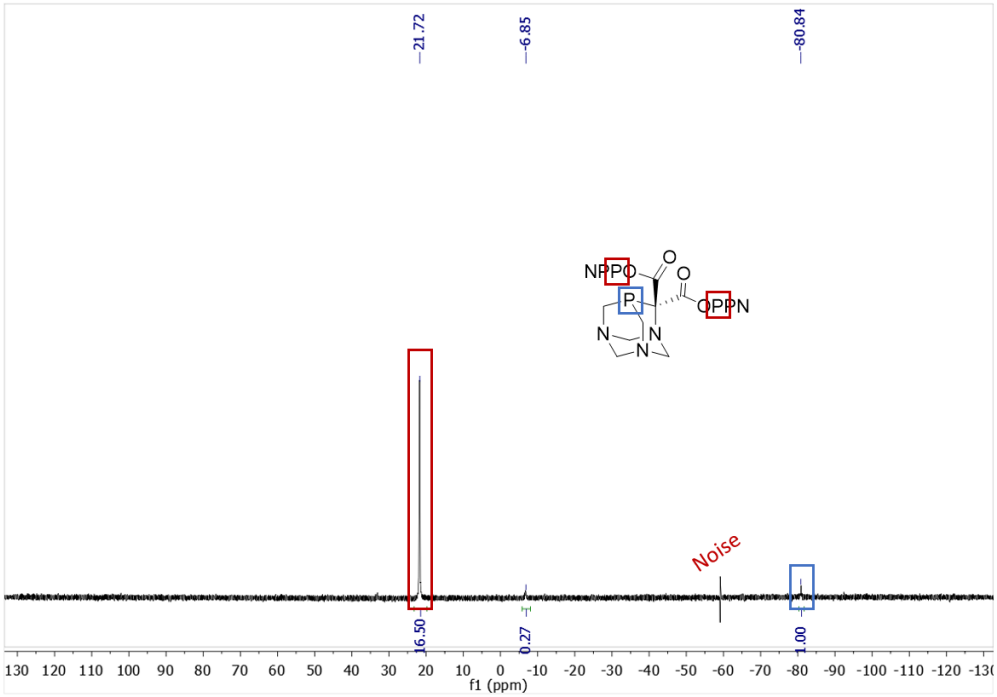

Figure A.21: Crude ^{31}P {^{1}H} NMR of the filtrate after attempted separation of **10** from **25** through cation exchange with PPN.

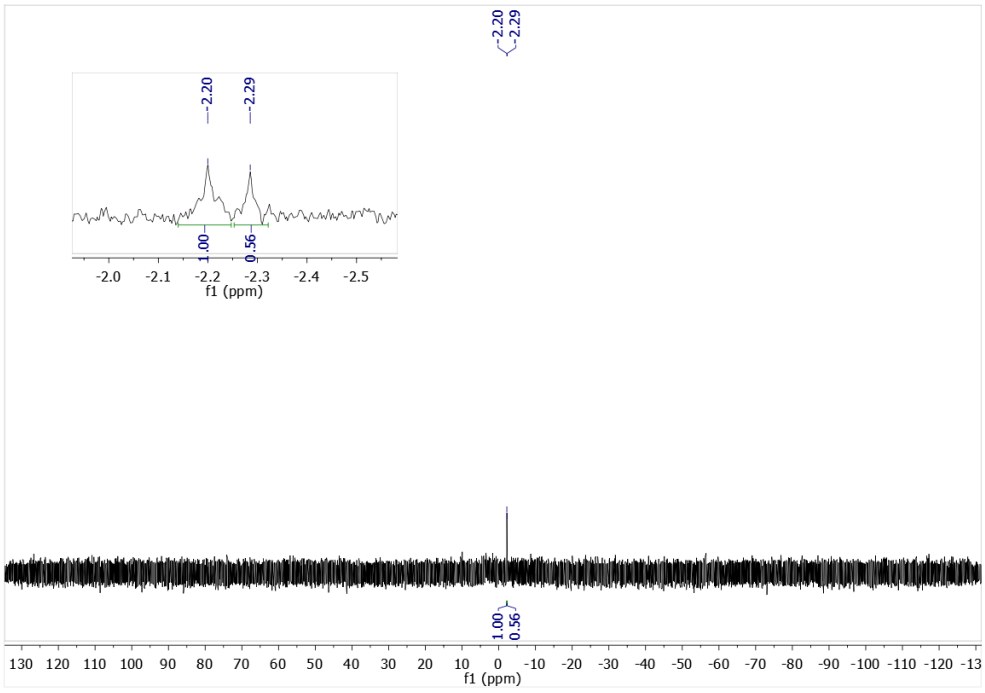

Figure A.22: Crude ^{31}P {^{1}H} NMR of the product from reaction between a 3:1 mixture of **10** to **25** and the $[RuCl_2(\eta^6\text{-toluene})]_2$ dimer.

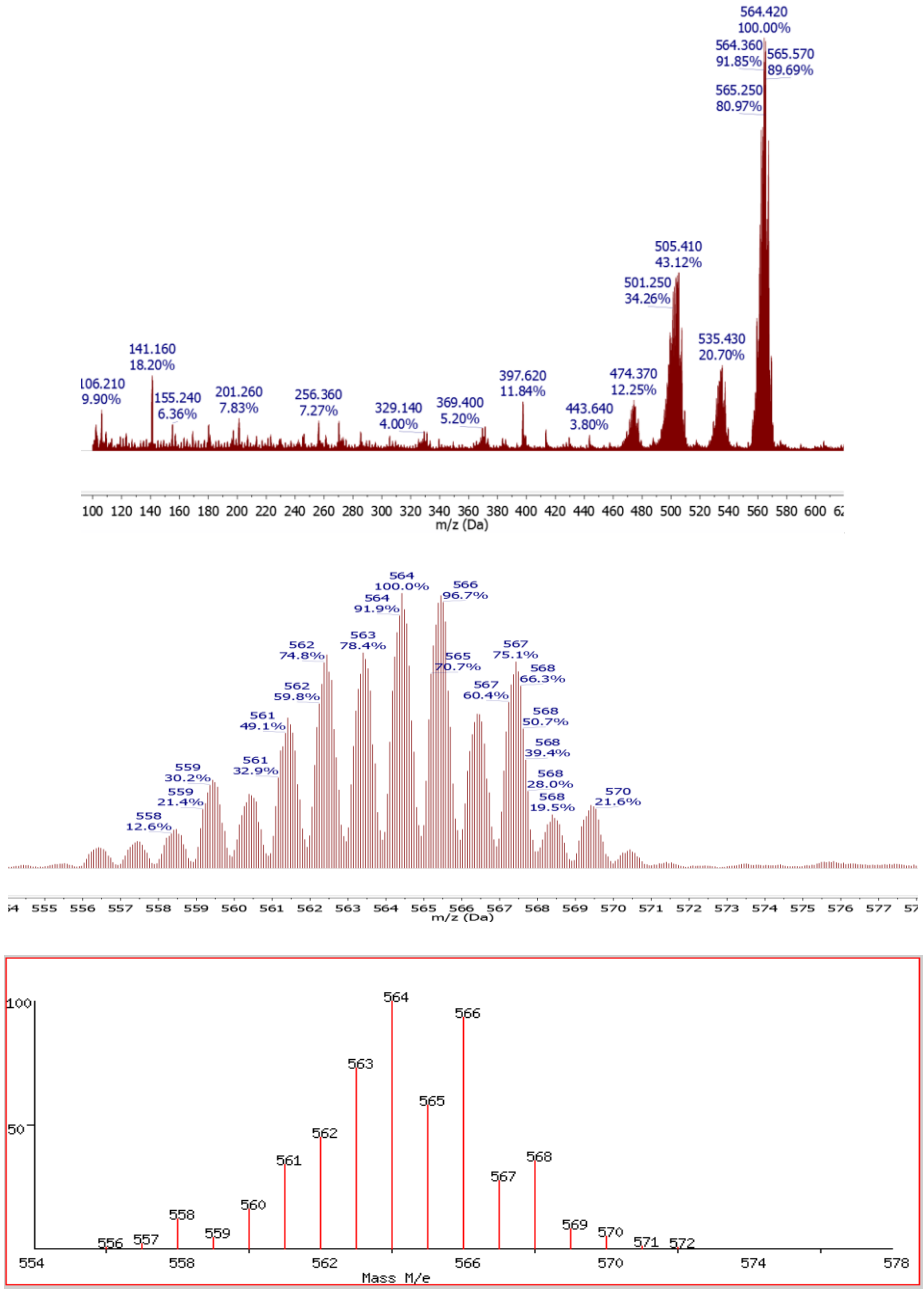

Figure A.23: Crude Mass Spectrum of the product from reaction between a 3:1 mixture of **10** to **25** and the $[RuCl_2(\eta^6\text{-cymene})]_2$ dimer (top). Zoomed in portions of the experimental (middle) and calculated (bottom) isotope distribution patterns of the product are included as well.

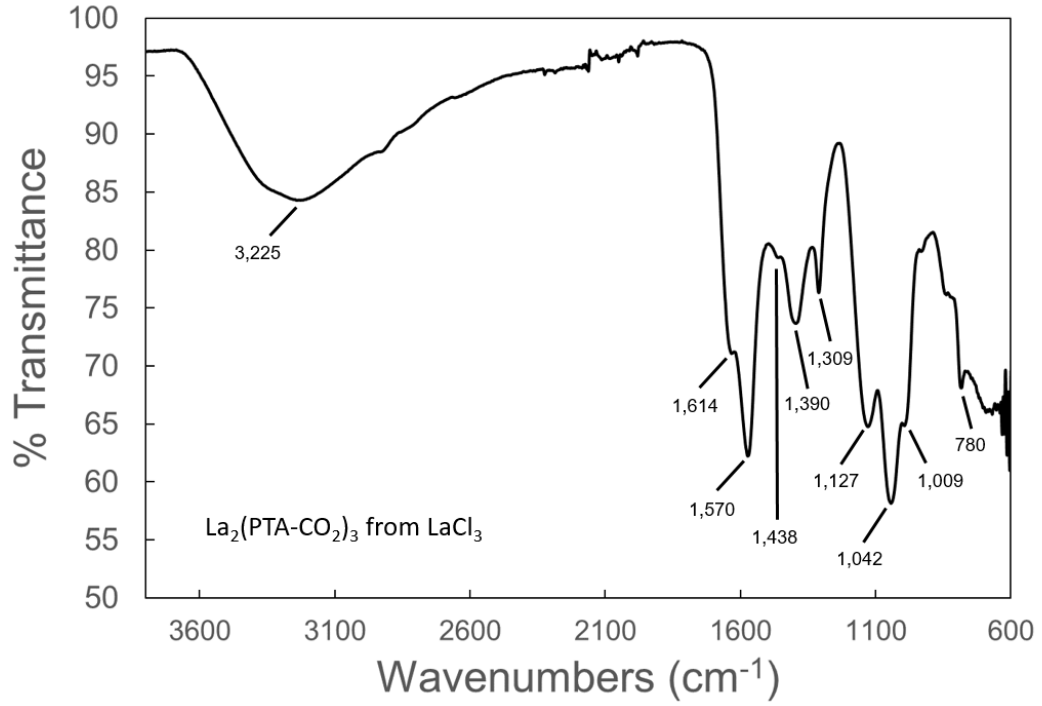

Figure A.24: Solid-state FT-IR of crude **32a** after synthesis and drying in air.

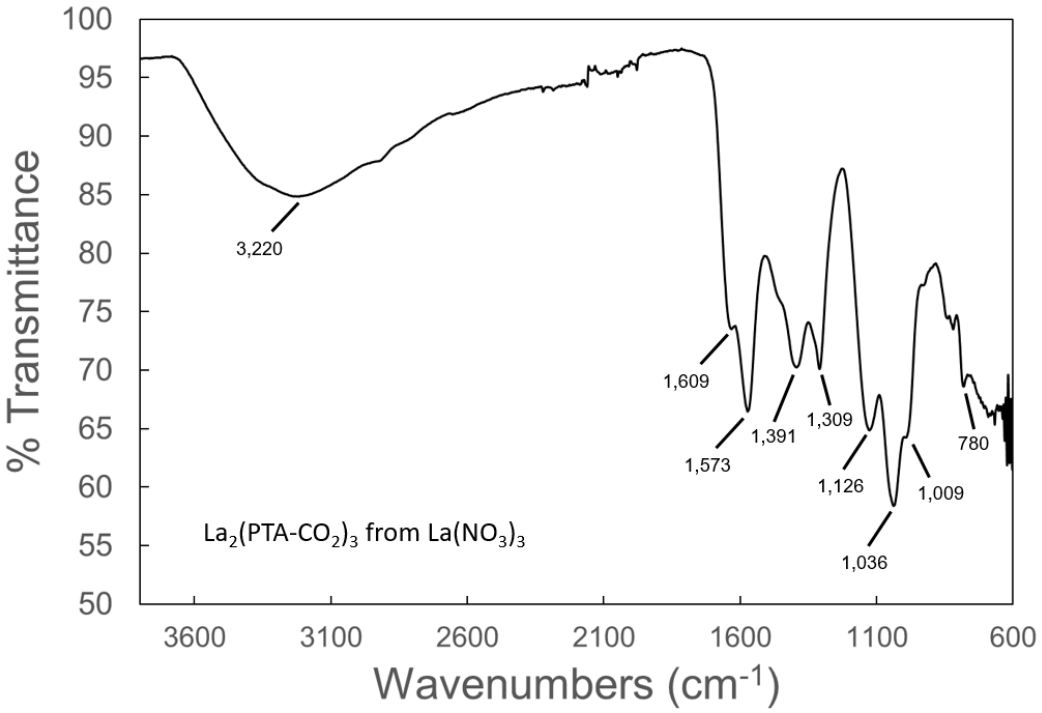

Figure A.25: Solid-state FT-IR of crude **32b** after synthesis and drying in air.

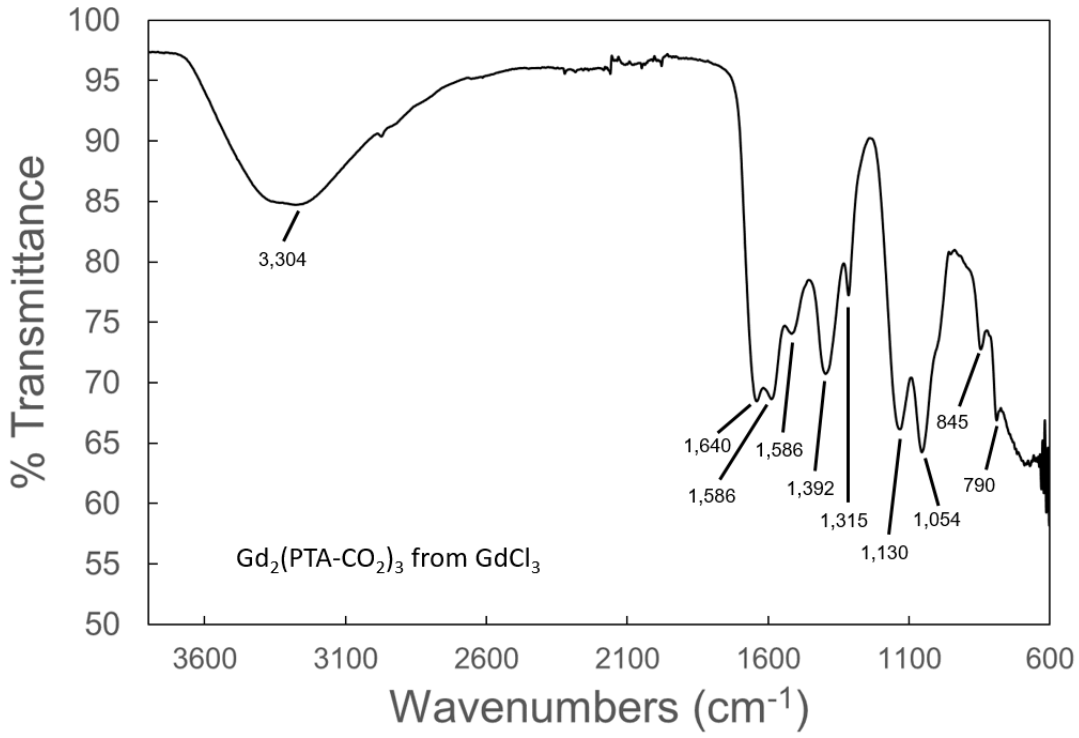

Figure A.26: Solid-state FT-IR of crude **33a** after synthesis and drying in air.

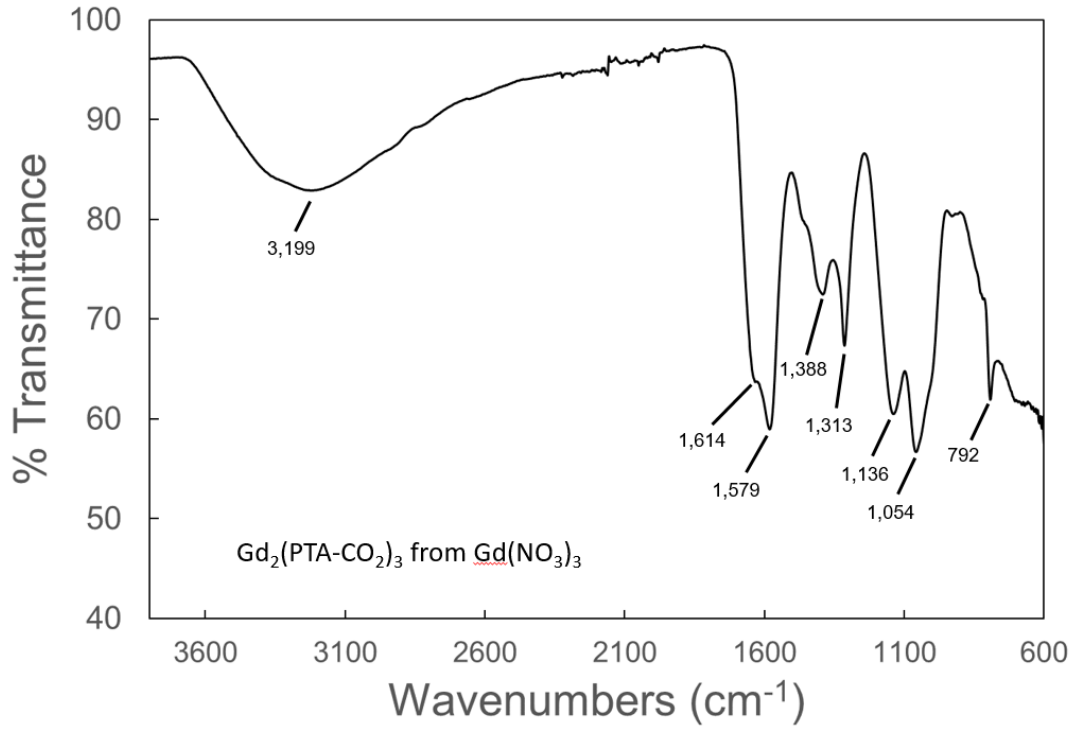

Figure A.27: Solid-state FT-IR of crude **33b** after synthesis and drying in air.

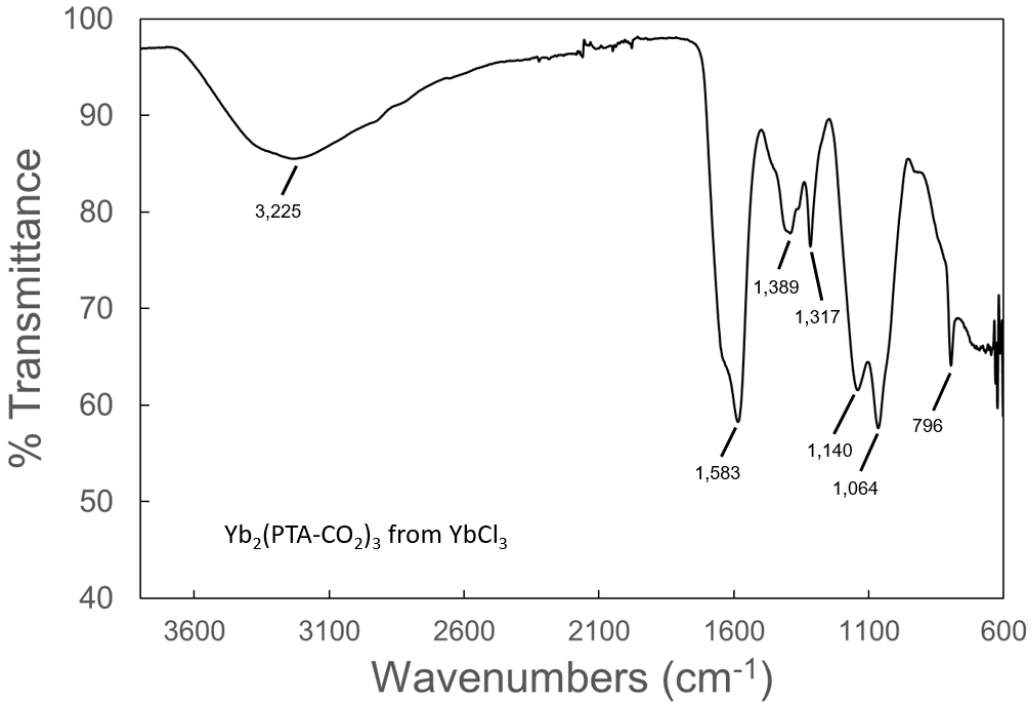

Figure A.28: Solid-state FT-IR of crude **34a** after synthesis and drying in air.

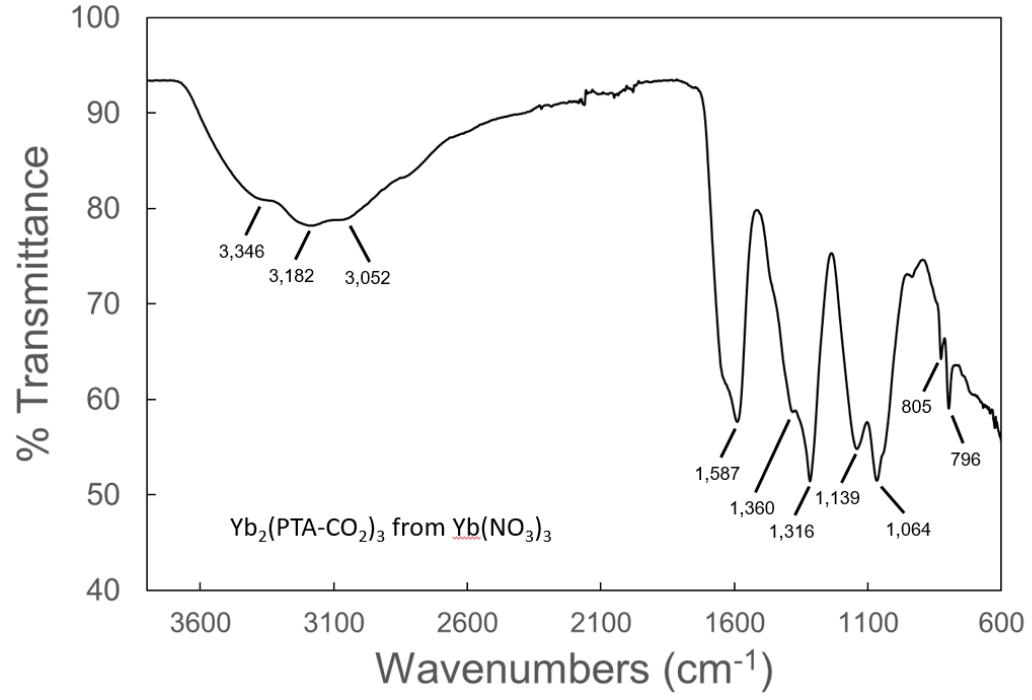

Figure A.29: Solid-state FT-IR of crude **34b** after synthesis and drying in air.

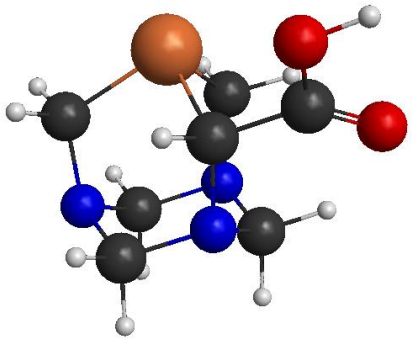

```
 $CONTRL SCFTYP=RHF RUNTYP=OPTIMIZE DFTTYP=B3LYP MAXIT=200 MULT=1 ISPHER=1
    COORD=CART $END
 $SYSTEM TIMLIM=525600 MWORDS=200 $END
 $BASIS GBASIS=TZV NDFUNC=1 DIFFSP=.TRUE. DIFFS=.TRUE. $END
 $SCF DIRSCF=.TRUE. $END
 $STATPT NSTEP=200 $END
 $DATA
(PTACOOH)
C1
N      7.0      2.05630    -0.91215    -0.75770
P     15.0      0.66248     1.58124    -0.53463
N      7.0     -0.27703    -1.05636    -0.09897
N      7.0      1.38935    -0.25230     1.50519
C      6.0      1.96441     0.44262    -1.34201
C      6.0      2.42778    -0.85568     0.66355
C      6.0      1.20268     1.18756     1.23785
C      6.0      0.84519    -1.66859    -0.91507
C      6.0     -0.70588     0.30458    -0.61811
C      6.0      0.17210    -0.98814     1.36892
H      1.0      2.94767     0.91180    -1.26336
H      1.0      1.74399     0.35182    -2.40891
H      1.0      2.61112    -1.87439     1.01458
H      1.0      3.35086    -0.28632     0.76866
H      1.0      2.14240     1.70435     1.44495
H      1.0      0.45380     1.58571     1.92504
H      1.0      0.52594    -1.68933    -1.95671
H      1.0      0.98932    -2.69067    -0.55795
C      6.0     -2.07053     0.62297     0.13700
H      1.0     -0.95601     0.15150    -1.67382
H      1.0     -0.64721    -0.53810     1.92232
H      1.0      0.30728    -2.02231     1.69094
O      8.0     -2.29488     1.81020     0.38321
O      8.0     -2.70848    -0.43476     0.37908
H      1.0     -2.83105    -0.53651     1.39669
 $END
```

Figure A.30: DFT-optimized structure for PTA-COOH and the input file used to calculate it and its energy.

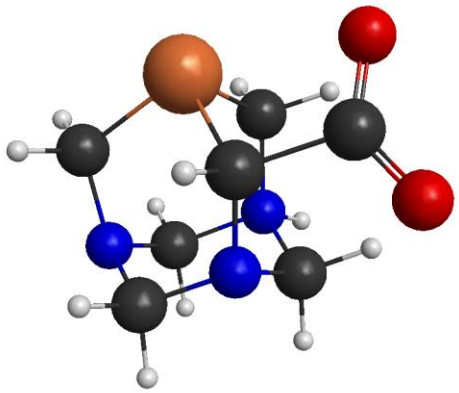

```
 $CONTRL SCFTYP=RHF RUNTYP=OPTIMIZE DFTTYP=B3LYP MAXIT=200 MULT=1 ISPHER=1
    COORD=CART $END
 $SYSTEM TIMLIM=525600 MWORDS=200 $END
 $BASIS GBASIS=TZV NDFUNC=1 DIFFSP=.TRUE. DIFFS=.TRUE. $END
 $SCF DIRSCF=.TRUE. $END
 $STATPT NSTEP=200 $END
 $DATA
 1N-[PTACO2-][H+]
C1
N      7.0      2.05630    -0.91215    -0.75770
P     15.0      0.66248     1.58124    -0.53463
N      7.0     -0.27703    -1.05636    -0.09897
N      7.0      1.38935    -0.25230     1.50519
C      6.0      1.96441     0.44262    -1.34201
C      6.0      2.42778    -0.85568     0.66355
C      6.0      1.20268     1.18756     1.23785
C      6.0      0.84519    -1.66859    -0.91507
C      6.0     -0.70588     0.30458    -0.61811
C      6.0      0.17210    -0.98814     1.36892
H      1.0      2.94767     0.91180    -1.26336
H      1.0      1.74399     0.35182    -2.40891
H      1.0      2.61112    -1.87439     1.01458
H      1.0      3.35086    -0.28632     0.76866
H      1.0      2.14240     1.70435     1.44495
H      1.0      0.45380     1.58571     1.92504
H      1.0      0.52594    -1.68933    -1.95671
H      1.0      0.98932    -2.69067    -0.55795
C      6.0     -2.07053     0.62297     0.13700
H      1.0     -0.95601     0.15150    -1.67382
H      1.0     -0.64721    -0.53810     1.92232
H      1.0      0.30728    -2.02231     1.69094
O      8.0     -2.29488     1.81020     0.38321
O      8.0     -2.70848    -0.43476     0.37908
H      1.0      1.68751    -0.33858     2.45580
 $END
```

Figure A.31: DFT-optimized structure for 1-*N* [PTA-COO^-][H^+] and the input file used to calculate it and its energy.

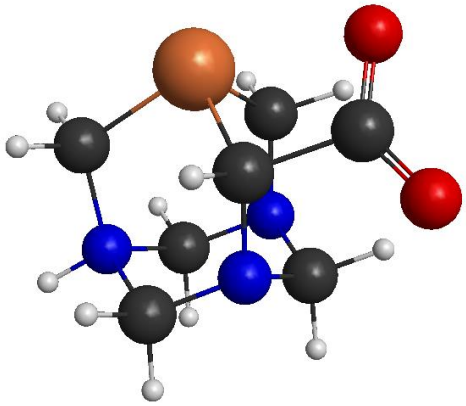

```
 $CONTRL SCFTYP=RHF RUNTYP=OPTIMIZE DFTTYP=B3LYP MAXIT=200 MULT=1 ISPHER=1
    COORD=CART $END
 $SYSTEM TIMLIM=525600 MWORDS=200 $END
 $BASIS GBASIS=TZV NDFUNC=1 DIFFSP=.TRUE. DIFFS=.TRUE. $END
 $SCF DIRSCF=.TRUE. $END
 $STATPT NSTEP=200 $END
 $DATA
 3N [PTACO2-][H+]
C1
N      7.0      2.05630    -0.91215    -0.75770
P     15.0      0.66248     1.58124    -0.53463
N      7.0     -0.27703    -1.05636    -0.09897
N      7.0      1.38935    -0.25230     1.50519
C      6.0      1.96441     0.44262    -1.34201
C      6.0      2.42778    -0.85568     0.66355
C      6.0      1.20268     1.18756     1.23785
C      6.0      0.84519    -1.66859    -0.91507
C      6.0     -0.70588     0.30458    -0.61811
C      6.0      0.17210    -0.98814     1.36892
H      1.0      2.94767     0.91180    -1.26336
H      1.0      1.74399     0.35182    -2.40891
H      1.0      2.61112    -1.87439     1.01458
H      1.0      3.35086    -0.28632     0.76866
H      1.0      2.14240     1.70435     1.44495
H      1.0      0.45380     1.58571     1.92504
H      1.0      0.52594    -1.68933    -1.95671
H      1.0      0.98932    -2.69067    -0.55795
C      6.0     -2.07053     0.62297     0.13700
H      1.0     -0.95601     0.15150    -1.67382
H      1.0     -0.64721    -0.53810     1.92232
H      1.0      0.30728    -2.02231     1.69094
O      8.0     -2.29488     1.81020     0.38321
O      8.0     -2.70848    -0.43476     0.37908
H      1.0      2.96584     0.55482     1.20595
 $END
```

Figure A.32: DFT-optimized structure for 3-*N* [PTA-COO^-][H^+] and the input file used to calculate it and its energy.

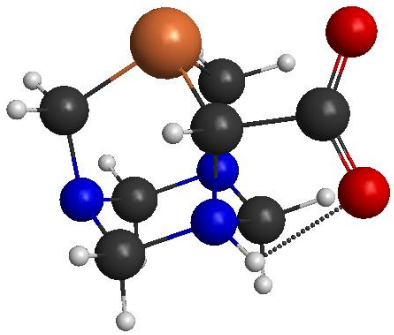

```
 $CONTRL SCFTYP=RHF RUNTYP=OPTIMIZE DFTTYP=B3LYP MAXIT=200 MULT=1 ISPHER=1
    COORD=CART $END
 $SYSTEM TIMLIM=525600 MWORDS=200 $END
 $BASIS GBASIS=TZV NDFUNC=1 DIFFSP=.TRUE. DIFFS=.TRUE. $END
 $SCF DIRSCF=.TRUE. $END
 $STATPT NSTEP=200 $END
 $DATA
 5N-[PTACO2-][H+]
C1
N      7.0      2.05630    -0.91215    -0.75770
P     15.0      0.66248     1.58124    -0.53463
N      7.0     -0.27703    -1.05636    -0.09897
N      7.0      1.38935    -0.25230     1.50519
C      6.0      1.96441     0.44262    -1.34201
C      6.0      2.42778    -0.85568     0.66355
C      6.0      1.20268     1.18756     1.23785
C      6.0      0.84519    -1.66859    -0.91507
C      6.0     -0.70588     0.30458    -0.61811
C      6.0      0.17210    -0.98814     1.36892
H      1.0      2.94767     0.91180    -1.26336
H      1.0      1.74399     0.35182    -2.40891
H      1.0      2.61112    -1.87439     1.01458
H      1.0      3.35086    -0.28632     0.76866
H      1.0      2.14240     1.70435     1.44495
H      1.0      0.45380     1.58571     1.92504
H      1.0      0.52594    -1.68933    -1.95671
H      1.0      0.98932    -2.69067    -0.55795
C      6.0     -2.07053     0.62297     0.13700
H      1.0     -0.95601     0.15150    -1.67382
H      1.0     -0.64721    -0.53810     1.92232
H      1.0      0.30728    -2.02231     1.69094
O      8.0     -2.29488     1.81020     0.38321
O      8.0     -2.70848    -0.43476     0.37908
H      1.0     -1.18355    -1.56574    -0.09810
 $END
```

Figure A.33: DFT-optimized structure for 5-*N* [PTA-COO$^-$][H$^+$] and the input file used to calculate it and its energy. The hydrogen bonding interaction between the proton and carboxylate is indicated with a dotted line.

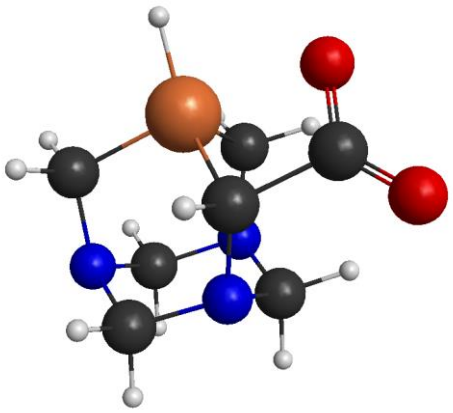

```
 $CONTRL SCFTYP=RHF RUNTYP=OPTIMIZE DFTTYP=B3LYP MAXIT=200 MULT=1 ISPHER=1
    COORD=CART $END
 $SYSTEM TIMLIM=525600 MWORDS=200 $END
 $BASIS GBASIS=TZV NDFUNC=1 DIFFSP=.TRUE. DIFFS=.TRUE. $END
 $SCF DIRSCF=.TRUE. $END
 $STATPT NSTEP=200 $END
 $DATA
P-[PTACOO-][H]
C1
N      7.0      2.05630    -0.91215    -0.75770
P     15.0      0.66248     1.58124    -0.53463
N      7.0     -0.27703    -1.05636    -0.09897
N      7.0      1.38935    -0.25230     1.50519
C      6.0      1.96441     0.44262    -1.34201
C      6.0      2.42778    -0.85568     0.66355
C      6.0      1.20268     1.18756     1.23785
C      6.0      0.84519    -1.66859    -0.91507
C      6.0     -0.70588     0.30458    -0.61811
C      6.0      0.17210    -0.98814     1.36892
H      1.0      2.94767     0.91180    -1.26336
H      1.0      1.74399     0.35182    -2.40891
H      1.0      2.61112    -1.87439     1.01458
H      1.0      3.35086    -0.28632     0.76866
H      1.0      2.14240     1.70435     1.44495
H      1.0      0.45380     1.58571     1.92504
H      1.0      0.52594    -1.68933    -1.95671
H      1.0      0.98932    -2.69067    -0.55795
C      6.0     -2.07053     0.62297     0.13700
H      1.0     -0.95601     0.15150    -1.67382
H      1.0     -0.64721    -0.53810     1.92232
H      1.0      0.30728    -2.02231     1.69094
O      8.0     -2.29488     1.81020     0.38321
O      8.0     -2.70848    -0.43476     0.37908
H      1.0      0.36074     2.62218    -0.90595
 $END
```

Figure A.34: DFT-optimized structure for *P*-[PTA-COO$^-$][H$^+$] and the input file used to calculate it and its energy.

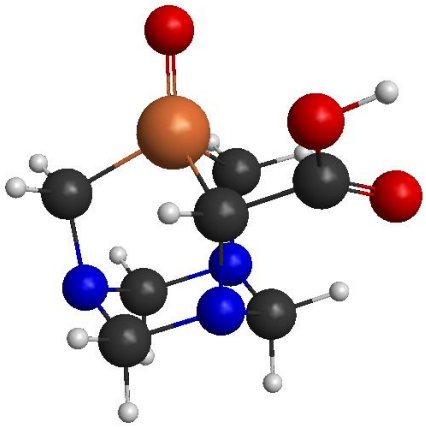

```
 $CONTRL SCFTYP=RHF RUNTYP=OPTIMIZE DFTTYP=B3LYP MAXIT=200 MULT=1 ISPHER=1
    COORD=CART $END
 $SYSTEM TIMLIM=525600 MWORDS=200 $END
 $BASIS GBASIS=TZV NDFUNC=1 DIFFSP=.TRUE. DIFFS=.TRUE. $END
 $SCF DIRSCF=.TRUE. $END
 $STATPT NSTEP=200 $END
 $DATA
(O=PTA-COOH)
C1
N      7.0      2.05630    -0.91215    -0.75770
P     15.0      0.66248     1.58124    -0.53463
N      7.0     -0.27703    -1.05636    -0.09897
N      7.0      1.38935    -0.25230     1.50519
C      6.0      1.96441     0.44262    -1.34201
C      6.0      2.42778    -0.85568     0.66355
C      6.0      1.20268     1.18756     1.23785
C      6.0      0.84519    -1.66859    -0.91507
C      6.0     -0.70588     0.30458    -0.61811
C      6.0      0.17210    -0.98814     1.36892
H      1.0      2.94767     0.91180    -1.26336
H      1.0      1.74399     0.35182    -2.40891
H      1.0      2.61112    -1.87439     1.01458
H      1.0      3.35086    -0.28632     0.76866
H      1.0      2.14240     1.70435     1.44495
H      1.0      0.45380     1.58571     1.92504
H      1.0      0.52594    -1.68933    -1.95671
H      1.0      0.98932    -2.69067    -0.55795
C      6.0     -2.07053     0.62297     0.13700
H      1.0     -0.95601     0.15150    -1.67382
H      1.0     -0.64721    -0.53810     1.92232
H      1.0      0.30728    -2.02231     1.69094
O      8.0     -2.29488     1.81020     0.38321
O      8.0     -2.70848    -0.43476     0.37908
O      8.0      0.66541     3.08642    -0.74065
H      1.0     -2.83105    -0.53651     1.39669
 $END
```

Figure A.35: DFT-optimized structure for O=PTA-COOH and the input file used to calculate it and its energy.

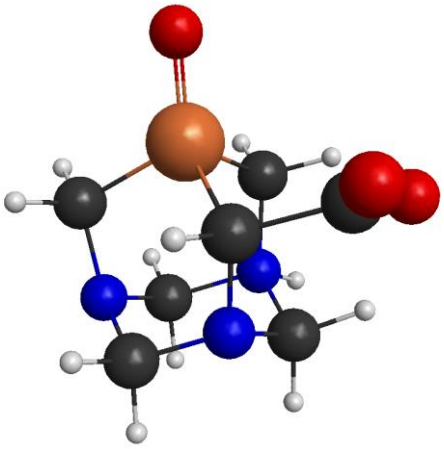

```
 $CONTRL SCFTYP=RHF RUNTYP=OPTIMIZE DFTTYP=B3LYP MAXIT=200 MULT=1 ISPHER=1
    COORD=CART $END
 $SYSTEM TIMLIM=525600 MWORDS=200 $END
 $BASIS GBASIS=TZV NDFUNC=1 DIFFSP=.TRUE. DIFFS=.TRUE. $END
 $SCF DIRSCF=.TRUE. $END
 $STATPT NSTEP=200 $END
 $DATA
1N-[O=PTACOO-][H+]
C1
N      7.0      2.17274      0.38404      0.73968
P     15.0      0.07820     -1.34975      0.15308
N      7.0     -0.02989      1.38785      0.46434
N      7.0      1.17600      0.53661     -1.49560
C      6.0      1.68954     -0.98498      1.02799
C      6.0      2.41034      0.56538     -0.70057
C      6.0      0.54632     -0.80588     -1.56088
C      6.0      1.28186      1.40304      1.22960
C      6.0     -0.87325      0.14686      0.71300
C      6.0      0.27945      1.55172     -1.03630
H      1.0      2.44846     -1.70427      0.71237
H      1.0      1.55401     -1.11444      2.10472
H      1.0      2.89438      1.53219     -0.85344
H      1.0      3.08540     -0.21429     -1.05120
H      1.0      1.24890     -1.51404     -2.00435
H      1.0     -0.34236     -0.77221     -2.19328
H      1.0      1.05464      1.25362      2.28490
H      1.0      1.72686      2.38992      1.09138
C      6.0     -2.29934      0.52040      0.08446
H      1.0     -1.00947      0.07015      1.79633
H      1.0     -0.67427      1.52862     -1.55599
H      1.0      0.72955      2.53946     -1.14527
O      8.0     -2.92800     -0.38187     -0.45312
O      8.0     -2.52236      1.74939      0.24311
O      8.0     -0.48508     -2.71557      0.39970
H      1.0      1.42997      0.77600     -2.43272
 $END
```

Figure A.36: DFT-optimized structure for 1*N*-[O=PTA-COO$^-$][H$^+$] and the input file used to calculate it and its energy.

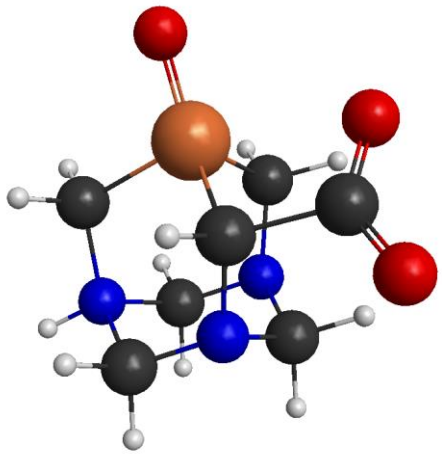

```
 $CONTRL SCFTYP=RHF RUNTYP=OPTIMIZE DFTTYP=B3LYP MAXIT=200 MULT=1 ISPHER=1
    COORD=CART $END
 $SYSTEM TIMLIM=525600 MWORDS=200 $END
 $BASIS GBASIS=TZV NDFUNC=1 DIFFSP=.TRUE. DIFFS=.TRUE. $END
 $SCF DIRSCF=.TRUE. $END
 $STATPT NSTEP=200 $END
 $DATA
3N-[O=PTACOO-][H+]
C1
N      7.0      2.17274      0.38404      0.73968
P     15.0      0.07820     -1.34975      0.15308
N      7.0     -0.02989      1.38785      0.46434
N      7.0      1.17600      0.53661     -1.49560
C      6.0      1.68954     -0.98498      1.02799
C      6.0      2.41034      0.56538     -0.70057
C      6.0      0.54632     -0.80588     -1.56088
C      6.0      1.28186      1.40304      1.22960
C      6.0     -0.87325      0.14686      0.71300
C      6.0      0.27945      1.55172     -1.03630
H      1.0      2.44846     -1.70427      0.71237
H      1.0      1.55401     -1.11444      2.10472
H      1.0      2.89438      1.53219     -0.85344
H      1.0      3.08540     -0.21429     -1.05120
H      1.0      1.24890     -1.51404     -2.00435
H      1.0     -0.34236     -0.77221     -2.19328
H      1.0      1.05464      1.25362      2.28490
H      1.0      1.72686      2.38992      1.09138
C      6.0     -2.29934      0.52040      0.08446
H      1.0     -1.00947      0.07015      1.79633
H      1.0     -0.67427      1.52862     -1.55599
H      1.0      0.72955      2.53946     -1.14527
O      8.0     -2.92800     -0.38187     -0.45312
O      8.0     -2.52236      1.74939      0.24311
O      8.0     -0.48508     -2.71557      0.39970
H      1.0      3.04799      0.49805      1.20972
 $END
```

Figure A.37: DFT-optimized structure for 3*N*-[O=PTA-COO$^-$][H$^+$] and the input file used to calculate it and its energy.

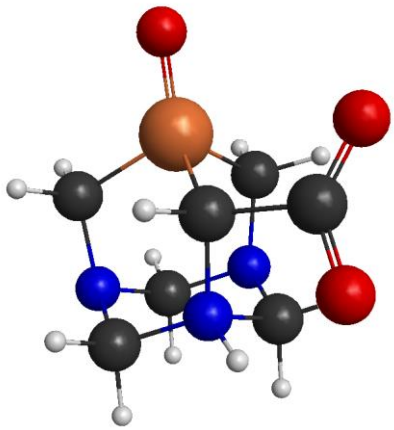

```
 $CONTRL SCFTYP=RHF RUNTYP=OPTIMIZE DFTTYP=B3LYP MAXIT=200 MULT=1 ISPHER=1
    COORD=CART $END
 $SYSTEM TIMLIM=525600 MWORDS=200 $END
 $BASIS GBASIS=TZV NDFUNC=1 DIFFSP=.TRUE. DIFFS=.TRUE. $END
 $SCF DIRSCF=.TRUE. $END
 $STATPT NSTEP=200 $END
 $DATA
5N-[O=PTACOO-][H+]
C1
N      7.0      2.05630    -0.91215    -0.75770
P     15.0      0.66248     1.58124    -0.53463
N      7.0     -0.27703    -1.05636    -0.09897
N      7.0      1.38935    -0.25230     1.50519
C      6.0      1.96441     0.44262    -1.34201
C      6.0      2.42778    -0.85568     0.66355
C      6.0      1.20268     1.18756     1.23785
C      6.0      0.84519    -1.66859    -0.91507
C      6.0     -0.70588     0.30458    -0.61811
C      6.0      0.17210    -0.98814     1.36892
H      1.0      2.94767     0.91180    -1.26336
H      1.0      1.74399     0.35182    -2.40891
H      1.0      2.61112    -1.87439     1.01458
H      1.0      3.35086    -0.28632     0.76866
H      1.0      2.14240     1.70435     1.44495
H      1.0      0.45380     1.58571     1.92504
H      1.0      0.52594    -1.68933    -1.95671
H      1.0      0.98932    -2.69067    -0.55795
C      6.0     -2.07053     0.62297     0.13700
H      1.0     -0.95601     0.15150    -1.67382
H      1.0     -0.64721    -0.53810     1.92232
H      1.0      0.30728    -2.02231     1.69094
O      8.0     -2.29488     1.81020     0.38321
O      8.0     -2.70848    -0.43476     0.37908
O      8.0      0.66541     3.08642    -0.74065
H      1.0     -1.12377    -1.47967    -0.03436
 $END
```

Figure A.38: DFT-optimized structure for 5*N*-[O=PTA-COO$^-$][H$^+$] and the input file used to calculate it and its energy.

Table A.1 Sample and crystal data for bjf496a, **17**.

Identification code	bjf496a	
Chemical formula	$C_{1.50}H_3Cl_{1.50}NNi_{0.75}P$	
Formula weight	163.23 g/mol	
Temperature	100(2) K	
Wavelength	0.71073 Å	
Crystal system	orthorhombic	
Space group	C m c a	
Unit cell dimensions	a = 9.530(9) Å	α = 90°
	b = 7.258(7) Å	β = 90°
	c = 23.98(2) Å	γ = 90°
Volume	1659.(3) $Å^3$	
Z	16	
Density (calculated)	2.615 g/cm^3	
Absorption coefficient	4.720 mm^{-1}	
F(000)	1288	

Table A.2 Data collection and structure refinement for bjf496a, **17**.

Theta range for data collection	1.70 to 28.01°	
Index ranges	-12<=h<=12, -9<=k<=9, -31<=l<=31	
Reflections collected	10378	
Independent reflections	1053 [R(int) = 0.1736]	
Coverage of independent reflections	99.4%	
Absorption correction	multi-scan	
Refinement method	Full-matrix least-squares on F^2	
Refinement program	SHELXL-2014/7 (Sheldrick, 2014)	
Function minimized	$\Sigma\, w(F_o^2 - F_c^2)^2$	
Data / restraints / parameters	1053 / 0 / 68	
Goodness-of-fit on F^2	1.163	
Final R indices	728 data; I>2σ(I)	R1 = 0.0908, wR2 = 0.2005
	all data	R1 = 0.1278, wR2 = 0.2157
Weighting scheme	$w=1/[\sigma^2(F_o^2)+(0.0709P)^2+38.3283P]$ where $P=(F_o^2+2F_c^2)/3$	
Extinction coefficient	0.0140(20)	
Largest diff. peak and hole	1.413 and -1.056 $eÅ^{-3}$	
R.M.S. deviation from mean	0.193 $eÅ^{-3}$	

Table A.3 Bond lengths (Å) for bjf496a, **17**.

Ni1-Ni1	0.34(3)	Ni1-Cl1	2.135(3)
Ni1-Cl1	2.135(3)	Ni1-P1	2.178(3)
Ni1-P1	2.178(3)	Cl1-Ni1	2.135(3)
P1-C1	1.804(11)	P1-C1	1.804(11)
P1-C2	1.818(13)	P1-Ni1	2.178(3)
N1-C4	1.429(10)	N1-C3	1.457(11)
N1-C1	1.470(9)	N2-C3	1.433(14)
N2-C3	1.433(14)	N2-C2	1.479(15)
C1-H1A	0.99	C1-H1B	0.99
C2-H2A	0.79(9)	C3-H3A	0.99
C3-H3B	0.99	C4-N1	1.429(10)
C4-H4A	0.99	C4-H4B	0.99

Table A.4 Bond angles (°) for bjf496a, **17**.

Ni1-Ni1-Cl1	85.5(5)	Ni1-Ni1-Cl1	85.5(5)
Cl1-Ni1-Cl1	171.0(9)	Ni1-Ni1-P1	85.6(5)
Cl1-Ni1-P1	86.97(13)	Cl1-Ni1-P1	92.34(13)
Ni1-Ni1-P1	85.6(5)	Cl1-Ni1-P1	92.34(13)
Cl1-Ni1-P1	86.97(13)	P1-Ni1-P1	171.2(9)
Ni1-Cl1-Ni1	9.0(9)	C1-P1-C1	98.5(6)
C1-P1-C2	99.1(4)	C1-P1-C2	99.1(4)
C1-P1-Ni1	121.1(5)	C1-P1-Ni1	113.5(5)
C2-P1-Ni1	121.3(4)	C1-P1-Ni1	113.5(5)
C1-P1-Ni1	121.1(5)	C2-P1-Ni1	121.3(4)
Ni1-P1-Ni1	8.8(9)	C4-N1-C3	108.1(9)
C4-N1-C1	110.7(7)	C3-N1-C1	111.2(6)
C3-N2-C3	107.5(10)	C3-N2-C2	111.3(6)
C3-N2-C2	111.3(6)	N1-C1-P1	111.6(7)
N1-C1-H1A	109.3	P1-C1-H1A	109.3
N1-C1-H1B	109.3	P1-C1-H1B	109.3
H1A-C1-H1B	108.0	N2-C2-P1	111.3(8)
N2-C2-H2A	112.(8)	P1-C2-H2A	114.(8)
N2-C3-N1	114.9(8)	N2-C3-H3A	108.5
N1-C3-H3A	108.5	N2-C3-H3B	108.5
N1-C3-H3B	108.5	H3A-C3-H3B	107.5
N1-C4-N1	115.2(9)	N1-C4-H4A	108.5
N1-C4-H4A	108.5	N1-C4-H4B	108.5
N1-C4-H4B	108.5	H4A-C4-H4B	107.5

Table A.5 Sample and crystal data for bjf495a, **18**.

Identification code	bjf495a	
Chemical formula	$C_{38}H_{70}Cl_4N_{18}Ni_2O_2P_6$	
Formula weight	1256.16 g/mol	
Temperature	100(2) K	
Wavelength	0.71073 Å	
Crystal size	0.027 x 0.052 x 0.083 mm	
Crystal system	triclinic	
Space group	P -1	
Unit cell dimensions	a = 10.039(4) Å	α = 90°
	b = 11.756(5) Å	β = 90°
	c = 22.667(10) Å	γ = 92.773(9)°
Volume	2672.(2) $Å^3$	
Z	2	
Density (calculated)	1.561 g/cm^3	
Absorption coefficient	1.139 mm^{-1}	
F(000)	1308	

Table A.6 Data collection and structure refinement for bjf495a, **18**.

Theta range for data collection	0.90 to 27.50°	
Index ranges	-13<=h<=13, -15<=k<=15, -29<=l<=29	
Reflections collected	55541	
Independent reflections	12228 [R(int) = 0.4410]	
Max. and min. transmission	0.9700 and 0.9110	
Refinement method	Full-matrix least-squares on F^2	
Refinement program	SHELXL-2014/7 (Sheldrick, 2014)	
Function minimized	$\Sigma\, w(F_o^2 - F_c^2)^2$	
Data / restraints / parameters	12228 / 0 / 621	
Goodness-of-fit on F^2	0.821	
Final R indices	4462 data; I>2σ(I)	R1 = 0.1065, wR2 = 0.1738
	all data	R1 = 0.2715, wR2 = 0.2251
Weighting scheme	$w=1/[\sigma^2(F_o^2)]$ where $P=(F_o^2+2F_c^2)/3$	
Largest diff. peak and hole	1.134 and -0.894 $eÅ^{-3}$	
R.M.S. deviation from mean	0.160 $eÅ^{-3}$	

Table A.7 Bond lengths (Å) for bjf495a, **18**.

Ni1-P3	2.140(3)	Ni1-P1	2.174(3)
Ni1-P2	2.179(3)	Ni1-Cl2	2.316(3)
Ni1-Cl1	2.370(3)	Ni2-P6	2.141(3)
Ni2-P4	2.177(3)	Ni2-P5	2.177(3)
Ni2-Cl4	2.329(3)	Ni2-Cl3	2.365(3)
P1-C2	1.836(9)	P1-C1	1.848(9)
P1-C3	1.863(8)	P2-C9	1.824(9)
P2-C8	1.855(9)	P2-C7	1.854(8)
P3-C15	1.834(9)	P3-C14	1.839(9)
P3-C13	1.864(9)	P4-C20	1.827(8)
P4-C21	1.832(9)	P4-C19	1.839(9)
P5-C26	1.826(9)	P5-C25	1.828(9)
P5-C27	1.849(9)	P6-C32	1.823(9)
P6-C33	1.847(10)	P6-C31	1.856(9)
N1-C4	1.444(12)	N1-C6	1.463(11)
N1-C1	1.472(10)	N2-C4	1.480(12)
N2-C5	1.481(11)	N2-C2	1.492(11)
N3-C6	1.464(11)	N3-C3	1.467(10)
N3-C5	1.480(11)	N4-C10	1.449(11)
N4-C7	1.453(10)	N4-C12	1.483(11)
N5-C10	1.456(11)	N5-C11	1.458(11)
N5-C8	1.472(10)	N6-C11	1.447(12)
N6-C12	1.482(11)	N6-C9	1.491(10)
N7-C13	1.456(11)	N7-C18	1.453(11)
N7-C16	1.456(12)	N8-C14	1.453(11)
N8-C16	1.462(11)	N8-C17	1.483(11)
N9-C18	1.457(11)	N9-C17	1.463(12)
N9-C15	1.475(11)	N10-C19	1.466(10)
N10-C22	1.469(11)	N10-C24	1.473(11)
N11-C22	1.459(12)	N11-C20	1.486(11)
N11-C23	1.504(11)	N12-C24	1.458(12)
N12-C21	1.464(10)	N12-C23	1.487(11)
N13-C30	1.456(11)	N13-C28	1.474(11)
N13-C25	1.483(11)	N14-C29	1.441(11)
N14-C28	1.471(11)	N14-C26	1.479(10)
N15-C27	1.454(11)	N15-C29	1.467(11)
N15-C30	1.476(11)	N16-C34	1.444(12)
N16-C36	1.454(11)	N16-C31	1.491(11)
N17-C34	1.456(11)	N17-C35	1.474(11)

N17-C32	1.481(11)	N18-C35	1.443(11)
N18-C36	1.467(10)	N18-C33	1.489(12)
C1-H1A	0.99	C1-H1B	0.99
C2-H2A	0.99	C2-H2B	0.99
C3-H3A	0.99	C3-H3B	0.99
C4-H4A	0.99	C4-H4B	0.99
C5-H5A	0.99	C5-H5B	0.99
C6-H6A	0.99	C6-H6B	0.99
C7-H7A	0.99	C7-H7B	0.99
C8-H8A	0.99	C8-H8B	0.99
C9-H9A	0.99	C9-H9B	0.99
C10-H10A	0.95	C11-H11A	0.95
C12-H12A	0.99	C12-H12B	0.99
C13-H13A	0.99	C13-H13B	0.99
C14-H14A	0.99	C14-H14B	0.99
C15-H15A	0.99	C15-H15B	0.99
C16-H16A	0.99	C16-H16B	0.99
C17-H17A	0.99	C17-H17B	0.99
C18-H18A	0.99	C18-H18B	0.99
C19-H19A	0.99	C19-H19B	0.99
C20-H20A	0.99	C20-H20B	0.99
C21-H21A	0.99	C21-H21B	0.99
C22-H22A	0.99	C22-H22B	0.99
C23-H23A	0.99	C23-H23B	0.99
C24-H24A	0.99	C24-H24B	0.99
C25-H25A	0.99	C25-H25B	0.99
C26-H26A	0.99	C26-H26B	0.99
C27-H27A	0.99	C27-H27B	0.99
C28-H28A	0.99	C28-H28B	0.99
C29-H29A	0.99	C29-H29B	0.99
C30-H30A	0.99	C30-H30B	0.99
C31-H31A	0.99	C31-H31B	0.99
C32-H32A	0.99	C32-H32B	0.99
C33-H33A	0.99	C33-H33B	0.99
C34-H34A	0.99	C34-H34B	0.99
C35-H35A	0.99	C35-H35B	0.99
C36-H36A	0.99	C36-H36B	0.99
C1S-O1S	1.440(14)	C2S-O2S	1.434(13)

Table A.8 Bond angles (°) for bjf495a, **18**.

P3-Ni1-P1	96.79(10)	P3-Ni1-P2	94.42(10)
P1-Ni1-P2	168.76(11)	P3-Ni1-Cl2	133.70(11)
P1-Ni1-Cl2	87.43(10)	P2-Ni1-Cl2	85.43(9)
P3-Ni1-Cl1	113.24(10)	P1-Ni1-Cl1	86.14(10)
P2-Ni1-Cl1	88.69(9)	Cl2-Ni1-Cl1	113.05(11)
P6-Ni2-P4	96.81(10)	P6-Ni2-P5	94.43(10)
P4-Ni2-P5	168.72(11)	P6-Ni2-Cl4	133.60(11)
P4-Ni2-Cl4	87.44(10)	P5-Ni2-Cl4	85.46(10)
P6-Ni2-Cl3	113.32(11)	P4-Ni2-Cl3	86.16(9)
P5-Ni2-Cl3	88.57(9)	Cl4-Ni2-Cl3	113.06(11)
C2-P1-C1	98.8(4)	C2-P1-C3	100.6(4)
C1-P1-C3	97.5(4)	C2-P1-Ni1	121.2(3)
C1-P1-Ni1	113.4(3)	C3-P1-Ni1	120.9(3)
C9-P2-C8	98.5(4)	C9-P2-C7	98.7(4)
C8-P2-C7	98.8(4)	C9-P2-Ni1	124.2(3)
C8-P2-Ni1	111.5(3)	C7-P2-Ni1	120.4(3)
C15-P3-C14	99.2(4)	C15-P3-C13	95.3(4)
C14-P3-C13	97.7(4)	C15-P3-Ni1	121.4(3)
C14-P3-Ni1	115.3(3)	C13-P3-Ni1	122.8(3)
C20-P4-C21	100.2(4)	C20-P4-C19	98.2(4)
C21-P4-C19	98.0(4)	C20-P4-Ni2	121.1(3)
C21-P4-Ni2	121.5(3)	C19-P4-Ni2	113.2(3)
C26-P5-C25	99.4(4)	C26-P5-C27	98.5(5)
C25-P5-C27	98.1(4)	C26-P5-Ni2	120.3(3)
C25-P5-Ni2	123.9(3)	C27-P5-Ni2	111.8(3)
C32-P6-C33	99.0(5)	C32-P6-C31	99.4(4)
C33-P6-C31	95.8(4)	C32-P6-Ni2	114.8(3)
C33-P6-Ni2	121.3(3)	C31-P6-Ni2	121.8(3)
C4-N1-C6	107.6(7)	C4-N1-C1	113.2(8)
C6-N1-C1	111.0(7)	C4-N2-C5	107.0(7)
C4-N2-C2	110.7(7)	C5-N2-C2	110.5(7)
C6-N3-C3	111.5(7)	C6-N3-C5	108.4(7)
C3-N3-C5	112.1(7)	C10-N4-C7	111.8(7)
C10-N4-C12	108.3(8)	C7-N4-C12	111.7(7)
C10-N5-C11	108.1(8)	C10-N5-C8	110.4(7)
C11-N5-C8	111.2(7)	C11-N6-C12	109.0(7)
C11-N6-C9	111.7(7)	C12-N6-C9	110.5(7)
C13-N7-C18	109.9(7)	C13-N7-C16	110.7(7)
C18-N7-C16	106.8(7)	C14-N8-C16	110.2(8)
C14-N8-C17	111.5(7)	C16-N8-C17	108.0(7)

C18-N9-C17	108.9(7)	C18-N9-C15	111.4(7)
C17-N9-C15	111.6(7)	C19-N10-C22	111.1(7)
C19-N10-C24	111.9(7)	C22-N10-C24	107.7(7)
C22-N11-C20	111.1(7)	C22-N11-C23	108.8(7)
C20-N11-C23	110.8(7)	C24-N12-C21	110.6(7)
C24-N12-C23	107.6(7)	C21-N12-C23	111.6(7)
C30-N13-C28	108.7(7)	C30-N13-C25	111.1(8)
C28-N13-C25	111.9(7)	C29-N14-C28	108.2(7)
C29-N14-C26	111.4(7)	C28-N14-C26	110.4(7)
C27-N15-C29	110.9(7)	C27-N15-C30	110.6(7)
C29-N15-C30	107.7(8)	C34-N16-C36	107.9(7)
C34-N16-C31	110.6(8)	C36-N16-C31	109.5(7)
C34-N17-C35	108.4(7)	C34-N17-C32	109.9(7)
C35-N17-C32	110.1(7)	C35-N18-C36	109.4(7)
C35-N18-C33	110.6(7)	C36-N18-C33	108.8(7)
N1-C1-P1	111.1(6)	N1-C1-H1A	109.4
P1-C1-H1A	109.4	N1-C1-H1B	109.4
P1-C1-H1B	109.4	H1A-C1-H1B	108.0
N2-C2-P1	111.9(6)	N2-C2-H2A	109.2
P1-C2-H2A	109.2	N2-C2-H2B	109.2
P1-C2-H2B	109.2	H2A-C2-H2B	107.9
N3-C3-P1	110.2(6)	N3-C3-H3A	109.6
P1-C3-H3A	109.6	N3-C3-H3B	109.6
P1-C3-H3B	109.6	H3A-C3-H3B	108.1
N1-C4-N2	115.6(8)	N1-C4-H4A	108.4
N2-C4-H4A	108.4	N1-C4-H4B	108.4
N2-C4-H4B	108.4	H4A-C4-H4B	107.4
N3-C5-N2	114.6(7)	N3-C5-H5A	108.6
N2-C5-H5A	108.6	N3-C5-H5B	108.6
N2-C5-H5B	108.6	H5A-C5-H5B	107.6
N1-C6-N3	114.2(7)	N1-C6-H6A	108.7
N3-C6-H6A	108.7	N1-C6-H6B	108.7
N3-C6-H6B	108.7	H6A-C6-H6B	107.6
N4-C7-P2	110.9(6)	N4-C7-H7A	109.5
P2-C7-H7A	109.5	N4-C7-H7B	109.5
P2-C7-H7B	109.5	H7A-C7-H7B	108.1
N5-C8-P2	111.2(6)	N5-C8-H8A	109.4
P2-C8-H8A	109.4	N5-C8-H8B	109.4
P2-C8-H8B	109.4	H8A-C8-H8B	108.0
N6-C9-P2	111.5(6)	N6-C9-H9A	109.3
P2-C9-H9A	109.3	N6-C9-H9B	109.3

P2-C9-H9B	109.3	H9A-C9-H9B	108.0
N4-C10-N5	115.9(7)	N4-C10-H10A	122.0
N5-C10-H10A	122.0	N6-C11-N5	115.0(8)
N6-C11-H11A	122.5	N5-C11-H11A	122.5
N6-C12-N4	112.6(7)	N6-C12-H12A	109.1
N4-C12-H12A	109.1	N6-C12-H12B	109.1
N4-C12-H12B	109.1	H12A-C12-H12B	107.8
N7-C13-P3	113.8(6)	N7-C13-H13A	108.8
P3-C13-H13A	108.8	N7-C13-H13B	108.8
P3-C13-H13B	108.8	H13A-C13-H13B	107.7
N8-C14-P3	112.8(6)	N8-C14-H14A	109.0
P3-C14-H14A	109.0	N8-C14-H14B	109.0
P3-C14-H14B	109.0	H14A-C14-H14B	107.8
N9-C15-P3	112.1(6)	N9-C15-H15A	109.2
P3-C15-H15A	109.2	N9-C15-H15B	109.2
P3-C15-H15B	109.2	H15A-C15-H15B	107.9
N7-C16-N8	116.9(7)	N7-C16-H16A	108.1
N8-C16-H16A	108.1	N7-C16-H16B	108.1
N8-C16-H16B	108.1	H16A-C16-H16B	107.3
N9-C17-N8	113.1(8)	N9-C17-H17A	109.0
N8-C17-H17A	109.0	N9-C17-H17B	109.0
N8-C17-H17B	109.0	H17A-C17-H17B	107.8
N9-C18-N7	115.3(8)	N9-C18-H18A	108.4
N7-C18-H18A	108.4	N9-C18-H18B	108.4
N7-C18-H18B	108.4	H18A-C18-H18B	107.5
N10-C19-P4	111.6(6)	N10-C19-H19A	109.3
P4-C19-H19A	109.3	N10-C19-H19B	109.3
P4-C19-H19B	109.3	H19A-C19-H19B	108.0
N11-C20-P4	111.5(6)	N11-C20-H20A	109.3
P4-C20-H20A	109.3	N11-C20-H20B	109.3
P4-C20-H20B	109.3	H20A-C20-H20B	108.0
N12-C21-P4	112.5(6)	N12-C21-H21A	109.1
P4-C21-H21A	109.1	N12-C21-H21B	109.1
P4-C21-H21B	109.1	H21A-C21-H21B	107.8
N11-C22-N10	114.3(8)	N11-C22-H22A	108.7
N10-C22-H22A	108.7	N11-C22-H22B	108.7
N10-C22-H22B	108.7	H22A-C22-H22B	107.6
N12-C23-N11	113.2(7)	N12-C23-H23A	108.9
N11-C23-H23A	108.9	N12-C23-H23B	108.9
N11-C23-H23B	108.9	H23A-C23-H23B	107.8
N12-C24-N10	115.4(8)	N12-C24-H24A	108.4

N10-C24-H24A	108.4	N12-C24-H24B	108.4
N10-C24-H24B	108.4	H24A-C24-H24B	107.5
N13-C25-P5	110.9(6)	N13-C25-H25A	109.5
P5-C25-H25A	109.5	N13-C25-H25B	109.5
P5-C25-H25B	109.5	H25A-C25-H25B	108.1
N14-C26-P5	111.9(6)	N14-C26-H26A	109.2
P5-C26-H26A	109.2	N14-C26-H26B	109.2
P5-C26-H26B	109.2	H26A-C26-H26B	107.9
N15-C27-P5	112.2(6)	N15-C27-H27A	109.2
P5-C27-H27A	109.2	N15-C27-H27B	109.2
P5-C27-H27B	109.2	H27A-C27-H27B	107.9
N14-C28-N13	113.8(7)	N14-C28-H28A	108.8
N13-C28-H28A	108.8	N14-C28-H28B	108.8
N13-C28-H28B	108.8	H28A-C28-H28B	107.7
N14-C29-N15	115.9(8)	N14-C29-H29A	108.3
N15-C29-H29A	108.3	N14-C29-H29B	108.3
N15-C29-H29B	108.3	H29A-C29-H29B	107.4
N13-C30-N15	114.3(7)	N13-C30-H30A	108.7
N15-C30-H30A	108.7	N13-C30-H30B	108.7
N15-C30-H30B	108.7	H30A-C30-H30B	107.6
N16-C31-P6	112.0(6)	N16-C31-H31A	109.2
P6-C31-H31A	109.2	N16-C31-H31B	109.2
P6-C31-H31B	109.2	H31A-C31-H31B	107.9
N17-C32-P6	112.4(6)	N17-C32-H32A	109.1
P6-C32-H32A	109.1	N17-C32-H32B	109.1
P6-C32-H32B	109.1	H32A-C32-H32B	107.8
N18-C33-P6	112.7(7)	N18-C33-H33A	109.0
P6-C33-H33A	109.0	N18-C33-H33B	109.0
P6-C33-H33B	109.0	H33A-C33-H33B	107.8
N16-C34-N17	117.4(8)	N16-C34-H34A	108.0
N17-C34-H34A	108.0	N16-C34-H34B	108.0
N17-C34-H34B	108.0	H34A-C34-H34B	107.2
N18-C35-N17	115.3(7)	N18-C35-H35A	108.5
N17-C35-H35A	108.5	N18-C35-H35B	108.5
N17-C35-H35B	108.5	H35A-C35-H35B	107.5
N16-C36-N18	115.9(7)	N16-C36-H36A	108.3
N18-C36-H36A	108.3	N16-C36-H36B	108.3
N18-C36-H36B	108.3	H36A-C36-H36B	107.4

Table A.9 Sample and crystal data for bjf471a, **20**.

Identification code	bjf471a	
Chemical formula	$C_{6.33}H_{12}Ce_{0.33}N_4O_{4.33}P$	
Formula weight	291.21 g/mol	
Temperature	100(2) K	
Wavelength	0.71073 Å	
Crystal size	0.040 x 0.090 x 0.100 mm	
Crystal system	trigonal	
Space group	P 3 1 c	
Unit cell dimensions	a = 15.4755(10) Å	α = 90°
	b = 15.4755(10) Å	β = 90°
	c = 7.7926(5) Å	γ = 120°
Volume	1616.2(2) $Å^3$	
Z	6	
Density (calculated)	1.795 g/cm^3	
Absorption coefficient	1.637 mm^{-1}	
F(000)	882	

Table A.10 Data collection and structure refinement for bjf471a, **20**.

Theta range for data collection	1.52 to 32.60°	
Index ranges	-23<=h<=22, -23<=k<=23, -11<=l<=11	
Reflections collected	34217	
Independent reflections	3830 [R(int) = 0.1028]	
Max. and min. transmission	0.9370 and 0.8530	
Refinement method	Full-matrix least-squares on F^2	
Refinement program	SHELXL-2014/7 (Sheldrick, 2014)	
Function minimized	$\Sigma\, w(F_o^2 - F_c^2)^2$	
Data / restraints / parameters	3830 / 1 / 151	
Goodness-of-fit on F^2	1.027	
Final R indices	3213 data; I>2σ(I)	R1 = 0.0383, wR2 = 0.0694
	all data	R1 = 0.0578, wR2 = 0.0756
Weighting scheme	$w=1/[\sigma^2(F_o^2)+(0.0318P)^2]$ where $P=(F_o^2+2F_c^2)/3$	
Absolute structure parameter	-0.0(0)	
Largest diff. peak and hole	1.520 and -1.182 $eÅ^{-3}$	
R.M.S. deviation from mean	0.123 $eÅ^{-3}$	

Table A.11 Bond lengths (Å) for bjf471a, **20**.

Ce1-O1	2.399(3)	Ce1-O1	2.399(3)
Ce1-O1	2.399(3)	Ce1-O2	2.566(4)
Ce1-O2	2.566(4)	Ce1-O2	2.566(4)
Ce1-O4	2.611(4)	Ce1-O4	2.611(4)
Ce1-O4	2.612(4)	Ce1-N4	3.016(4)
Ce1-N4	3.016(4)	Ce1-N4	3.016(4)
O1-P1	1.500(4)	O1S-C1S	1.322(15)
O2-N4	1.275(5)	O3-N4	1.219(5)
O4-N4	1.260(5)	P1-C3	1.803(5)
P1-C1	1.807(5)	P1-C2	1.810(5)
N1-C6	1.469(7)	N1-C1	1.485(6)
N1-C4	1.485(7)	N2-C4	1.473(7)
N2-C5	1.475(7)	N2-C2	1.479(7)
N3-C6	1.460(7)	N3-C3	1.473(7)
N3-C5	1.475(7)	N4-O4	1.260(5)
C1S-O1S	1.322(15)	C1S-O1S	1.322(15)
C1-H1A	0.99	C1-H1B	0.99
C2-H2A	0.99	C2-H2B	0.99
C3-H3A	0.99	C3-H3B	0.99
C4-H4A	0.99	C4-H4B	0.99
C5-H5A	0.99	C5-H5B	0.99
C6-H6A	0.99	C6-H6B	0.99

Table A.12 Bond angles (°) for bjf471a, **20**.

O1-Ce1-O1	82.31(13)	O1-Ce1-O1	82.31(13)
O1-Ce1-O1	82.31(13)	O1-Ce1-O2	82.76(13)
O1-Ce1-O2	146.16(12)	O1-Ce1-O2	125.30(12)
O1-Ce1-O2	125.30(12)	O1-Ce1-O2	82.76(13)
O1-Ce1-O2	146.16(12)	O2-Ce1-O2	81.45(14)
O1-Ce1-O2	146.16(12)	O1-Ce1-O2	125.30(12)
O1-Ce1-O2	82.76(13)	O2-Ce1-O2	81.45(14)
O2-Ce1-O2	81.45(14)	O1-Ce1-O4	76.20(11)
O1-Ce1-O4	75.41(12)	O1-Ce1-O4	150.75(12)
O2-Ce1-O4	71.61(12)	O2-Ce1-O4	49.12(11)
O2-Ce1-O4	125.70(12)	O1-Ce1-O4	75.41(12)
O1-Ce1-O4	150.75(12)	O1-Ce1-O4	76.20(11)
O2-Ce1-O4	49.12(11)	O2-Ce1-O4	125.70(12)
O2-Ce1-O4	71.61(12)	O4-Ce1-O4	116.26(5)

O1-Ce1-O4	150.75(12)	O1-Ce1-O4	76.20(11)
O1-Ce1-O4	75.41(12)	O2-Ce1-O4	125.70(12)
O2-Ce1-O4	71.61(12)	O2-Ce1-O4	49.12(11)
O4-Ce1-O4	116.26(5)	O4-Ce1-O4	116.26(5)
O1-Ce1-N4	75.74(12)	O1-Ce1-N4	157.19(12)
O1-Ce1-N4	100.57(12)	O2-Ce1-N4	24.77(11)
O2-Ce1-N4	104.88(13)	O2-Ce1-N4	77.42(12)
O4-Ce1-N4	93.18(11)	O4-Ce1-N4	24.54(11)
O4-Ce1-N4	126.54(11)	O1-Ce1-N4	100.57(12)
O1-Ce1-N4	75.74(12)	O1-Ce1-N4	157.19(12)
O2-Ce1-N4	77.42(12)	O2-Ce1-N4	24.77(11)
O2-Ce1-N4	104.88(13)	O4-Ce1-N4	24.54(11)
O4-Ce1-N4	126.54(11)	O4-Ce1-N4	93.18(11)
N4-Ce1-N4	102.06(10)	O1-Ce1-N4	157.19(12)
O1-Ce1-N4	100.57(12)	O1-Ce1-N4	75.74(12)
O2-Ce1-N4	104.88(13)	O2-Ce1-N4	77.42(12)
O2-Ce1-N4	24.77(11)	O4-Ce1-N4	126.54(11)
O4-Ce1-N4	93.18(11)	O4-Ce1-N4	24.54(11)
N4-Ce1-N4	102.06(10)	N4-Ce1-N4	102.06(10)
P1-O1-Ce1	143.4(2)	N4-O2-Ce1	97.8(3)
N4-O4-Ce1	96.0(3)	O1-P1-C3	116.4(2)
O1-P1-C1	115.8(2)	C3-P1-C1	101.2(3)
O1-P1-C2	117.3(2)	C3-P1-C2	102.1(2)
C1-P1-C2	101.5(3)	C6-N1-C1	110.2(4)
C6-N1-C4	108.1(4)	C1-N1-C4	110.4(4)
C4-N2-C5	109.1(4)	C4-N2-C2	111.4(4)
C5-N2-C2	111.2(4)	C6-N3-C3	110.8(4)
C6-N3-C5	108.3(4)	C3-N3-C5	110.7(4)
O3-N4-O4	122.5(4)	O3-N4-O2	121.3(4)
O4-N4-O2	116.2(4)	O3-N4-Ce1	171.9(3)
O4-N4-Ce1	59.4(2)	O2-N4-Ce1	57.4(2)
O1S-C1S-O1S	97.5(12)	O1S-C1S-O1S	97.5(12)
O1S-C1S-O1S	97.5(12)	N1-C1-P1	109.9(3)
N1-C1-H1A	109.7	P1-C1-H1A	109.7
N1-C1-H1B	109.7	P1-C1-H1B	109.7
H1A-C1-H1B	108.2	N2-C2-P1	108.6(3)
N2-C2-H2A	110.0	P1-C2-H2A	110.0
N2-C2-H2B	110.0	P1-C2-H2B	110.0
H2A-C2-H2B	108.3	N3-C3-P1	109.6(4)
N3-C3-H3A	109.7	P1-C3-H3A	109.7
N3-C3-H3B	109.7	P1-C3-H3B	109.7

H3A-C3-H3B	108.2	N2-C4-N1	114.1(4)
N2-C4-H4A	108.7	N1-C4-H4A	108.7
N2-C4-H4B	108.7	N1-C4-H4B	108.7
H4A-C4-H4B	107.6	N2-C5-N3	114.3(4)
N2-C5-H5A	108.7	N3-C5-H5A	108.7
N2-C5-H5B	108.7	N3-C5-H5B	108.7
H5A-C5-H5B	107.6	N3-C6-N1	116.2(4)
N3-C6-H6A	108.2	N1-C6-H6A	108.2
N3-C6-H6B	108.2	N1-C6-H6B	108.2
H6A-C6-H6B	107.4		

Bio

Travis David Cournoyer was born in Woonsocket, Rhode Island in 1990. He grew up working for his father as a mechanic at Roger's Tires Front End Care Center, but discovered his love of chemistry as soon as he enrolled in college at Roger Williams University in Bristol, RI. He obtained his Bachelor of Scheince degree in Chemistry with Mathematics as a minor while conducting research with dye-sensitized solar cells (DSSCs) under the direction of Dr. Cliff J. Timpson. He then enrolled at the University of Nevada, Reno where he later joined Dr. Brian J. Frost's research group and realized a fond appreciation for green chemistry. His research focused on the synthesis of upper-rim PTA amides for cancer research as well as the precipitation of rare earth metals from aqueous media for potential use in the extraction and/or separation of rare earths during their mineral extraction. In 2015, Travis embarked on a 15 month internship with Tesla Motors, Inc. to conduct R&D on battery pack components for the Model 3. He then started working full time for Faraday Future in Los Angeles as a battery hardware design release engineer 9 months prior to his graduation from UNR. He would love to welcome any questions, comments, or counsel. (Contact: tcournoyer098@gmail.com)

TRAVIS COURNOYER

American • Clean Driver's License • BD: 02/10/1990

Education

University of Nevada, Reno (UNR) – Reno, NV **Aug 2017**
Ph.D. in Chemistry
Focus: Green Chemistry: Synthesis & Characterization of Water-Soluble Phosphines & Derivatives

Roger Williams University (RWU) – Bristol, RI **May 2012**
Bachelor of Science in Chemistry
Focus: Construction of Solar Cells with Microwave Radiation
Minor: Mathematics

Professional Experience

- **Design Release Engineer [*Battery Hardware*], Faraday Future** **Nov 2016 – *current***
  Design release engineering for battery pack adhesives, coatings, sealants, fluids, and intumescent materials.

- **Intern – Tesla Motors, Inc. (Battery Technology)** **Aug 2015 – Oct 2016**
  Adhesive & coating testing, validation, and process development. Design, construction, and SOP development for the quality assurance laboratory at the "Gigafactory." Worked closely with the Tesla Environment Health & Safety representative to assist with construction of Chemical Hygiene Plan and Safety Data Sheet manifest.

- **Automotive Mechanic (Roger's Tires / Woonsocket, RI)** **Feb 2006 – May 2012**
  Front end and suspension work for vehicles without a bias on make or model.

Research and Teaching Experience

- **Research Assistant, Brian J. Frost, UNR** **Apr 2014 – Aug 2017**

  Synthesize and characterize water-soluble organometallic compounds while maintaining a safe, clean, organized work environment. Also, mentor younger undergraduate research students.

- **Teaching Assistant, UNR** **Aug 2012 – May 2016**

  Courses: General Chemistry I & II Lab (CHEM 121L & 122L), General Chemistry for Scientists and Engineers I & II Lab (CHEM 201L & 202L), Advanced Chemical Synthesis Lab (CHEM 435R).

- **Research Assistant, Cliff J. Timpson, RWU** **Aug 2008 – May 2012**

  Synthesized and characterized ruthenium dyes for incorporation into solar cells constructed *via* microwave radiation while maintaining safe, clean, organized working environments in the laboratory and training new members to the research group.

- **ChemHelp Center Assistant Director** **Aug 2014 – Dec 2014**

  Tutor students in courses ranging from general chemistry through advanced organic, inorganic, and physical chemistry courses. Also, as assistant manager, ensure students are receiving the help they need from all tutors in the ChemHelp center, organize Excel macros to organize student sign-in data to investigate trends, and routinely report the condition of the center to the ChemHelp center Director.

Awards and Certifications

- Jerry & Betty Wilson Graduate Scholarship (UNR, 2016)
- OSHA 10 Hour Construction (Tesla Motors, 2016) *[License: 17733862]*
- Graduate Student Research Grant (UNR, 2015)
- Gene and Carla LeMay Summer Research Scholarship (UNR, 2013)
- CEED Student Research Grant (RWU, 2011 / 2012)
- Rhode Island Space Grant Consortium (RWU, 2011)
- CITI Physical Science Responsible Conduct of Research Certified (RWU, 2011)